MODELLING OCEAN CIRCULATION WITH THE LARGE-SCALE SEMI-GEOSTROPHIC EQUATIONS

A thesis presented for the degree of
Doctor of Philosophy of the University of London
and the
Diploma of Imperial College
by

James Robert Shepherd

Department of Mathematics
Imperial College of Science, Technology and Medicine
London SW7 2BZ

October 1999

Abstract

The Large-scale Semi-Geostrophic Equations (LSGE, Salmon[73]) are three-dimensional equations valid for an ocean with a rigid lid and length scales much greater than the internal deformation radius (about $40km$).

In this thesis I reduce the LSGE to a pair of two-dimensional equations via the ansatz that the temperature is independent of the vertical co-ordinate. I refer to these as the Depth-Independent-Temperature (DIT) equations. Whilst this is regarded as a paradigm for the entire ocean, the reduction is similar in spirit to that utilised by many authors for modelling the mixed layer of the ocean. The equations of this thesis differ from the work of such mixed layer models because they involve no *ad hoc* vertical averaging and so solutions to these equations are also solutions to the full three-dimensional LSGE. The DIT are arguably the simplest equations for ocean circulation to include the effects of inertia, topography and baroclinicity.

The DIT are studied both analytically and numerically. It is shown that the model exhibits baroclinic instabilities and analogies are drawn with classical Rayleigh-Bénard convection. It is shown that both viscosity and thermal diffusivity are required to avert an ultra-violet catastrophe. Numerical simulations of turbulence demonstrate that the long-time behaviour resembles barotropic flow and that the temperature is reduced to the role of a passive tracer unless large-scale thermal structure is imposed externally on the flow.

One of the advantages of the current model over the more widely used quasi-geostrophic models is that there is no restriction on the vertical extent of the bottom topography. This allows the simulation of idealised oceanic basin circulations in which the depth of the ocean vanishes smoothly at boundaries. These ocean simulations are used to study the sensitivity of the model to the Rossby Number, Ekman Number and forcing parameters. Comparison of a barotropic and a DIT ocean reveals the influence of baroclinicity in the latter model. Characteristic features of the Gulf Stream such as meandering, recirculation gyres and the shedding of warm and cold core rings are reproduced by the DIT model and the simple nature of the equations permits an interpretation of these features.

Acknowledgements

First and foremost I should like to express my gratitude to Dr Rupert Ford who has somehow managed to steer me through three years of a mathematical adventure. I should also thank Dr Rick Salmon, not only for giving me something to study by inventing the LSGE in the first place, but also for a helpful suggestion along the way.

Thanks to all my friends who have helped me to retain at least some of the little sanity I had when I started. In no particular order: Dawn, David, David, Gavin, Will, Steve, Martin, Michael, Sioned, James, John, Gowshihan, $\Theta o \delta \omega \rho o \varsigma$, Andreas, Adam and Jeff.

One friend has had to put up with me both at home and at IC, so I owe a special debt of gratitude to Mark Blyth.

Financial support from EPSRC is gratefully acknowledged.

Finally, a special thank you to my family: Emma, Kate and Dad for laughing at me when I needed it and Mum for lemon meringue pie and an annual supply of mince pies without which I know I would not have got this far!

Preface



ceans cover 71% of the Earth's surface. They serve as a source of food, as a highway for commercial ships and as a vital component of the weather and climate systems. Most human beings live on, or near, coastlines and human history is closely linked to the oceans. Oceanography is the study of all aspects of the oceans including their chemistry, biology and their physical properties such as temperature, currents, tides, waves and depth. Mathematics has played an important role in all of these areas. The aims of oceanography are twofold: to understand the present state of the oceans and to predict what will happen to them in the future.

Humans have observed the oceans since ancient times but oceanography, as a science, did not begin until the middle of the nineteenth century. The founder of oceanography is often regarded to be Matthew Fontaine Maury of the USA Navy. In 1842 he was appointed as head of the Charts and Instruments Depot (the forerunner of the USA Naval Office). He began a coordinated effort to map the major currents of the oceans (particularly the North Atlantic[1]) by compiling the journey logs of all ships leaving and entering the country. In 1848 Maury published the first charts of the major wind and current fields of the North Atlantic. Maury's principal concern was to reduce journey times for commercial and passenger ships. In the latter half of the nineteenth century the sea-journey of the New Yorker travelling to San Francisco (before the construction of the Panama Canal) was reduced by 47 days.

Oceanography became firmly established as a scientific discipline with the 1872-76 voyage of the British research ship, the *Challenger*, whose sole purpose was to study the oceans. Under the leadership of Sir C.W. Thomson, scientists on board charted $364 \times 10^6 km^2$ of

[1]The Atlantic Ocean is the Sea of Atlas, so named because it lies just to the East of Mount Atlas in North Africa.

ocean and discovered 4417 new biological species.

Over the last century oceanography has been studied by increasing numbers of people from increasingly diverse backgrounds. Much of the research is still funded by Maury's US Naval Office. Several academic institutes are devoted entirely to the study of the oceans. Amongst these are the Southampton Oceanography Centre and the Proudman Institute in the UK and the Scripps and Woods Hole Institutes in the USA.

This thesis is concerned with **physical oceanography** which is the study of physical characteristics of the ocean such as temperature and velocity. There are many reasons why the ability to understand and predict these properties is important. Maury's original concern with reducing travelling times is *still* a concern today. Most of the world's oil and industrial output is transported via ocean-going ships. Economic issues are of paramount importance and it is vital to transfer goods from source to destination as rapidly as possible. Additionally, the risk of losing the cargos must be minimised. Insurance markets (in particular, Lloyds[2] of London) were originally set up in the seventeenth century to insure against the loss of valuable goods (such as tea, spices and silk from the Orient) caused by ships being wrecked in violent storms. The oceans have a major role to play in the development of many of the biggest storms and help to control their path. As storm tracking and prediction has improved ships can be warned in advance and take avoiding action.

In recent years another great concern for the insurance market has also involved the ocean. Large deposits of oil have been discovered off the coast of Newfoundland in Canada. Unfortunately, these deposits lie directly in the path of massive ice-bergs which are carried southwards down the east coast of Canada by the Labrador Current from where they break off the Greenland ice-sheet. Despite consisting only of water, many ice-bergs are sufficiently massive to easily destroy an oil-rig if they should hit one. The *Titanic* was sunk by just such an ice-berg. Following the failure of several innovative efforts by the US Navy to destroy these bergs (including bombing them and coating them in black powder[3]) the original approach of the oil companies was to construct mobile rigs. These rigs would then be physically moved out of the path of an approaching ice-berg. Recently, however, in an attempt to access deeper oil-fields, there has been no viable alternative to the construction of static oil-rigs. In 1997 the world's largest single insurance policy was taken out against the risk of an ice-berg hitting and destroying the *Hyperion* oil-rig in the Newfoundland oil-field. Calculating the probability of such an event requires an understanding of the

[2]Lloyds started life as the coffee house of Edward Lloyd in Tower Street on the banks of the Thames. Wealthy gentlemen of London came to the house in order to pass time "with good company of the merchant adventurers".

[3]to hasten the absorption of heat and hence encourage more rapid melting.

Labrador Current.

The coastal regions of the Atlantic are of interest for another reason. In addition to the cold waters of the Labrador Current which are rich in nutrients such as phytoplankton, the Grand Banks are also fed by warm water from the Caribbean by the Gulf Stream which is rich in marine life. Fish feed off the phytoplankton and so are particularly numerous where the two currents meet. This has made the Grand Banks one of the world's most fertile hunting grounds for fishermen. In the fifteenth century Bristolean fishermen considered it worthwhile to cross the Atlantic from England to catch their fish. They were probably unaware of the existence of America but, following Columbus' discovery of Hispañola[4], in 1495 one of these fishermen, John Cabot, became the first European[5] to reach the American mainland.

Despite being of interest to many other groups of people, probably the most important function of the ocean is the part that it plays in the global climate system. To give an example, London, Winnipeg, Moscow and Irkutsk are all located at approximately the same longitude ($50^oN - 56^oN$) so one might expect all four cities to have similar climates. However, the average winter temperature of London is 11^oC higher than any of the other three cities[6]. This is because London is located on the eastern edge of the Atlantic whereas the other three cities are shielded by continental land masses. As a consequence, London is fed by mild, favovian air pushed across the Atlantic by the Gulf Stream which brings warm water from the Caribbean into the northern and eastern Atlantic.

Although the ocean probably does not have very much influence on day to day variations in the state of the atmosphere (namely, the weather), it certainly does have a large part to play on longer time scales. Interannual (one to ten years) and interdecadal (ten or more years) variations are, in the main, due to the ocean and atmosphere acting together as a single coupled system. Many climatological oscillations cannot be reproduced by models that consider only one or the other in isolation. The most famous of these interannual oscillations is the El-Niño Southern Oscillation (ENSO) more commonly known as just *El Niño*. This has a period of about three to ten years and results in the waters in the southern tropical Pacific[7] warming by $2-8^oC$ above normal. It is believed to be caused by a weakening in the Pacific trade winds although the whole concept of cause and effect is still an unanswered question. The most direct effect is that warm waters flow eastwards towards

[4]Today's Haiti/Dominican Republic.

[5]since the Vikings

[6]Average midday temperature in March :: London :7^oC, Moscow: -4^oC, Winnipeg: -8^oC, Irkutsk: -9^oC. To give a comparison, during an ice age, the average temperature might be only 6^oC lower than it is today.

[7]The *Pacific* was named by Magellan on account of the benign conditions (in comparison to the notoriously treacherous conditions of Cape Horn) he encountered on entering the ocean.

South America and then southwards down the coast of Peru. This phenomenon was first noticed by the Spanish conquistadors after Francisco Pizarro invaded Peru in 1535. The warm current was called "La Corriente de El Niño" by the Peruvian fishermen in the nineteenth century because it usually arrives during the Christmas period[8]. The current has had serious repercussions for the Peruvians. The warm waters increase the abundance of fish and sea-mammals in the area and they feed off the large number of anchovies to be found there. By the late 1960's the Peruvian economy was highly dependent on the anchovy catch. In fact, in 1971, Peru was the world's biggest fisher (harvesting 13 million tons) based very heavily on the one product[9]. In 1982-83 a severe El Niño current virtually wiped out the entire anchovy crop. This had devastating effects for the whole economy which collapsed. The Peruvian anchovy stock has never recovered and today El Niño forecasts are taken into account for economic planning.

The effects of El Niño are not restricted to the local Peruvian region. The 1991 El Niño was blamed for droughts in Australia and for an increase in the number of typhoons in Japan. In 1939-1940, it caused drought and famine in Bengal. With slightly less evidentiary documentation, it has been suggested that an El Niño in about 1789 caused a famine[10] in France which was one of the causes of the French Revolution and it has also been blamed for several smallpox and plague epidemics in Europe in the seventeenth century.

El Niño has been proposed as one of the factors infiuencing the frequency of hurricanes[11] and other tropical cyclones[12]. The early stages of the development of hurricanes is more directly linked to the ocean. Hurricanes take their energy from excess heat in the ocean and one of the main requirements for the formation of hurricanes is that the Sea Surface Temperature (SST) is greater than $18^{o}C$. A hurricane can be one of the most destructive natural phenomena and there is a vast industry dedicated to predicting their formation and subsequent path. In 1998 there were 14 tropical storms in the Atlantic, 10 of which became hurricanes. Seven of the tropical storms hit the USA causing an estimated $6.5 billion's worth of damage. *Hurricane Georges* alone was responsible for $5.1 billion. *Hurricane Mitch*, which formed 360 miles south of Jamaica on 22nd October 1998 and on 26th October reached its peak to become the fourth strongest Atlantic hurricane on record, made land-fall on 29th October at Honduras and killed an estimated 10–20 thousand

[8] El Niño is Spanish for Christ-child.

[9] Anchovies are used to produce fishmeal which is then exported and used as a feed supplement for livestock.

[10] The poor harvest in 1789 lead Marie Antoinette to retort to the starving peasants, "Let them eat cake".

[11] Hurricanes are named after the Carib god of evil, *Hurican*,

[12] *Hurricane* refers to a tropical cyclone in the North Atlantic in which the wind speeds exceed $121 km\ hr^{-1}$ (force 12 on the Beaufort Scale). A *typhoon* refers to exactly the same phenomenon in the West Pacific; in Australia it is called a *Willy-Willy*; elsewhere, it is simply a tropical cyclone.

people in Central America. Over one million people were displaced from their homes and 100,000 buildings were destroyed. The UN has warned that the economies of Honduras and neighbouring countries may take decades to recover.

The legacies of Atlantic hurricanes span many cultures and thousands of years. Whilst evidence of strong cyclones can be found in geological data, the first human records are found in Mayan hieroglyphics. Shakespeare's *The Tempest* was inspired by a hurricane in 1609 which drove a fleet of ships travelling from England to Virginia into Bermuda. The passengers remained on the island, became its first inhabitants and placed it under British rule. There has also been speculation that a hurricane was responsible for the mysterious abandonment of Britain's first colony in the New World on Roanoke Island, North Carolina in about 1588. This event has lead to the legend of the "Lost Colony". The strongest gusts ever recorded were due to *Typhoon*[13] *Paka*. Wind speeds of $380km\ hr^{-1}$ were measured when Paka slammed into the island of Guam on 16^{th} December 1997. The most destructive tropical cyclone on record killed an estimated 300,000 people in Bengal in 1970. In an attempt to prevent such catastrophes, several programmes studied ways to "defuse" hurricanes in the initial stage of development. However, they have all proved unsuccessful and our best hope lies with early-warning systems which rely on improved prediction.

Understanding the currents and thermal structure of the ocean could help us to predict the formation of and path of these hurricanes. It could help to predict the El Niño. Such forecasts will allow us to minimise the damage caused by these phenomena, to make allowances in economic forecasting and to save countless numbers of lives. Ocean currents affect (and throughout history have affected) people from many walks of life from financiers to fishermen, from oil companies and businesses to navies. In one way or another, ocean currents affect virtually everybody on the planet.

[13] From the Chinese *Tai fung* meaning big, or great, wind.

Contents

Abstract 2

Acknowledgements 3

Preface 4

1 Introduction 12

1.1 Primitive equations of ocean circulation 13

1.2 Balanced models of ocean circulation 16

1.3 The Large-scale Semi-Geostrophic Equations 19

1.3.1 Lagrangian formulation 21

1.4 Wind driven ocean circulation 24

1.4.1 Vertical structure 24

1.4.2 Mixed layers and Depth-Independent-Temperature models 26

1.4.3 Non-conservative effects 27

1.4.4 Topographic effects 30

1.5 Thesis layout 31

2 Two-Layer Model 33

2.1 Derivation of equations 34

2.1.1 Viscous terms 34

2.1.2 Wind forcing and Ekman layers 35

2.1.3 Singularity at the equator 36

2.1.4 The barotropic streamfunction 37

2.1.5 The baroclinic flow: an evolution equation for the interface height 38

2.2 Baroclinic instability 40

2.2.1 The two-layer Phillips model 41

2.2.2 The quasi-geostrophic limit 43

2.2.3 Non quasi-geostrophic instability 44
2.2.4 Effect of a stratified layer 53
2.2.5 Small interface slope 54
2.2.6 Steeper interfaces 54
2.2.7 Summary 58

3 Depth Independent Temperature Model **59**

3.1 Derivation of equations 60
3.1.1 Interpretation of DIT as QG 62
3.2 Conservation of energy 64
3.3 Linear thermal gradient 68
3.3.1 Linear analysis 69
3.3.2 Weakly nonlinear analysis 74
3.3.3 Numerical simulations 77
3.3.4 Summary 82
3.4 Gaussian temperature anomalies 86
3.4.1 Solution in the neighbourhood of critical points 91
3.4.2 Solution in the neighbourhood of the origin 93
3.4.3 Matching the regions together 94
3.4.4 Special cases 95
3.4.5 Numerical simulations 97
3.4.6 Summary 101
3.5 Localised temperature anomalies and turbulence 105
3.5.1 An isolated temperature anomaly 107
3.5.2 A pair of temperature anomalies 111
3.5.3 Turbulence 116
3.5.4 Summary 125
3.6 Topography 126
3.6.1 Linear thermal gradient 126
3.6.2 Turbulence 138
3.6.3 Summary 141

4 Ocean Basins **150**

4.1 Barotropic ocean basins 150

4.1.1 The barotropic vorticity equation 152

4.1.2 Scaling of parameters 153

4.1.3 Numerical solution of the BVE 154

4.1.4 Flat bottom 155

4.1.5 Coastal slopes 155

4.1.6 80% wind gyre 162

4.1.7 Summary 165

4.2 DIT ocean basins 169

4.2.1 Coastal slopes and the SG co-ordinate transformation 169

4.2.2 Thermal forcing 173

4.2.3 Additional parameters 187

4.2.4 Inertia 193

4.2.5 Summary 207

5 Conclusions and further work **210**

5.1 Conclusions 210

5.2 Further work 213

A Generalised Two-Layer Equations **215**

A.1 Derivation of the GTLE 216

B Numerical Methods **220**

B.1 Upwinding methods 220

B.2 Adams-Bashforth-Moulton methods 222

B.3 Multigrid methods 226

B.4 Newton-Raphson methods 227

C Weakly Nonlinear Analysis for DIT baroclinic instability **230**

C.1 Equations for η_n 230

C.2 Linear operators 230

C.3 Nonlinear terms 231

C.4 Equations for ϕ_n 232

Chapter 1

Introduction

It is a remarkable fact that, despite large variations in size, shape, location and climate, all the oceans on Earth display similar large-scale characteristic features. The most widespread and easily recognisable of these are large, wind-driven gyres and intense western boundary currents. Henry Stommel[82] produced the first theory to explain the existence of western boundary currents in 1948. During the subsequent half-century several attempts have been made to improve this theory with the inclusion of inertia, baroclinicity and topography, all of which Stommel neglected completely. This thesis is one such attempt.

Western boundary currents (WBC's) are fast flowing currents which are only found, as the name suggests, on the western edges of oceans. It seems evident that inertia, baroclinicity and topography, in addition to friction, all have an important role to play in determining their dynamics. The two most well known WBC's are the *Kuroshio*[1] in the Pacific and the *Gulf Stream* in the Atlantic (Figure 1.1). They transport vast amounts of water, and therefore heat, around the earth. Consequently, they have a role to play in determining the climate of our planet.

The Gulf Stream (Figure 1.1) originates in the Caribbean Sea and flows northwards past the Florida coast. At Miami it is approximately $80km$ wide and transports 30 Sverdrups ($Sv = 10^6 m^3 s^{-1}$). It continues northwards along the continental shelf to Cape Hatteras where it separates from the coast and heads towards the Grand Banks and out into the Atlantic. Here it is about $150km$ wide and transports about $100Sv$. The current is very deep; appreciable currents have been detected at depths of $2000m$. Surface velocities can be as high as $2.0ms^{-1}$. This compares to a typical ocean speed of $0.05ms^{-1}$. Once in the open ocean, the Gulf Stream meanders about and ejects warm and cold core rings (eddies) which transfer its energy away into distant parts of the ocean. These rings have a

[1] Black Current

radius of approximately $50 - 200km$ and can survive for one to three months. This thesis offers a modest contribution towards understanding aspects of the Gulf Stream such as its direction, meandering and eddy-shedding.

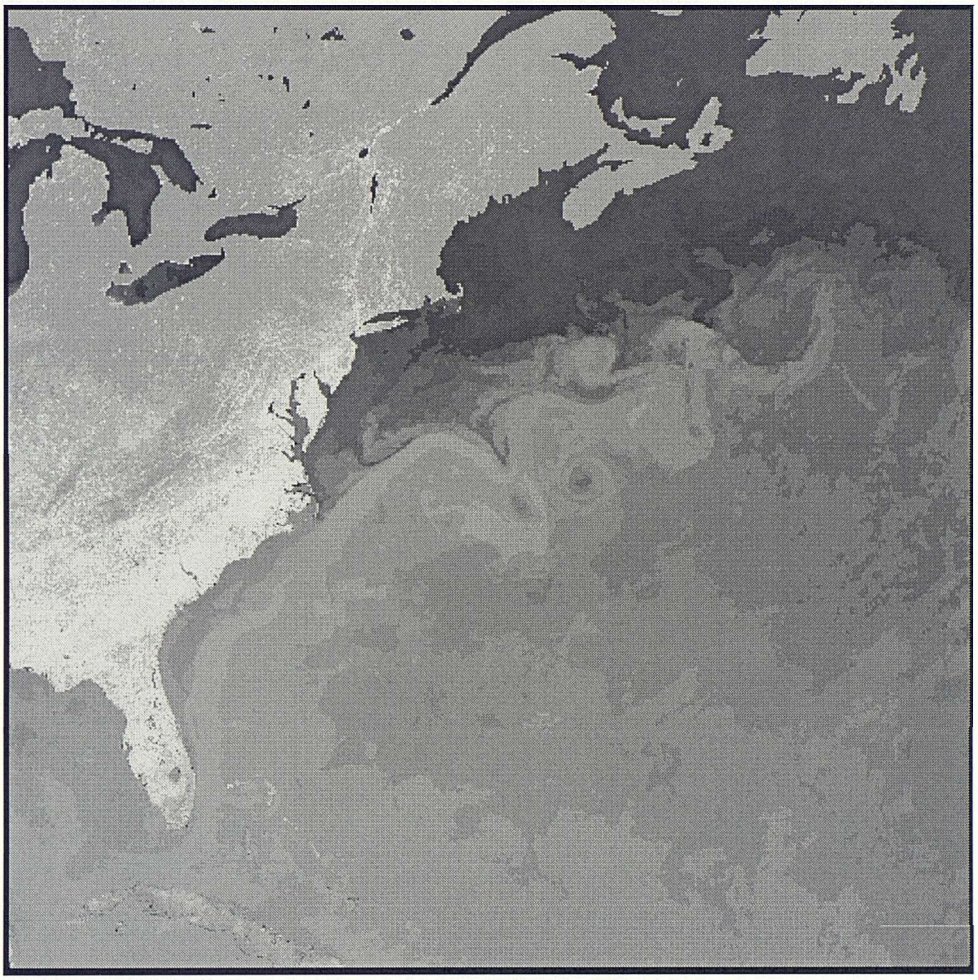


Figure 1.1: Thermal-image satellite-picture of the Gulf Stream and the east coast of the USA (June 1984).

Physical oceanographers using simple models (amongst which I include the work described here, see §§1.2 - 1.4) aim to model, reproduce and hence understand features such as these. Additionally, we hope to incorporate other gross characteristics of oceans such as a zonal sea-surface temperature and a circulating gyre structure. In order to do so it is necessary to lay down a mathematical framework to describe the ocean.

1.1 Primitive equations of ocean circulation

The mathematics of oceanic and atmospheric fluid dynamics is essentially the application of Newton's laws of motion to a rotating fluid. The *hydrostatic Boussinesq primitive equations* (1.1a-e, below) represent the Navier-Stokes equations in a rotating frame of

reference. Rotation adds an extra term to the equations: that of the Coriolis force. The magnitude of this force is $f \equiv 2\Omega \sin\theta$ where Ω is the rate of rotation of the earth $= 2\pi day^{-1} \equiv 7.29 \times 10^{-5} s^{-1}$ in S.I. units, and θ is the latitude. The Coriolis force is a virtual force which we only see because we are on a rotating sphere. It acts at right angles, to the right (left) in the Northern (Southern) Hemisphere, to the velocity of any particle. The only important component of the rotation, Ω, (for oceanography) is that which is normal to the Earth's surface. This component is zero at the equator and takes on its maximum value at the poles. The **hydrostatic approximation** says that we may entirely neglect the effects of vertical inertia. The **Boussinesq approximation** says that the density of the ocean is approximately constant (namely, the density of water $\equiv 1000 kg\ m^{-3}$). Therefore, density variations are small and it is a consistent approximation to neglect their effect on the mass (that is, inertia) but to retain their effect on the weight of the fluid. That is, we may neglect horizontal accelerations due to density variations but must include buoyancy effects. One additional approximation made throughout this thesis is to **neglect completely the effect of salinity**. This means that the density of the ocean is a function of the temperature only.

Therefore, the mathematical description of the ocean requires five equations. Three of them (1.1a-c) encapsulate Newton's Second Law "$F = ma$" in three dimensions with the hydrostatic and Boussinesq approximations. One (1.1d) is equivalent to the assertion that the water in the ocean is incompressible and that there are no sources or sinks of fluid[2]. Finally, we have an equation (1.1e) describing the advection of buoyancy by the flow. These five equations are known as **The Primitive Equations of Ocean Circulation** (see, for example, Salmon[74]).

$$\frac{Du}{Dt} - fv = -\frac{\partial \phi}{\partial x} \tag{1.1a}$$

$$\frac{Dv}{Dt} + fu = -\frac{\partial \phi}{\partial y} \tag{1.1b}$$

$$0 = -\frac{\partial \phi}{\partial z} - g + \theta \tag{1.1c}$$

$$\frac{\partial u}{\partial x} + \frac{\partial v}{\partial y} + \frac{\partial w}{\partial z} = 0 \tag{1.1d}$$

$$\frac{D\theta}{Dt} + w\frac{\partial \theta}{\partial z} = 0 \tag{1.1e}$$

[2]This is not strictly true due to inflows from the larger rivers such as the Amazon which act as sources of fluid. Additionally, there is a constant evaporation and precipitation but this interaction with the atmosphere will also be neglected.

where

$$\frac{D}{Dt} \equiv \frac{\partial}{\partial t} + \mathbf{u}.\nabla$$
$$\mathbf{u} \equiv (u, v), \qquad \nabla \equiv \left(\frac{\partial}{\partial x}, \frac{\partial}{\partial y}\right).$$

Here $(\mathbf{u}, w) = (u, v, w)$ is the fluid velocity in the direction (x, y, z) where z is the vertical co–ordinate, pointing upwards; y is pointing northwards along lines of constant longitude and x is pointing eastwards along lines of constant latitude; f is the Coriolis parameter; ϕ is the pressure; g is the gravitational acceleration, and θ is the buoyancy. Since we shall neglect salinity throughout this thesis, θ is linearly related to the temperature and so we shall frequently refer to θ as the temperature.

Boundary conditions are imposed by constraining the fluid to lie between a rigid lower boundary at $z = -H(x, y)$ where H is the depth of the ocean and an upper free surface at $z = \eta(x, y)$. The surface of the ocean is a material surface so particles starting on the surface stay on it. Application of this kinematic boundary condition at the surface and enforcement of no normal flow through the ocean floor lead to

$$\frac{D(z - \eta)}{Dt} = 0 \text{ at } z = \eta \tag{1.2a}$$
$$w = -\frac{DH}{Dt} \text{ at } z = -H. \tag{1.2b}$$

The ultimate aim of theoretical oceanography is to solve this innocuous looking set of equations (1.1a-e, 1.2a, b). To date, nobody has come close to obtaining an analytical solution (except in a few specific circumstances) and so we are left with trying to solve the equations numerically. In principle, this task is possible. However, it is not necessarily the best way to develop understanding of the dynamics of the ocean and atmosphere. The primitive equations contain two types of wave-like motion. There are "slow" large-scale *Rossby waves.* These result from an approximate balance between the pressure gradient and the Coriolis force. This is called **Geostrophic Balance**. The second type of waves are "fast" *inertia-gravity waves.* Many features of ocean circulation can be described in terms of "slow" waves only. Moreover, the "fast" waves present a big problem from a numerical point of view. In order to resolve all the dynamics satisfactorily the largest possible time step that a numerical scheme can take is equal to the time taken for the fastest wave to traverse one spatial grid step. $\Delta t < c_{max}\Delta x$. This is called the *Courant-Friedrich-Lewy* (CFL) Condition (see Appendix B). Clearly, the presence of fast inertia-gravity waves severely reduces the maximum time step that can be taken. In practice, this means that it is impossible to simulate with the primitive equations. Consequently, researchers have attempted to approximate the primitive equations in such a way that slow, geostrophic waves are retained but fast, inertia-gravity waves are removed. Such sets of equations are called balanced models.

1.2 Balanced models of ocean circulation

There are several balanced models in existence. The most severe approximation that can be made is to neglect everything except the leading order geostrophic balance $f\mathbf{k} \times \mathbf{u} = -\nabla\phi$. Equations based on this simplification are called the **planetary geostrophic equations** (Robinson & Stommel [63]). They ignore inertia completely. Whilst this is clearly a drastic assumption, it has the tremendous advantage of removing all the nonlinearity from the first two equations. Furthermore, the circulation determined by these equations closely resembles the time-averaged circulation determined by more sophisticated models; in rapidly rotating flow, the terms of the geostrophic balance dominate all the others (see Figures 4.18, 4.19). The main drawback is that the *evolution* of the barotropic flow cannot be predicted. Although time dependence is retained in (1.1e), numerical simulations suggest that solutions of the planetary geostrophic equations tend towards a steady state. In particular, the complete neglect of inertia prohibits the presence of time-dependent eddies in the circulation. Nevertheless, ocean models based on the planetary geostrophic equations have been used successfully by many authors, for example Salmon[70] and Samelson & Vallis[76].

Whilst the planetary geostrophic equations comprise a useful pedagogical tool, a more accurate description of oceanic circulation requires that some of the inertial, ageostrophic terms be retained. Oceanographers are interested in *nearly geostrophic* flow. The names of many balanced models (see below) reflect this fact. The degree of departure from geostrophy is indicated by an important parameter, the **Rossby Number,** Ro. This is the ratio of magnitude of the inertial terms to the geostrophic terms, $\mathsf{Ro} \equiv \frac{U}{fL}$ where U is a typical velocity and L is a typical length scale. In the ocean, velocities are small compared to the length scales and to the rotation of the Earth (see §4.1.2). Hence, $\mathsf{Ro} \ll 1$. Geostrophic flow corresponds to $\mathsf{Ro} = 0$. In the balanced models described below, $0 < \mathsf{Ro} \ll 1$.

The first, and still the most widely used, balanced model to include inertia is the **Quasi-Geostrophic** (QG) model (see [57]) which was developed by Charney[17] and Eady[25] about 50 years ago. The main advantage of this model is that it is relatively simple and so rapid progress can be made in understanding and interpreting the solutions. This explains why, despite the development of several more accurate balanced models since 1948, QG remains a widely employed tool today. However, QG suffers from a major drawback in that one of its assumptions requires that the isopycnals (isograms of constant density) are relatively horizontal. Specifically, their variation from a prescribed mean state is assumed to be $O(\mathsf{Ro})$. This is far from being true in frontal regions. By definition, frontal regions (see, for example, [20]) are those in which the isopycnals are steep. They comprise an

important feature of oceanic and atmospheric flows and are responsible for much of the transportation carried out by both systems. Moreover, QG additionally assumes that the topographic gradients are $O(\mathrm{Ro}) \ll 1$. In the atmosphere, the bottom can safely considered to be relatively flat because even Mount Everest only represents a modest bump on the vertical scales involved. However, the depth of the ocean varies considerably. The average depth of the ocean is $3795m$. The deepest point is the *Mariana Trench* at $11034m$ and, the shallowest point, obviously, is the entire coast line where the depth is $0m$. Clearly, there is an $O(1)$ variation in the depth of the ocean and so one must be careful in using the QG model for large-scale ocean circulation.

This, it should be pointed out, has not prevented the QG model being used very widely and successfully. Many researchers, for example, Berloff & Meacham[9], [10], [11] have confined attention to flat-bottomed models with vertical side-walls. Others, such as Özgökmen *et al.*[56] and Dewar[24] have considered models in which topography is present. The former, [56], studied the influence of the topography in the neighbourhood of Cape Hatteras on the separation of the Gulf Stream from the USA coast. The latter, [24], examined the effect of localised topography (for example, the Azores). However, both studies were restricted to topography that only varied by about 20% in extent. This is as a result of the QG assumption concerning flat topography and also because they utilised a **layer model** (see §1.4.1) in which it is problematic to consider topography extending above the bottom layer of the model. In this thesis we will consider both an alternative to the QG model and an alternative to the layer models, both of which facilitate the consideration of arbitrary topography.

There are several other balanced models in addition to the QG model. An extensive study of many of them can be found in McWilliams & Gent [47], Allen Barth & Newberger[2], [3], Barth, Allen & Newberger[5] and Allen & Newberger[4]. Cushman-Roisin [20], [21] developed a model for use in frontal regions which is of similar simplicity to the QG equations but is relevant in precisely those regions in which the QG equations are not relevant. In the three-part study [2], [3], [5], 13 such models are identified. These include models derived in many different manners. In the semi-geostrophic model of Hoskins[36], for example, the full velocity advects only the geostrophic momentum:

$$\frac{D\mathbf{u}}{Dt} \equiv \frac{D}{Dt}(\mathbf{u_G} + \mathbf{u_{AG}}) \rightarrow \frac{D\mathbf{u_G}}{Dt}. \tag{1.3}$$

In a series of papers, [66],[67],[68], Salmon used a Hamiltonian approach to develop a similar set of equations. In the case of a constant Coriolis Force they are equivalent to the semi-geostrophic equations. More recently, Salmon[73] has used the same approach to derive a set of Large-scale Semi-Geostrophic Equations (LSGE, see §1.3) on which this thesis is based.

The various models are evaluated (in [2]) on how accurately they can reproduce results of the shallow water equations (a reduction of the primitive equations based on the approximation that the ocean is homogeneous, but which retain the inertia-gravity waves (see, for example, [74])) in idealised steady and unsteady problems. The most accurate models ([2]) in this respect are a family of models known as **Balance Equations** (Gent & McWilliams [28]). These models are derived by splitting the velocity not into geostrophic and ageostrophic components (as in the semi-geostrophic type models) but into rotational (ψ) and divergent (ζ) components:

$$u = -\psi_y + \epsilon\xi_x, \qquad v = \psi_x + \epsilon\xi_y \tag{1.4}$$

Approximations are then made based on the assumption that ϵ is a small parameter. According to Allen *et al.*[2], the least successful at reproducing the results of the shallow water model is Salmon's model [67]. However, this is an unfair comparison because Salmon's model is constructed in a manner to incorporate inertia at *exactly* the same order as the QG equations whereas the remaining models in [2] incorporate inertia up to a higher order of Ro. In principle, the techniques of Salmon[66] can be applied to produce a model that is as accurate to any order of Ro as desired.

Numerical studies of flows over topography are also performed (in [5], [3]). This is precisely the situation in which the QG approximation fails. In addition to how well the model reproduces the results of the primitive (or shallow water) equations, other issues to consider when evaluating its usefulness include the ease with which the equations can be adapted to numerical simulation and the ease of interpreting and analysing its behaviour. The QG model has proved so popular because of these latter qualities. Barth *et al.*[5], Allen *et al.*[3] include, amongst the analytical models, a purely numerical model referred to as the SEMI model. This model is based on the exact shallow water equations but uses a semi-implicit (hence the name) time-stepping routine. This technique allows time-steps to be larger than the CFL condition and numerically filters out the inertia-gravity waves. The SEMI model is found to be the most accurate of all the models studied. However, it is not very often used in simple oceanic studies. It is suggested in [5] that this may be due to problems adapting the SEMI model to stratified oceans. It may also owe something to the fact that analysing the model is equivalent to analysing the more complicated shallow-water equations so the results are more difficult to interpret.

Intermediate models can possess other "desirable" properties. Ideally they should preserve the conservation laws of the primitive equations. In particular, the buoyancy and potential vorticity (PV) are materially conserved (that is, conserved on fluid parcels) and energy and mass are globally conserved. Conservation of mass and buoyancy are easily achieved via equations (1.1d, 1.1e) and specifying a condition of no normal flow at all solid boundaries

of the domain. Since (1.1d, 1.1e) are unchanged in the geostrophic limit, all balanced models preserve the conservation. However, the approximation of terms in (1.1a, b) by balanced models often destroys the conservation of energy and PV.

For the three-dimensional Boussinesq primitive equations (1.1a-e) the potential vorticity is given by $PV = (f\mathbf{k} + \nabla \times \mathbf{u}).\nabla\theta$. In the shallow water equations, it is given by $PV = \frac{f\mathbf{k}+\nabla\times\mathbf{u}}{H}$. The huge importance of the conservation of this quantity to the shallow water equations is reflected by the fact that the governing equations can be expressed as $\frac{D}{Dt}PV = 0$. Despite this, some of the balanced models of Allen *et al.*[2] fail to conserve PV. Moreover, even the "conservative" equations fail to globally conserve energy. Energy conservation is important because then any loss of energy in a model can be directly attributed to the dissipative terms alone. Of the 13 models discussed in [2] only the QG model and the two semi-geostrophic models both materially conserve PV *and* globally conserve energy. Some authors (for example, Tang & Cushman-Roisin[83]) elect to add arbitrary small terms to their consistently derived equations in order to restore conservation of energy. Although this is not too difficult to achieve, it *is* difficult to add arbitrary terms in such a way that conservation of both energy *and* PV is restored.

The LSGE of §1.3 are derived via a Hamiltonian method so all conservation laws are preserved. The DIT model of §3.1 is derived from the LSGE by requiring the PV to identically vanish everywhere. This is a most emphatic method of ensuring that any quantity is preserved. Energy conservation within the DIT is discussed in some detail in §3.2.

1.3 The Large-scale Semi-Geostrophic Equations

The Large-scale Semi-Geostrophic Equations (LSGE) are introduced in Salmon[73]. They incorporate inertia at the same order as the QG equations. However, whereas the QG model places a restriction on the vertical scales that are allowable, the LSGE place the restriction on the horizontal length scales. The derivation of the LSGE is the subject of §§2-4 of [73] so only a brief outline is given here.

The primitive equations are non-dimensionalised on the following scales; x and y are scaled on the ocean basin width, $L = 4000km$. There are two vertical length scales of interest. $H_0 = 4km$ is a typical ocean depth and ΔH is a typical isopycnal displacement. $\mathbf{u}$ is scaled by U and we choose U such that $H_0UL = 30Sv$ which is a realistic Sverdrup transport. This gives $U = 2mm\ s^{-1}$. The Coriolis parameter is scaled by a typical mid-latitude value of $f_0 = 10^{-4}s^{-1}$. An advective time-scale is used so t is scaled by $T = L/U$.

Additionally, we insist that the terms of geostrophic balance have approximately the same

magnitude and this determines the scale for the pressure, $\phi \sim f_0 UL$. This scaling leads to the non-dimensional primitive equations, which have only one non-dimensional parameter, $\epsilon \equiv \frac{U}{f_0 L}$, the **Rossby Number**[3] which gives the ratio between the inertial and the advective time scales.

$$\epsilon \frac{Du'}{Dt'} - f'v' = -\frac{\partial \phi'}{\partial x'} \tag{1.5a}$$

$$\epsilon \frac{Dv'}{Dt'} + f'u' = -\frac{\partial \phi'}{\partial y'} \tag{1.5b}$$

$$0 = -\frac{\partial \phi'}{\partial z'} - g + \theta', \tag{1.5c}$$

$$\frac{\partial u'}{\partial x'} + \frac{\partial v'}{\partial y'} + \frac{\partial w'}{\partial z'} = 0 \tag{1.5d}$$

$$\frac{D\theta'}{Dt'} = 0. \tag{1.5d}$$

Using the typical oceanic values for U, f_0, L we conclude that $\epsilon \equiv \frac{U}{f_0 L} \sim 5 \times 10^{-6} \ll 1$. This implies that oceanic circulation *is* almost geostrophic.

The hydrostatic equation (1.1c) yields another scaling for ϕ and here the appropriate vertical scale is the isopycnal displacement ΔH. The buoyancy is scaled with the *reduced gravity* $g' = N^2 \Delta H$ where N, the Brunt-Väisälä frequency, is a typical value of $\frac{\partial \theta}{\partial z}$. Thus, we obtain $\phi \sim g' \Delta H$ and combining this with the scaling of geostrophic balance, we obtain a new expression for the Rossby Number:

$$\epsilon = \left(\frac{g' H_0}{f_0^2 L^2}\right)\left(\frac{\Delta H}{H_0}\right) \equiv \left(\frac{\lambda_{int}}{L}\right)^2 \left(\frac{\Delta H}{H_0}\right) \tag{1.6}$$

We see from (1.6) that there are two ways to satisfy the empirically determined condition $\epsilon \ll 1$. Either $\Delta H \ll H_0$ or $\lambda_{int} \ll L$. Quasi-geostrophy proceeds by adopting the first scaling and therefore permits $L \sim \lambda_{int}$. Here, however, we wish to permit $O(1)$ variations in the displacement of isopycnals (that is $\Delta H \sim H_0$) and so we require $\lambda_{int} \ll L$. This is the most important approximation made in the derivation of the LSGE. It is necessary to remember that they are formally only valid in the limit in which length scales are (much) larger than the internal deformation radius.

It turns out that this is not actually too severe a restriction for ocean circulation models because the (first) internal deformation radius in the ocean is about $40km$. A typical ocean is approximately hundreds of times bigger than this in horizontal extent. Even the

[3]Throughout this thesis, Ro and ϵ are equivalent. Both refer to the Rossby Number. The Ro notation is used most often where a physical interpretation is important. Elsewhere, where the emphasis is on the fact that the Rossby Number is small, the ϵ notation is used. This is to preserve backward compatibility with Salmon[73] in which the LSGE are derived.

most sophisticated ocean models tend not to be able to resolve scales smaller than $20km$[4]. However, the deformation radius in the atmosphere is approximately ten times greater (about $400km$). It is, therefore, less justifiable to neglect length scales of this magnitude and so the LSGE should probably not be applied to atmospheric dynamics.

Henceforth we shall drop the primes on all variables and assume that everything is non-dimensional.

The boundary conditions (1.2a, b) are unaffected by the non-dimensionalisation but we additionally replace the upper boundary condition of a free surface by a **rigid lid**

$$w = 0 \text{ at } z = 0. \tag{1.7}$$

This has the effect of filtering out all the fast, inertia-gravity waves, the benefits of which are explained in §1.1.

1.3.1 Lagrangian formulation

Let $\mathbf{x}(\mathbf{a}, \tau) = (x(a,b,c,\tau), y(a,b,c,\tau), z(a,b,c,\tau))$ be the location of the fluid particle identified by the labelling co-ordinates (a,b,c) at time τ. The labelling co-ordinates move with the flow and so $\frac{\partial}{\partial \tau} \equiv \frac{D}{Dt}$. There is a degree of freedom in assigning these co-ordinates which we use up by insisting that $dadbdc \equiv d(mass)$. Then the Lagrangian corresponding to the scaled primitive equations (1.5a-e) is

$$\mathbf{L} = \iiint d\mathbf{a} \left\{ \left(\epsilon u - R\left(x,y\right)\right) \frac{\partial x}{\partial \tau} + \left(\epsilon v + P\left(x,y\right)\right) \frac{\partial y}{\partial \tau} \right\} - \mathcal{H} \tag{1.8}$$

where

$$\mathcal{H} = \iiint d\mathbf{a} \left\{ \frac{1}{2}\epsilon \left(u^2 + v^2\right) - \left(\theta\left(a,b,c\right)\right) z - \phi \left[\frac{\partial\left(x,y,z\right)}{\partial\left(a,b,c\right)} - \alpha_0 \right] \right\}. \tag{1.9}$$

Here $R(x,y)$ and $P(x,y)$ are any two functions satisfying $\frac{\partial R}{\partial y} + \frac{\partial P}{\partial x} = f(x,y)$.

We can derive (1.5a-d) by invoking *Hamilton's principle* that $\delta \int \mathbf{L} d\tau = 0$ for arbitrary independent variations $\delta\mathbf{x}(\mathbf{a},\tau), \delta\phi(\mathbf{a},\tau)$. For further background see the review article [69].

Now, we define the new co-ordinates in which, to within an error of $O(\epsilon^2)$, the Lagrangian (1.8) takes its simplest, canonical form. The LSGE requirement that $L \gg \lambda_{int}$ allows us to replace $\mathbf{u}$ in the Hamiltonian (1.9) with (1.12, 1.13) below.

[4] Resolution is often quoted in degrees longitude and latitude. A high resolution model, for example the GFDL-MOM[16], may be described as having a resolution of $(\frac{1}{5}^o, \frac{1}{6}^o)$ which corresponds to a grid size of $(\Delta x, \Delta y) = (22.2, 18.2)km$ in mid-latitudes. A grid-resolution of $20km$ is used by many authors, e.g. Jiang *et al.*[38], Özgökmen *et al.*[56].

Like many of the balanced models of §1.2, the velocity is split into two components. In this instance, it is split into the vertical average and the remainder. Let

$$u(\mathbf{a},\tau) \equiv \bar{u} + \hat{u}, \quad v(\mathbf{a},\tau) \equiv \bar{v} + \hat{v} \tag{1.10}$$

and then define the new co-ordinates

$$x_s(\mathbf{a},\tau) = x(\mathbf{a},\tau) + \epsilon\frac{\hat{v}}{\tilde{f}} \tag{1.11a}$$

$$y_s(\mathbf{a},\tau) = y(\mathbf{a},\tau) - \epsilon\frac{\hat{u}}{\tilde{f}} \tag{1.11b}$$

$$z_s(\mathbf{a},\tau) = z(\mathbf{a},\tau) + \epsilon\int_{z_s}^{0}\left[\frac{\partial}{\partial x_s}\left(\frac{\hat{v}}{\tilde{f}}\right) - \frac{\partial}{\partial y_s}\left(\frac{\hat{u}}{\tilde{f}}\right)\right]dz_s' \tag{1.11c}$$

where

$$(\bar{u},\bar{v}) \equiv \frac{1}{H_s}\int_{-H_s}^{0}\left(\frac{\partial x_s}{\partial\tau},\frac{\partial y_s}{\partial\tau}\right)dz_s \tag{1.12}$$

and $(\hat{u},\hat{v})$ is defined by

$$\frac{\partial}{\partial z_s}(\hat{u},\hat{v}) = \frac{1}{\tilde{f}}\left(-\frac{\partial\theta}{\partial y_s},\frac{\partial\theta}{\partial x_s}\right) \text{ and } \int_{-H_s}^{0}(\hat{u},\hat{v})dz_s = 0. \tag{1.13}$$

Here

$$f_s \equiv f(x_s,y_s), \qquad H_s \equiv H(x_s,y_s) \tag{1.14}$$

and finally

$$\tilde{f} \equiv f_s + \epsilon\frac{\partial\bar{v}}{\partial x_s} - \epsilon\frac{\partial\bar{u}}{\partial y_s}. \tag{1.15}$$

Thus, $(\bar{u},\bar{v})$ is the vertically averaged flow and $(\hat{u},\hat{v})$ obeys a thermal wind type equation (1.13) in our new co-ordinates (1.11a-c)[5]. They are a generalisation of the semi-geostrophic (SG) co-ordinates of Hoskins[36] and throughout this thesis I shall refer to them as *SG co-ordinates.* Steps similar to those of [73] show that $z = -H(x,y)$ is equivalent to $z_s = -H(x_s,y_s)$ and $z = 0$ is equivalent to $z_s = 0$. These two relations are important because they imply that, even though the co-ordinate transformation changes with time, the topography of the basin in SG co-ordinates remains constant. The assumption that the motion is approximately geostrophic allows the Lagrangian (1.8) to be approximated (up to $O(\epsilon^2)$) by

$$\mathbf{L}' = \iiint d\mathbf{a}\left\{\left(\epsilon\bar{u} - R\left(x_s,y_s\right)\right)\frac{\partial x_s}{\partial\tau} + \left(\epsilon\bar{v} + P\left(x_s,y_s\right)\right)\frac{\partial y_s}{\partial\tau}\right\} - \mathcal{H} \tag{1.16}$$

[5]These co-ordinates differ slightly, but unimportantly, from those of [73]. In that paper, f_s replaces $\tilde{f}$ in (1.11a-e, 1.13). This leads to $O(\epsilon^2)$ differences between this thesis and [73]. However, the Lagrangian (1.16) contains a further $O(\epsilon^2)$ approximation into which these differences are absorbed.

where $\mathcal{H}$ is given by (1.9).

Arbitrary, independent variations $\delta\mathbf{x_s}(\mathbf{a},\tau), \delta\phi_s(\mathbf{a},\tau)$ of $\int \mathbf{L}'$, some tedious, but not entirely straightforward, algebra and $\frac{\partial\theta}{\partial\tau} = 0$ lead to the LSGE (1.17a-e) of Salmon[73].

$$\epsilon\frac{\partial\bar{u}}{\partial t_s} - \tilde{f}V = -\frac{\partial\Phi}{\partial x_s} + \epsilon\theta\frac{\partial}{\partial x_s}(\nabla_s.\mathbf{A}) \tag{1.17a}$$

$$\epsilon\frac{\partial\bar{v}}{\partial t_s} + \tilde{f}U = -\frac{\partial\Phi}{\partial y_s} + \epsilon\theta\frac{\partial}{\partial y_s}(\nabla_s.\mathbf{A}) \tag{1.17b}$$

$$0 = -\frac{\partial\Phi}{\partial z_s} + \theta + \epsilon\theta\frac{\partial}{\partial z_s}(\nabla_s.\mathbf{A}) \tag{1.17c}$$

$$\frac{\partial U}{\partial x_s} + \frac{\partial V}{\partial y_s} + \frac{\partial W}{\partial z_s} = 0 \tag{1.17d}$$

$$\frac{\partial\theta}{\partial t_s} + U\frac{\partial\theta}{\partial x_s} + V\frac{\partial\theta}{\partial y_s} + W\frac{\partial\theta}{\partial z_s} = 0 \tag{1.17e}$$

where

$$\Phi = \phi + \frac{1}{2}\epsilon(\bar{\mathbf{u}} + \hat{\mathbf{u}})^2 \tag{1.18a}$$

$$\phi = \phi_s - \epsilon\bar{\mathbf{u}} - \epsilon\hat{\mathbf{u}} + \epsilon\bar{\mathbf{u}}\cdot(\mathbf{U} - \mathbf{u}) + \epsilon\theta(\nabla_s.\mathbf{A}) \tag{1.18b}$$

and

$$\mathbf{A} = -\int_{z_s}^{0}\left(\frac{\hat{v}}{\tilde{f}}, -\frac{\hat{u}}{\tilde{f}}, 0\right)dz_s'. \tag{1.19}$$

$$\mathbf{U} \equiv (U,V) \equiv \left(\frac{\partial x_s}{\partial\tau}, \frac{\partial y_s}{\partial\tau}\right). \tag{1.20}$$

The first two equations, (1.17a) and (1.17b) correspond to the advection of horizontal momentum while the hydrostatic approximation is contained within (1.17c); (1.17d) is the continuity equation (conservation of mass). Finally, (1.17e) represents the advection of θ, the buoyancy, which we shall call the temperature.

The form of Φ (1.18a, b) is unimportant because the LSGE (1.17a-e) are five equations in five unknowns U, V, W, θ, Φ. However, (1.18a, b) *are* required to show the equivalence between these equations and the primitive equations in standard Cartesian co-ordinates (see [73]). The velocity of the particle, $\mathbf{U} \neq \bar{\mathbf{u}} + \hat{\mathbf{u}}$. This is because $\mathbf{u}$ is the velocity of the particle at $\mathbf{x}$ whereas $\mathbf{U}$ is the velocity at $\mathbf{x}_s$. Thus, $\mathbf{u}$ and $\mathbf{U}$ differ by $O(\epsilon)$. Note that (1.19) is slightly different from the definition given in [73]. It results in a simpler expansion of $\nabla_s.\mathbf{A}$ but produces identical dynamics to those of [73] up to $O(\epsilon^2)$.

The advantage of the LSGE is that the horizontal inertial equations (1.17a,b) appear to be linear in $\mathbf{U}$ and so therefore are more closely related to the planetary geostrophic equations than the primitive equations. It would seem that they only include the inertia of the vertically averaged flow ($\epsilon\frac{\partial\bar{\mathbf{u}}}{\partial t_s}$). However, the baroclinic momentum is included in the nonlinear terms involving $\nabla_s.\mathbf{A}$.

Since this thesis is concerned with solutions of the LSGE (1.17a-e), henceforth, all 's' subscripts will be dropped. If a variable bears no subscript then it will be in SG co-ordinates. (1.11a-c). Anything in Cartesian (physical) space will have a 'C' subscript (e.g. u_C).

1.4 Wind driven ocean circulation

The aim of using simplified equation sets (such as those described in §§1.2, 1.3) is to attempt to reproduce the major features of ocean circulation and to understand what influences the characteristics of these features. Once an understanding has been developed, it can be used to improve larger, more accurate, numerical circulation models such as the NCAR Climate System Model Ocean Component (Gent *et al.*[29]) and the GFDL Modular Ocean Model (Chao *et al.*[16]). These models incorporate several concepts and parametrisations that have been suggested from simpler studies and which enable the numerical simulations to run more rapidly and efficiently without compromising too much accuracy.

1.4.1 Vertical structure

All the balanced models described in §§1.1, 1.2, 1.3 are three-dimensional conservative models. Three-dimensional equations are much harder to solve (analytically or numerically) than two-dimensional equations so many studies make an assumption concerning the vertical structure of the ocean (often based on physical grounds[6]) to reduce the problem to two dimensions.

The simplest possible assumption is that the ocean consists of one homogeneous layer of fluid. This is also known as a **barotropic ocean**. In this instance, all fields are two-dimensional and the temperature (buoyancy) is constant. Many authors have used this model to examine particular aspects of the flow. Dengg[23] considered the problem of Gulf Stream separation. Kamenkovich *et al.*[43] and Sheremet *et al.*[79] performed a detailed series of numerical simulations of the time-dependent flow in a barotropic subtropical gyre. Ierley & Sheremet[37] and Cessi & Ierley[15] have shown the existence of multiple steady state solutions. The existence and stability of these solutions is dependent on the values of inertia and of lateral diffusion. Meacham & Berloff[49], [50] have also investigated the bifurcation structure of solutions in a homogeneous flat bottomed small, closed basin (they

[6]There is a symbiosis between mathematics and physics; just as simple mathematical concepts can explain and/or parametrise the physics in complicated models such as [29], mathematics is guided by the physics of the real world.

cite the example of the Black Sea) leading to multiple steady states, unsteady states and eventually chaos. Becker & Salmon[7] studied the effect of smooth coastal slopes on the stability of the steady states (see §4.1). Although it has much to offer to our physical understanding of large-scale circulation, the biggest deficiency of the barotropic ocean is the complete neglect of stratification, or **baroclinicity**.

There are many ways to include the effects of baroclinicity (that is, of vertical variations in the density of the ocean). One approach that has been widely used, especially in simple studies, is to construct a **layer model**. These consist of two or more homogeneous layers of fluid of varying depth. The temperature (buoyancy) of each layer is constant. Models of this type range from the **equivalent-barotropic model** ($1\frac{1}{2}$ layer model which contains one normal layer sitting on top of a second layer of infinite depth; the second layer is at rest.) e.g. Berloff & Meacham[9], [11], to those containing several layers. Clearly, more layers result in a more realistic model but also in more impermeable analysis, reduced understanding and slower simulations. A popular compromise is to use two or three layers e.g. Berloff & Meacham[10], [11]; Dewar[24], who studied the effect of localised topography on the flow, and Özgökmen *et al.*[56], who studied the influence of topography on Gulf Stream separation.

A drawback of layer models is that it is difficult to couple them to an atmospheric model to study a *complete climate system.* This is because the atmospheric component requires the ocean to provide the temperature distribution at its base (the Sea Surface Temperature (SST)). However, since the top layer of the model dominates much of the ocean surface and the temperature of any given layer is constant, this gives a poor model of the actual SST. This problem is ameliorated by adding more layers to the model but the SST remains piecewise constant. More complicated models employ many layers and a large vertical diffusion near the surface to steepen the isopycnals (layer interfaces). A further problem afflicts layer models (particularly those with few layers) in coastal slope regions. On the shore-ward side of intersection of the interface with either the sea surface or the bottom of the ocean, a two-layer model reduces to a barotropic one. Even tracking this *outcropping* point is a numerical headache. On one side of the outcrop the wind-forcing must be applied to the top layer whilst on the other side there is *no* top layer and so the forcing must be instantaneously transferred to the second layer. Since many numerical schemes (including QG) involve the inversion of an elliptical operator to extract the streamfunction from the vorticity, the numerics are now faced with solving an elliptic problem in an irregular domain. This is an unwanted technical difficulty for the simple models that we have in mind. These problems are illustrated in the cartoon Figure 1.2.

A solution to the problem of modelling the SST is to create a **mixed layer**. This layer represents the top few hundred metres of the ocean and has different dynamics from the

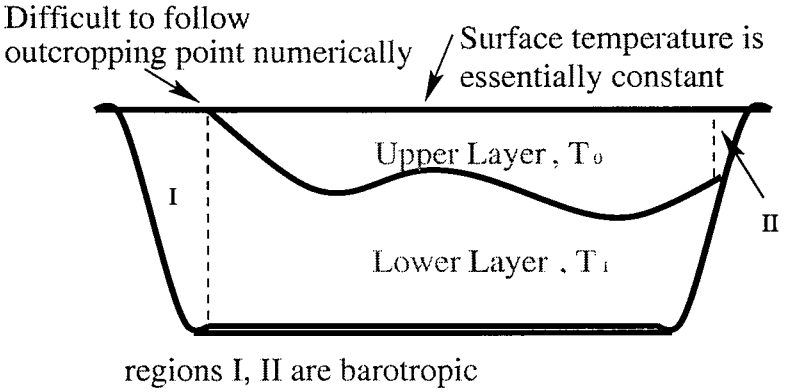


Figure 1.2: A two-layer ocean.

layers below. In the mixed layer an approximation is made that the temperature of the ocean is independent of (or only weakly dependent on) the depth within the layer.

1.4.2 Mixed layers and Depth-Independent-Temperature models

No definition of the mixed layer is universally accepted. Haine & Marshall [31] define the mixed layer depth to be the depth at which the density exceeds the surface density by $0.05kg\ m^{-3}$; the mixed layer is everything above that depth. This depth can vary from about $10m$ to $1km$. It is smallest in summer and greatest in winter (Bhatt *et al.*[12]).

The properties of the layer are set by vertical mixing caused by stirring from the wind, surface gravity wave breaking and small scale convective mechanisms induced by buoyancy exchanges at the surface. This is often parametrised by adding large vertical diffusivities to the model (Gent *et al.*[29]) or by relaxing the layer to a prescribed mixed state (Young[86]).

An alternative strategy is to accept *a priori* that the layer has been mixed and specify a vertical structure in which all the dynamical fields (namely, velocity and temperature) are independent of the vertical co-ordinate. This is the approach taken in Chapter 3. The strategy adopted there is to assume that the *temperature of the ocean is everywhere independent of* z, rather than simply near the surface. The idea is illustrated in Figure 1.3. The motivation behind this approach is that it enables more rapid analytical progress to be made. It is also justified on mathematical grounds because it is arguably the simplest inertial, non-barotropic model to conserve potential vorticity (see §3.1).

In the atmospheric community, many people studying interannual and interdecadal variations in coupled atmosphere-ocean models employ an extremely simplified mixed-layer ocean model (e.g. Battisti *et al.*[6]) which contains little or no dynamics. They merely allow for the temperature to spread diffusively and be advected by a prescribed mean flow. Such models (if seeded with the correct mean flow which can be obtained empirically via back-fitting) are fairly successful at modelling the climatic fluctuations except ([6]) near

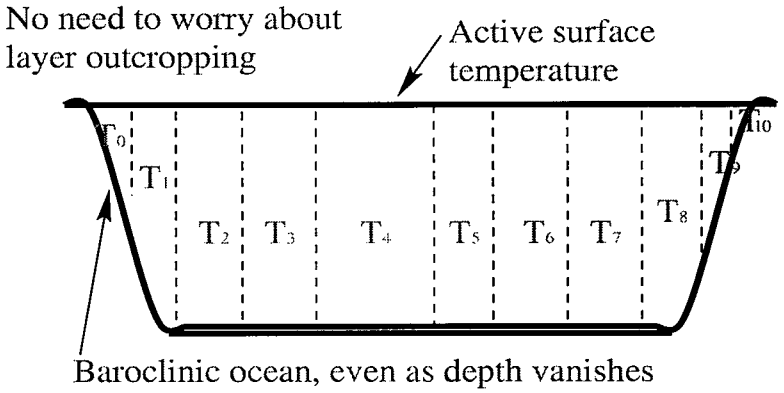


Figure 1.3: A Depth-Independent-Temperature (DIT) ocean.

the Gulf Stream.

The models of Zebiak & Cane[88] and McCreary & Anderson[51] are more complicated. They are both reduced gravity (equivalent-barotropic) linear models with a vertically averaged temperature. However, it is pointed out in Cushman-Roisin *et al.*[22] that the reduced gravity model is a poor approximation to a two-layer model in frontal regions (that is, where the horizontal and vertical length scales are large).

A review of many of the oceanographic assaults on modelling the mixed layer can be found in Ripa[60], [61]. The original model of Lavoie[44] utilised a vertically averaged velocity field and a vertically averaged temperature field. It is pointed out in [60] that this implies the absence of a thermal wind relationship between vertical velocity gradients and horizontal thermal gradients. Generalisations of Lavoie[44] are discussed and their strengths and weaknesses are outlined. However, what all these models have in common is that they involve some sort of *ad hoc* averaging process (for example, nonlinear variables are replaced by their vertical mean). In contrast, the Depth-Independent-Temperature (DIT) model developed in Chapter 3 involves no further approximations beyond those of the LSGE (§1.3). Thus, solutions of the DIT are also special case solutions of the full three-dimensional LSGE. Contrariwise, the LSGE are only valid for large length scales ($L \gg \lambda_{int}$). This restriction does not apply to the models of [60], [61]. However, in the latter paper, it is noted that the models are most accurate in precisely this limit. In fact, the model of Young[86] reduces to the flat-bottomed version of the DIT in the limit of $L \gg \lambda_{int}$.

1.4.3 Non-conservative effects

Non-conservative effects are those which do not conserve energy. They include forcing and dissipation. Forcing refers to terms such as wind-forcing and thermal forcing (that is, the effect of the sun warming the ocean or heat being lost from the surface of the ocean to a

colder atmosphere). Dissipative effects are shrouded in mystery. The formal derivation of the Navier-Stokes equations for a Newtonian fluid (e.g. water) leads to a Laplacian (∇^2) term (to which I shall refer throughout this thesis as lateral diffusion). However, various authors in the oceanographic community have employed terms of the general form:

$$\Sigma_{n=0}^{n=N}(-1)^{n+1}a_n\nabla^{2n}(\mathbf{u}) \tag{1.21}$$

where N is a positive integer (usually, but not exclusively $N \leq 2$, for example, Becker & Salmon[7](n=0), Berloff & Meacham[9], [10], [11](n=1), Özgökmen *et al.*[56](n= 0, 1), Dewar[24](n= 0, 2), Held *et al.*[33](n=4)). Numerical experiments have been performed (e.g. Hecht *et al.*[32]) to determine what form of the dissipative terms give the most reasonable physical results. This has lead to many authors employing a hyperdiffusive term ($\nabla^4\mathbf{u}$). Some form of diffusion is needed in all numerical models to stabilise the simulations. One of the effects of inertia is that it produces progressively finer spatial scales within the flow. Without any diffusion, these scales will eventually become smaller than the numerical resolution. The presence of diffusive terms keeps the scales to within the limits of the numerical spatial resolution. From a physical standpoint, such terms are to be regarded as *parametrising* the sub-grid-scale, unresolvable features. Larger values of n in (1.21) are more scale-selective. That is, they effectively damp very small scale oscillations but have little effect on the large-scale disturbances. Many numerical codes include explicit terms of high order for this reason. In the numerical simulations of Chapter 4 I use a linear frictional term ($-\nu\mathbf{u}$) and a numerical scheme called upwinding (Hecht *et al.*[32], Becker & Salmon[7]). This has the effect of adding an implicit hyperdiffusion term ($\nabla^4\mathbf{u}$). The validity and benefits of this approach are further explored in §4.1. Further details concerning upwinding can be found in appendix B.1.

In addition to the various frictional terms used by different authors, a further complication is caused by boundary conditions employed at the edge of the ocean. Many balanced models (such as QG) impose a restriction on the vertical variation of the bathymetry. This condition prohibits the ocean depth from vanishing at the coastline and hence many simple studies have oceans with vertical side-walls at which boundary conditions must be applied. The obvious choice for the first condition is of **no normal flow**. However, unless all the dissipative terms involve no further derivatives, at least one extra condition must be specified. The two most common choices are

- no slip
- no stress (also known as free slip)

It remains a matter of dispute as to which of the above conditions is the more appropriate for ocean modelling. From a theoretical fluid dynamics point of view, *no slip* is the correct

condition. However, as mentioned in §1.3, numerical grids have resolutions of, at best, about $20km$. Therefore the first grid point in from the boundary is at least $20km$ away from the boundary and it is far from clear that the no slip condition is still correct at this distance. Mixed conditions, known as *partial slip*, can also be applied (see, for example, Jiang *et al.*[38]).

With a choice of frictional terms and a choice of boundary conditions, there are several different studies that can be performed. The very first model of wind driven ocean circulation was developed in 1948 by Henry Stommel[82]. He used a linear friction term and showed that the westward intensification of currents is a result of the planetary vorticity gradient (that is, the variation in the Coriolis parameter, f). However, his model had many shortcomings. Stommel's ocean possessed no inertia (that is to say, it was based on the planetary geostrophic equations) and a flat bottom. It was also a barotropic ocean. As a result, it did a poor job of predicting the width or direction of the western boundary currents and had nothing to say at all about the temperature distribution in the ocean. Nevertheless, most subsequent studies have begun either with Stommel's model or the 1950 model of Munk[52] which is identical except for the use of lateral diffusion in preference to linear friction for the viscous terms. Munk's model gave qualitatively the same picture in that it also predicted the gyre structure, westward intensification and jet-like WBC. The difference between Stommel[82] and Munk[52] lies in the detailed structure of the WBC. Despite their shortcomings, these two pioneering studies are two of the most successful in oceanography; they transparently explain the gyre structure and westward intensification observed in all oceans[7].

The inclusion of inertia makes the equations nonlinear and so much less vulnerable to attack by analytical techniques. Veronis[84] numerically obtained a series of steady solutions at varying Rossby Number, Ro, and bottom friction ranging from Stommel's solution at $\mathsf{Ro} = 0$ to Fofonoff's[26] fully inertial solution at $\mathsf{Ro} = \infty$. On the other hand, Bryan[14] showed that with lateral diffusion (as in Munk's solution), no slip on meridional walls, free slip on zonal walls and non-zero Rossby number, non-steady solutions can be obtained. These two studies demonstrate the qualitative difference between lateral diffusion and linear friction. Moro[53] found significant differences in the value of the critical Reynolds Number (ratio of inertial to viscous terms) below which the steady state is stable in barotropic models with no slip and free slip. Dengg[23] showed that the separation of the Gulf Stream is sensitive to choice of boundary conditions; free slip conditions cause the current to remain trapped to the coastline whereas no slip conditions lead to a sharp separation at a corner.

[7] except the Antarctic Ocean which has no western boundary.

1.4.4 Topographic effects

The majority of the work discussed in §§1.4.1-1.4.3 relates to oceans with flat bottoms or in which the topography only varies by a small ($< 10\%$) fraction of the ocean depth. In the case of QG models, this restriction is enforced, but there is no such restriction when using a primitive equation model. As can be seen in §4.1, the inclusion of $O(1)$ topographic variation does not add any significant difficulties to the numerical solution of the problem in the barotropic case. However, in contrast to the wealth of literature on flat bottomed models, there is a relative paucity of material on models with sloping boundaries. Indeed, as recently as 1990, Allen *et al.*[3] commented that "There exist no applications of intermediate models to oceanographic flow fields over bottom topography typical of the continental margin".

Holland[35] solved the steady, wind-driven problem with lateral diffusion in 1967. He pointed out that in the limit of negligible inertia and negligible friction the flow is parallel to the isopleths of constant f/H where f is the Coriolis parameter and H is the depth of the ocean. Welander[85] further demonstrated the importance of these isopleths by showing how the structure of the WBC is affected by the meridional derivative of f/H. Becker & Salmon[7] have recently shown how the presence of a continental slope on the western boundary of the ocean qualitatively affects the flow and stability of the solutions. With a continental slope present, eddies are shed periodically by the WBC, whereas at corresponding values of Ekman (ratio of frictional to Coriolis terms) and Rossby Numbers, no eddies are found in the flat bottomed model. The majority of ocean basins considered in this thesis incorporate coastal slopes, similar to those of Salmon[72] and Salmon & Ford[75].

In the light of §1.4.3, I would like to emphasise one advantage of sloping boundaries over vertical side-walls. The various studies referenced in §1.4.3 demonstrate that with vertical side-walls the precise choice of viscous terms and boundary conditions have a dramatic impact on qualitative aspects of the flow. In contrast, in §4.1 it shall be shown that with sloping boundaries, the form of the dissipative terms and the boundary conditions have virtually no effect whatsoever on the flow, even quantitatively. This is because with side-walls, friction is important in a boundary layer on the western boundary of the domain. With sloping boundaries, friction is only important in the south-western corner of the domain.

The ocean basin simulations of Chapter 4 show that a large proportion of the dynamics occurs on the sloping western boundary. Moreover, the influence of a continental slope on the western boundary of the ocean is felt throughout the whole basin. Consequently, understanding the role of topography is central to understanding the large-scale charac-

teristic features of ocean circulation.

1.5 Thesis layout

In Chapter 1 I have stated the aims of the thesis, outlined the mathematical foundations of physical oceanography (§1.1) and described some intermediate models (§1.2). In §1.3 I have introduced the LSGE on which the rest of the thesis is based. I have explored the large body of literature on wind-driven ocean circulation (§1.4) and attempted to point out where the work of this thesis fits in with these lucubrations.

In Chapter 2 I discuss a two-layer model based on the LSGE. The derivation of the governing equations (§2.1) provides a template upon which to base the derivation of a whole class of similar models. Baroclinic instability is investigated and results are compared and contrasted with the QG model. In §2.2.4 I generalise the two-layer model by including a thin stratified layer between the top and bottom layers. The extra layer is shown to have a small stabilising influence.

In Chapter 3, the Depth-Independent-Temperature (DIT) model is developed and discussed. This model is similar in spirit to the mixed layer models of §1.4.2 but is, I believe, the first *exact* nonlinear model of such a layer. That is to say, it is the first model (that includes inertia) to be consistently derived from a fully three-dimensional system of equations without recourse to any *ad hoc* averaging process. However, throughout Chapters 3 and 4, we regard the DIT model as a paradigm for the whole ocean, rather than for the mixed layer. In this respect, the DIT model can be regarded in the same way as the shallow water equations; as a simple theoretical tool rather than an accurate representation of reality. In §3.3 we consider baroclinic instability in the simplest possible configuration of the DIT. The importance of baroclinic instability in the mixed layer is emphasised in Haine & Marshall[31]. I then proceed to consider baroclinic instability induced by localised thermal anomalies. I also present a variety of turbulence simulations (§3.5) to further characterise the behaviour of the DIT. The effect of topography is studied in §3.6.

In Chapter 4 the theory of the previous two chapters is applied to understanding a series of numerical ocean basin simulations. In §4.1 barotropic oceans are considered. In addition to the effect of a western slope, we also briefly consider the effect of the northern and eastern slopes. The influence of Ro is investigated. In §4.2 DIT oceans are considered. The effects of baroclinicity can be seen by comparing and contrasting results from the two sections. As in the barotropic case, we also investigate the influence of Ro. The features are interpreted using results from Chapter III and related to observed features in oceans.

Finally, *in Chapter 5*, I discuss the main conclusions of the thesis and I indicate how

the work can be extended in the future. *The appendices* contain a brief discussion of generalised two-layer equations, some details of the numerical techniques employed, and an exposition of the equations of the weakly nonlinear instability analysis of §3.3.2.

Chapter 2

Two-Layer Model

In this chapter a two-layer model based on the LSGE is developed. Two-layer versions of several balanced models (§1.2) have been studied. Some of the most popular are based on the quasi-geostrophic equations, shallow water equations and the planetary geostrophic equations. For a review, see, for example, Salmon[74]. Cushman-Roisin *et al.*[22] derived a general class of two-layer models. Of particular interest here is the frontal geostrophic limit of these equations. This limit corresponds to $O(1)$ variations of the interface between the two layers and to horizontal length scales greater than the deformation radius. Two-layer models are a useful pedagogical tool because they offer a simple means of incorporating (at least some of) the effects of vertical stratification in the ocean without having to solve more complicated three-dimensional equations. One important phenomenon present in real-world atmospheric and oceanic flows, but not captured by a barotropic model is that of *baroclinic instability* which is responsible for mid-latitude synoptic storms in the atmosphere and mesoscale eddies in the ocean.

The aims of this chapter are:

- to derive the equations and explain the general methods involved in deriving models based on the LSGE. It is also shown how to incorporate non-conservative effects such as wind-forcing and viscosity, and to deal with a singularity at the equator. The same methods used to derive (2.22, 2.31) are employed to derive a large class of reductions, including (3.2, 3.4), (A.1, A.9), of the LSGE.

- to compare and contrast the model based on the LSGE with other two-layer models. The assumption of large horizontal scales and no restriction on the vertical scales is virtually opposite to the assumptions and restrictions of QG. It is, however, similar to the two-layer frontal geostrophic equations of Cushman-Roisin *et al.*[22].

- to study baroclinic instability in two-layer and quasi-two-layer flows. The effects of

a large interface slope and of including a third (thin) stratified layer into the model are investigated.

2.1 Derivation of equations

A two-layer model can be derived from the LSGE (1.17a-e) by making an assumption about the temperature, $\theta(x, y, z, t)$

$$\theta(x, y, z, t) = T\mathbb{H}(z + h) \tag{2.1}$$

where $h(x, y, t)$ is the depth of the upper layer, T is some prescribed (positive) constant determining the temperature difference between the top and bottom layers and $\mathbb{H}(z + h)$ is the Heaviside function.

We can further simplify the problem by introducing a streamfunction, ψ, which satisfies the continuity equation, (1.17d)

$$\bar{u} = -\frac{1}{H}\frac{\partial \psi}{\partial y}, \quad \bar{v} = \frac{1}{H}\frac{\partial \psi}{\partial x}. \tag{2.2}$$

The problem is then reduced to finding equations to describe the evolution of ψ and of h, both of which are functions of x, y and t only. That is, the z dependence has been completely removed by the assumption (2.1). There are several possible assumptions that can be made about θ all of which have the beneficial result of reducing the number of independent variables from four (namely, three spatial plus time) to three (namely, two spatial plus time). The Depth-Independent-Temperature assumption (DIT) of Chapter 3 resides in this class as does the Generalised-Two-Layer-Equation (GTLE) assumption of Appendix A. All three resulting equation-sets comprise an equation for the evolution of the streamfunction, ψ, and a further equation describing the evolution of another dependent variable, analogous to h here, which represents the baroclinic flow.

2.1.1 Viscous terms

We incorporate the effects of viscosity by adding linear drag terms to the RHS of both the horizontal equations of the LSGE, thus modifying (1.17a, b) to

$$\epsilon\frac{\partial \bar{u}}{\partial t_s} - \tilde{f}V = -\frac{\partial \Phi}{\partial x_s} + \epsilon\theta\frac{\partial}{\partial x_s}(\nabla_s.\mathbf{A}) - \nu U \tag{2.3a}$$

$$\epsilon\frac{\partial \bar{v}}{\partial t_s} + \tilde{f}U = -\frac{\partial \Phi}{\partial y_s} + \epsilon\theta\frac{\partial}{\partial y_s}(\nabla_s.\mathbf{A}) - \nu V. \tag{2.3b}$$

Here, ν is the coefficient of *Rayleigh friction*[1]. We choose to use Rayleigh friction rather than horizontal diffusion or hyperdiffusion because it greatly simplifies the resulting equations. The inclusion of diffusive $\nabla^2\mathbf{U}$ terms would require the solution of a Poisson-type equation at every vertical level of the ocean. This is an extra burden to the numerical scheme employed to solve the equations. However, experiments in a barotropic ocean basin (§4.1.3) show that the precise form of the non-conservative terms is unimportant.

Thermal diffusion is also modelled. This is considerably less problematic than the inertial viscosity and so we can simply add a three-dimensional thermal diffusion term to the right hand side of the temperature equation (1.17e):

$$\frac{\partial\theta}{\partial t_s} + U\frac{\partial\theta}{\partial x_s} + V\frac{\partial\theta}{\partial y_s} + W\frac{\partial\theta}{\partial z_s} = \kappa\left(\nabla^2\theta + \frac{\partial^2\theta}{\partial z^2}\right). \tag{2.3e}$$

Here, and throughout this thesis, κ is the coefficient of thermal diffusion. It is always assumed to be a constant.

2.1.2 Wind forcing and Ekman layers

To deal with the wind-forcing in a consistent manner, we need to add an Ekman Boundary layer at the top of the ocean. Wind-forcing will produce horizontal motion in such a layer and conservation of mass requires that in regions of horizontal divergence, fluid will be *sucked* upwards from the main body of the ocean below. This is known as **Ekman suction**. Conversely, in regions of horizontal convergence within the Ekman Layer, fluid will be *pumped* downwards into the ocean. This is **Ekman pumping**. The influence of the wind-forcing can be parametrised by specifying a horizontal velocity, $\mathbf{u_E}$, in the Ekman Layer. The assumption that $\mathbf{u_E}$ is non-zero *only* in the thin Ekman layer at $z = 0$ leads to a modified form for the boundary condition at the surface of the main ocean (which is now the top of the internal fluid where it interfaces with the parametrised Ekman Layer, see Figure 2.1).

$$W_T = \nabla.(H\bar{\mathbf{u}}_\mathbf{E}) \tag{2.4a}$$

$$W_B = -\mathbf{U}.\nabla H \tag{2.4b}$$

where $\bar{\mathbf{u}}_\mathbf{E}$ denotes the vertical average.

These boundary conditions and conservation of mass of the internal fluid (flowing with velocity $\mathbf{U}$), can be jointly satisfied by a modified streamfunction, ψ, such that

$$H\bar{u} = -\psi_y - H\bar{u}_E, \quad H\bar{v} = \psi_x - H\bar{v}_E. \tag{2.5}$$

[1]Rayleigh friction is more conventionally represented by ϵ. However, throughout this thesis ϵ always represents the Rossby number.

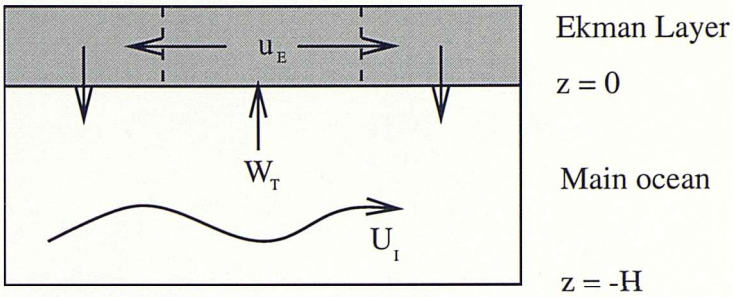


Figure 2.1: The Ekman layer sits on top of the main ocean. Horizontal divergence (convergence) of $\mathbf{u}_E$ corresponds to positive (negative) vertical velocities at the surface of the main ocean, W_T. The relative depth of the Ekman layer is *greatly* exaggerated here.

Now, the velocity is composed of three parts:

$$\mathbf{U} = \mathbf{u_E} + \bar{\mathbf{u}} + \hat{\mathbf{U}} \tag{2.6}$$

The Ekman velocity $\mathbf{u}_E$ is only non-zero near the surface although we shall not need to know its precise vertical structure; it turns out that the only additional characteristic required is the vertical average.

2.1.3 Singularity at the equator

The co-ordinate transformation (1.11a-c) contains a singularity at the equator. For example,

$$x_s = x_c + \epsilon \frac{\hat{v}}{\tilde{f}} \tag{2.7}$$

where $\tilde{f} = 0$ at $y_c = y_s = 0$. However, all the dynamics can be studied and computed in the Semi-Geostrophic co-ordinate frame and so the only place where this singularity becomes an issue (apart from transforming back to Cartesian co-ordinates) is in the terms involving $\nabla.\mathbf{A}$. This singularity can be removed by modifying the equation (1.19) for $\mathbf{A}$ to

$$\mathbf{A} = -\int_{z_s}^{0} \left(\frac{\hat{v}}{\tilde{f}_{eq}}, -\frac{\hat{u}}{\tilde{f}_{eq}} \right) dz'_s. \tag{2.8}$$

$\hat{u}$ and $\hat{v}$ are now defined by

$$\frac{\partial}{\partial z_s}(\hat{u}, \hat{v}) = \frac{1}{\tilde{f}_{eq}} \left(-\frac{\partial \theta}{\partial y_s}, \frac{\partial \theta}{\partial x_s} \right) \text{ and } \int_{-H_s}^{0} (\hat{u}, \hat{v}) dz_s = 0 \tag{2.9}$$

where

$$\tilde{f}_{eq} \equiv \sqrt{\tilde{f}^2 + \delta_{eq}^2}. \tag{2.10}$$

δ_{eq} is a small prescribed (real) constant. The modified equations are the same as the unmodified equations outside a region of thickness $O(\delta_{eq})$ in the neighbourhood of the equator. A similar modification is required for the non-inertial GTLE (Salmon[72]).

2.1.4 The barotropic streamfunction

An evolution equation for the barotropic streamfunction, ψ, is obtained by integrating both the horizontal momentum equations (2.3a, b) and using the hydrostatic equation (1.17c) to write

$$\int_{-H}^{0} dz \frac{\partial \Phi}{\partial x} + H\frac{\partial}{\partial x}(\Phi(x,y,-H)) - \frac{\partial}{\partial x}\int_{-H}^{0} z\left[\theta + \epsilon\theta\frac{\partial}{\partial z}\nabla.\mathbf{A}\right]dz, \text{ etc.} \tag{2.11}$$

Dividing by H and cross-differentiating removes all the Φ terms and results in an equation for the vertically averaged relative vorticity, ζ (2.19, below). After a little algebra, we obtain

$$\begin{aligned}\epsilon\frac{\partial \zeta}{\partial t} =& J\left(\frac{\tilde{f}}{H},\psi\right) + J\left(\frac{1}{H},\gamma\right) + \epsilon\left\{J\left(\frac{1}{H},\sigma_z\right) - \frac{\partial}{\partial x}\left[\frac{1}{H}\sigma_y\right] + \frac{\partial}{\partial y}\left[\frac{1}{H}\sigma_x\right]\right\} \\ & - \nu\zeta + \mathsf{W}(x,y)\end{aligned} \tag{2.12}$$

where

$$\gamma \equiv \int_{-H}^{0} z\theta dz \tag{2.13}$$

$$\sigma_z \equiv \int_{-H}^{0} z\frac{\partial\theta}{\partial z}\nabla.\mathbf{A}dz \tag{2.14}$$

$$\sigma_x \equiv \int_{-H}^{0} \frac{\partial\theta}{\partial x}(\nabla.\mathbf{A})dz \tag{2.15}$$

$$\sigma_y \equiv \int_{-H}^{0} \frac{\partial\theta}{\partial y}(\nabla.\mathbf{A})dz \tag{2.16}$$

and

$$\mathsf{W}(x,y) \equiv \nabla.\left(\tilde{f}\bar{\mathbf{u}}_E\right) - \nu\left(\frac{\partial \bar{v}_E}{\partial x} - \frac{\partial \bar{u}_E}{\partial y}\right). \tag{2.17}$$

Here, and everywhere else throughout this thesis,

$$J(F_1,F_2) \equiv \frac{\partial(F_1,F_2)}{\partial(x,y)} \equiv \frac{\partial F_1}{\partial x}\frac{\partial F_2}{\partial y} - \frac{\partial F_1}{\partial y}\frac{\partial F_2}{\partial x} \tag{2.18}$$

is the horizontal Jacobian operator in semi-geostrophic co-ordinates and

$$\zeta \equiv \nabla.\left(\frac{1}{H}\nabla\psi\right) \tag{2.19}$$

is the barotropic relative vorticity.

Thus far, we have not required any assumption concerning the vertical structure of the temperature. All such information is included within the terms involving $\nabla.\mathbf{A}$. This term, and hence $\gamma, \sigma_z, \sigma_x, \sigma_y$ must be evaluated separately for each assumption made. In the case of a barotropic flow, $\nabla.\mathbf{A} = 0$. In the case of a two-layer flow,

$$\begin{aligned}\nabla.\mathbf{A} = &-\frac{2}{\tilde{f}_{eq}^3}\nabla\tilde{f}_{eq}.\nabla(hT)\left\{(z+h)\mathbb{H}(z+h) - \frac{h}{H}(z+H)\right\} \\ &+\frac{1}{\tilde{f}_{eq}^2}\left[T\nabla^2 h\left\{(z+h)\mathbb{H}(z+h) - \frac{h}{H}(z+H)\right\}\right. \\ &\left. -T\nabla h.\left\{\nabla h\left[\mathbb{H}(z+h) - (z+h)\delta(z+k)\right] + \nabla\left(\frac{h}{H}(z+H)\right)\right\}\right].\end{aligned} \tag{2.20}$$

Here, $\delta(.)$ is the *Dirac Delta Function.* Since all terms of (2.12) involving $\nabla.\mathbf{A}$ occur in integrals in which there is also a derivative of θ, it turns out that, in fact, we only require the value of $\nabla.\mathbf{A}$ at the point where $z = -h$. This is because it is at precisely this depth that $\delta(z+h)$ is non-zero.

$$\begin{aligned}\alpha \equiv \nabla.\mathbf{A}(x,y,-h) = &\frac{T}{f_{eq}^2}\left\{-h\left(\nabla^2 h - 2\frac{\nabla h.\nabla f_{eq}}{\tilde{f}_{eq}}\right)\left(1-\frac{h}{H}\right)\right. \\ &\left. +\nabla h.\left[\frac{1}{2}\nabla h - \nabla\left(\frac{1}{2}\frac{h}{H}\right)(H-h) - \frac{h}{H}gradH\right]Biggr\}.\right.\end{aligned} \tag{2.21}$$

Substituting (2.21) into (2.12) yields an equation for the barotropic vorticity.

$$\begin{aligned}\epsilon\frac{\partial\zeta}{\partial t} + J\left(\psi, \frac{f}{H}\right) + \epsilon J\left(\psi, \frac{\zeta}{H}\right) - J\left(\frac{1}{H}, -\frac{1}{2}Th^2\right) - \epsilon J\left(\frac{h}{H}, T\alpha\right) \\ = -\nu\zeta + \mathsf{W}(x,y).\end{aligned} \tag{2.22}$$

The last two terms on the LHS of (2.22) represent the baroclinic feedback on the barotropic flow. The first of the two, $J\left(\frac{1}{H}, -\frac{1}{2}Th^2\right)$ is known as the *Joint Effect of Baroclinicity And Relief* (*JEBAR*) term. The second of the two involves a combined effect of baroclinicity, relief *and* inertia.

2.1.5 The baroclinic flow: an evolution equation for the interface height

We obtain an equation for the depth of the upper layer, h, by integrating the temperature equation (2.3e) from the bottom of the ocean to the surface.

$$\int_{-H}^{0}\frac{\partial\theta}{\partial t}dz + \nabla.\int_{-H}^{0}\mathbf{U}\theta dz = \kappa\nabla.\int_{-H}^{0}\nabla\theta dz + \mathsf{Q}(x,y) \tag{2.23}$$

where $\mathsf{Q}(x,y)$ is a term representing a prescribed surface heating. We shall assume that the ocean floor is perfectly insulating and so there is no heat flux through $z = -H$. The

first and penultimate terms in (2.23) are easy to evaluate and the only hard work is to be found in simplifying the second of the terms.

Now, from (2.6) we have that[2]

$$\int_{-H}^{0} \mathbf{U}\theta dz = \int_{-H}^{0} \bar{\mathbf{u}}\theta dz + \int_{-H}^{0} \hat{\mathbf{U}}\theta dz + \int_{-H}^{0} \mathbf{u}_E\theta dz \tag{2.24}$$

and from (2.5), that

$$\int_{-H}^{0} \bar{\mathbf{u}}\theta dz = \int_{-H}^{0} \frac{1}{H}(-\psi_y, \psi_x)\theta dz - \int_{-H}^{0} \bar{\mathbf{u}}_E\theta dz. \tag{2.25}$$

Combining (2.23, 2.24, 2.25) and using the fact that $\mathbf{u}_E$ is non-zero only near $z = 0$, so we can replace

$$\int_{-H}^{0} \mathbf{u}_E\theta dz \qquad \text{with} \qquad \theta|_{z=0} \int_{-H}^{0} \mathbf{u}_E dz = TH\bar{\mathbf{u}}_E, \tag{2.26}$$

yields

$$\nabla. \int_{-H}^{0} \mathbf{U}\theta dz = J\left(\psi, \frac{h}{H}T\right) + \nabla.\left[H\bar{\mathbf{u}}_E T(1 - \frac{h}{H})\right] + \int_{-H}^{0} \hat{\mathbf{U}}\theta dz. \tag{2.27}$$

The task is now to determine $\hat{\mathbf{U}}$. This is achieved by differentiating (2.3a, b) with respect to z to remove the vertically averaged component of $\mathbf{U}$ and then solving the two simultaneous equations for $\hat{U}_z$ and $\hat{V}_z$. The procedure yields

$$\hat{U}_z = \frac{1}{f^2 + \nu^2}\left\{-\nu\theta_x - \tilde{f}\theta_y + \epsilon\tilde{f}\left[\theta_z(\nabla.\mathbf{A})_y - \theta_y(\nabla.\mathbf{A})_z\right]\right\} \tag{2.28}$$

There is a similar expression for $\hat{V}_z$. In (2.28) we have neglected terms of magnitude $O(\epsilon\nu)$ as both parameters are considered to be small.

We obtain $\hat{U}$ from (2.28) via

$$\hat{U} = G\left[\hat{U}_z\right] \tag{2.29}$$

where

$$G[r(z)] \equiv \int_{-H}^{z} r(z')dz' + \frac{1}{H}\int_{-H}^{0} z'r(z')dz'. \tag{2.30}$$

After some tedious, but relatively straightforward, algebra we eventually obtain an explicit expression for the final term of (2.27). This is substituted, along with the other terms of (2.27), into (2.23) to finally arrive at the equation for the evolution of the interface depth:

$$\begin{aligned} &T\frac{\partial h}{\partial t} + J\left(\psi, T\frac{h}{H}\right) + J\left(Th - \epsilon\alpha, \frac{T\tilde{f}h\left(1 - \frac{h}{H}\right)}{\tilde{f}^2 + \nu^2}\right) \\ &\quad = \kappa T\nabla^2 h + \nu\nabla.\left[\frac{T^2 h\nabla h}{\tilde{f}^2 + \nu^2}\left(1 - \frac{h}{H}\right)\right] + \nabla.\left[T\bar{\mathbf{u}}_{\mathbf{E}}(h - H)\right] + \mathrm{Q}(x, y). \end{aligned} \tag{2.31}$$

[2]Recall that $\bar{\mathbf{u}} = \bar{\mathbf{U}}$, but $\hat{\mathbf{u}} \neq \hat{\mathbf{U}}$.

Clearly, for this equation to make any physical sense, we require that $0 \leq h \leq H$. That is, the interface must lie somewhere between the surface and bottom of the ocean.

Before investigating solutions of (2.22, 2.31) it is illuminating to compare them with other two-layer models. In the geostrophic limit of $\epsilon = 0$, we recover the two-layer thermocline equations (2.6, 2.7) of Salmon[71]. In fact, [71] also restricts attention to $\kappa = \mathsf{W} = \mathbf{u_E} = 0$ and additionally simplifies $f^2 + \nu^2$ to f^2. This is because the focus of that paper is the mid-latitude Gulf-Stream. Hence $f \gg \nu$ everywhere.

Of the models to retain inertia, our equations most closely resemble the frontal geostrophic equations (37, 38) of Cushman-Roisin *et al.*[22]. In that paper, in common with many other models in the literature, many additional restrictions are imposed. The frontal geostrophic equations impose a flat-bottom ($H = 0$), small variation in Coriolis parameter ($f = \beta y, \beta \ll 1$), large horizontal length-scales ($L \gg \lambda_{int}$) and an upper layer depth which is much smaller than the entire depth of the ocean. The QG equations (which are obtained as a separate reduction in [22]) impose further restrictions on ∇h although the assumption $L \gg \lambda_{int}$ is relaxed. The two-layer LSGE equations (2.22, 2.31) allow for $O(1)$ variations in topography and Coriolis parameter and make no assumption concerning the relative depths of the two layers. In the limit of $\nabla f \ll 1, H = 1, \frac{h}{H} = \delta \leq \epsilon$ our equations reduce to those of [22] except for the fact that we cannot consistently retain the quadratic $\frac{\delta}{\epsilon} h \frac{\partial h}{\partial x}$ term of (38 of [22]). This is a consequence of the *a priori* respective assumptions of small and $O(1)$ upper layer depths in [22] and this thesis.

It is also worthy of comment that (37, 38) of [22] are equations in physical space whereas (2.22, 2.31) here, are in SG co-ordinates (1.11a-c). The transformation back to physical co-ordinates is a non-trivial matter. The details, if not the final outcome, depend on the precise depth (z_s) at which the transformation is executed. For example, if we consider making the transformation somewhere in the lower layer we find that the Jacobian in SG co-ordinates, $J_s(F, G)$, is related to the Jacobian in physical co-ordinates, $J_c(F, G)$ via

$$J_s(F, G) = \left[1 + \epsilon \nabla . \left(\frac{h}{H f^2} \nabla h\right)\right] J_c(F, G). \tag{2.32}$$

Hence, the equations in physical co-ordinates differ from (2.22, 2.31) by terms of magnitude $O(\epsilon^2, \epsilon\delta, \epsilon\beta)$. All these terms are neglected by [22]. To see that the QG equations cannot be obtained in any limit of (2.22, 2.31) note that the nonlinear h terms are cubic whereas the nonlinearity in the two-layer QG equations (28, 29 of [22]) are quadratic.

2.2 Baroclinic instability

In this section we study a set of solutions of the conservative two-layer equations (2.22, 2.31, $\nu = \kappa = \mathsf{Q} = \mathsf{W} = 0$) with the intention of investigating the phenomenon of

baroclinic instability. Baroclinic instabilities are caused, primarily, by vertical variation in the potential vorticity (e.g. Pedlosky[57]) and so are relatively unaffected by non–conservative forces, bottom topography and the precise form of the Coriolis parameter. The essential ingredients are **stratification and rotation**. Baroclinic instabilities are an important mechanism in ocean circulation theory. They provide a means for transporting energy away from regions in which it is highly concentrated and so prevent the build up of unsustainably large gradients. Of course, this process is also achieved by diffusion, but baroclinic instability comes into play when the viscous terms cannot diffuse energy away rapidly enough. In the non-inertial studies of the GTLE [72] and of the depth-independent temperature equations [75], there is no baroclinic instability and shocks (literally, infinitely large gradients) form close to the western boundary as the $\frac{f}{H}$ contours converge. Baroclinic instability provides a means of preventing such unphysical behaviour. Finally, in §2.2.4 we use the GTLE (Appendix A) to extend the notion of a two-layer ocean to one in which a third, stratified layer is present.

2.2.1 The two-layer Phillips model

The model now considered is a simple two-layer, flat-bottomed, channel. There are solid walls at the northern and southern boundaries where we apply no normal flow. Periodic boundary conditions are applied at the East and West. This model was considered by Phillips[58] to study quasi-geostrophic baroclinic instability. Additionally, we restrict attention to an f-plane.

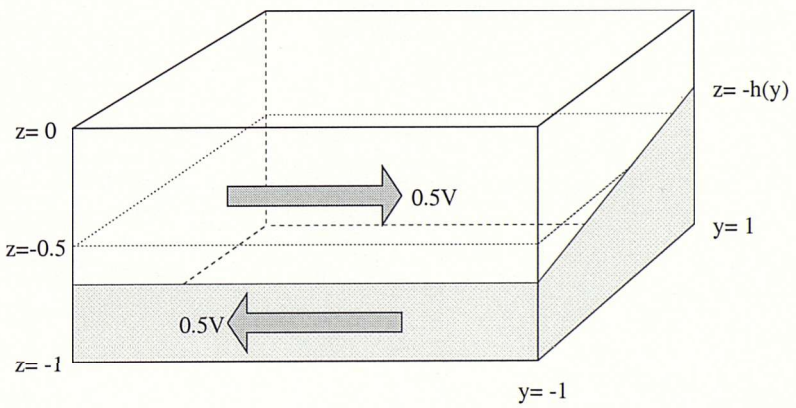


Figure 2.2: Two-layer ocean.

These simplifications reduce (2.22) and (2.31) to

$$\nabla^2\psi_t + J\left(\psi, \nabla^2\psi\right) + J\left(\sigma, h\right) = 0 \tag{2.33}$$

and

$$h_t + \epsilon(1-2h)\left[\nabla^2\psi_t + J\left(\psi, \nabla^2\psi\right)\right] + J\left(\psi, h\right) - \frac{\epsilon}{\tilde{f}}h(h-1)J(h, \nabla^2\psi) = 0 \tag{2.34}$$

where

$$\sigma = -\frac{1}{2}|\nabla h|^2 - h\nabla^2 h + h\left(|\nabla h|^2 + h\nabla^2 h\right). \tag{2.35}$$

The solution corresponding to purely baroclinic flow (that is, no mean flow) is

$$\psi = \frac{1}{2}V^2y^2, \qquad h = \frac{1}{2} - Vy. \tag{2.36}$$

We add a small disturbance to this basic state:

$$\psi = \frac{1}{2}V^2y^2 + \phi(x,y,t), \qquad h = \frac{1}{2} - Vy + \eta(x,y,t) \tag{2.37}$$

where

$$\phi,\ \eta \ll 1. \tag{2.38}$$

This solution (2.37) is substituted back into (2.33) and (2.34) to yield a pair of equations for η and ϕ:

$$\nabla^2\phi_t - V^2y\nabla^2\phi_x - 2V^3y\eta_{xy} - V\left(V^2y^2 - \frac{1}{4}\right)\nabla^2\eta_x = 0 \tag{2.39}$$

$$\eta_t + 2\epsilon Vy\nabla^2\phi_t - V\phi_x - V^2y\eta_x - 2\epsilon V^3y^2\nabla^2\phi_x + \epsilon V\left(V^2y^2 - \frac{1}{4}\right)\nabla^2\phi_x = 0. \tag{2.40}$$

We seek solutions that are wave-like in the East-West direction.

$$\eta = \hat{\eta}(y)e^{i(kx-\omega t)}, \qquad \phi = \hat{\phi}(y)e^{i(kx-\omega t)}. \tag{2.41}$$

This leaves us with a pair of complex eigenvalue equations for $\hat{\eta}$ and $\hat{\phi}$ with complex eigenvalue ω.

$$-\omega\left(\hat{\phi}'' - k^2\hat{\phi}\right) - V^2ky\left(\hat{\phi}'' - k^2\hat{\phi}\right) - 2V^3ky\hat{\eta}' - Vk\left(V^2y^2 - \frac{1}{4}\right)\left(\hat{\eta}'' - k^2\hat{\eta}\right) = 0 \tag{2.42}$$

$$-\omega\hat{\eta} - 2\epsilon\omega Vy\left(\hat{\phi}'' - k^2\hat{\phi}\right) - Vk\hat{\phi} - V^2ky\hat{\eta} - 2\epsilon V^3ky^2\left(\hat{\phi}'' - k^2\hat{\phi}\right) + \epsilon Vk\left(V^2y^2 - \frac{1}{4}\right)\left(\hat{\phi}'' - k^2\hat{\phi}\right) = 0. \tag{2.43}$$

There are two extra degrees of freedom in the problem which we use up by specifying an amplitude condition and a phase condition on the waves.

- $\| \hat{\eta} \|^2 + \| \hat{\phi} \|^2 = 1$ (amplitude condition)
- $\mathbb{I}\left(\hat{\phi}(-1)\right) = 0$ (phase condition)

The problem is now well posed and can be solved numerically. I did this by guessing an initial solution and using a Newton-Raphson iterative scheme to improve it. See B.4, [59] or [81] for further details.

2.2.2 The quasi-geostrophic limit

An initial guess can be obtained by looking at a (vanishingly) small interface gradient. This is the QG limit studied by Phillips[58]. This procedure yields

$$\nabla^2 \hat{\phi}_t + \frac{1}{4} V \nabla^2 \hat{\eta}_x = 0 \tag{2.44}$$

$$\hat{\eta}_t - V \hat{\phi}_x - \frac{1}{4} \epsilon V \nabla^2 \hat{\phi}_x = 0 \tag{2.45}$$

which admit solutions of the form

$$\hat{\eta}(y) = A_\eta e^{ily}, \qquad \hat{\phi}(y) = A_\phi e^{ily}. \tag{2.46}$$

Substituting (2.46) into (2.44, 2.45) gives

$$\omega K^2 A_\phi - \frac{1}{4} k V K^2 A_\eta = 0 \tag{2.47}$$

$$\omega A_\eta + k V A_\phi - \frac{1}{4} \epsilon k V K^2 A_\phi = 0. \tag{2.48}$$

where

$$K^2 = k^2 + l^2.$$

This has non-trivial solutions if and only if

$$\omega^2 - \frac{1}{4} k^2 V^2 \left(\frac{1}{4} \epsilon K^2 - 1 \right) = 0. \tag{2.49}$$

ω is purely imaginary for

$$K^2 < \frac{4}{\epsilon} \equiv k_{int}^2 \tag{2.50}$$

and it is purely real for wavenumbers bigger than (2.50). This is the same condition for stability found by Phillips[58] for the QG model. The fastest growing wavelength can be found by setting

$$\frac{\partial}{\partial k}, \frac{\partial}{\partial l} \mathbb{I}(\omega) = 0$$

to obtain

$$(k,l)_{fastest} = \left(\frac{1}{\sqrt{2}}k_{int}, 0\right).$$

In the ocean, this corresponds to a wavelength of about $56km$. As a comparison, Phillips obtained a fastest growing wavenumber of $(0.644k_{int}, 0)$.

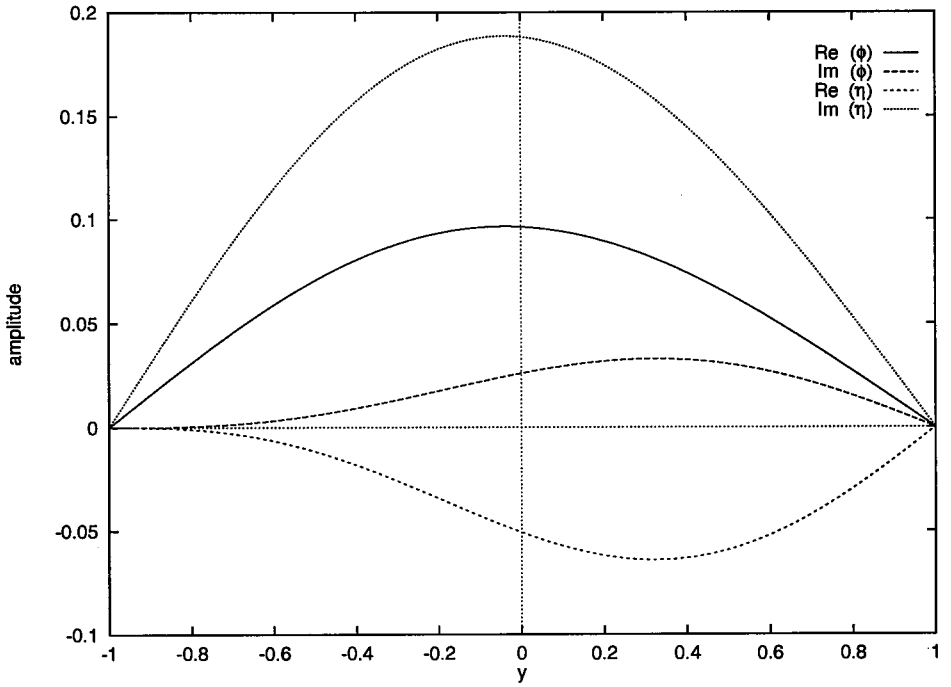
As a test of the numerical code, we can use small values of the interface slope V and plot the shapes of the resulting eigenfunctions. The results for the $l = 1$ and $l = 2$ modes are shown in Figure 2.3(a) and Figure 2.3(b) respectively. As predicted by the theory, they are approximately sinusoidal. The dispersion relation for the QG limit is shown in Figure 2.4.

2.2.3 Non quasi-geostrophic instability

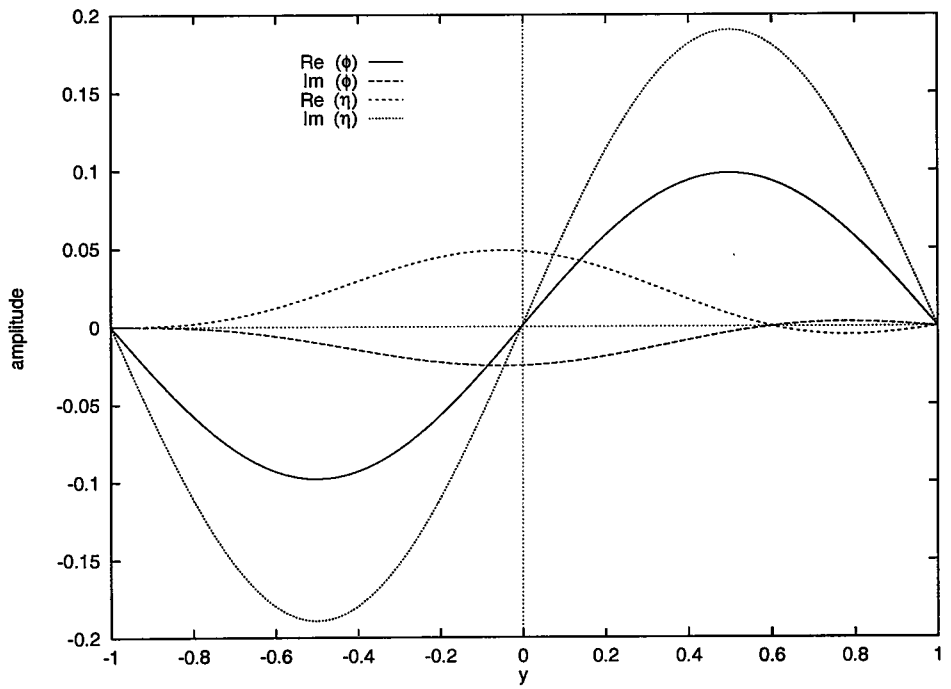
The LSGE are not restricted to small interface slopes so we can increase the parameter V in the eigenvalue equations (2.42, 2.43). A summary of the results is:

- The peak of the disturbance moves away from the centre of the channel towards one of the boundaries (Figure 2.6)
- The disturbance initially becomes more unstable but as V is increased further it becomes less unstable (Figure 2.11(a))
- the disturbance is no longer stationary, that is, the wave becomes both a travelling and a growing wave (Figure 2.11(b))
- The most unstable mode moves to a shorter wavelength (larger k (Figure 2.10(a))

The key to the other properties lies in understanding the first; that the peak of the disturbance moves from the centre of the channel, towards one of the edges. Sakai[62] models baroclinic instability as an interaction of two Rossby waves, one in the top layer and one in the bottom. In the QG limit, the different (symmetric, sinusoidal) modes are orthogonal to each other and so there can be no interactions except for between the i^{th} mode of the top layer and the i^{th} mode of the bottom layer. Thus, the resulting disturbance is sinusoidal and symmetric. However, as the interface gradient, V increases, we have to incorporate the terms that are nonlinear in V. These are precisely the terms that the QG approximation neglects *a priori*. This means that the Fourier modes are no longer mutually orthogonal and so the i^{th} mode of the top layer can interact with the j^{th} mode of the bottom layer. The greatest interaction occurs when $i = j$, leading to a symmetric solution. The second largest degree of interaction occurs when $|i - j| = 1$. In



(a) $l = 1$



(b) $l = 2$

Figure 2.3: The eigensolutions in QG limit, $V = 0.01$; $k = \frac{1}{2^{\frac{1}{2}}} k_{int}$.

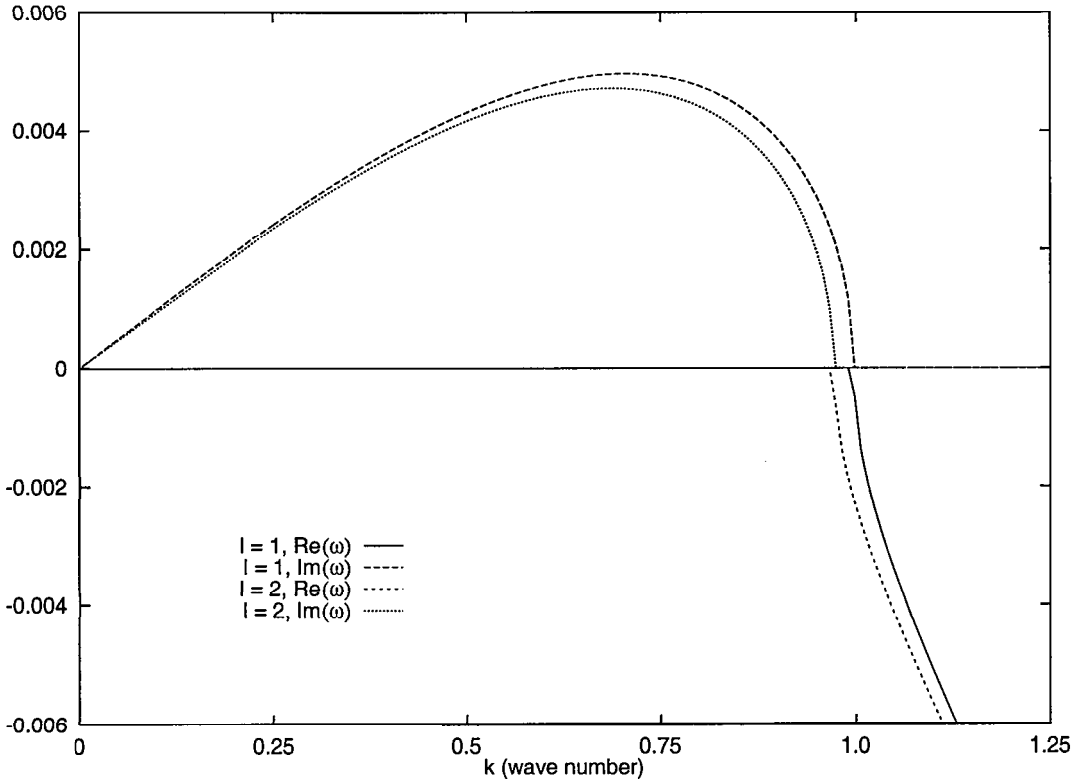


Figure 2.4: The dispersion relation in QG limit, $V = 0.01$; k is scaled on $k_{int} = \frac{4}{\epsilon}$.

particular, the first and second modes will interact quite strongly. Thus, we might expect the solutions that have proceeded from the $l = 1$ QG limit and the $l = 2$ QG limit to look similar to each other. This is, in fact, precisely what happens, (Figures 2.6(c), 2.7). If we consider the cross channel shape of a linear combination of the first and second modes we might expect something like Figure 2.5 in which the peak magnitude of the linear combination of modes $l = 1, l = 2$ is not located in the centre of the channel. In fact, $\mathbb{R}(\phi, \eta)$ of Figure 2.6(a) bear a striking similarity to the mixed mode of Figure 2.5.

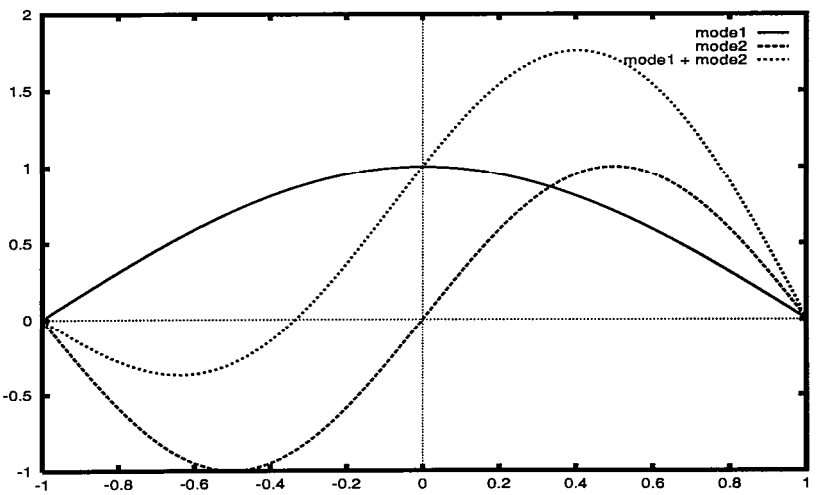
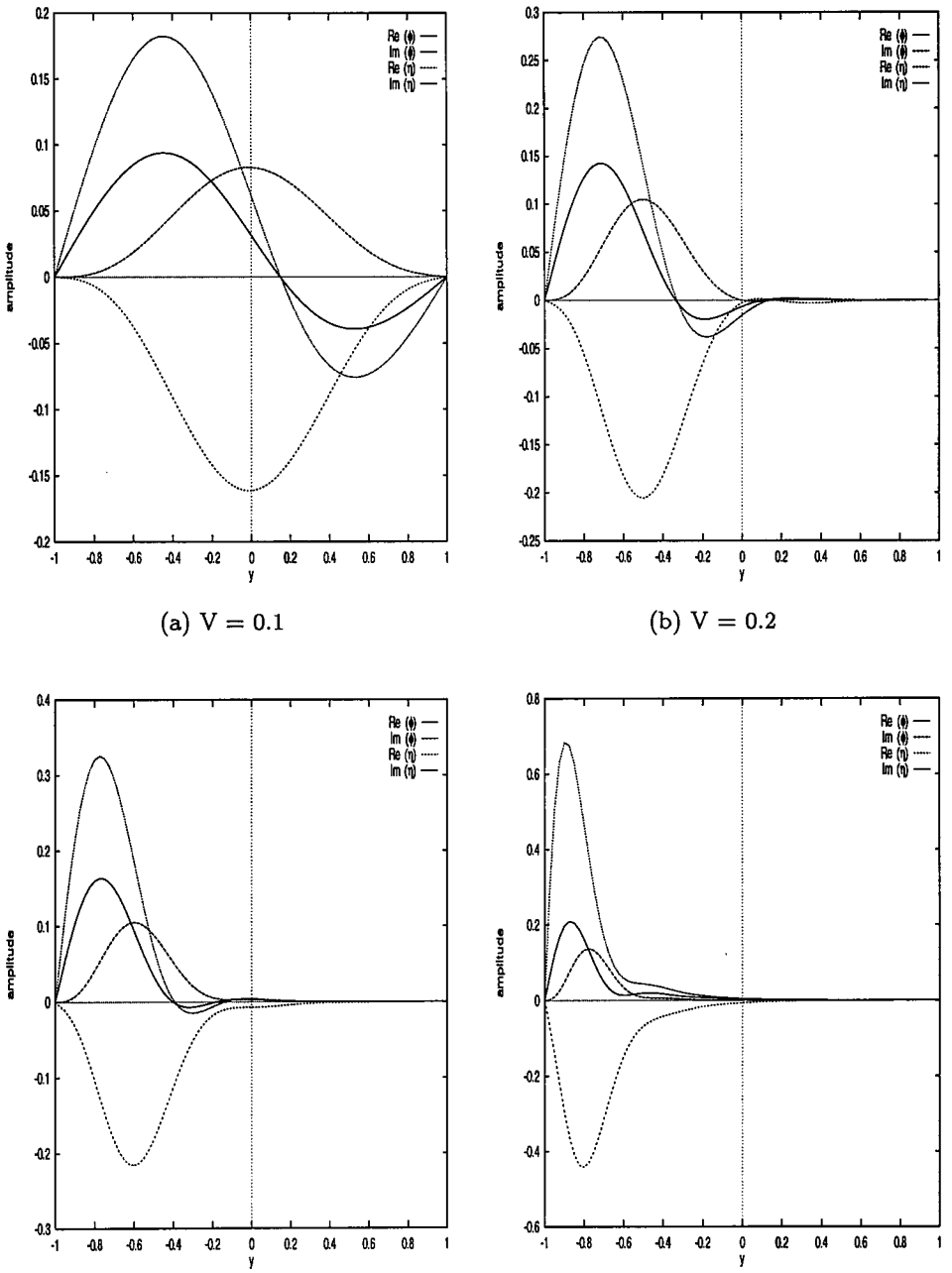


Figure 2.5: A combination of two symmetric modes can lead to an asymmetric solution.



(a) V = 0.1

(b) V = 0.2

(c) V = 0.3

(d) V = 0.45

Figure 2.6: Eigensolutions for $k = \frac{1}{2^{\frac{1}{2}}} k_{int}$ at various V; l = 1. The peak of the disturbance moves progressively further away from the centre of the channel.

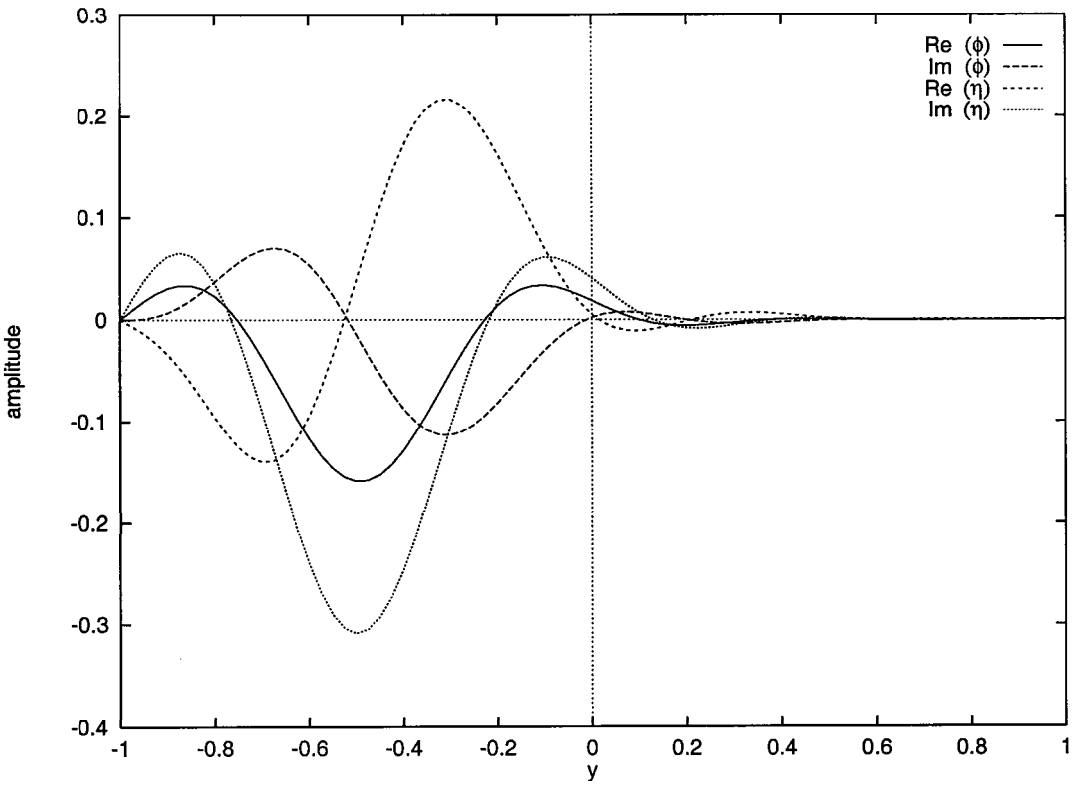


Figure 2.7: $l = 2, k = \frac{1}{2\frac{1}{2}} k_{int}$ mode at $V = 0.2$.

Once we have seen that the peak of the disturbance moves away from the centre of the channel, then the rest of the phenomena, listed above, can be explained upon consideration of the internal Rossby deformation radius, λ_{int}:

$$\lambda_{int} = \frac{\sqrt{g'h(H-h)}}{\tilde{f}\sqrt{H}}. \tag{2.51}$$

Furthermore, recall that baroclinic instabilities preferentially occur on length-scales only slightly bigger than the deformation radius ([57]). From (2.51) we see that the maximal value of λ_{int} occurs in the centre of the channel and decreases towards both boundaries.

Baroclinic instabilities are fuelled by the conversion of available potential energy (APE) into kinetic energy (KE). As the interface steepens, there is more APE and so the disturbance becomes more unstable (Figure 2.11(a)). This is the QG explanation for the change in instability. However, QG theory, which predicts linear growth with increasing V, does not take account of the changing λ_{int}. As the interface steepens, the peak of the wave moves closer to the edge of the channel and so its wavelength becomes larger with respect to λ_{int}. Thus, the APE is less likely to be converted into KE in that particular mode. Consequently, for any given mode, once the interface gradient has increased beyond some threshold level, the wave becomes less unstable (Figure 2.11(a)). What happens to the excess APE? This energy is converted to KE of different modes, namely the modes which are now closer to the internal Rossby radius at that particular point of the channel (that

is, the shorter ones) (Figure 2.10(a)).

Furthermore, away from the centre of the channel, there exists a mean flow. The depth averaged velocity is given by $\bar{u} = -\frac{\partial \psi}{\partial y} = -V^2 y$. Fluid in the bottom layer travels at one velocity whereas fluid in the top layer travels at the opposite velocity (see Figure 2.2). Hence, where the top layer is thicker there is a net positive flow in the channel and vice versa. Consequently, if the wave peak moves to one side or the other, it experiences a mean flow and is "dragged along" with it (Figure 2.11(b)).

Finally, note that, as shown in Figure 2.10(a), the form of the dispersion relation remains relatively unchanged except for a scaling factor, proportional to the interface gradient, V; that is, for very small k, ω is approximately linearly related to k. A peak value of the instability is reached for some $k \leq k_{int}$ and then the growth rate rapidly decreases as length-scales become progressively smaller.

Possibly the most important result of the analysis is that baroclinic instability *does* occur and is restricted to long waves. This is good for two reasons. Firstly, it means that the model is accurate over the baroclinically unstable scales. Secondly, *no* instability is produced over scales where the model is inaccurate. Should the model have predicted that short waves were baroclinically unstable, care must be taken in interpreting the numerical simulations. Compare this baroclinic instability analysis with that of §3.3 in which the small scales are the most unstable.

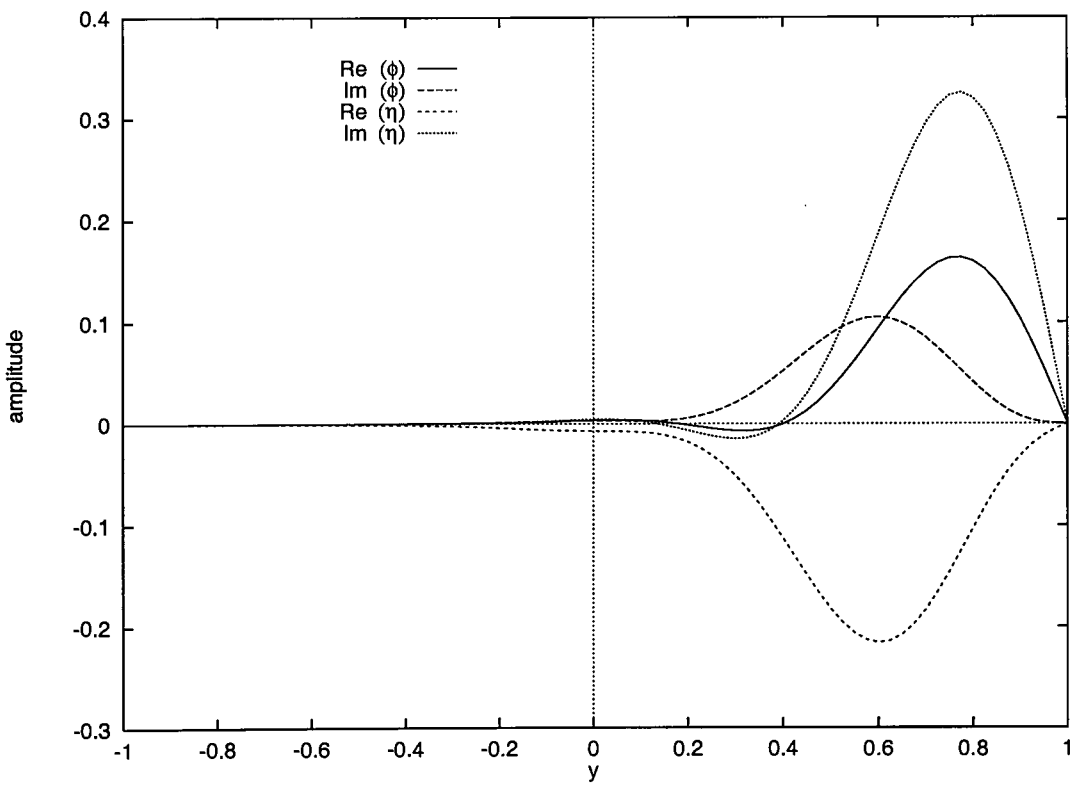


Figure 2.8: Right mode eigensolution for $k = \frac{1}{2^{\frac{1}{2}}} k_{int}, l = 1, V = 0.3$.

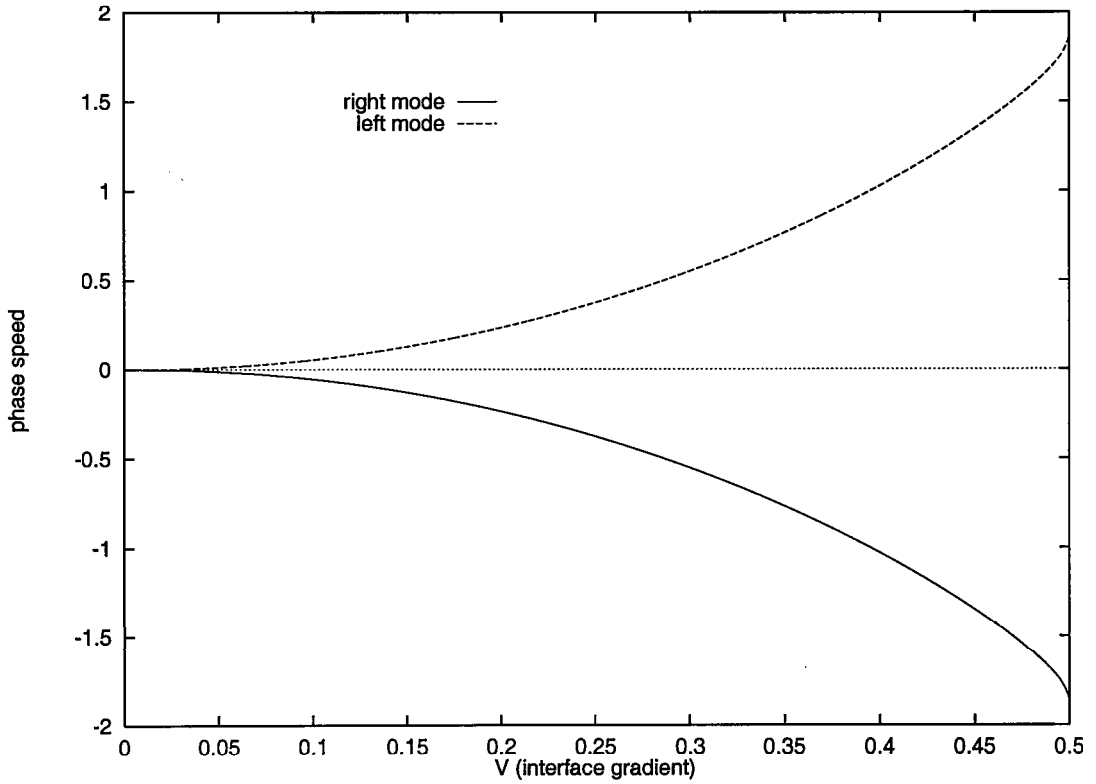
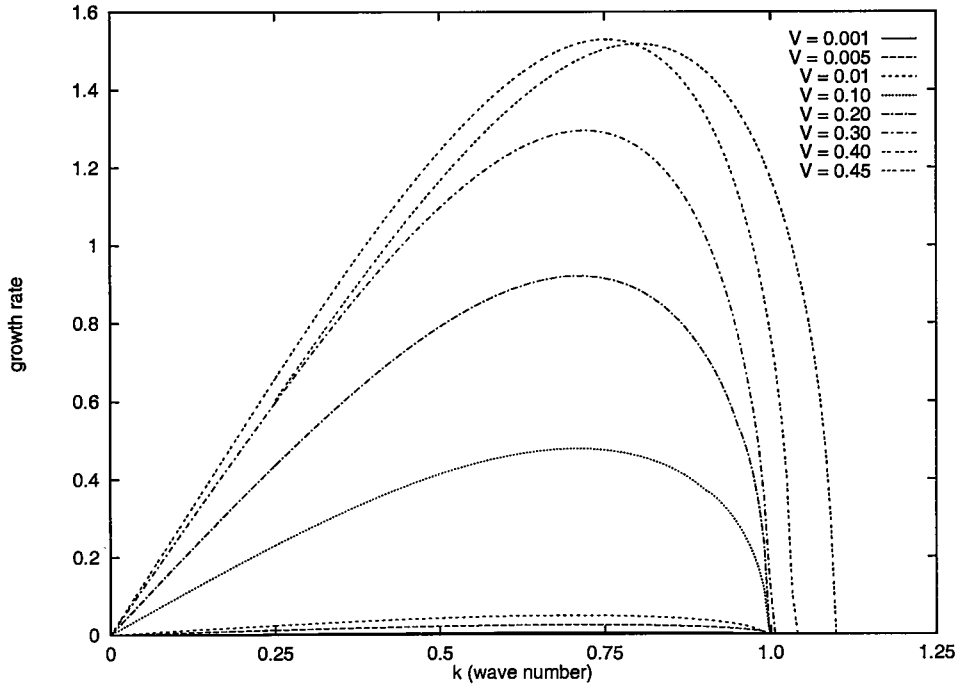
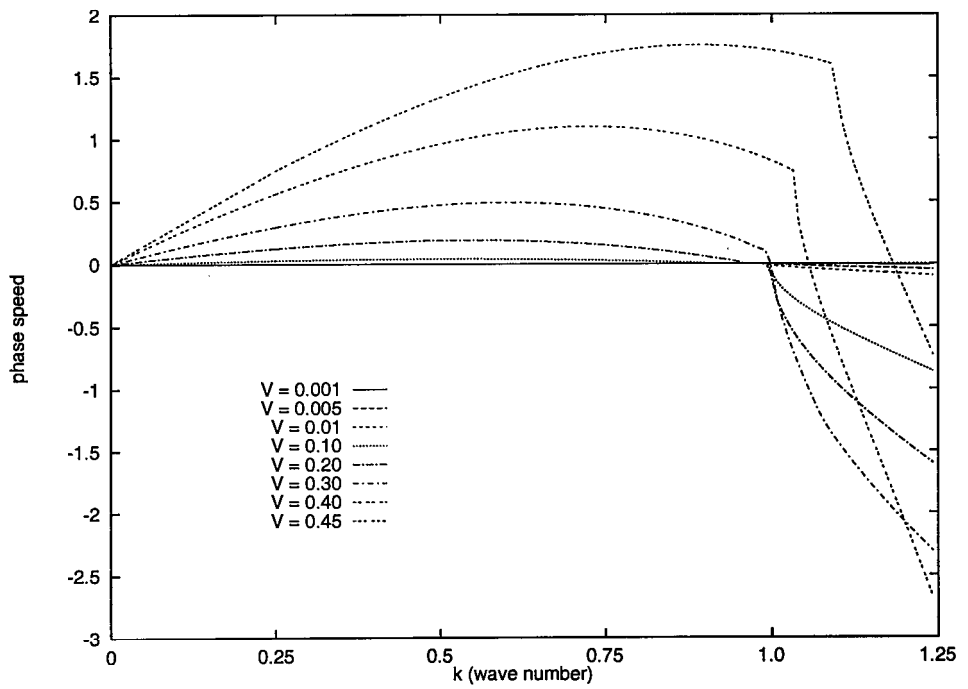


Figure 2.9: Phase speeds for both modes (left and right) at $k = \frac{1}{2^{\frac{1}{2}}} k_{int}$, $l = 1$, $V = 0.3$.

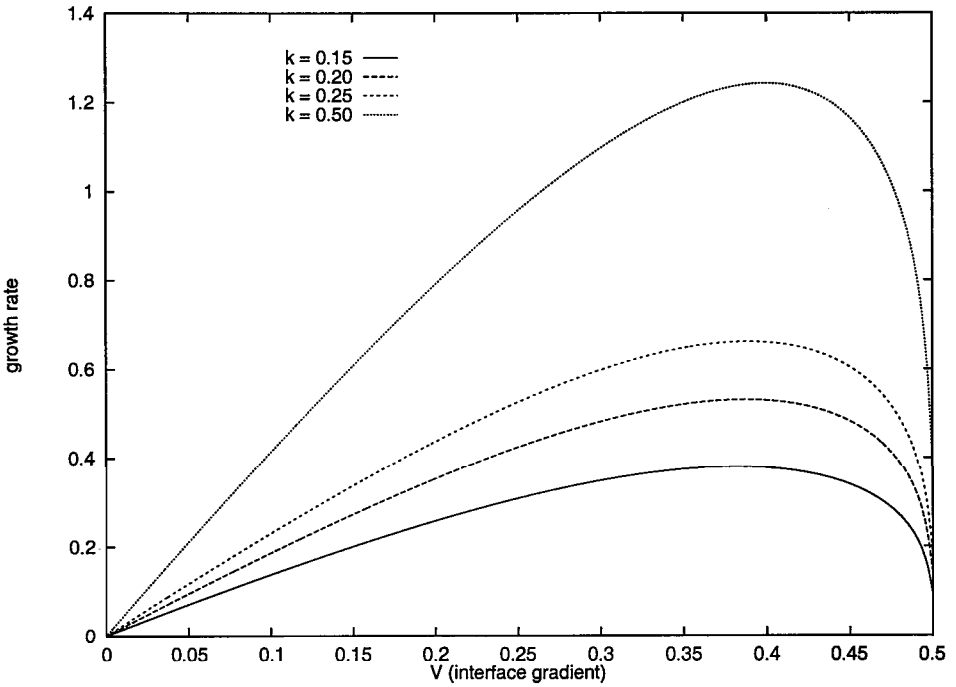


(a) $\mathbb{I}(\omega)$

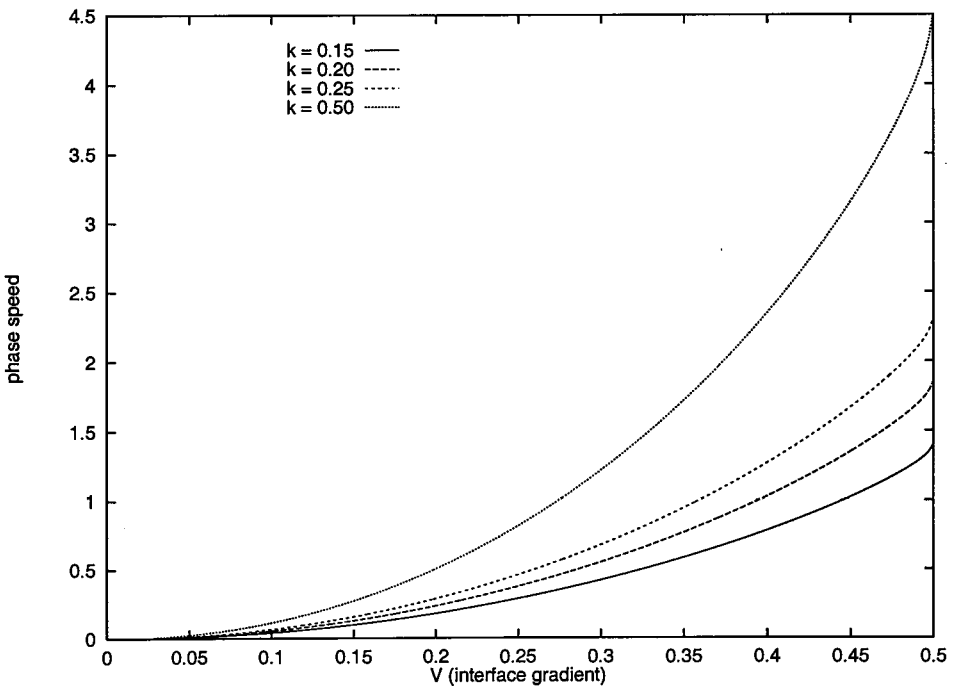


(b) $\mathbb{R}(\omega)$

Figure 2.10: Dispersion relations; $l = 1$. k is scaled on $k_{int} = \frac{4}{\epsilon}$.



(a) $\mathbb{I}(\omega)$



(b) $\mathbb{R}(\omega)$

Figure 2.11: Relationship of ω to V; $l = 1$. k is scaled on $k_{int} = \frac{4}{\epsilon}$.

2.2.4 Effect of a stratified layer

There are many ways to reduce the LSGE to a pair of two-dimensional (in space) equations by using an alternative ansatz to (2.1). One very general choice that can be made leads to the Generalised Two-Layer Equations (GTLE, Appendix A). The greatest two simplifications of the GTLE lead to the barotropic ocean (4.1) and to the two-layer equations of §2.1, namely (2.22, 2.31). One generalisation of the two-layer model is to incorporate a (thin) stratified layer between the top and bottom layers (Figure 2.12). This extra layer permits a continuous vertical temperature profile to be introduced. Such a profile can be as smooth as desired; from the C^∞ tanh function to the simplest function in this class, that of a piecewise-linear profile given by (2.52):

$$\theta(\xi) = \begin{cases} 1 & \xi > \delta \\ \frac{1}{2\delta}(\xi + \delta) & \delta > \xi > -\delta \\ 0 & -\delta > \xi \end{cases} \tag{2.52}$$

Here $\xi = z + h$, h is the depth of the middle of the stratified layer and the thickness of this layer is 2δ.

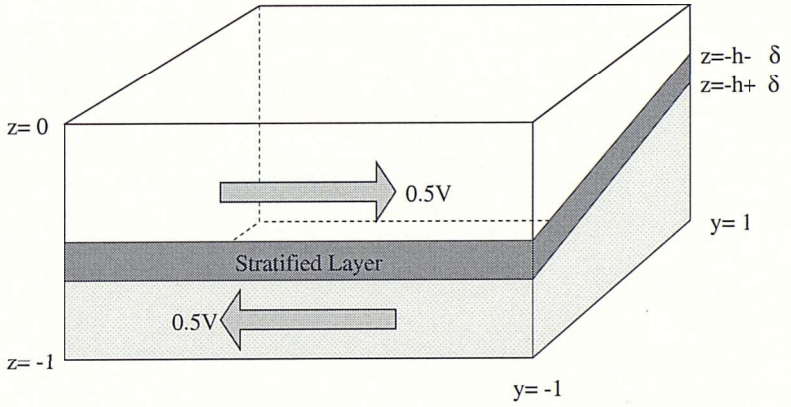


Figure 2.12: Two-layer ocean with extra stratified layer.

Following the same steps as in §2.2.1, we arrive at a pair of equations for ϕ and η, (2.53, 2.54, below). Clearly, these two equations reduce to the two–layer equations (2.39, 2.40) in the limit $\delta \to 0$.

$$\nabla^2\phi_t - V^2 y\nabla^2\phi_x - 2V^3 y\eta_{xy} - V\left(V^2y^2 - \frac{1}{4}\right)\nabla^2\eta_x - \frac{1}{3}V\delta\nabla^2\eta_x = 0 \tag{2.53}$$

$$\begin{aligned} \eta_t + 2\epsilon V y\nabla^2\phi_t - V\phi_x - V^2 y\eta_x - 2\epsilon V^3 y^2\nabla^2\phi_x \\ + \epsilon V\left(V^2y^2 - \frac{1}{4} - \frac{1}{3}\delta^2\right)\nabla^2\phi_x \\ + \frac{1}{6}\epsilon\delta V\left[-2V\eta_{xy} + 2\delta V\left(y\nabla^2\eta_x + 2\eta_{xy}\right)\right] = 0. \end{aligned} \tag{2.54}$$

We again look for wave–like solutions in the East–West direction to obtain a pair of eigenvalue equations equivalent to (2.42, 2.43). This is then solved in the same manner as before.

2.2.5 Small interface slope

In the limit of $V \to 0$ the eigenvalue equations reduce (at $O(V^2)$) to

$$\omega A_\phi - \frac{1}{4}VkA_\eta + \frac{1}{3}Vk\delta A_\eta = 0 \tag{2.55}$$

$$\omega A_\eta + VkA_\phi - \epsilon VkK^2\left[\frac{1}{4} + \frac{1}{3}\delta^2\right]A_\phi = 0 \tag{2.56}$$

where the eigensolutions are given by

$$\eta = A_\eta e^{i(kx+ly-\omega t)} \qquad \phi = A_\phi e^{i(kx+ly-wt)}. \tag{2.57}$$

This has non–trivial solutions if the dispersion relation

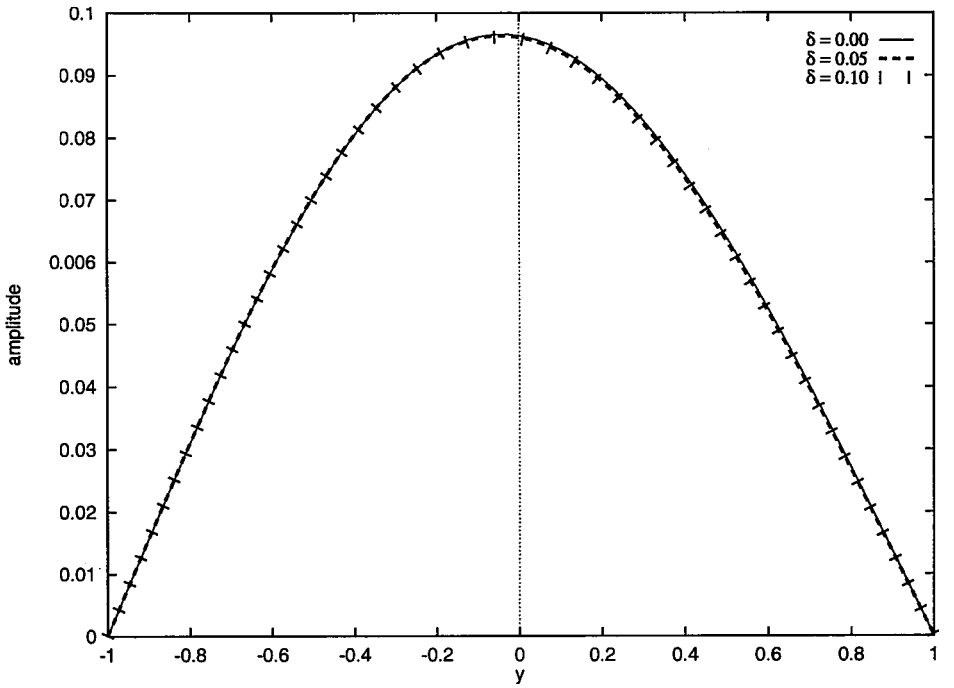
$$\omega^2 - V^2k^2\left[\frac{1}{4} - \frac{\delta}{3}\right]\left(\epsilon K^2\left[\frac{1}{4} + \frac{\delta^2}{3}\right] - 1\right) = 0 \tag{2.58}$$

is satisfied. (2.58) is the generalisation of (2.49). Comparison of these two equations show that in the QG limit we should expect very similar solutions here as in the genuine two–layer case, namely sinusoidal modes (Figure 2.13(a)); for $\delta = 0, 0.05, 0.1$ and small interface slope, V, the eigensolutions look virtually identical. The inclusion of the extra layer has made the all modes slightly less unstable by an non-dimensional amount $\frac{\delta}{3}$. Additionally, the cutoff wavenumber (above which there is no instability) is smaller by an amount $\frac{\delta^2}{3}$. Both of these effects suggest that the extra stratified layer has a stabilising influence on the system.

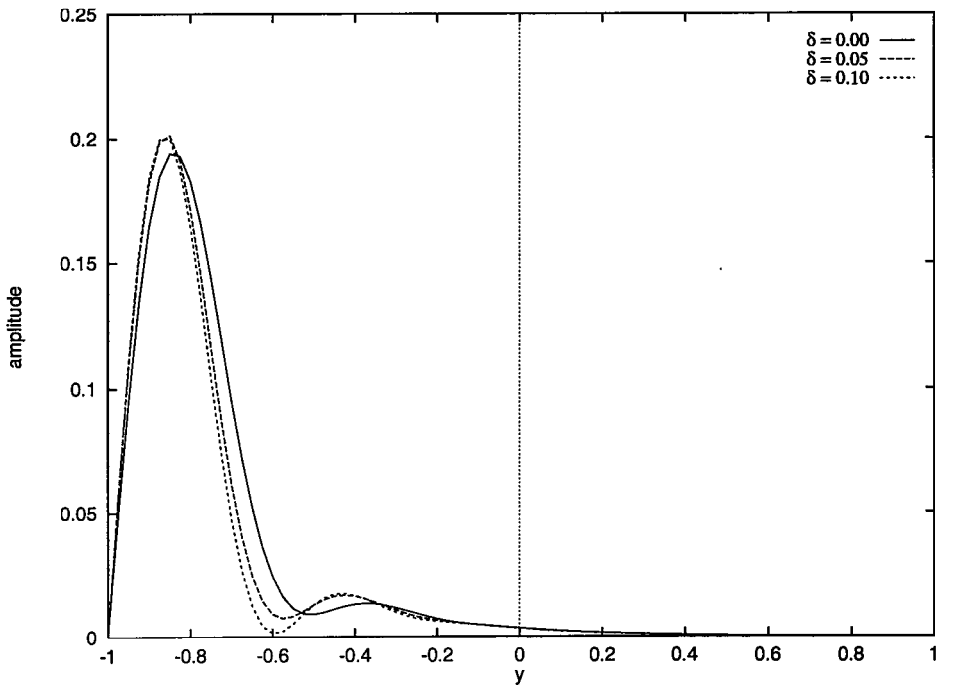
2.2.6 Steeper interfaces

Once an analytical starting point has been established (via the small slope approximation), we can numerically investigate the solutions for non-vanishing V. The extra, intermediate layer seems only to have a small effect on the system. As might be expected, since δ only ever appears in products with V in (2.53, 2.54), the effect becomes more noticeable for larger interface slopes (Figure 2.13). However, at $V = 0.4$ we observe the shift of the wave-peak towards one or other of the edges of the channel and the solution is qualitatively very similar to the two-layer case.

As in the pure two-layer model, we see (Figure 2.14) that, as the interface steepens, initially the waves become more unstable but eventually this trend reverses. For all values of V,



(a) $V = 0.01$



(b) $V = 0.4$

Figure 2.13: Comparison of eigensolutions at different δ; $k = \frac{1}{2^{\frac{1}{2}}} k_{int}$, $l = 1$. Only $\mathbb{R}(\phi)$ is shown. The stratified layer has little effect.

thicker intermediate layers correspond to greater stability. Thicker layers cause both the wavenumber and the interface slope cutoffs to decrease. That is, the range of wavenumbers for a given interface slope *and* the range of interface slopes for a given wavenumber both decrease.

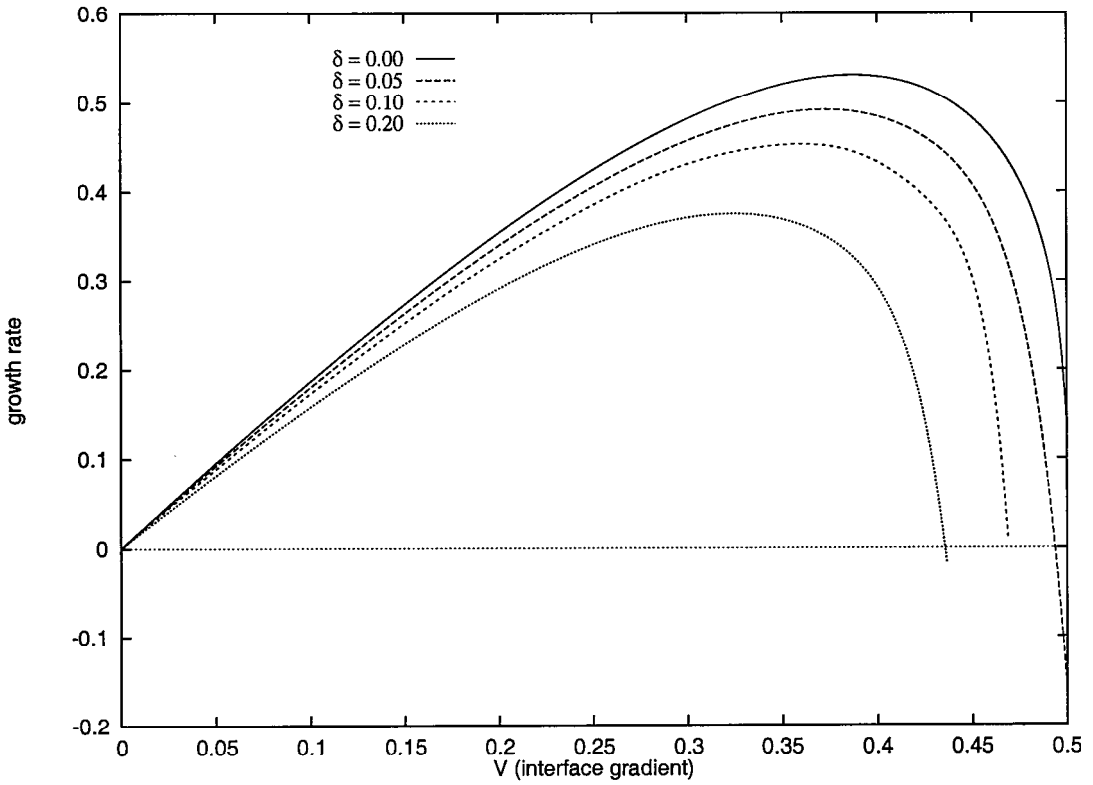
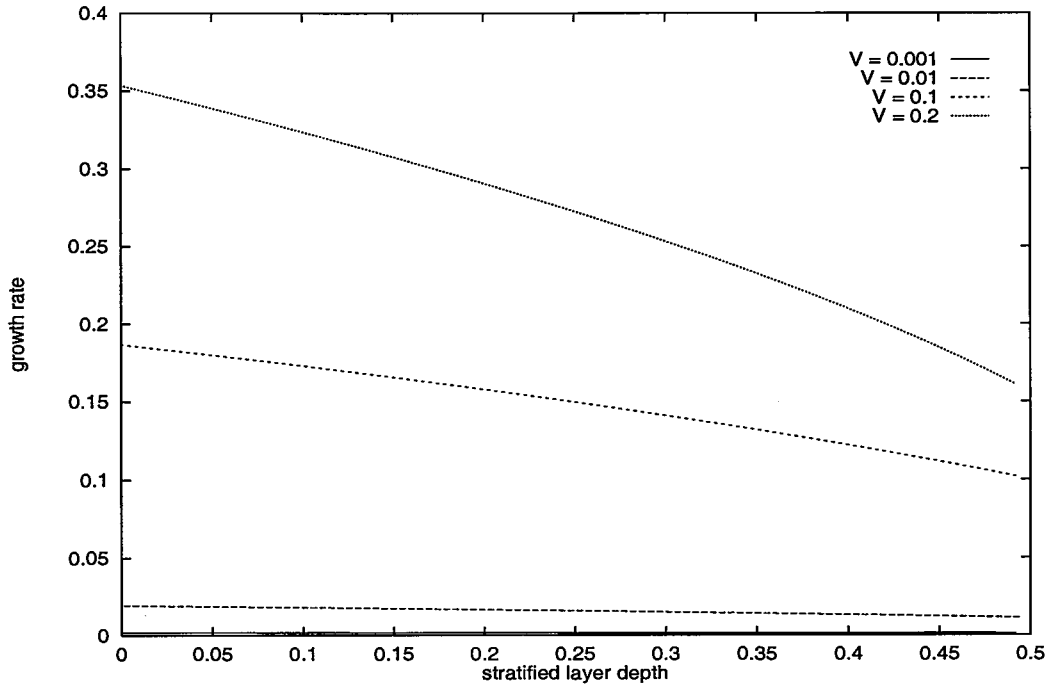


Figure 2.14: Growth rates at different δ; $k = \frac{1}{2^{\frac{1}{2}}}, l = 1$. Thicker intermediate layers correspond to reduced growth rates and a smaller cutoff value of V.

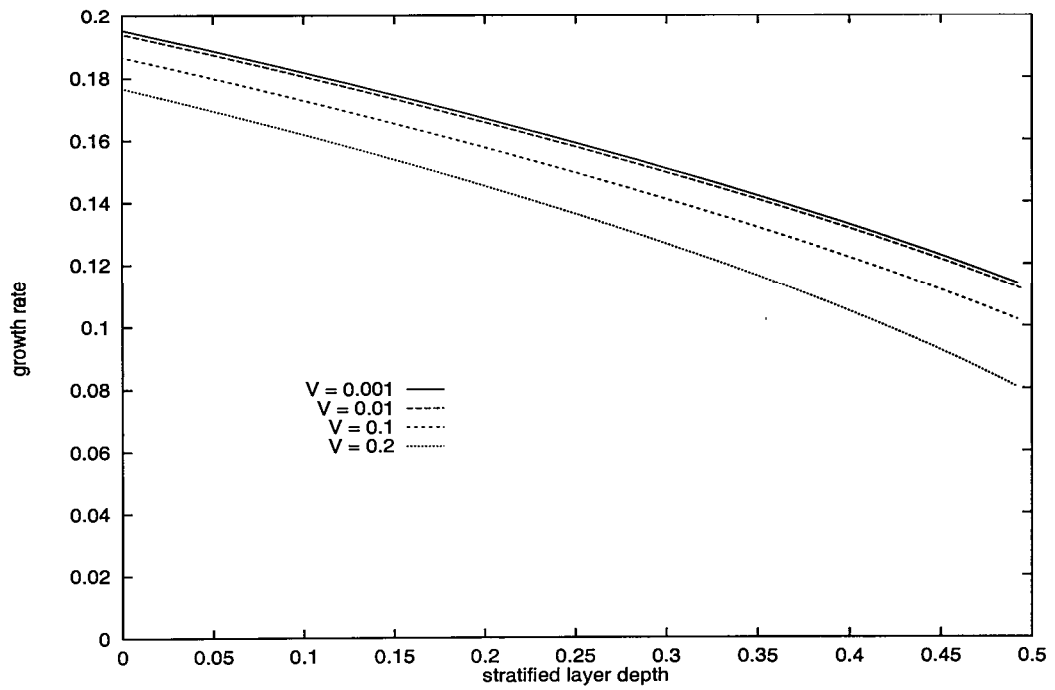
For a given wavenumber (namely $\frac{1}{\sqrt{2}}k_{int}$) and given interface slope we see (Figure 2.15(a)) that as δ increases the growth rate of the waves slowly decreases (approximately linearly with δ). Figure 2.15(a) gives the actual growth–rates for three different choices of V. In Figure 2.15(b) I have rescaled the growth rates with V and we see that the growth rate is close to being directly proportional to the interface slope at all thicknesses of the intermediate layer.

The main effect of the intermediate layer is to slightly increase the stability of the system (Figures 2.14,2.15) while hardly affecting the shape of the eigensolutions (Figure 2.13) at all. A smaller instability growth rate is expected because baroclinic instability occurs when there is a vertical variation in the buoyancy θ. It seems reasonable that a more rapid change in θ will lead to a greater degree of instability. A particle instability argument helps to clarify the point.

Consider a particle near the top of the lower layer with $\theta = 0$. If it is displaced upwards slightly then in the two–layer model (Figure 2.2) it will find itself in the top layer sur-



(a) unscaled



(b) scaled with V

Figure 2.15: Variation of growth rates with δ; k $= \frac{1}{2\frac{1}{2}}, l = 1$. Thicker intermediate layers correspond to smaller growth rate but the effect is small. (a) shows that the effect is more noticeable with increasing interface slope, V. (b) shows that the effect is almost linear in V (If it were exactly linear then all four curves would exactly collapse onto each other).

rounded by particles with $\theta = 1$. Consequently, there will be a strong restoring force attempting to push our particle back again. If an intermediate layer is present (Figure 2.12), however, then our particle will find itself in this layer surrounded by particles of $\theta = \frac{\Delta h}{\delta}$ where $\Delta h < \delta$ is the small vertical distance moved. In this situation, there is a smaller restoring force and hence the particle is less likely to be subjected to wild oscillations. That is, the situation appears more stable.

It is more difficult to construct an argument here based upon the APE. It is easy to calculate that this is given by APE $= \frac{1}{3}V^2$ and is thus independent of the thickness of the intermediate layer.

2.2.7 Summary

In this section we have shown

- the model *does* incorporate baroclinic instability.
- results are in good agreement with QG theory at the shallow interface limit for a two-layer model.
- QG theory overestimates the instability growth rates for finite interface slopes because it does not account for the varying Rossby radius across the channel. For large interface slopes, growth rates decrease rather than increase.
- The addition of a small stratified layer in between the top and bottom layers has a small stabilising influence on the model. The structure of the solutions remains unchanged. The stabilisation can be explained in terms of a particle-instability mechanism.

Chapter 3

Depth Independent Temperature Model

Layer models have traditionally been used as a simple theoretical tool for examining oceanic processes. However, as discussed in §1.4.1, they suffer from several drawbacks. In particular, their piecewise-constant sea surface temperature distributions are not suitable for coupling to an atmospheric component. Additionally, if $O(1)$ topography is to be modelled then a two-layer model reduces to a barotropic model on the inshore side of any outcropping lines (see Figure 1.2). Our aim in this chapter is to develop and examine a model which possesses an active sea surface temperature and which is baroclinic everywhere, but which is of similar complexity to a two-layer model.

An alternative ansatz (to (2.1)) that can be made about the temperature structure of the ocean is that it is independent of the depth. This does not mean that the flow is barotropic since the thermal wind equations (1.13) relate horizontal gradients of temperature to vertical gradients of velocity. I do not claim that this is a particularly realistic assumption for oceanic applications since fluid nearer the top of the ocean ought to be warmer than that nearer the bottom, but it does have the advantage of producing much simpler, and hence more tractable, equations. It is arguably the *simplest* model to include the effects of baroclinicity, topography and inertia. Despite this simplicity, it will be shown that DIT flows bear some resemblance to the circulation in the North Atlantic (Figure 1.1). Thus, it seems likely that this model captures much of the essential physics.

The fundamental depth-independent assumption has been made by several authors, particularly within the atmospheric community (for a review of such models, see Ripa[60], [61]), who require a simple ocean with a continuously varying sea surface temperature. Barotropic and two-layer models fail to satisfy this requirement. Such authors regard their models to approximate only the upper few hundred metres of the ocean. This is

the approximate depth of the mixed layer in which the temperature *is* comparatively uniform with increasing depth. They are consequently called *mixed-layer models.* Many are equivalent-barotropic models (in which the ocean beneath the mixed layer is considered to be infinitely deep). However, Cushman-Roisin *et al.*[22] shows that the equivalent-barotropic model is a poor approximation to a two-layer model (even when the bottom layer is very deep) for length scales greater than the deformation radius. Since our aim is to develop a *simple* model of circulation in an *entire* ocean basin, it seems reasonable to consider the simplest possible mixed-layer-type model (that is, a model with one layer) and then move directly to a two-layer model (see §5.2). Furthermore, mixed layer models are usually derived via some sort of *ad hoc* vertical averaging process. This can lead to inconsistencies (see Ripa[60]) such as the lack of a thermal wind relation. They also rely on assumptions similar to those of quasi-geostrophy such as requiring the bottom of the layer to be relatively flat or the Coriolis parameter to only vary by $O(\mathsf{Ro})$. This makes such models unsuitable for simulations of ocean basins where neither assumption is realistic and also destroys some of the conservation laws of the primitive equations. The derivation of the DIT, below, makes no further assumptions or approximations beyond those of the LSGE (namely, that $\mathsf{Ro} \ll 1$ and $L \gg \lambda_{int}$).

The aims of this chapter are

- to derive the DIT model equations and compare it to other simple models, in particular, the two-layer QG model (§3.1).
- to discuss the mechanisms by which energy is transferred from potential to kinetic form. (§3.2).
- to investigate baroclinic instability in a channel model and in the open ocean (§§3.3, 3.4).
- to study the interaction of localised anomalies and turbulence (§3.5).
- to examine the effects of topography on baroclinic instability and turbulence (§3.6).

The knowledge and insight developed in this chapter will be used to interpret the ocean-basin simulations of §4.2.

3.1 Derivation of equations

We now make the depth independent assumption precise by enforcing the condition that the temperature, θ, is independent of z and that it is a function only of x, y and t:

$$\theta \equiv T(x, y, t) \tag{3.1}$$

Note that, since $\mathbf{x}_s \neq \mathbf{x}_C$, a column of constant temperature (see Figure 1.3) is not exactly vertical in physical space. This is unimportant from a physical standpoint because the assumption is unrealistic for the ocean anyway. The choice of (3.1) is mathematically convenient because the LSGE conserve potential vorticity (PV) in the form $\tilde{f}\frac{\partial\theta}{\partial z}$. Consequently, the DIT ansatz is equivalent to insisting that the PV of the system is identically zero. A similar rationale is used in Held *et al.*[33] in which the Surface Quasi-Geostrophic equations are derived from QG by making the PV vanish.

With (3.1) rather than (2.1) as our fundamental ansatz we can proceed, as before, to derive two equations for the barotropic streamfunction and for the temperature.

The vorticity equation is identical to the two-layer equivalent, (2.12), except that now all the integrals involving $\nabla.\mathbf{A}$ are very much simpler and we can evaluate them analytically to yield

$$\epsilon\frac{\partial\zeta}{\partial t} + J\left(\psi, \frac{f}{H}\right) + \epsilon J\left(\psi, \frac{\zeta}{H}\right) + \frac{1}{2}J\left(T, H\right) + \epsilon J\left(T, \Gamma\right) = \nu\nabla^2\zeta + \mathsf{W}(x, y) \tag{3.2}$$

where

$$\Gamma \equiv \frac{H}{12\tilde{f}_{eq}^2}\left[H\left(\nabla^2 T - \frac{2\nabla T.\nabla\tilde{f}_{eq}}{\tilde{f}_{eq}}\right) + 3\nabla T.\nabla H\right]. \tag{3.3}$$

As in Chapter 2, ψ is the barotropic streamfunction, $\zeta \equiv \nabla.\left(\frac{1}{H}\nabla\psi\right)$ and $\mathsf{W}(x, y)$ is the wind-stress curl (2.17). Notice that in (3.2) we retain a Laplacian diffusion term rather than the simpler linear friction term of (2.22). This is because Laplacian diffusion is *required* to prevent an ultra-violet catastrophe in the baroclinic instability analysis of §3.3. However, in the ocean basin simulations of §4.2, we revert to a linear term which is supplemented by an implicit hyperdiffusive term.

The $J(T, H)$ term is the *Joint Effect of Baroclinicity And Relief* (*JEBAR*) term of Sarkisyan & Ivanov[78] (see also, Salmon & Ford[75]). In the non-inertial limit this term is the *only* feedback of the baroclinicity on the barotropic flow. In [75], Salmon & Ford show how this term may explain the northward overshoot of the Gulf Stream at its separation point.

The $J(T, \Gamma)$ term is the new component of this particular model. Although it involves topographic and rotational effects, the two essential ingredients are baroclinicity and inertia. For this reason, and to draw analogies with *JEBAR* , we shall refer to this term as the *Joint Effect of Baroclinicity And Inertia*, *JEBAI* .

By integrating[1] the temperature equation of the LSGE (1.17e) from top to bottom we find that

$$H\frac{\partial T}{\partial t} + J\left(\psi, T\right) = \kappa H\nabla^2 T + \mathsf{Q}(x, y) \tag{3.4}$$

[1]Integration is not necessary as the equations can be solved at *every* (x, y, z).

where $\mathsf{Q}(x,y)$ is the surface heating (which I also refer to as "thermal forcing"). Equations (3.2, 3.4) are the generalisations of the equations in Salmon & Ford [75] to include inertia. In fact, (3.4) is identical to their temperature equation. However, in that paper, it is argued that dissipative effects are sufficiently small that they may be neglected. Further, numerical experiments with the full planetary geostrophic equations (Salmon[71]) and with the GTLE of Salmon[72] show that, in the absence of inertia, solutions tend towards steady states. Thus, the leading order behaviour of (3.4) is $J(\psi,T)=0$ which has solution $T=F(\psi)$ for some arbitrary function, $F(.)$. Whilst this reduction has the benefit of making the dynamics more transparent, it has the disadvantage in ocean simulations (see §4.2) that since $\psi=0$ on all boundaries of the ocean, the value of T on the northern boundary (that is, the North Pole) must be equal to the value of T on the southern boundary (that is, the equator). Moreover, numerical experiments when inertia *is* retained ([7], Chapter 4) show that the solutions do not tend to steady states (except for very small values of the Rossby Number). Additionally, in §§3.3-3.6 it is shown that a non-zero thermal diffusivity is essential. Accordingly, no further simplification is made to the advection-diffusion equation (3.2).

3.1.1 Interpretation of DIT as QG

There exists an interesting interpretation of the flat-bottomed DIT equations in terms of a two-layer QG model in the limit of $L \gg \lambda_{int}$.

Two-layer quasi-geostrophy (for an ocean with a rigid lid) is described ([74]) by

$$\frac{\partial q_i}{\partial t} + J(\psi_i, q_i) = 0 \tag{3.5}$$

where

$$q_i \equiv \nabla^2\psi_i + f - \frac{f_0^2}{H_i g'}(-1)^i(\psi_1-\psi_2). \tag{3.6}$$

The subscript/exponent $i=1,2$ refers to the upper and lower layers respectively. H_i is the constant mean depth of each layer (where we have non-dimensionalised the total depth of the basin to $H_1+H_2=1$); f_0 is the constant mean value of the Coriolis parameter, f, and $g' \equiv \frac{\rho_1-\rho_2}{\rho_1}g$ is the reduced gravity. In order to derive (3.5) from the two-layer shallow water equations, we make the standard QG approximations that the Coriolis force and layer depths vary from their mean values by $O(\mathsf{Ro})$ only.

Taking linear combinations of (3.5) we obtain

$$\begin{aligned}\nabla^2\frac{\partial}{\partial t}\left(\psi_1+\mathcal{A}\psi_2\right) + J\left(\psi_1+\mathcal{A}\psi_2, f\right) + J(\psi_1,\nabla^2\psi_1) + \mathcal{A}J(\psi_2,\nabla^2\psi_2) \\ - \frac{f_0^2}{g'}\left[\left(\frac{1}{H_1}-\frac{\mathcal{A}}{H_2}\right)\frac{\partial}{\partial t}(\psi_1-\psi_2) + \left(\frac{1}{H_1}-\frac{\mathcal{A}}{H_2}\right)J(\psi_1,\psi_2)\right] = 0,\end{aligned} \tag{3.7}$$

and

$$\nabla^2\frac{\partial}{\partial t}(\psi_1-\mathcal{B}\psi_2)+J(\psi_1-\mathcal{B}\psi_2,f)+J(\psi_1,\nabla^2\psi_1)-\mathcal{B}J(\psi_2,\nabla^2\psi_2) \\ -\frac{f_0^2}{g'}\left[\left(\frac{1}{H_1}+\frac{\mathcal{B}}{H_2}\right)\frac{\partial}{\partial t}(\psi_1-\psi_2)+J\left(\psi_1+\mathcal{B}\psi_2,\psi_1-\psi_2\right)\right]=0 \tag{3.8}$$

where $\mathcal{A}$ and $\mathcal{B}$ are arbitrary scalar constants. We choose $\mathcal{A}=\mathcal{B}=\frac{H_2}{H_1}$. This causes the coefficient of $\frac{f_0^2}{g'}$ in (3.7) to vanish. Furthermore, we observe that, since length scales are large in comparison to the deformation radius, $\frac{f_0^2}{g'}\gg\nabla^2$ and, because of the QG relation,

$$\psi_1-\psi_2=\frac{g'H_1}{f_0^2}h_1'\ll 1 \tag{3.9}$$

where h_1' is the deviation of the upper layer depth from its mean, H_1. This means that the leading order behaviour of (3.8) is the term enclosed within [...].

We now define

$$\psi=H_1\psi_1+H_2\psi_2,\qquad \tau=\psi_1-\psi_2. \tag{3.10}$$

A little algebra yields, as the leading order behaviour of (3.7, 3.8),

$$\nabla^2\frac{\partial\psi}{\partial t}+J(\psi,f)+J(\psi,\nabla^2\psi)+\frac{H_2}{H_1}J(\tau,\nabla^2\tau)=0 \tag{3.11a}$$

$$\frac{\partial\tau}{\partial t}+J(\psi,\tau)=0. \tag{3.11b}$$

Up to a trivial rescaling of $T\equiv 12^{\frac{1}{2}}\left(\frac{H_2}{H_1}\right)^{\frac{1}{2}}\tau$, (3.11a, 3.11b) are identical to (3.2, 3.4) if $H=$ *const.* and non-conservative terms are temporarily omitted in the latter pair. The physical interpretation lies within (3.9, 3.10). Together, these equations form a thermal wind type relationship. τ is linked to velocity variations between the top and bottom layers via (3.10), which, in turn, are linked to variations in the interface height via (3.9). Moreover, $T>0$ corresponds to $\psi_1>\psi_2$ which, in turn, corresponds to $h_1'>0$. Consequently, locally, the upper layer, which we assume to be the warmer of the two (to ensure stable stratification), dominates a larger fraction of the overall depth. Thus, warm (cold) water in the DIT is associated with a thick (thin) upper layer in QG.

This additional QG interpretation of the flat-bottomed DIT is interesting given that it is virtually orthogonal to the original interpretation. The basic DIT assumption is that the temperature does not vary in the vertical axis whereas the two-layer QG equations assume, because the isobars can only vary from their horizontal rest state by $O(\mathsf{Ro})$, that the temperature does not vary very much in the horizontal plane. It is worth noting that although the two systems are formally equivalent, the DIT equations are in Semi-Geostrophic co-ordinates (1.11a-c) whereas the QG equations are valid in physical (Cartesian) co-ordinates. Consequently, the two systems differ by $O(\epsilon)$. Furthermore, the QG

equations are only valid for small variations in both the interface height, h, and Coriolis parameter whereas the DIT are valid for $O(1)$ variations of both T and f. We correctly recover the exact QG equations in physical co-ordinates in the limit $\nabla T = O(\epsilon)$ because, in this instance, SG and physical co-ordinates differ by only $O(\epsilon^2)$.

It is interesting that if we *do* restrict ourselves to small variations in the extent of both the topography and Coriolis parameter ($\Delta H, \Delta f \ll 1$) then the derivation of the DIT follows through with the slightly more general ansatz $\theta \equiv T(x,y,t) + \bar{T}(z)$. The large-scale motions are unaffected by the background stratification $\bar{T}$ (see Benilov[8]). However, since our ultimate goal in this thesis is to examine flows in oceanic basins across which there are $O(1)$ variations in both topography and Coriolis, we restrict ourselves to consideration of buoyancy profiles of the form (3.1).

Finally, it is worth comparing the DIT (3.2, 3.4) and the LSGE two-layer equations (2.22, 2.31). The latter system, as noted in §2.1, more closely resembles the frontal two-layer equations of Cushman-Roisin *et al.*[22] than the QG two-layer equations. The DIT equations (even with topography included) are simpler than the two-layer equations. The nonlinearity in the baroclinic feedback term is only quadratic whereas there is a cubic nonlinearity in the two-layer equations. Furthermore, the interpretation of the temperature evolution equation (3.4) is transparent whereas the same claim cannot be made of the interface evolution equation (2.31). However, with the additional interpretation of the DIT, both systems describe the evolution of a two-layer flow on length scales larger than the deformation radius. My primary aim in this thesis is to develop insight into the behaviour of the LSGE; it seems evident that this can be more easily achieved via the DIT equations rather than the two-layer equations.

3.2 Conservation of energy

The *conservative* DIT equations conserve energy in the form

$$\begin{aligned} E &= \int dxdxdz \left\{ \frac{1}{2}\epsilon \left(\bar{\mathbf{u}}^2 - \hat{\mathbf{u}}^2 \right) - \theta z \right\} \\ &\equiv \int dxdy \left\{ \frac{1}{2}\epsilon \left(\frac{1}{H} \left(\nabla\psi \right)^2 - \frac{H^3}{12f^2} \left(\nabla T \right)^2 \right) + \frac{1}{2} H^2 T \right\}. \end{aligned} \tag{3.12}$$

To see this, note that the rate of change of energy is given by

$$\frac{dE}{dt} = \int dxdy \left\{ \frac{1}{2} H^2 \frac{\partial T}{\partial t} + \frac{\epsilon}{H} \nabla\psi . \nabla \frac{\partial \psi}{\partial t} - \frac{\epsilon H^3}{12 f^2} \nabla T . \nabla \frac{\partial T}{\partial t} \right\}. \tag{3.13}$$

Using the boundary conditions[2] of no normal flow ($\psi = 0$), and $H = 0$ we can integrate the second and third terms of (3.13) by parts to give

$$\frac{dE}{dt} = \int dxdy \left\{ \frac{1}{2}H^2 \frac{\partial T}{\partial t} - \epsilon\psi \frac{\partial \zeta}{\partial t} + \frac{\epsilon}{12}\frac{\partial T}{\partial t}\left(\frac{H^3}{f^2}\nabla^2 T + \nabla T.\nabla \frac{H^3}{f^2} \right) \right\}. \tag{3.14}$$

Now we can use the DIT, (3.2, 3.4) to substitute in for the time derivatives to yield

$$\begin{aligned} \frac{dE}{dt} = \int dxdy \Bigg\{ & -\frac{1}{2}HJ(\psi, T) + \psi \Bigg[J\left(\psi, \frac{f}{H}\right) + \epsilon J\left(\psi, \frac{\zeta}{H}\right) + \frac{1}{2}J(T, H) \\ & - \epsilon J\left(T, \frac{-H^2}{12f^2}\nabla^2 T\right) - \epsilon J\left(T, \frac{1}{12H}\nabla T.\nabla \frac{H^3}{f^2}\right) \Bigg] \\ & + \frac{\epsilon}{12H} J(\psi, T)\left(\frac{-H^3}{f^2}\nabla^2 T + \nabla T.\nabla \frac{H^3}{f^2} \right) \Bigg\}. \end{aligned} \tag{3.15}$$

Integrating the entire second term ($\psi[\ldots]$) by parts and noting that all the boundary terms vanish again gives the desired result that

$$\frac{dE}{dt} = 0. \tag{3.16}$$

Of course, this conservation of energy is expected because the DIT are derived from the LSGE, which themselves are derived by a Hamiltonian method and so conservation of energy should be a trivial issue. However, it seems surprising that the total energy (in 3.12) *appears* to be of the form

$$\text{Total Energy} = \text{Potential Energy} + \text{Barotropic K.E.} - \text{Baroclinic K.E}$$

Furthermore, since the potential energy is apparently given by $E_{pot} = \int \frac{1}{2}H^2 T dxdy$, it is clear that this quantity is conserved under the conservative form of the flat-bottomed ($H = 1$) DIT (3.2, 3.4). Thus it would appear that the potential energy, and hence the kinetic energy, are also both invariant under DIT dynamics with no topography. This suggests that in the flat-bottomed model, it is impossible to convert potential energy into kinetic energy and therefore baroclinic instability will not be present. On the other hand, the energy (3.12) is not a positive definite quantity and the "$-$" should have profound implications for the stability of the system; it may be possible for two of the terms to grow without bound whilst still preserving a constant total energy[3].

It is the co-ordinate transformation to generalised Semi-Geostrophic space (1.11a-c) which contains the missing physics and describes the release of potential energy and hence baroclinic instability.

[2] in §§3.3-3.6 we also examine doubly periodic domains in which $H \neq 0$ at the boundaries. In these instances there are no boundary terms to consider.

[3] Benilov[8] finds (3.12) to be the Hamiltonian of a similar system (with $H = 1, \Delta f \ll 1$) in Cartesian co-ordinates and states that the physical interpretation is unclear.

The transformation can be reversed back to Cartesian co-ordinates. It is only necessary to consider the potential energy term because the kinetic energy terms already include one factor of ϵ; since Semi-Geostrophic and Cartesian co-ordinates only differ by a further factor of ϵ, the kinetic energy terms will only differ by a factor of $O(\epsilon^2)$. This is the same size as the original LSGE approximations (see §1.3). Using (1.11a-c) we find that

$$\begin{aligned} E_P &\equiv -\int dxdydz\,[z\theta] \\ &= -\int dx_C dy_C dz_C \left[z_C\theta + \epsilon\theta \int_z^0 dz' \left\{ \frac{\partial}{\partial x}\left(\frac{\hat{v}}{f}\right) - \frac{\partial}{\partial y}\left(\frac{\hat{u}}{f}\right) \right\} \right] + O(\epsilon^2). \end{aligned} \tag{3.17}$$

The second term can be integrated with respect to x_C to yield

$$\begin{aligned} &\int dx_C dy_C dz_C \left[\theta \int_z^0 dz' \frac{\partial}{\partial x}\left(\frac{\hat{v}}{f}\right) \right] \\ &\quad = \int dy_C dz_C \left[\left[\theta \int_z^0 dz' \left(\frac{\hat{v}}{f}\right) \right]_{x_C=0}^{x_C=L} - \left[\int dx_C \theta_x \int_z^0 dz' \left(\frac{\hat{v}}{f}\right) \right] \right]. \end{aligned} \tag{3.18}$$

The first term on the right hand side vanishes because of the thermal wind equations (1.13) and the boundary conditions[4]. The second term can be integrated with respect to z_C giving

$$\begin{aligned} &\int dx_C dy_C dz_C \left[\theta_x \int_z^0 dz' \left(\frac{\hat{v}}{f}\right) \right] \\ &\quad = \int dx_C dy_C \left[\left[\int_0^z dz' \theta_x . \int_z^0 dz' \left(\frac{\hat{v}}{f}\right) \right]_{z=-H}^{z=0} + \int dz_C \left[\frac{\hat{v}}{f} \int_0^z dz' \theta_x \right] \right]. \end{aligned} \tag{3.19}$$

Once again, the boundary term vanishes[5] because of our definition that $\int_{-H}^0 \hat{v} dz = 0$. One final application of the thermal wind equations gives the result that

$$\int dx_C dy_C dz_C \left[\frac{\hat{v}}{f} \int_0^z dz' \theta_x \right] = \int dx_C dy_C dz_C \left[\hat{v}\hat{v} \right]. \tag{3.20}$$

Similar manipulations can be applied to the final term of (3.17) and after unravelling all the sign changes, we obtain

$$E_P = -\int dx_C dy_C dz_C z_C \left[\theta - \epsilon \hat{\mathbf{u}}^2 \right]. \tag{3.21}$$

Consequently, the energy in Cartesian (physical) coordinates is found to be

$$E_{tot} = \int dx_C dy_C dz_C \left[\frac{1}{2}\epsilon \left(\bar{\mathbf{u}}^2 + \hat{\mathbf{u}}^2 \right) - z_C\theta \right] \tag{3.22}$$

[4]Note that since everything is now already $O(\epsilon)$ it is unimportant (up to $O(\epsilon^2)$) whether derivatives are taken with respect to the semi-geostrophic co-ordinate (x) or the Cartesian co-ordinate (x_C). Consequently, to make reading the equations easier, I do not include any subscript on the derivatives.

[5]Up to $O(\epsilon^2)$ the boundary conditions may be applied at either z or z_C.

which is a more familiar expression for the energy than (3.12). Moreover, it suggests that we regard the potential energy of the DIT (3.2, 3.4) not to be $E_{pot} = -\int z\theta$ but rather,

$$E_{pot} \equiv -\int z_c \theta \mathbf{dx_C} = -\int z\theta \mathbf{dx} - \epsilon \int \hat{\mathbf{u}}^2 \mathbf{dx} \tag{3.23}$$

and that the kinetic energy

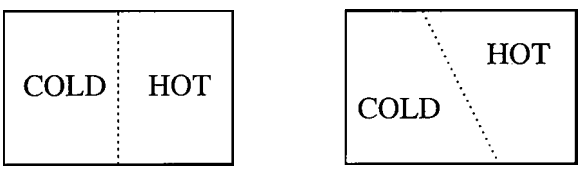
$$E_{kin} \equiv \frac{1}{2}\epsilon \int \left[\bar{\mathbf{u}}^2 + \hat{\mathbf{u}}^2\right] \mathbf{dx_C} = \frac{1}{2}\epsilon \int \left[\bar{\mathbf{u}}^2 + \hat{\mathbf{u}}^2\right] \mathbf{dx}. \tag{3.24}$$

If (3.23, 3.24) are adopted in preference to the more superficially obvious choice from (3.12) then it is possible for energy to be converted from potential to kinetic (or vice versa) since neither (3.23) nor (3.24) are individually conserved by even the flat-bottomed DIT. Of course, all this applies to the LSGE (1.17a-e) in general rather than to the DIT specifically.

The above argument can also be expressed in a slightly different manner. The co-ordinate transformation reveals that a vertical isotherm in SG co-ordinates is *not* a vertical isotherm in Cartesian (that is, physical) co-ordinates. Indeed,

$$x_s = x_C + \epsilon \frac{(2z + H)}{2f^2} \frac{\partial T}{\partial x} \tag{3.25}$$

and so a strong East-West thermal gradient can lead to strongly tilted isotherms. There is a similar expression relating y_s to y_C (1.11b) so North-South thermal gradients also lead to tilted isotherms. As an isotherm is tilted further (in the correct direction, see Figures 3.1, 3.2) more potential energy will be released.



SG co-ords Physical co-ords

Figure 3.1: A vertical column in SG space is a tilted column in physical space; $T > 0$. Moreover, $\frac{\partial T}{\partial x} > 0$ in SG space. Therefore physical columns are tilted to produce stable stratification. Increasing $\frac{\partial T}{\partial x}$ will increase the degree of stable stratification.

This suggests that potential energy can be released by the fluid attempting to rearrange itself to *increase* horizontal thermal gradients. It is easy to see from (3.23, 3.24) that this process will decrease the potential energy and increase the kinetic energy (Recall that, because of thermal wind (1.13), $\hat{\mathbf{u}} \sim \nabla T$). Furthermore, it is not simply $\int \hat{\mathbf{u}}^2 \mathbf{dx}$ which will increase; conservation of kinetic energy (in the flat-bottom model) requires that $\int \bar{\mathbf{u}}^2 \mathbf{dx}$ will increase by an identical amount. This makes it clear that instability occurs by

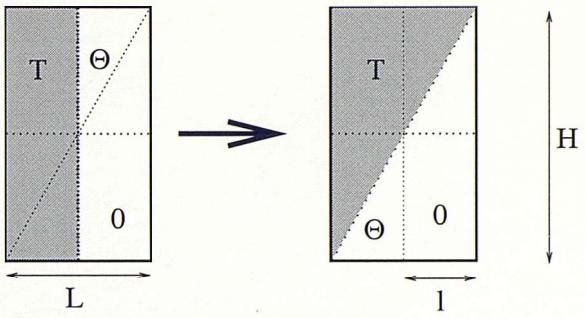


Figure 3.2: As thermal gradients increase further, physical columns tilt over (see previous figure) and potential energy $= -\int zT dx dz$ is released. Consider the triangle Θ. This has temperature 0 and so is "heavy" ($T > 0$). Θ is moved downwards during the rearrangement; this releases potential energy.

increasing thermal gradients (that is, creating finer scales) and that this process transfers baroclinic energy to barotropic energy and potential energy to kinetic energy.

The prospect of a fluid trying to rearrange itself in order to *increase* horizontal thermal gradients seems counter-intuitive. This reveals that the important role that thermal diffusivity, κ, has to play in the dynamics of the DIT. Thermal diffusion has exactly the opposite effect; that of decreasing thermal gradients. Without it, there is nothing to stop the DIT from cascading to finer and finer scales. In §3.3 diffusive terms are *required* to prevent an ultra-violet catastrophe.

The rationale behind diffusive terms such as $\kappa\nabla^2 T$ and $\nu\nabla^2\zeta$ is that they parametrise small-scale processes not included in the dynamics or not resolvable by the numerics. The DIT are unaware of any processes occurring on a length scale smaller than the deformation radius; consequently, there are more processes to be approximated by the diffusive terms than in models that do not explicitly neglect sub-deformation-radius scales. Consequently, we might expect viscous terms to be more important than in other models.

3.3 Linear thermal gradient

In this section we examine baroclinic instability within the DIT. The simplest possible case to consider is a fluid basin with a flat bottom and constant rotation; that is, $H = f = 1$. This reduces (3.2, 3.4) to

$$\frac{\partial}{\partial t}\nabla^2\psi + J\left(\psi, \nabla^2\psi\right) + \frac{1}{12}J\left(T, \nabla^2 T\right) = \mathsf{Re}^{-1}\nabla^4\psi \tag{3.26a}$$

$$\frac{\partial}{\partial t}T + J\left(\psi, T\right) = \kappa\nabla^2 T \tag{3.26b}$$

where $\mathsf{Re} \equiv \frac{\epsilon}{\nu}$ is the Reynolds Number. Note that although f does not explicitly appear in (3.26a, b), rotation is responsible for the *validity* of these equations and so they are

indeed equations for *rotating* flow.

At this stage we will also anticipate future results and define a Rayleigh Number

$$\mathsf{Ra} \equiv \frac{T_0^2}{\mathsf{Re}^{-1}\kappa} \equiv \frac{\epsilon T_0^2}{\nu\kappa}. \tag{3.27}$$

Ra is a measure of the strength of the buoyancy forces relative to the diffusion.

The simplest, nontrivial, buoyancy-driven flow that satisfies (3.26a, b) is

$$T = T_0 y, \qquad \psi = 0. \tag{3.28}$$

Consider the problem which is bounded by vertical walls[6] at $0 \leq y \leq 1$, is periodic in x and in which the temperature is maintained at either end of the domain ($T = 0$ at $y = 0, T = T_0$ at $y = 1$). This is the DIT equivalent of the classical Rayleigh-Bénard convection problem. It is also the DIT equivalent of the more familiar two-layer baroclinic instability problem of §2.2. The baroclinic nature of the instability of the present problem is discussed in §3.2.

3.3.1 Linear analysis

The linear instability of this flow is investigated in the usual manner by adding a small perturbation and considering the linearised equations. Hence:

$$T = T_0 y + \eta(x, y, t), \qquad \psi = \phi(x, y, t) \tag{3.29}$$

where

$$\eta, \phi \ll 1 \tag{3.30}$$

and we seek wave-like solutions of the form

$$\eta = \hat{\eta}(y) e^{ikx - i\omega t}, \qquad \phi = \hat{\phi}(y) e^{ikx - i\omega t}. \tag{3.31}$$

The boundary conditions are those of no normal flow ($\hat{\phi} = 0$) and constant prescribed temperature ($\hat{\eta} = 0$) at $y = 0, 1$. In addition there are two configurations to consider; those of no slip ($\hat{\phi}' = 0$) and no stress ($\hat{\phi}'' = 0$) at $y = 0, 1$.

[6] This is one of few occasions in this thesis in which we consider a domain with vertical side-walls. As we shall see, boundary conditions at vertical walls have a big influence, which is a good argument for looking at ocean basins in which the depth vanishes smoothly.

No stress. We consider first the easier problem of no stress. Substituting (3.31) into (3.26a, b), the solution is easily seen to be of the form

$$\hat{\eta}(y) = \hat{\eta}_0 \sin(ly), \quad \hat{\phi}(y) = \hat{\phi}_0 \sin(ly) \tag{3.32}$$

where $\hat{\eta}_0, \hat{\phi}_0$ are constants and, in order to satisfy all three boundary conditions, $l = n\pi$ for some integer, n.

Substituting (3.31, 3.32) into (3.26a, b) leads to the linearised equations

$$\omega\hat{\phi}_0 + \frac{1}{12}kT_0\hat{\eta}_0 + i\mathsf{Re}^{-1}K^2\hat{\phi}_0 = 0 \tag{3.33a}$$

$$\omega\hat{\eta}_0 - kT_0\hat{\phi}_0 + i\kappa K^2\hat{\eta}_0 = 0 \tag{3.33b}$$

where

$$K^2 = k^2 + l^2. \tag{3.34}$$

The solvability condition for (3.33a, b) yields

$$\omega = \frac{1}{2}\left[-iK^2(\kappa + \mathsf{Re}^{-1}) \pm \sqrt{-\frac{1}{3}k^2T_0^2 - K^4(\mathsf{Re}^{-1} - \kappa)^2}\right] \tag{3.35}$$

and we also obtain the relationship

$$\hat{\phi}_0 = \frac{1}{kT_0}(\omega + i\kappa K^2)\hat{\eta}_0. \tag{3.36}$$

Returning to the analogy between DIT and two-layer QG models, the growth rate (3.35) with $\kappa = \mathsf{Re}^{-1} = 0$ is equivalent, in QG language, to $\omega = ikU$ where $\tau = Uy$ and U is the mean flow speed in the upper layer of the two-layer model. This corresponds, as it should, to the long-wave limit of the classical Phillips model ([58]) of baroclinic instability in which $\omega^2 = k^2U^2\frac{K^2-k_{int}^2}{K^2+k_{int}^2}$. The long wave limit corresponds to $k_{int}^2 \gg K^2$.

Young & Chen[87] also derive (3.35). They note, as I do here, the problem of the implied ultra-violet catastrophe of the conservative form of these equations. In [87] two possible remedies are suggested. The first involves adding vertical stratification to the temperature field. This modifies the equations in the direction of the Eady[7] model (see Pedlosky[57]) which does have a finite wavenumber cutoff. The second remedy is that of diffusion. In [87], the first of these solutions is preferred, following a simple scaling argument. The Eady model cutoff occurs at length scales of $k_E^{-1} = 2km$ whereas the viscous damping cutoff occurs at much smaller length scales of $k_D^{-1} = 3m$. It is therefore argued that the dominant effect is that of stratification. However, the viscous cutoff is a function of the layer depth.

[7]The growth rate of (3.35) also corresponds to the long wave limit of the growth rate in the Eady problem.

From (3.35), the cutoff occurs at $k_D^{-1} = \frac{2\sqrt{3\mathsf{Re}^{-1}\kappa}}{T}$. Using the values of [87](p3184) we use a climatological horizontal temperature gradient of $T = 0.01m\ s^{-2}$ (see also, §4.2.2) and $\nu \sim \kappa \sim \frac{H_0^2}{\tau_v}$ where τ_v is a vertical mixing time scale $\tau_v \approx 10^5 s$. In contrast to Young & Chen[87], we regard H_0 to be the depth of the entire ocean ($H_0 \sim 4km$) rather than the depth of the mixed layer ($H_0 \sim 100m$). This yields a diffusive cutoff length scale of $k_D^{-1} = 1600 \times 3m = 4.8km > k_E^{-1}$ and suggests that, for the DIT model, diffusion is more important than stratification.

Of particular interest is the critical Rayleigh Number, Ra_0 at which the wave is on the verge of losing stability. At this point $\mathbb{I}(\omega) = 0$, since $\mathbb{I}(\omega) > 0$ corresponds to instability whereas $\mathbb{I}(\omega) < 0$ corresponds to decaying modes and stability.

Setting $\omega = 0$ in (3.33a, b), we easily obtain

$$\mathsf{Ra}_0 = 12\frac{\left(n^2\pi^2 + k^2\right)^2}{k^2}. \tag{3.37}$$

Minimising (3.37) with respect to k gives *the* critical Rayleigh Number, Ra_c at which the first mode becomes unstable.

$$\mathsf{Ra}_c = 48\pi^2 \text{ at a critical wavenumber } k = \pi. \tag{3.38}$$

See Figure 3.5. This result compares with classical Rayleigh-Bénard convection ([13]) in which $\mathsf{Ra}_c = \frac{27}{4}\pi^4$ occurring at $k = \frac{\pi}{2}$.

We can also calculate the most unstable mode (k_u). This depends not only on Ra but also the Prandtl Number ($\sigma = \frac{\mathsf{Re}^{-1}}{\kappa}$). Interestingly, however, k_u is independent of Re.

$$k_u^2 = -n^2\pi^2 - \frac{\mathsf{Ra}\sigma^{-1}}{6(\sigma^{-1}-1)^2} + \frac{\mathsf{Ra}^{\frac{1}{2}}(\sigma^{-1}+1)}{12(\sigma^{-1}-1)^2}\sqrt{\mathsf{Ra}\sigma^{-1} + 12n^2\pi^2(\sigma^{-1}-1)^2} \tag{3.39}$$

unless $\sigma = 1$ in which case

$$k_u^2 = \frac{\mathsf{Ra}}{48}. \tag{3.40}$$

Clearly $k = \pi, \mathsf{Ra} = 48\pi^2$ must be a solution of both (3.39) for all $\sigma \neq 1$, and (3.40). See Figure 3.3.

Before dealing with the no-slip problem, we first note the effect of variable rotation. If, instead of solid body rotation ($f = 1$), we make the beta-plane approximation ($f = 1+\beta y$), and additionally assume that $\beta \ll 1$ then the dispersion relation (3.35) becomes

$$\omega = -\frac{1}{2}\frac{\beta k}{\epsilon K^2} - iK^2(\kappa + \mathsf{Re}^{-1}) \pm \frac{1}{2}\sqrt{\frac{\beta^2 k^2}{\epsilon^2 K^4} - \frac{1}{3}k^2 T_0^2 - K^4(\mathsf{Re}^{-1} - \kappa)^2 + \frac{2i\beta k}{\epsilon}(\mathsf{Re}^{-1} - \kappa)} \tag{3.41}$$

If $\kappa = \nu = 0$ then (3.41) gives, as it must, the correct large wavelength limit of the standard two-layer QG beta-plane instability problem (see, for example, Salmon[74]). The *beta effect*

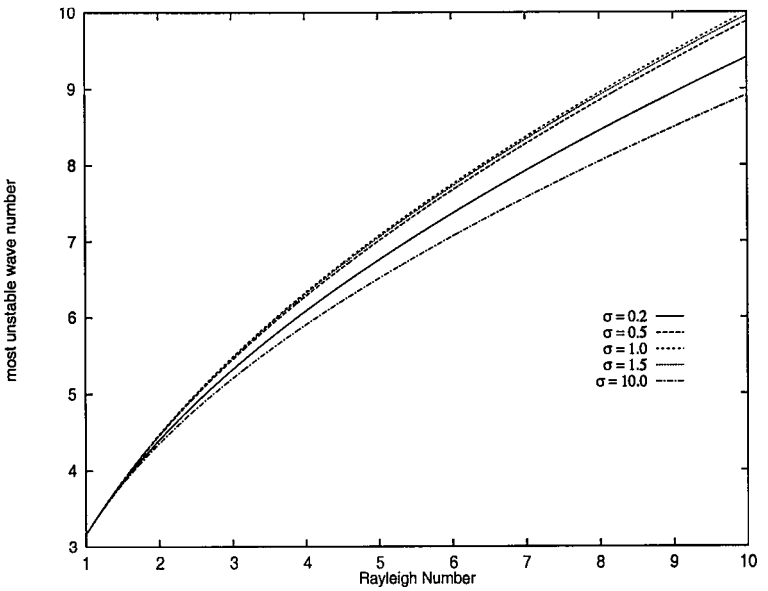


Figure 3.3: Most unstable wavenumbers, k_u for varying Ra, σ. Largest k_u occurs for $\sigma = 1$. Ra is scaled on Ra_c.

is two-fold; first, ω now always contains a non-zero real component at all wavelengths. This corresponds to the barotropic free Rossby wave. Second, the non-zero β has a stabilising effect on the flow. Unfortunately, this stabilising effect is greatest at large wavelengths. Consequently, the most unstable wavenumber is increased as shown in Figure 3.4.

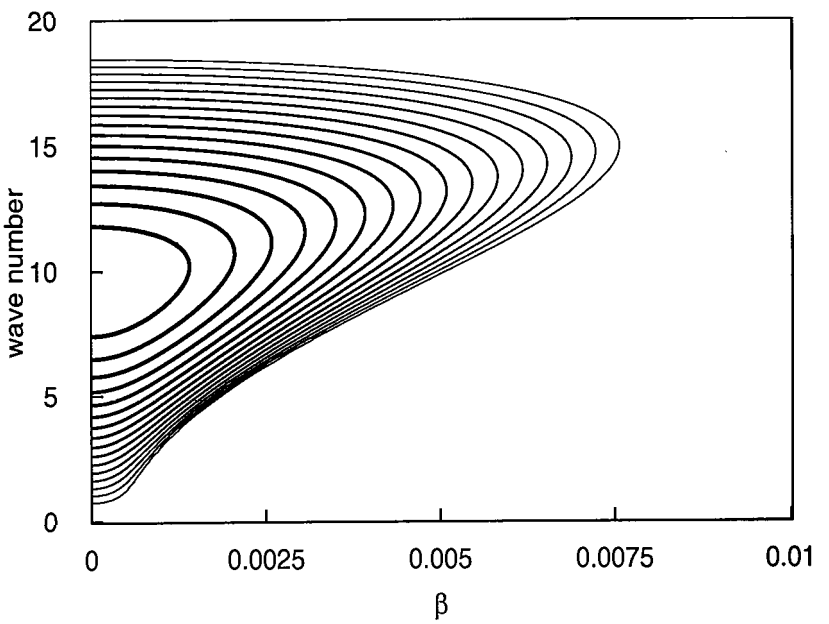


Figure 3.4: β effect for no-slip baroclinic instability problem. $\mathsf{Re}^{-1} = 1.5 \times 10^{-2}, \kappa = 1.5 \times 10^{-2}, \epsilon = 10^{-4}$. Isopleths of $\mathbb{I}(\omega)$ are shown. Higher values are represented by darker isopleths. The β effect is a stabilising influence and also increases the most unstable wavenumber.

No slip. We now turn our attention to the more tricky problem of no-slip boundary conditions. At the point of marginal stability, the solution is stationary and we have

$$\frac{1}{12}\mathsf{Ra}k^2(D^2-k^2)\hat{\eta}(y) = (D^2-k^2)^3\hat{\eta}(y) \tag{3.42a}$$

$$iT_0k\hat{\phi}(y) = \kappa(D^2-k^2)\hat{\eta}(y) \tag{3.42b}$$

where $Df(y) \equiv f'(y)$. We look for even solutions to (3.42a) of the form

$$\hat{\eta} = \Sigma_{j=1}^{j=3} A_j \cosh\left[\alpha_j\left(y-\frac{1}{2}\right)\right]. \tag{3.43}$$

In order to satisfy (3.42a) we require

$$\frac{1}{12}\mathsf{Ra}(\alpha_j^2-k^2)k^2 = (\alpha_j^2-k^2)^2 \tag{3.44}$$

which has solutions

$$\alpha_1 = k, \quad \alpha_2^2 = k^2 + k\sqrt{\frac{\mathsf{Ra}}{12}}, \quad \alpha_3^2 = k^2 - k\sqrt{\frac{\mathsf{Ra}}{12}}. \tag{3.45}$$

It is quite possible that α_3 will turn out to be imaginary, but this is still acceptable since $\cosh(i\alpha) = \cos(\alpha)$. In order to satisfy the boundary conditions ($\hat{\phi} = \hat{\eta} = \hat{\phi}' = 0$ on $y = 0, 1$) we obtain three homogeneous equations involving A_j and α_j. The solvability condition for these three equations yields

$$\alpha_2\cosh(\tfrac{1}{2}\alpha_3)\sinh(\tfrac{1}{2}\alpha_2) - \alpha_3\cosh(\tfrac{1}{2}\alpha_2)\sinh(\tfrac{1}{2}\alpha_3) = 0. \tag{3.46}$$

The solution (which is obtained numerically by a Newton-Raphson method) of (3.46) gives the curve of marginal stability of the no-slip problem. The Critical Rayleigh Number is given by the minimum of this curve viewed as $\mathsf{Ra}_0 = f(k)$. We obtain $\mathsf{Ra}_c = 825.601...$ at a critical wavenumber of $k_c = 4.754....$ These values compare with the classical Rayleigh Bénard values of $\mathsf{Ra}_c = 1708...$ at $k_c = 3.12....$ If we look for odd solutions of (3.42a) then we obtain an equation similar to (3.46), namely

$$\alpha_3\cosh(\tfrac{1}{2}\alpha_3)\sinh(\tfrac{1}{2}\alpha_2) - \alpha_2\cosh(\tfrac{1}{2}\alpha_2)\sinh(\tfrac{1}{2}\alpha_3) = 0. \tag{3.47}$$

However, the only solution of this problem is $k = \mathsf{Ra}_0 = 0$. The critical Rayleigh Number in the no-slip case differs significantly from its value in the no-stress problem (see Figure 3.5.) suggesting that the precise form of the boundary conditions at vertical side-walls has an important effect on the large-scale features of the flow. Figure 3.5 shows that, as $k \to \infty$, the critical Rayleigh Numbers for both boundary conditions approach each other. The greatest difference occurs for the large-scale (small k) waves. This is because the boundary conditions have a more global effect on the large-scale waves whereas the small-scale waves do not transport the effects of the boundary so efficiently into the interior of the domain.

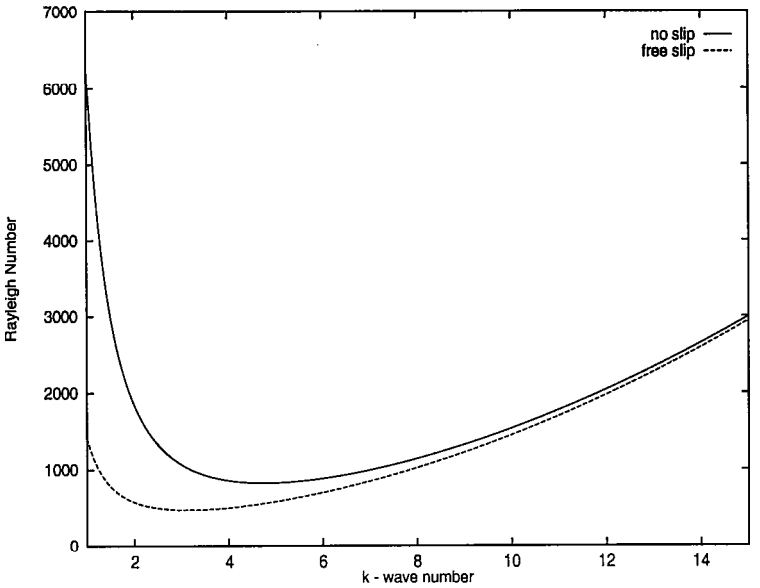


Figure 3.5: Critical Rayleigh Numbers for DIT convection for no-slip and free-slip boundary conditions.

In classical Rayleigh-Bénard convection, the more natural boundary conditions are those of no-slip because most fluids have a rigid boundary at the bottom (to hold them in place) and either a rigid lid or atmosphere (which is often considered to be a rigid lid, as indeed it is in this thesis) above them. However, for the DIT we are more fortunate because the natural conditions are those of no-stress which is easier to analyse. This is because the horizontal convection problem of this section can be thought of as a paradigm for baroclinic instability across a WBC. Figure 1.1 shows that there is a steep thermal gradient across the Gulf Stream. The temperature on its northern border is maintained by cold water from the Arctic Ocean and the temperature on the southern border is maintained by warm Caribbean water. Thus, there are no solid walls in the problem that we wish to model and so no-stress conditions seem more appropriate. Consequently, we return to that problem.

3.3.2 Weakly nonlinear analysis

Following Newell & Whitehead[54], the flnite amplitude problem is considered in the neighbourhood of the critical Rayleigh Number. The restriction to this region allows the definition of a new small parameter, $\delta \ll 1$, such that

$$\frac{\mathsf{Ra} - \mathsf{Ra}_c}{\mathsf{Ra}_c} = \chi\delta^4 \tag{3.48}$$

where χ is an $O(1)$ parameter determining whether we are in the subcritical ($\chi = -1$) or supercritical ($\chi = 1$) regime.

Before making use of δ we first use (3.26b) to eliminate ϕ from the linear part of (3.26a).

This yields

$$\nabla^2\left[\partial_t - \mathsf{Re}\nabla^2\right]\left[\kappa\nabla^2 - \partial_t\right]\eta - \frac{T^2}{12}\partial_x^2\nabla^2\eta = T\partial_x\left[\partial_y\phi\nabla^2\partial_x\phi - \partial_x\phi\nabla^2\partial_y\phi + \frac{1}{12}\left\{\partial_y\eta\nabla^2\partial_x\eta - \partial_x\eta\nabla^2\partial_y\eta\right\}\right] - \nabla^2\left[\partial_t - \mathsf{Re}^{-1}\nabla^2\right]\left[\partial_y\phi\partial_x\eta - \partial_x\phi\partial_y\eta\right] \tag{3.49}$$

where we have introduced the shorthand notation $\partial_x \equiv \frac{\partial}{\partial x}$ etc. $T^2 \equiv T_c^2(1+\chi\delta^4)$ where T_c is the temperature gradient corresponding to Ra_c. Also required is the secondary equation,

$$\nabla^2\left[\partial_t - \mathsf{Re}^{-1}\nabla^2\right]\phi = \frac{1}{12}T\partial_x\nabla^2\eta + \partial_y\phi\partial_x\nabla^2\phi - \partial_x\phi\partial_y\nabla^2\phi + \frac{1}{12}\left(\partial_x\nabla^2\eta + \partial_y\eta\partial_x\nabla^2\eta - \partial_x\eta\partial_y\nabla^2\eta\right). \tag{3.50}$$

The dependent variables η, ϕ are expanded as a power series in δ

$$f = \delta f_1 + \delta^2 f_2 + \delta^3 f^3 + ..., \quad f = (\eta, \phi). \tag{3.51}$$

In this expansion η_1 and ϕ_1 are given by the modified neutral mode solutions

$$\eta_1 = \left[A(\xi,\tau)e^{ikx} + A^*(\xi,\tau)e^{-ikx}\right]\sin(\pi y) \tag{3.52a}$$

$$\phi_1 = \frac{iK^2\kappa}{Tk}\left[A(\xi,\tau)e^{ikx} - A^*(\xi,\tau)e^{-ikx}\right]\sin(\pi y) \tag{3.52b}$$

where the amplitude A is a slowly varying function of position and time and A^* is the complex conjugate of A. The appropriate scaling is

$$\xi = \delta^2 x, \qquad \tau = \delta^4 t. \tag{3.53}$$

The exponents of this scaling are determined by arranging for the slow evolution of the amplitude, A, to balance the largest nonlinear resonant feedback terms. In classical Rayleigh-Bénard convection, this feedback first occurs at $O(\delta^3)$ whereas here it occurs at $O(\delta^5)$ owing to the $O(\delta^3)$ nonlinear terms cancelling each other.

This scaling (3.53) modifies the derivative operators in (3.49) to

$$\partial_x \to \partial_x + \delta^2\partial_\xi, \quad \partial_t \to \partial_t + \delta^4\partial_\tau \tag{3.54}$$

Progress is made by substituting (3.51, 3.52a, 3.52b, 3.54) into (3.49, 3.50) and equating the coefficients at increasing orders of the small parameter δ. The details of the equations, including explicit representations of the linear operators $\mathcal{L}_n$ and the nonlinear terms N_n, are presented in Appendix C.

At $O(\delta)$ we recover the linear equations (3.33a, b). This justifies our choice of (3.52a, 3.52b).

At $O(\delta^2)$ the balance is of the form

$$-\mathcal{L}_0\eta_2 = N_2 \equiv -\mathsf{Re}^{-1}\left(\nabla^2\right)^2\{\partial_y\phi_1\partial_x\eta_1 - \partial_x\phi_1\partial_y\eta_1\} \tag{3.55}$$

where $\mathcal{L}_0$ is the $O(1)$ differential operator (that is, the differential operator of the linear problem) and $\mathcal{L}_1$ is the $O(\delta)$ differential operator. The solution of (3.55) gives the second harmonic response to be

$$\eta_2 = \frac{\pi}{T_c}|A|^2\sin(2\pi y) \tag{3.56a}$$

$$\phi_2 = 0. \tag{3.56b}$$

The $O(\delta^3)$ the balance is of the form

$$-\mathcal{L}_0\eta_3 + \mathcal{L}_2\eta_1 = N_3 \tag{3.57}$$

where N_3 represents all the $O(\delta^3)$ terms on the RHS of (3.49). By virtue of the fact that $\mathsf{Ra} = \mathsf{Ra}_C + O(\delta^4)$, $\mathcal{L}_2\eta_1 = 0$ and (3.57) simplifies to

$$-\mathcal{L}_0\eta_3 = 2\pi^6\left(-\frac{1}{12} + \frac{100}{\mathsf{Ra}_C}\right)|A|^2\left[Ae^{ikx} + A^*e^{-ikx}\right]\sin(3\pi y) \tag{3.58}$$

The solution of (3.58) is given by

$$\eta_3 = \frac{\pi^2}{5T_c^2}|A|^2\left[Ae^{ikx} + A^*e^{-ikx}\right]\sin(3\pi y). \tag{3.59}$$

We can now solve the $O(\delta^3)$ balance of (3.50); the solution is found to be

$$\phi_3 = \frac{2i\kappa\pi^3}{T_c^3}|A|^2\left[Ae^{ikx} - A^*e^{-ikx}\right]\sin(\pi y). \tag{3.60}$$

The $O(\delta^4)$ balance of (3.49) is of the form

$$-\mathcal{L}_0\eta_4 + \mathcal{L}_2\eta_2 = N_4. \tag{3.61}$$

The solution of (3.61) yields

$$\eta_4 = \frac{4\pi^3}{5T_c^3}|A|^4\sin(2\pi y) + \frac{i}{2T_c}\left[AA_X^* - A_XA^*\right]\sin(2\pi y) + \ldots. \tag{3.62}$$

η_4 contains some terms of the form $\sin(2\pi y)$ and some of the form $\sin(4\pi y)$. These latter terms are represented by "..." because they will not be able to produce any nonlinear resonant (that is, of the form $\sin(\pi y)$) feedback at $O(\delta^5)$ and so their precise form will not be important until a higher order. The solution of the $O(\delta^4)$ balance of (3.50) is

$$\phi_4 = \frac{2i\kappa\pi^4}{5T_c^3}|A|^2\left[A^2e^{2ikx} - (A^*)^2e^{-2ikx}\right]\sin(2\pi y) + \ldots \tag{3.63}$$

$O(\delta^5)$ is the first order at which there is a non-vanishing, nonlinear, resonant feedback. The equation is

$$-\mathcal{L}_0\eta_5 + \mathcal{L}_2\eta_3 + \mathcal{L}_4\eta_1 = N_5. \tag{3.64}$$

Following Newell & Whitehead[54], it is not necessary to solve this equation. Instead, we note that in order to solve (3.64), in the presence of the linear equation $\mathcal{L}_0\eta_1 = 0$, a compatibility condition must be satisfied. This condition is that the coefficients of all the resonant terms (that is, $e^{\pm i\pi x}\sin(\pi y)$) must balance. This yields, after much tedious algebra, the solvability condition:

$$\begin{aligned} 4\pi(\kappa + \mathsf{Re}^{-1})\partial_\tau A - 8\mathsf{Re}^{-1}\kappa\partial_\xi^2 A = &\left(\frac{\chi T_c^2\pi}{6} - \frac{\pi^5}{15T_c^2}|A|^4\right)A \\ &+ \frac{i\pi^2}{6}\left(\partial_\xi\left[|A|^2\right]A + 2|A|^2\partial_\xi A\right). \end{aligned} \tag{3.65}$$

This equation (3.65) shows that $A = 0$ is a stable solution in the subcritical regime, $\chi = -1$, whereas $A = 0$ is an unstable solution in the supercritical regime. Thus, linear stability of the linear solution (3.32, 3.36) exactly coincides with weakly nonlinear stability of the weakly non-linear solution. In the supercritical regime, $\chi = 1$, there exists a stable solution (if we ignore the spatial derivatives ∂_ξ) given by $A = \left(\frac{5}{2}\right)^{\frac{1}{4}}\frac{T_c}{\pi}$. This appears to be verified in the case $\mathsf{Ra} = 1.05\mathsf{Ra}_c, T_c = 1$ by fully nonlinear simulations (Figures 3.6, 3.7).

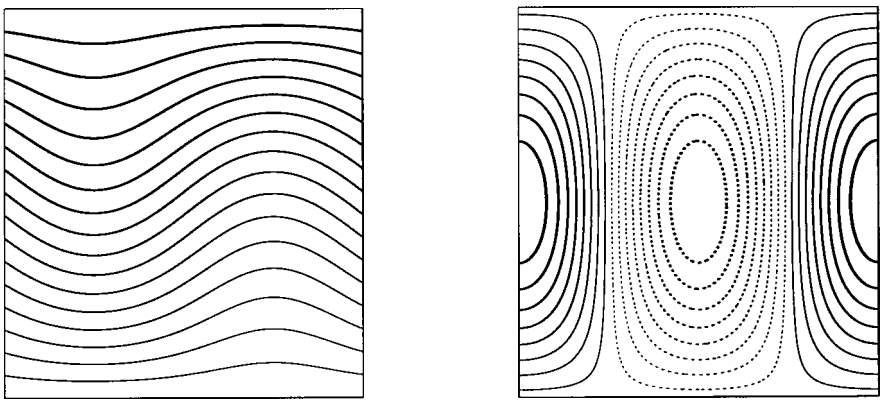
3.3.3 Numerical simulations

To investigate the nonlinear behaviour in the regime away from Ra_C a series of numerical simulations is performed. There are three non-dimensional parameters in the problem: $\mathsf{Ra}, \mathsf{Re}, \sigma$. To investigate the entire three-dimensional phase-space would require a considerable CPU effort and so we restrict attention principally to an investigation of the effect of increasing Ra. Furthermore, we consider only the more physically relevant problem of free-slip boundary conditions.

The simulations are initialised with the linear solution (3.32, 3.36). The steady state solution in the marginally supercritical case ($\mathsf{Ra} = 1.05\mathsf{Ra}_c, T_c = 1$) is shown in Figure 3.6. It is not clear that the solution differs from the linear, sinusoidal solution. However, the magnitude of the leading order term of the weakly nonlinear solution is in good agreement with the theoretical value. Furthermore, the magnitude of the next order correction to the linear solution has magnitude $\approx 0.01 \ll T_c$.

The evolution of the flow is summarised by the time-series of the Nusselt Number (Figure 3.7),

$$\mathsf{Nu} \equiv \frac{\lambda}{T_c}, \qquad \lambda \equiv \left(\frac{\partial T}{\partial y}\right)_{y=0}. \tag{3.66}$$



(a) T (b) ψ

Figure 3.6: Steady state solution of instability problem, $\mathsf{Ra} = 1.05\mathsf{Ra}_c, T_c = 1.0, t = 0.75$. Fourier analysis of T field gives $A = 0.247....$ Weakly nonlinear theory predicts a stable steady state at $A = 0.253...$

That is, Nu is the ratio of the attained heat flux through the basin (achieved through a combination of down-gradient diffusion and convection) to the heat flux through the basin achieved by diffusion alone[8].

Figure 3.7 shows that, initially, $\mathsf{Nu} = 1$. This is because the linear solution (3.31, 3.32) does not transfer any heat across the domain. Nu appears to asymptote to a value of $\mathsf{Nu} = 1.252....$ This suggests that a stable steady state is attained. Moreover, the weakly nonlinear analysis gives a solution with $\mathsf{Nu} = 1 + \frac{2\pi^2|A|^2\delta^2}{T_c^2} + ... = 1.283...$ indicating that the analysis and numerics are in good agreement.

The behaviour of the slightly supercritical flow ($\mathsf{Ra} = 10\mathsf{Ra}_c$) is shown in Figures 3.8, 3.9. The weakly nonlinear solution remains a reasonably good approximation to the flow for a significant period of time (Figures 3.8(b), 3.9(b)). The $\sin(2\pi y)$ component (3.56b) is clearly visible in Figure 3.8(b). There then appears to be a secondary instability associated with very large gradients in the boundary layer (Figures 3.8(d), 3.9(d)) It is worth asking the question whether this is a genuine instability or a manifestation of the numerics being unable to handle the boundary layer sufficiently accurately. In order to answer this question, I repeated the simulations at twice the resolution in the meridional co-ordinate, y. However, the instability occurred at precisely the same time and location. Furthermore, if the numerics were unable to resolve the flow sufficiently accurately, this

[8] In practice, in all Figures in this section, I take the average of the heat flow at the top and bottom boundaries because, at any given instant the two are not necessarily equal.

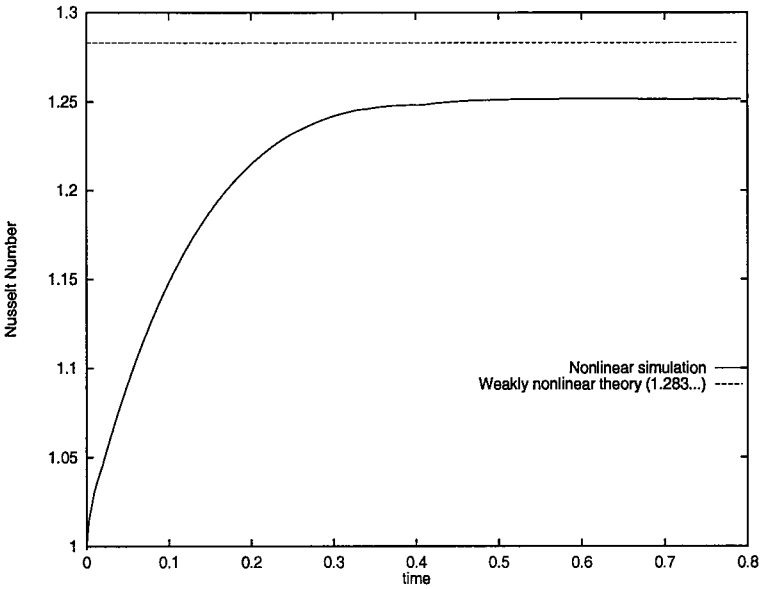


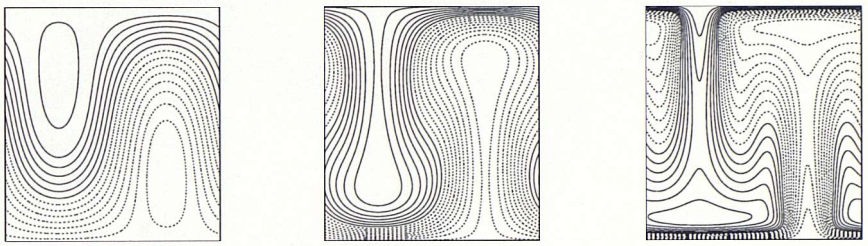
Figure 3.7: Comparison of numerically obtained Nu and theoretical value Nu = 1.283 for $\mathsf{Ra} = 1.05\mathsf{Ra}_c, T_c = 1.0$.

would be likely to result in the energy no longer being conserved. There is actually no longer any reason to expect the energy to be conserved at all because, in order to maintain fixed temperatures at the N/S boundaries, the essential condition for the flat-bottomed model of double-periodicity has been dropped. However, it is reasonable to expect that the flux of temperature through the southern boundary is approximately equal to the flux of heat through the northern boundary and so, *on average*, there is no normal temperature flux. This is borne out by the numerical simulations.

After undergoing this secondary instability, the enters a transitional period of turbulence (Figures 3.8(f), 3.9(f)) before eventually settling down to a steady state (Figures 3.8(i), 3.9(i)).

Figure 3.10 shows that the flow has indeed reached a steady state by $t = 3.1$. In this configuration it is able to transport approximately six times as much heat through the domain as the unstable linear solution is able to transport. On the other hand, it transports much less heat than the, now unstable, weakly nonlinear solution. The initial growth of Nu is in reasonably good agreement with the predictions of the weakly nonlinear theory. However, at $t = 0.55$, Nu, and hence the thermal gradients near the boundaries, become unsustainably large and the secondary instability occurs.

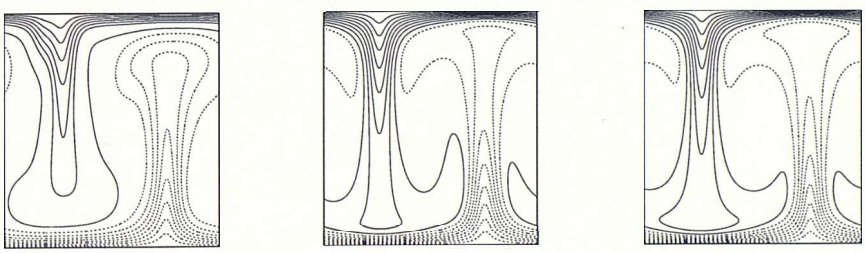
The vorticity of the steady state (Figure 3.9(i)) is concentrated in two parallel sheets. We may therefore expect that as these sheets grow in strength (as Ra is increased) a Kelvin-Helmholtz shear instability will develop and these plumes will be unable to retain their steady form.



(a) t = 0.0 (b) t = 0.25 (c) t = 0.50

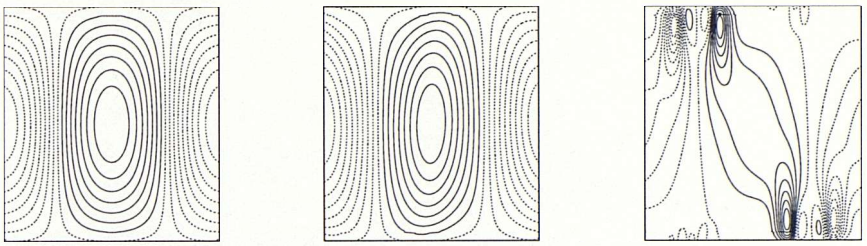


(d) t = 0.57 (e) t = 0.70 (f) t = 0.80

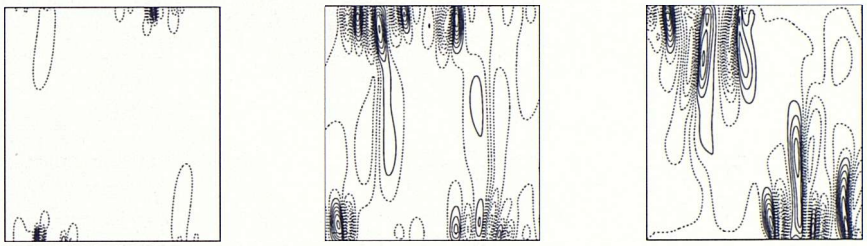


(g) t = 1.20 (h) t = 1.95 (i) t = 3.20

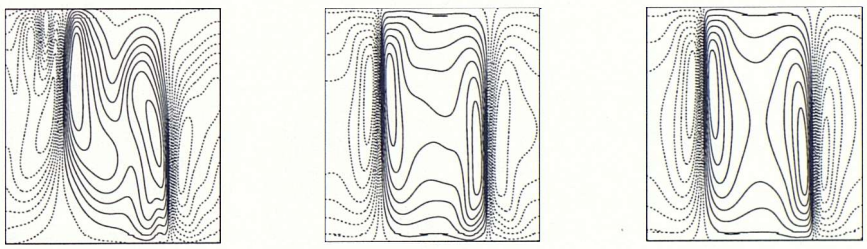
Figure 3.8: Baroclinic instability driven by linear thermal gradient, $\mathsf{Ra} = 10\mathsf{Ra}_c$; T field.



(a) t = 0.0 (b) t = 0.25 (c) t = 0.50



(d) t = 0.57 (e) t = 0.70 (f) t = 0.80



(g) t = 1.20 (h) t = 1.95 (i) t = 3.20

Figure 3.9: Baroclinic instability driven by linear thermal gradient, $\mathsf{Ra} = 10\mathsf{Ra}_c$; ζ field.

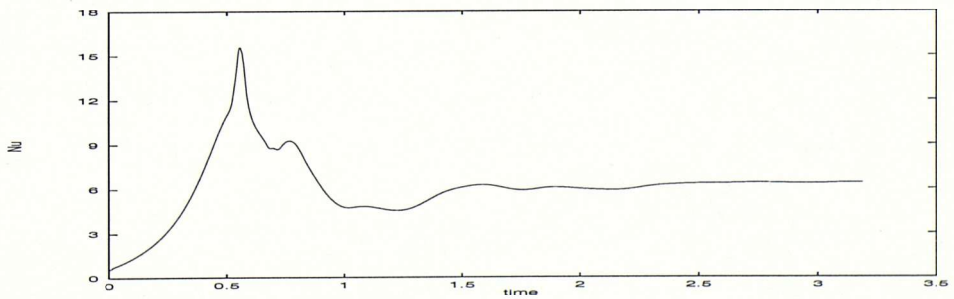


Figure 3.10: Time series of Nusselt number, $\mathsf{Ra} = 10\mathsf{Ra}_c$.

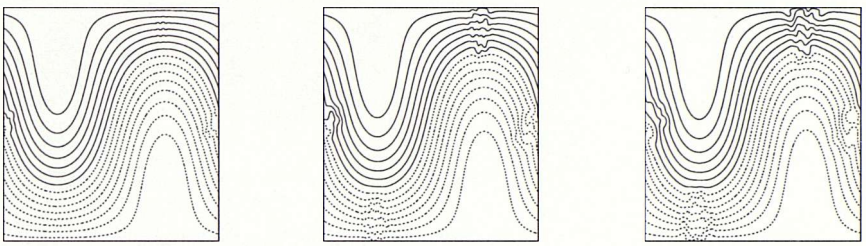
At larger values of Ra (Figures 3.11, 3.12, 3.13), the flow undergoes a secondary instability at the point of inflection in the mid-latitude point of the domain in addition to the instability already experienced near the boundaries of the domain. Figure 3.11(c) shows that this is another region of the domain in which the temperature gradients are particularly high so this instability can be interpreted as baroclinic in nature. The flow then undergoes a period of turbulence before returning to a regime in which there are two plumes in the domain as there are in the marginally supercritical instance. However, at this higher value of Ra, these two plumes are not steady (see Figures 3.11, 3.12). Instead, they oscillate (quasi-periodically) backwards and forwards and intermittently eject fluid from their tips towards the opposite boundary layer. Since this instability is located in the middle of the strong vortex sheets (Figures 3.9(i), 3.12(i)) it should be interpreted as a Kelvin-Helmholtz instability.

The quasi-periodic nature of the flow is shown most clearly by the time-series of the Nusselt Number (Figure 3.13). A maximum of the large scale oscillation corresponds to the situation in which the two plumes are relatively parallel and intact (e.g. Figure 3.11(i)) whereas a minimum corresponds to the situation in which a patch of temperature is ejected from the tip of each plume towards the opposite boundary layer (e.g. Figure 3.11(g, h)).

At still higher values of Ra, the flow is typical of that seen in *hard convective turbulence*[40], [41]. It is dominated by unsteady plumes which emanate from both boundaries. The interior of the domain becomes fairly homogenised (Figures 3.14, 3.15). After the initial linear solution has completely disappeared most of the vorticity is concentrated in the upper and lower boundary layers. As time progresses, the vorticity migrates back out into the centre of the domain. Although plume structures can be seen in the temperature field (Figure 3.14), the two vortex sheets of Figure 3.9(i) have completely disappeared in Figure 3.15. The vorticity field of Figure 3.15(c) is considerably more chaotic than that of the marginally supercritical vorticity field.

3.3.4 Summary

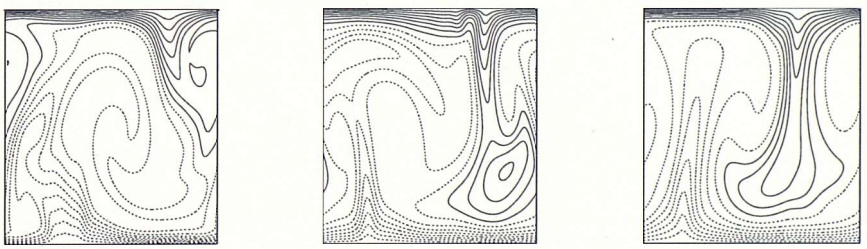
In §3.3 I have examined baroclinic instability in the simplest possible configuration of the DIT; that of a linear thermal gradient across a channel of finite width. The behaviour examined here reveals that the fundamental *JEBAI* effect is to create baroclinic instability. In the absence of either thermal diffusivity, κ, or viscosity, ν, all wavenumbers are unstable and the growth rate is proportional to the thermal gradient. When diffusive effects are incorporated, the problem resembles that of classical Rayleigh-Bénard convection. Linear solutions are presented for both no-stress and no-slip. The large difference in Ra_c for the



(a) t = 0.48 (b) t = 0.59 (c) t = 0.65

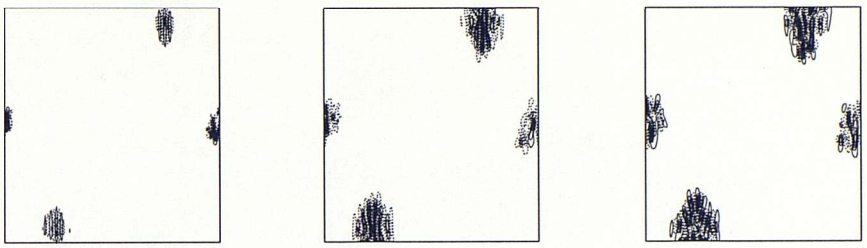


(d) t = 1.01 (e) t = 2.53 (f) t = 3.84

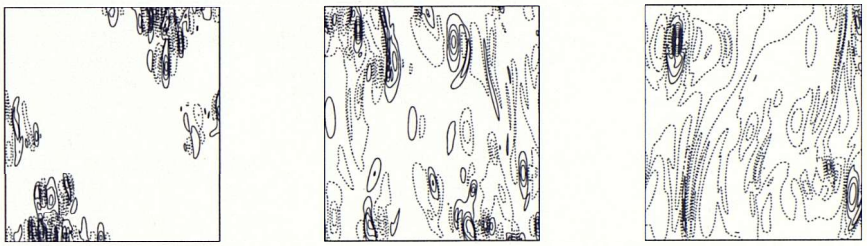


(g) t = 5.82 (h) t = 7.30 (i) t = 8.50

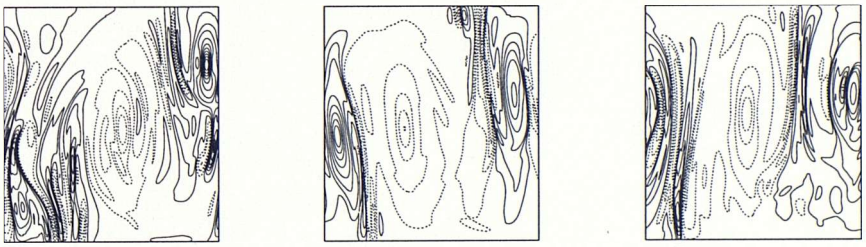
Figure 3.11: Baroclinic instability driven by linear thermal gradient, $\mathsf{Ra} = 200\mathsf{Ra}_C$; T field.



(a) t = 0.48 (b) t = 0.59 (c) t = 0.65



(d) t = 1.01 (e) t = 2.53 (f) t = 3.84



(g) t = 5.82 (h) t = 7.30 (i) t = 8.50

Figure 3.12: Baroclinic instability driven by linear thermal gradient, $\mathsf{Ra} = 200\mathsf{Ra}_C$; ζ field.

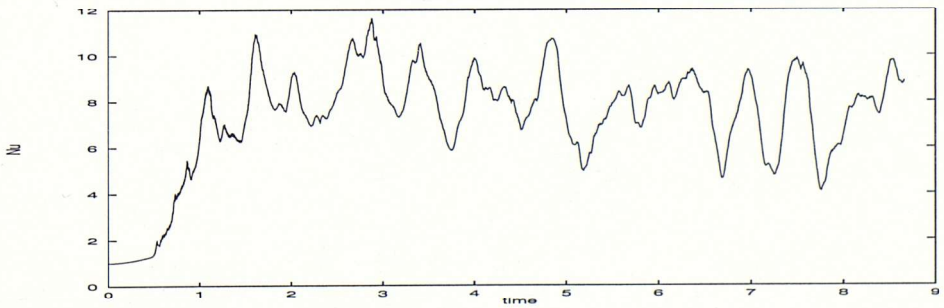
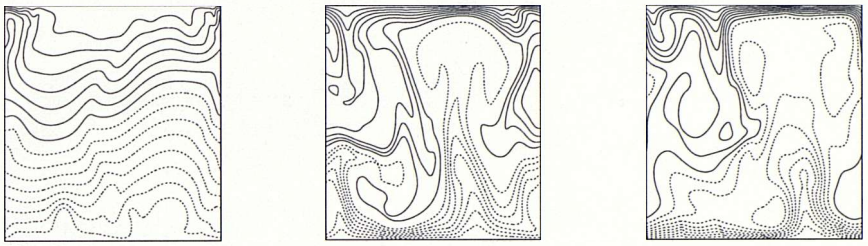
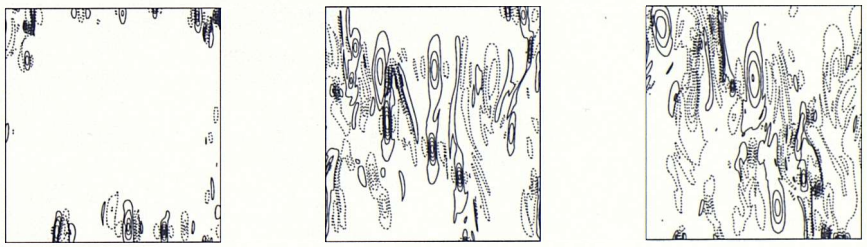


Figure 3.13: Time series of Nusselt number, $\mathsf{Ra} = 200\mathsf{Ra}_C$.



(a) t = 0.48 (b) t = 3.59 (c) t = 6.65

Figure 3.14: Baroclinic instability driven by linear thermal gradient, $\mathsf{Ra} = 2 \times 10^5 \mathsf{Ra}_C$; T field.



(a) t = 0.48 (b) t = 3.59 (c) t = 6.65

Figure 3.15: Baroclinic instability driven by linear thermal gradient, $\mathsf{Ra} = 2 \times 10^5 \mathsf{Ra}_C$; ζ field.

two cases highlights the dramatic impact that the choice of boundary conditions has on the whole flow. This is extended into a weakly nonlinear analysis for the no-stress case (§3.3.2) in which it is shown that there is a stable solution at a finite amplitude. The fully nonlinear simulations (§3.3.3) appear to confirm this prediction but suggest that a secondary instability then occurs. For moderately supercritical cases a new stable steady state eventually emerges. In the highly supercritical case, hard rotating turbulence evolves with unsteady plumes dominating the flow.

3.4 Gaussian temperature anomalies

A basic flow with linear thermal gradient is a special case because $\nabla^2\bar{T} = 0$ where $\bar{T}$ is the basic, non-perturbed Temperature. In general, this will not be the case. In this section we study a localised temperature profile, specifically, a Gaussian-strip temperature anomaly in which the basic temperature is given by

$$\bar{T} = e^{-y^2}. \tag{3.67}$$

The motivation behind this particular profile is our continuing aim of attempting to model and understand western boundary currents. Figure 1.1 shows that, just after separating from the coast, the Gulf Stream resembles a warm jet of fluid flowing through colder North Atlantic. Our Gaussian strip, (3.67), is intended to approximate this. Although high velocities are undoubtedly an important characteristic of WBC's, their effect is neglected here; the streamfunction, ψ, is therefore everywhere small. It is easy to extend the analysis of §3.3.1 to show that if the fluid in the channel has a constant velocity, $\psi = Py$, then the stability of the flow is unchanged. We might expect a similar result here.

The choice of a Gaussian strip means that the solutions of the linear problem are no longer the sinusoidal (in y) normal modes. We therefore seek solutions to the DIT of the form

$$T = \bar{T} + \eta = \bar{T} + \hat{\eta}(y)e^{ikx-i\omega t}, \qquad \psi = \hat{\phi}(y)e^{ikx-i\omega t} \tag{3.68}$$

where $\hat{\eta}, \hat{\phi} \ll 1$.

In fact, even the basic state ($T = \bar{T}, \psi = 0$) is not an exact solution of (3.26a, b) because the thermal diffusion term is left unbalanced. Although $\nabla^2\bar{T} \neq 0$ we choose to neglect the thermal diffusion of the basic temperature $\kappa\nabla^2\bar{T}$ because this will occur on a time-scale very much greater than the time-scale of the disturbance growth rate. Thus, the disturbance growth will have reached the nonlinear phase well before the diffusion of the background temperature has any significant effect on the flow. Having made this assumption we proceed and we shall verify that it is a reasonable assumption through

numerical simulations in §3.4.5. Additionally, we shall set the viscosity, $\nu = 0$ in order to simplify the analysis[9].

Substituting (3.68) into (3.26a, b) (and neglecting the thermal diffusion of the basic state) leads to the two equations

$$\omega\hat{\eta} + 2k\hat{\phi}ye^{-y^2} = i\kappa\left(\hat{\eta}'' - k^2\hat{\eta}\right) \tag{3.69a}$$

$$12\omega\left(\hat{\phi}'' - k^2\hat{\phi}\right) - \left[\left(12 - 8y^2 - 2k^2\right)y\hat{\eta} + 2y\hat{\eta}''\right]ke^{-y^2} = 0. \tag{3.69b}$$

We use (3.69a) to solve for $\hat{\phi}$ in terms of $\hat{\eta}$ and then substitute this and all its derivatives into (3.69b). This yields a fourth order differential equation for $\hat{\eta}$:

$$\begin{aligned}\omega\Bigg\{ & i\kappa\hat{\eta}^{(iv)} + i\kappa\hat{\eta}'''\left[4y - \frac{2}{y}\right] + \hat{\eta}''\left[-2i\kappa k^2 - \omega + i\kappa\left(4y^2 - 2 + \frac{2}{y^2}\right)\right] \\ & + \hat{\eta}'\left[-i\kappa k^2 - \omega\right]\left[4y - \frac{2}{y}\right] + \hat{\eta}\left[-i\kappa k^2 - \omega\right]\left[4y^2 - 2 + \frac{2}{y^2} - k^2\right]\Bigg\} \\ & - \frac{1}{3}y^2e^{-2y^2}k^2\Bigg\{\hat{\eta}'' + \hat{\eta}\left[6 - 4y^2 - k^2\right]\Bigg\} = 0.\end{aligned} \tag{3.70}$$

In §3.3.1, in the absence of any diffusive terms, it is found that the fastest growing waves are those with the highest wavenumber ($w \sim iT_0k$). In the present section, $\nu = 0$ and $\kappa \ll 1$ in order to justify neglecting the diffusion of the basic state. Therefore, we again expect the highest wavenumbers to be those which grow the fastest. This motivates solving (3.70) by using the WKBJ method; that is, we assume that there are solutions for $\hat{\eta}$ in the form

$$\hat{\eta} = A(y)e^{k\int g(y)dy} \tag{3.71}$$

where $k \gg 1$. We can easily differentiate (3.71); our assumption that $k \gg 1$ means that we can immediately discard low powers of k so, for example,

$$\hat{\eta}^{(iv)} = k^4g^4A + k^3\left(6g^2g'A + 4g^3A'\right) + O(k^2). \tag{3.72}$$

We also express ω in powers of k thus:

$$\omega = k\left(\omega_0 + \frac{1}{k}\omega_1 + \cdots\right). \tag{3.73}$$

In order to obtain a meaningful balance within (3.70) we also need to rescale κ such that $\kappa \equiv \frac{1}{k}\hat{\kappa}$.

To obtain equations for both g and A we need to retain the highest two powers of k in each expression. Equating like powers of k we then find at $O(k^4)$

$$\tilde{\omega}_0\hat{\kappa}g^4 - 2\tilde{\omega}_0\hat{\kappa}g^2 + \tilde{\omega}_0\hat{\kappa} + (\omega_0^2 + \alpha^2)(g^2 - 1) = 0 \tag{3.74}$$

[9] A non-zero ν leads to a sixth, rather than a fourth, order system.

where

$$\alpha(y) \equiv \frac{y}{\sqrt{3}} e^{-y^2} \tag{3.75}$$

and the notation $\tilde{\omega}_0 = -i\omega_0$ is introduced for convenience. (3.74) is easily solved to yield

$$g^2 = \frac{-(\omega_0^2 + \alpha^2) + 2\tilde{\omega}_0\hat{\kappa} \pm (\omega_0^2 + \alpha^2)}{2\tilde{\omega}_0\hat{\kappa}}. \tag{3.76}$$

The thermal diffusivity, even the rescaled version $\hat{\kappa}$, is to be regarded as being small and so in the limit of $\hat{\kappa} \to 0$ we have

$$g(y) \to \pm 1, \quad \pm i\sqrt{\frac{\omega_0^2 + \alpha^2}{\tilde{\omega}_0\hat{\kappa}}}. \tag{3.77}$$

The former of the solutions in (3.77) is the solution of the inviscid problem. It turns out that it is impossible to match an inner solution onto $g = \pm 1$ (see §3.4.1). Thus, we proceed with the second solution. The boundary conditions for this problem are of no flow at infinity so we require $\hat{\eta} \to 0$ as $y \to \infty$. In this limit $\alpha \to 0$ so $g(y) \to \pm\sqrt{\frac{\tilde{\omega}_0}{\hat{\kappa}}}$. This requires that $\tilde{\omega}_0$ must have a real component (so that $\hat{\eta} \sim e^{\pm c_0 ky}$) and hence ω_0 must have an imaginary component. Furthermore, it is clear that no linear combination of the two solutions can satisfy both boundary conditions at $\pm\infty$. At $+\infty$ the solution must look like e^{-ky} and at $-\infty$ the solution must look like e^{+ky}. Consequently, there is a need for at least one critical point where the solution can *jump* from one branch to the other. Such a critical point must occur where $\omega_0^2 + \alpha^2 = 0$ since it is precisely in the neighbourhood of these points that the validity of the solution (3.77) breaks down. This means that ω_0^2 is purely imaginary and Figure 3.16 shows that, in general, there are four critical points where the solution can jump from one branch to another. We denote these points $\pm y_{0_i}$, $(i = 1, 2)$ where $y_{0_1} < y_{0_2}$ and $y_{0_i} > 0$ [10]. The special cases of $\omega_0^2 = -\max(\alpha^2)$ and $\omega_0 = 0$ will be dealt with in §3.4.4.

Note that this analysis provides an upper bound for the growth rate of the disturbance, namely $\omega_0 = i\sqrt{\frac{1}{6}e^{-1}}$.

In the neighbourhood of the critical points, y_0,

$$\omega_0^2 + \alpha^2 \to \omega^* \tilde{y} \equiv \left.\frac{\partial(\alpha^2)}{\partial y}\right|_{y=y_0} \tilde{y} = \left(4y_0 - \frac{2}{y_0}\right)\omega_0^2 \tilde{y} \tag{3.78}$$

where $\tilde{y} \equiv y - y_0$. Therefore

$$g \sim i\left(\frac{\omega^*}{\tilde{\omega}_0\hat{\kappa}}\right)^{\frac{1}{2}} \tilde{y}^{\frac{1}{2}} \tag{3.79}$$

[10] To prevent a plethora of multiple subscripts, we shall refer to y_0 as a generic critical point if the meaning is unambiguous.

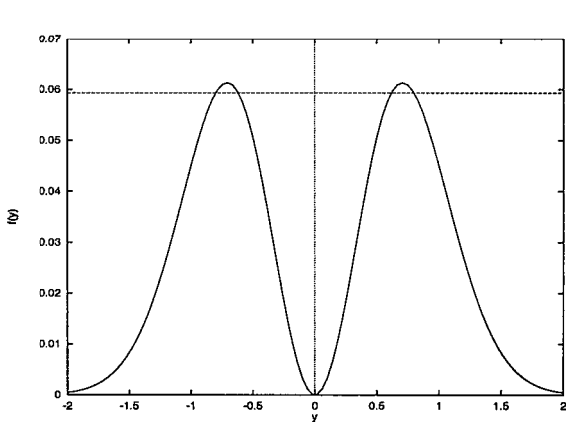


Figure 3.16: $f(y) = \alpha^2(y)$. Intersections with $f(y) = 0.0593$ reveal the location of the four critical points $\pm y_{0_i} = \pm 0.618, \pm 0.8$ at which WKBJ approximations break down. Maximum value of $\alpha^2(y)$ shows maximum possible growth rate of disturbance.

and hence

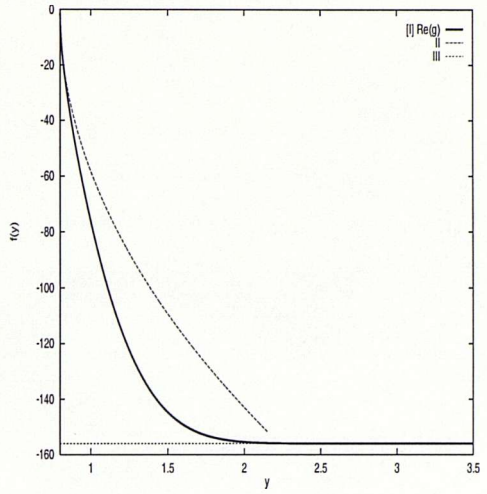
$$\hat{\eta}(y) \sim A(y) e^{\pm \frac{2}{3} k \left(\frac{\omega^*}{\tilde{\omega}_0 \hat{\kappa}}\right)^{\frac{1}{2}} \tilde{y}^{\frac{3}{2}}}. \tag{3.80}$$

Note that at $y_{0_1}, \omega^* > 0$ and so from (3.80) we would expect oscillatory behaviour in $y > y_{0_1}$ and exponential behaviour in $y < y_{0_1}$. Conversely, at $y_{0_2}, \omega^* < 0$ and so from (3.80) we would expect oscillatory behaviour in $y < y_{0_2}$ and exponential behaviour in $y > y_{0_2}$ (see Figure 3.19).

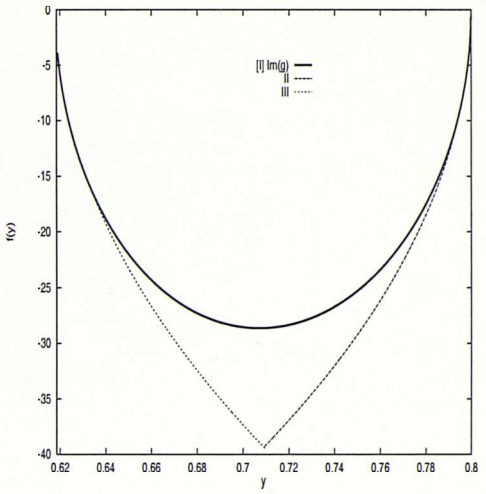
In Figure 3.17 the phase (3.76) has been plotted for various values of the diffusion $\hat{\kappa}$. As an illustration, we arbitrarily choose, in Figure 3.17, $y_{0_2} = 0.8$. This implies that $y_{0_1} \sim 0.618124$. For $\hat{\kappa} = 10^{-5}$, both the real (Figure 3.17(a)) and imaginary (Figure 3.17(b)) components approximate their asymptotic values in the neighbourhood of the critical points y_0 and also as $y \to \infty$.

For larger values of $\hat{\kappa}$ the phase still tends towards a constant value as $y \to \infty$ (Figure 3.17(c). This corresponds to $e^{\pm ky}$ type behaviour) but this value is more negative than the asymptotic solution, $\sqrt{\frac{\tilde{\omega}_0}{\hat{\kappa}}}$. This means that $\eta \to 0$ more rapidly than the small $\hat{\kappa}$ asymptotics predicts. For $y \sim y_{0_2}$ (Figure 3.17(d)) the real component of the phase, g, does not vanish. Instead, g gains an oscillatory component which becomes more and more important as $\hat{\kappa}$ increases which implies that the oscillatory nature of the solution is not confined to $y_{0_1} < y < y_{0_2}$.

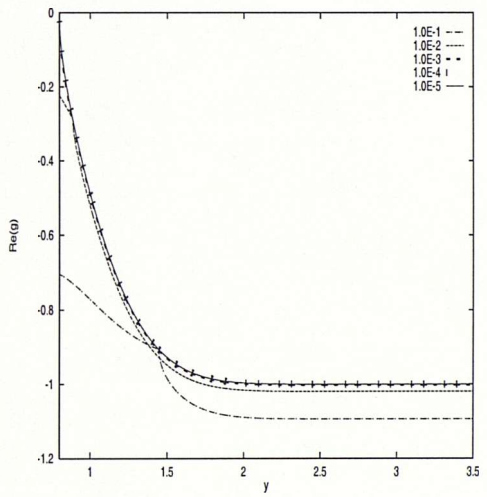
Having solved the $O(k^4)$ equation to obtain the phase of the solution, we now proceed to



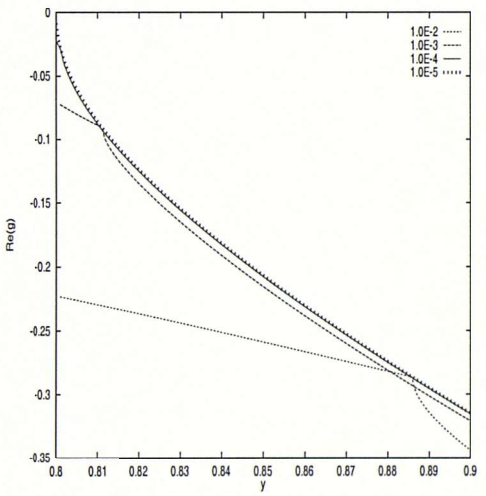
(a) $f(y) = (I)\,\mathbb{R}(g), (II)\,\left(\frac{\omega^*}{\hat{\kappa}}(y - y_{0_2})\right)^{\frac{1}{2}}$, $(III)\,\left(\frac{\tilde{\omega}_0}{\hat{\kappa}}\right)^{\frac{1}{2}}$ $(\hat{\kappa} = 10^{-5})$



(b) $f(y) = (I)\,\mathbb{I}(g), (II)\,\left(\frac{\omega^*}{\hat{\kappa}}(y_{0_2} - y)\right)^{\frac{1}{2}}$, $(III)\,\left(\frac{\omega^*}{\hat{\kappa}}(y - y_{0_1})\right)^{\frac{1}{2}}$. $(\hat{\kappa} = 10^{-5})$



(c) The phase for $y > y_{0_2}$ at different values of $\hat{\kappa}$. All solutions have been scaled by $\left(\frac{\tilde{\omega}_0}{\hat{\kappa}}\right)^{\frac{1}{2}}$ so that they may be shown on the same axes. The curves for $\kappa = 10^{-3}, 10^{-4}, 10^{-5}$ all collapse onto each other.



(d) The same as (c) but for $y_{0_2} < y < y_{0_2} + \delta$. The $\hat{\kappa} = 10^{-4}, 10^{-5}$ still collapse onto each other.

Figure 3.17: The phase $(g(y))$ of the Gaussian temperature anomaly solution for η. ω^* is based on $y_{0_2} = 0.8; y_{0_1} = 0.618....$ Also shown are the asymptotes of the real and imaginary parts of the phase (see text for further explanation).

the $O(k^3)$ equation to solve for A which we think of as the amplitude:

$$\tilde{\omega}_0\hat{\kappa}\left[4g^3A' + 6g^2g'A\right] + \tilde{\omega}_0\hat{\kappa}\left[4y - \frac{2}{y}\right]g^3A - \left[2\tilde{\omega}_0\hat{\kappa} - \omega_0^2\right]\left[2gA' + g'A\right]$$
$$- \left[\tilde{\omega}_0\hat{\kappa} - \omega_0^2\right]\left[4y - \frac{2}{y}\right]gA + \alpha^2[2gA' + g'A] + \omega_1\left[i\hat{\kappa}(g^2 - 1) - 2\omega_0\right](g^2 - 1)A = 0. \tag{3.81}$$

Recalling that $\hat{\kappa} \ll 1$ and that $g \sim \hat{\kappa}^{-\frac{1}{2}}$ yields the leading order behaviour of (3.81):

$$\omega_1 A \left(i\hat{\kappa} g^4 - 2\omega_0 g^2\right) = 0. \tag{3.82}$$

Since we require $A, g \neq 0$, at least in the neighbourhood of the critical points, we deduce that $\omega_1 = 0$. We can now solve (3.81) numerically, using the solution for g from (3.76). Of particular interest is the asymptotic form of the solution in the neighbourhood of the critical point y_0. In this region we can use (3.79) to simplify (3.81) to

$$-4\omega^* A'\tilde{y} - 3\omega^* A + \left[w_0^2 - \tilde{y}\omega^*\right]\left[4y_0 - \frac{2}{y_0} + \left(4 + \frac{2}{y_0^2}\right)\tilde{y}\right] A\tilde{y} + 2\omega^*\tilde{y}A' + \frac{1}{2}\omega^* A = 0. \tag{3.83}$$

Using (3.78) we can solve (3.83) to give

$$A(y) = A_0 \tilde{y}^{-\frac{3}{4}} e^{-\beta\frac{\tilde{y}}{2} - \frac{1}{4}\gamma\left(1-\frac{1}{\beta}\right)\tilde{y}^2} \tag{3.84}$$

where

$$\beta \equiv 4y_0 - \frac{2}{y_0}, \qquad \gamma \equiv 4 + \frac{2}{y_0}. \tag{3.85}$$

Finally, we see that combining (3.80), (3.84) yields

$$\hat{\eta}(y) \sim A_0 \tilde{y}^{-\frac{3}{4}} e^{\pm k\frac{2}{3}\left(\frac{\omega^*}{\omega_0 \hat{\kappa}}\right)^{\frac{1}{2}} \tilde{y}^{\frac{3}{2}}} \tag{3.86}$$

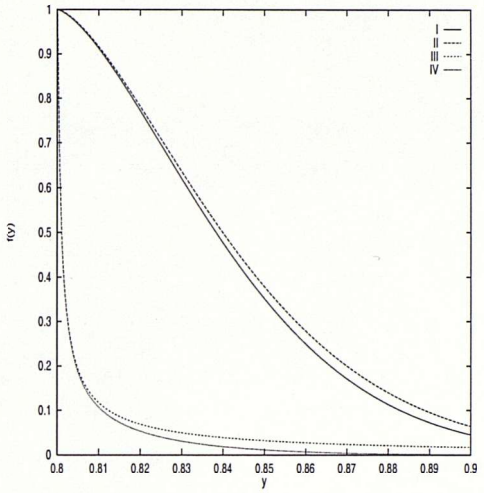
as $\tilde{y} \to y_{0_i}$. Note, from (3.77), $\hat{\eta}$ = constant, A_1 say, is also a solution corresponding to $g^2 = 1$. This is the completely inviscid limit obtained by neglecting κ entirely.

As $y \to \infty$, substitution of the solution $g_0 = const.$ into the amplitude equation (3.83) reduces that equation to $A' = 0$ and so the asymptotic nature of the full solution is $\hat{\eta}(y) \sim A_0 e^{\pm\sqrt{\frac{\tilde{\omega}_0}{\hat{\kappa}}} ky}$.

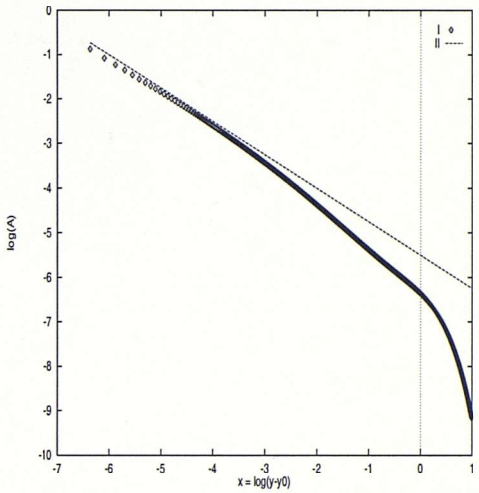
Figure 3.18 shows plots of the amplitude, A, and solution, η, for the same set of parameters as in Figure 3.17. The amplitude is obtained by numerically solving (3.81) using the value of g from (3.76). Figures 3.18(a),(c) show that the solution is very localised to the region surrounding the critical points ($y_{0_2} = 0.8$ in this case). The singularity in A dominates the behaviour of η in this region. This is especially true for $y < y_{0_2}$ where the curves for A and η are indistinguishable. Figure 3.18(a) further plots the $e^{\int g dy}$ component of the solution, η and its asymptotic structure (3.80). Figure 3.18(b) demonstrates that as $y \to y_{0_2}$, $A(y) \to (y - y_{0_2})^{-\frac{3}{4}}$ as asserted in (3.84).

3.4.1 Solution in the neighbourhood of critical points

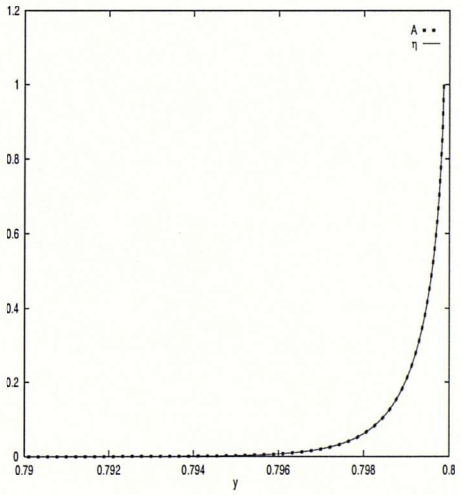
As noted earlier, it is not possible for one branch of the outer solution, η, to satisfy no flow everywhere at infinity. Furthermore, η has a singularity at $y = y_0$, (3.86, Figure 3.18).



(a) $f(y) = (I)\ e^{\int(g(y')dy'}$, (II) $e^{-\frac{2}{3}\left(\frac{\omega^*}{\kappa}\right)^{\frac{1}{2}}(y-y_{0_2})^{\frac{1}{2}}}$, (III) $\mathbb{R}(A)$, (IV) $\eta(y)$ for $y > y_{0_2}$.



(b) $f(y) = (I)\ \log(A)$, (II) $-\frac{3}{4}x + C$.



(c) $f(y)$ = Amplitude, A, and solution, $\eta(y)$, for $y < y_{0_2}$. The two curves collapse onto each other.

Figure 3.18: The amplitude, A, and complete outer solution, η, for the Gaussian temperature anomaly. All parameters identical to Figure 3.17. See text for further explanation.

Consequently, we need to find a solution in the neighbourhood of the critical points which allows the solution to jump from one branch to another and avoid the singularity.

We rescale the original equation for $\hat{\eta}$ (3.70) with a small parameter δ so that

$$y = y_0 + \delta Y, \qquad \omega = k\omega_0, \qquad \kappa = \frac{\delta^3 \hat{\kappa}}{k}. \tag{3.87}$$

The scaling of $\hat{\kappa}$ with δ^3 is chosen as being the only scaling to produce a *balanced* equation at the lowest power of δ, namely at $O(\frac{1}{\delta})$. This procedure yields

$$\tilde{\omega}_0 \hat{\kappa} \hat{\eta}^{(iv)} + \omega^* k^2 \left(\hat{\eta}'' Y + \hat{\eta}' \right) = 0 \tag{3.88}$$

where we have again had to use the relationship (3.78) between ω^* and ω_0. We can integrate (3.88) once to obtain

$$\tilde{\omega}_0 \hat{\kappa} \eta''' + k^2 \omega^* Y \eta' = C_3 \tag{3.89}$$

which is an inhomogeneous Airy equation for $\hat{\eta}'$. The method of variation of parameters leads to the solution

$$\hat{\eta}'(\tilde{Y}) = C_1 Ai(\tilde{Y}) + C_2 Bi(\tilde{Y}) + C_3 \int^{\tilde{Y}} \frac{Ai(\xi)Bi(\tilde{Y}) + Ai(\tilde{Y})Bi(\xi)}{Ai'(\xi)Bi(\xi) - Bi'(\xi)Ai(\xi)} d\xi \tag{3.90}$$

where $Ai(x)$ and $Bi(x)$ are the standard Airy functions and $\tilde{Y} = -Y \left(\frac{k^2 \omega^*}{\tilde{\omega}_0 \hat{\kappa}} \right)^{\frac{1}{3}}$. The Wronskian $W(Ai, Bi) = \pi^{-1}$ and Abramowitz & Stegun[1] states that the remaining integral can be expressed as a sum of two standard integrals so (after some absorption of constants into C_i) we are left with

$$\hat{\eta} = C_1 \int^{\tilde{Y}} Ai(\xi) d\xi + C_2 \int^{\tilde{Y}} Bi(\xi) d\xi + C_3 \int^{\tilde{Y}} Gi(\xi) d\xi + C_4. \tag{3.91}$$

Abramowitz & Stegun[1] gives the asymptotic form of each of these terms as $\tilde{Y} \to \infty$ which we would like to match onto the asymptotic form of the outer solution (3.86) as $y \to y_0$. This can easily be achieved by setting $C_3 = 0$ to leave

$$\hat{\eta}(Y) = C_1 \int^{\tilde{Y}} Ai(\xi) d\xi + C_2 \int^{\tilde{Y}} Bi(\xi) d\xi + C_4. \tag{3.92}$$

3.4.2 Solution in the neighbourhood of the origin

The WKBJ solution (3.77) is also invalid as $y \to 0$ because this solution neglects the $\frac{1}{y}$ terms of the exact equation for $\hat{\eta}$, (3.70). To take account of such terms we rescale (3.70)

via $y = \delta_0 Y$, $\kappa = \frac{\delta_0^2}{k}\hat{\kappa}$ and $\omega = k\omega_0$ as before. This leads to a new equation, at $O(\delta_0^{-2})$, for $\hat{\eta}$:

$$\tilde{\omega}_0\hat{\kappa}\left\{\hat{\eta}^{(iv)} - \frac{2}{Y}\hat{\eta}''' + \frac{2}{Y^2}\hat{\eta}''\right\} + \omega_0^2 k^2\left\{\hat{\eta}'' - \frac{2}{Y}\hat{\eta}' + \frac{2}{Y^2}\hat{\eta}\right\} = 0 \tag{3.93}$$

which implies that

$$\hat{\eta}'' - k^2\frac{\tilde{\omega}_0}{\hat{\kappa}}\hat{\eta} = 0. \tag{3.94}$$

Since $\tilde{\omega}_0$ is a positive, real constant, (3.94) has solution

$$\hat{\eta} = C_{origin_1}\cosh\left(k\sqrt{\frac{\tilde{\omega}_0}{\hat{\kappa}}}Y\right) + C_{origin_2}\sinh\left(k\sqrt{\frac{\tilde{\omega}_0}{\hat{\kappa}}}Y\right). \tag{3.95}$$

3.4.3 Matching the regions together

The analysis is completed by matching up the all the inner and outer solutions and determining which branch of the outer solution to use in the different regions. To aid clarity, we shall consider only the even (cosh()) solutions although it is, of course, easy to drop this restriction if desired. For $y \geq 0$ there are two critical points where the outer solution breaks down. There is also the inner region at the origin. Thus, there are 11 separate regions to consider. Since the problem is linear, we have the freedom to choose the value of exactly one of the many constants and so we choose to set the asymptotic solution as $y \to \infty$ to $\hat{\eta} \to e^{-\sqrt{\frac{\tilde{\omega}_0}{\hat{\kappa}}}ky}$. Then, working back towards $y = -\infty$ we can match all the constants up as follows:

Let $\hat{\eta}_+$ be the outer solution corresponding to $g_0 = +\sqrt{\frac{\tilde{\omega}_0}{\hat{\kappa}}}$ as $y \to \infty$ and $\hat{\eta}_-$ be the outer solution corresponding to $g_0 = -\sqrt{\frac{\tilde{\omega}_0}{\hat{\kappa}}}$ as $y \to \infty$

$y_{0_2} \ll y < \infty$	Outer Solution	$\hat{\eta} = \hat{\eta}_- \sim e^{-k\sqrt{\frac{\tilde{\omega}_0}{\hat{\kappa}}}y}$ as $y \to \infty$
$y \sim y_{0_2}$	Inner Solution	$\hat{\eta} = -2\sqrt{\pi}\int Ai - \frac{2\sqrt{\pi}}{3}$
$y_{0_1} \ll y \ll y_{0_2}$	Outer Solution	$\hat{\eta} = e^{-i\frac{\pi}{4}}\hat{\eta}_+ + e^{i\frac{\pi}{4}}\hat{\eta}_- - \frac{2\sqrt{\pi}}{3}$
$y \sim y_{0_1}$	Inner Solution	$\hat{\eta} = -2\sqrt{\pi}\int Ai - \frac{2\sqrt{\pi}}{3}$
$0 \ll y \ll y_{0_1}$	Outer Solution	$\hat{\eta} = \hat{\eta}_+$
$y \sim 0$	Solution at Origin	$\cosh\left(k\sqrt{\frac{\tilde{\omega}_0}{\hat{\kappa}}}Y\right)$
$-y_{0_1} \ll y \ll 0$	Outer Solution	$\hat{\eta} = \hat{\eta}_-$
$y \sim -y_{0_1}$	Inner Solution	$\hat{\eta} = -2\sqrt{\pi}\int Ai - \frac{2\sqrt{\pi}}{3}$
$-y_{0_2} \ll y \ll -y_{0_1}$	Outer Solution	$\hat{\eta} = e^{-i\frac{\pi}{4}}\hat{\eta}_+ + e^{i\frac{\pi}{4}}\hat{\eta}_- - \frac{2\sqrt{\pi}}{3}$
$y \sim -y_{0_2}$	Inner Solution	$\hat{\eta} = -2\sqrt{\pi}\int Ai - \frac{2\sqrt{\pi}}{3}$
$-\infty < y \ll -y_{0_2}$	Outer Solution	$\hat{\eta} = \hat{\eta}_+ \sim e^{k\sqrt{\frac{\tilde{\omega}_0}{\hat{\kappa}}}y}$ as $y \to -\infty$

A pictorial representation of the solution for $y \geq 0$ is given in Figure 3.19. The solution is normally one of the outer solutions, that is $e^{\pm ky}$. These are the WKBJ solutions in the inviscid limit. The solution can "flip" from one root to the other by passing through either two Airy-like inner regions or one hyperbolic-trigonometric inner region. Thus, it is easy to see that as y ranges from $-\infty$ to $+\infty$, the solution flips three times and consequently we achieve the desired effect of getting from e^{+ky} at $-\infty$ to e^{-ky} at $+\infty$.

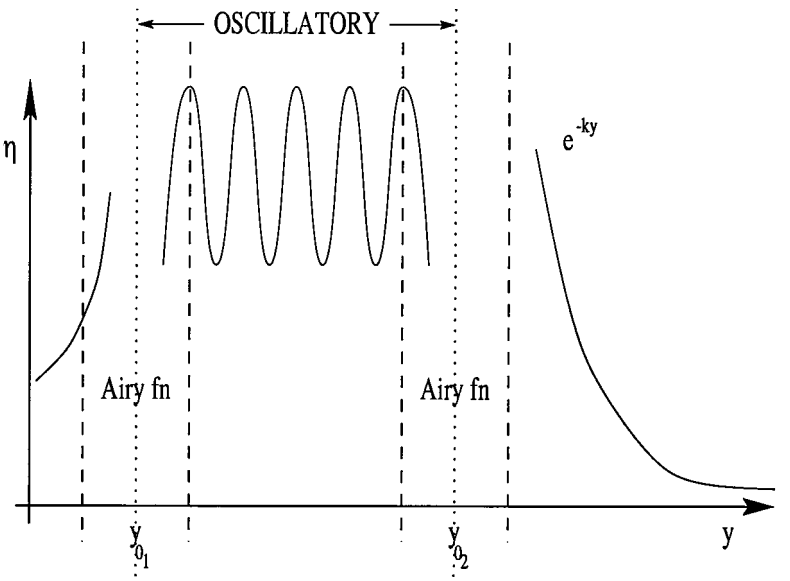


Figure 3.19: Structure of complete solution for $y \geq 0$.

3.4.4 Special cases

There are two special cases when the above solution structure (Figure 3.19) is not valid. The first is when the critical points occur at the origin $y_{0_1} = 0$. This case is unimportant because the corresponding eigenvalue is zero ($\omega_0 = 0$) and so the solution does not grow at all (to leading order). This is the degenerate case.

The other situation to consider is when the critical points merge at the point of inflection of the basic state ($y_{0_1} = y_{0_2} = \sqrt{\frac{1}{2}}$). It can be seen from Figure 3.16 that this corresponds to the maximum possible growth rate.

At this point $\omega^* = 0$ so we have to proceed to the next term in the Taylor expansion of $\omega_0^2 + \alpha^2$ in the neighbourhood of the critical points (y_0). With this one proviso, the procedure is exactly the same as for the general case. There is no change to the general form of the phase, g (3.76). However, in the neighbourhood of $y_0 \equiv \sqrt{\frac{1}{2}}$, the equivalent of (3.79) is now

$$g^2 \sim \frac{-\omega^{**}\tilde{y}^2}{2\tilde{\omega}_0\hat{\kappa}} \tag{3.96}$$

where

$$\omega^{**} \equiv \left.\frac{\partial^2 \alpha^2}{\partial y^2}\right|_{y=\sqrt{\frac{1}{2}}} = \frac{-4}{3}e^{-1}. \tag{3.97}$$

Thus, in the limit of $\hat{\kappa} \to 0$, the phase is always real and so there is no oscillation. Substitution of (3.96) into the amplitude equation (3.81) yields an expression for the amplitude.

$$A = \tilde{y}^{\frac{-3}{2}} e^{-2\tilde{y}^2} \to \tilde{y}^{\frac{-3}{2}} \text{ as } \tilde{y} \to 0. \tag{3.98}$$

Therefore,

$$\hat{\eta}_{outer} \to A_0 \tilde{y}^{\frac{-3}{2}} e^{k\frac{1}{2}\left(\frac{-\omega^{**}}{2\tilde{\omega}_0\hat{\kappa}}\right)^{\frac{1}{2}}\tilde{y}^2} \text{ as } \tilde{y} \to 0. \tag{3.99}$$

We obtain the inner solution in the same fashion as before. Now, to obtain a reasonable balance, κ must be scaled with δ^4. This scaling leads, at $O(1)$, to

$$\tilde{\omega}_0\hat{\kappa}\hat{\eta}^{(iv)} + k^2\frac{1}{2}\omega^{**}Y\hat{\eta}'' + k^2\omega^{**}Y\hat{\eta}' = 0. \tag{3.100}$$

We can integrate (3.100) once to obtain

$$\tilde{\omega}_0\hat{\kappa}\hat{\eta}''' - \left(-\frac{1}{2}k^2\omega^{**}\right)Y^2\hat{\eta}' = C_0. \tag{3.101}$$

(3.101) is a non-homogeneous parabolic cylinder equation for $\hat{\eta}'$. The transformation

$$\tilde{Y}^2 = 2\left(\frac{-k^2\omega^{**}}{2\tilde{\omega}_0\hat{\kappa}}\right)^{\frac{1}{2}}Y^2 \tag{3.102}$$

converts (3.101) into one of the two standard forms ([1]) of parabolic cylinder equations:

$$\hat{\eta}''' - \frac{1}{4}\tilde{Y}^2\hat{\eta}' = C_0. \tag{3.103}$$

Abramowitz & Stegun[1] gives two independent solutions for the homogeneous solution for $\hat{\eta}'$; $U(0,x)$, $V(0,x)$ and asymptotic expansions for both. As before, the aim is to match our inner solution to the limit of the outer solution already obtained. For this, we only require $U(0,\tilde{Y})$.

$$U(0,\tilde{Y}) \sim e^{-\frac{1}{4}\tilde{Y}^2}\tilde{Y}^{-\frac{1}{2}}\left\{1 - \frac{3}{8\tilde{Y}^2} + \ldots\right\} \text{ as } \tilde{Y} \to \infty. \tag{3.104}$$

Integrating (3.104) by parts gives the leading order term of $\int U(0,x)$ to be

$$\int^x U(0,\xi)d\xi \sim -2\tilde{Y}^{-\frac{3}{2}}e^{-\frac{1}{4}\tilde{Y}^2} + \text{const.} \tag{3.105}$$

and we can absorb the constant into the fourth solution of the original ODE (3.100). Note finally, that the parabolic cylinder functions are even functions so $U(0,-\tilde{Y})$ is also a solution. Re-substituting Y from (3.102) gives the final form of the inner solution to be

$$\hat{\eta}(Y) = C_O + C_1 \int^{Y\sqrt{2\sqrt{-\frac{k^2\omega^{**}}{2\bar{\omega}_0\hat{\kappa}}}}} U(0,\xi)d\xi. \tag{3.106}$$

We see that, as is required, the $Y \to \infty$ limit of the inner solution (3.105, 3.106) matches the $y \to y_0$ limit of the outer solution (3.103).

Perhaps it should come as no surprise that we obtain the integrals of parabolic cylinder functions (PCF) in this instance; when two Airy functions merge the resulting function is a PCF so we might expect the merger of two Airy Integrals to produce the integral of a PCF.

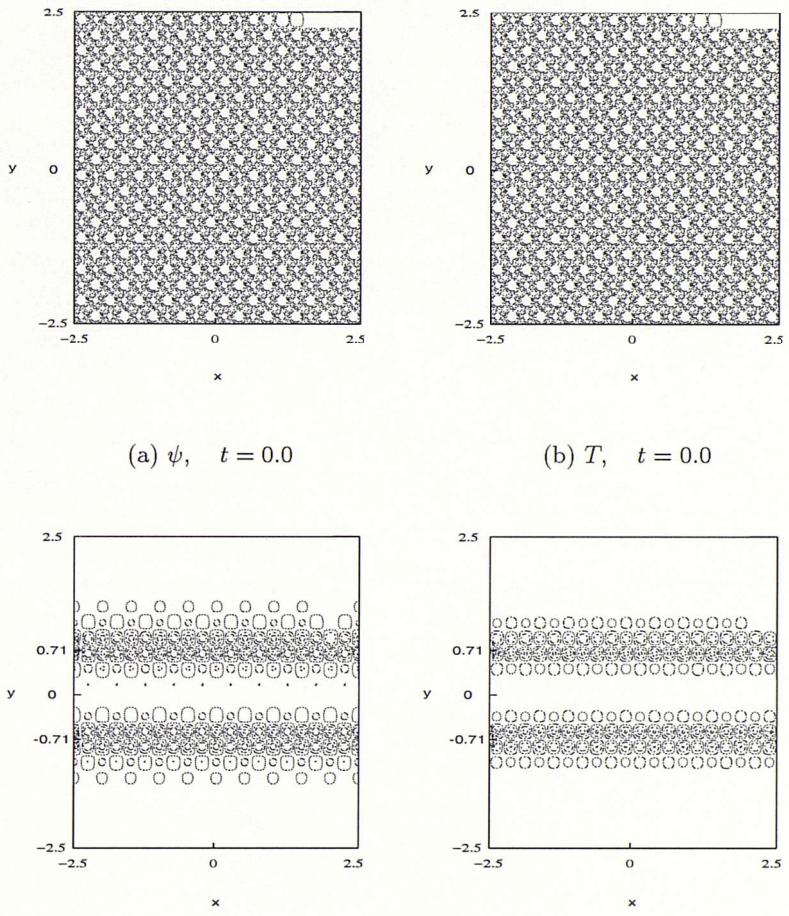
The most important result of the preceding analysis is that a consistent solution can be found to the problem if and only if we account for thermal diffusivity, κ, everywhere. If that is done, then instability is centred on the regions of highest thermal gradient.

Finally, we return to the question of whether we can safely neglect the diffusion of the basic state. The time scale of the instability is $t_I \sim \omega^{-1} = \sqrt{6e} \approx 4$ whereas the diffusive time scale is $t_D \sim \frac{L^2}{\kappa}$. The horizontal length scale, L, is given by the width of the Gaussian strip (3.67) so $t_D \sim \kappa^{-1} \approx 10^5 \gg t_I$. Hence, the diffusion of the basic state is unlikely to have any impact on the development of the instability, particularly in the initial, linear stages.

3.4.5 Numerical simulations

Linear simulations. The time dependent DIT equations (3.2, 3.4) were linearised and then run on a 257×257 grid to obtain the linear growth behaviour. The results of a typical simulation ($k = 4\pi$) are shown in Figure 3.20. This shows the evolution of the disturbance of both temperature, η, and the streamfunction, ϕ. A cross-section of the temperature disturbance is shown in Figure 3.21. Disturbances are initialised everywhere in the periodic domain but by $t = 1$ it is clear that the most unstable region is centred on the two points of inflection of the Gaussian e^{-y^2}. Figure 3.21 reveals that the disturbance is neither odd nor even.

The growth rate of the disturbance can also be obtained from these simulations. The growth rates at various values of the wavenumber k are plotted in Figure 3.22. As predicted by the WKBJ analysis, the growth rate is proportional to the wavenumber. Further simulations (not shown) demonstrate that the growth rate is independent of the value of the temperature diffusion κ. Again, this agrees with the WKBJ analysis. In Figure 3.23



(a) ψ, $t = 0.0$ (b) T, $t = 0.0$

(c) ψ, $t = 1.0$ (d) T, $t = 1.0$

Figure 3.20: Linear simulations of the growth of a small disturbance on a Gaussian temperature anomaly. (a) and (b) are at t = 0.0 to show the initial disturbance pattern. Range of values is (-0.01, 0.01). (c) and (d) are at t = 1.0 which is the largest time for which the simulation can be said to be linear. The disturbance is now centred on $y = \pm 0.71$ as predicted by the linear analysis. Range of values is (-0.25,0.25). (a, c) show the streamfunction, ψ, whereas (b, d) show the temperature, T.

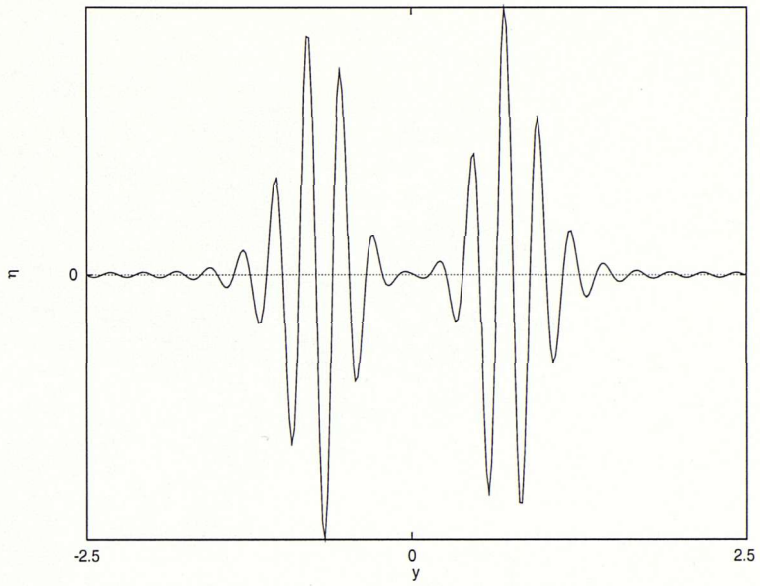


Figure 3.21: Cross-section of the numerically obtained temperature disturbance, $\hat{\eta}$.

the numerically obtained growth rates are compared with the predicted growth rates and the two are shown to be in good agreement. There is a *small* difference between the two rates for small wavenumber but this is to be expected as the WKBJ analysis only applies to large wavenumber disturbances. However the large k asymptotics appear to be valid for a wide range of actual wavenumbers (that is to say, K does not actually have to be particularly large for the asymptotics to give a good estimate of the growth rate). For very small wavenumbers there appears to be a finite cutoff; *very* large wavelengths ($k > 1.5$) are stable.

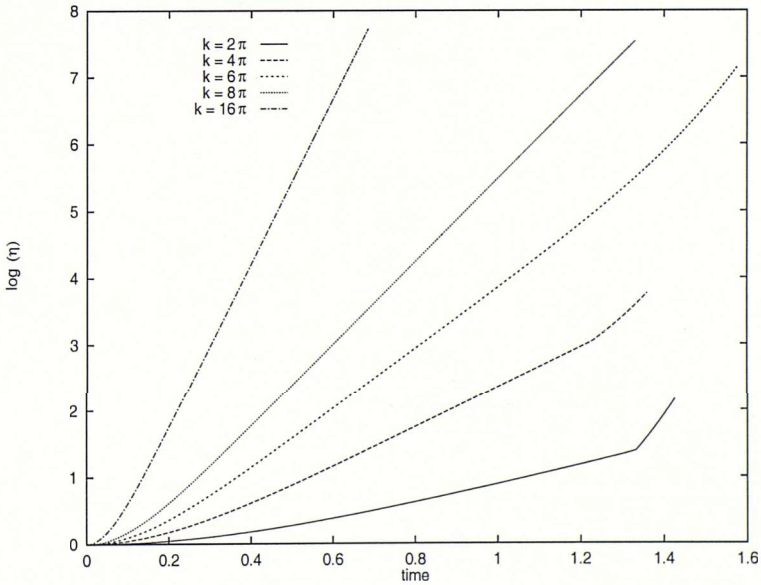


Figure 3.22: Numerical growth rates of linear temperature disturbance at different values of the wavenumber, k ($\hat{\kappa} = 10^{-4}$). $\log(\eta) \sim \omega t$ for linear solutions.

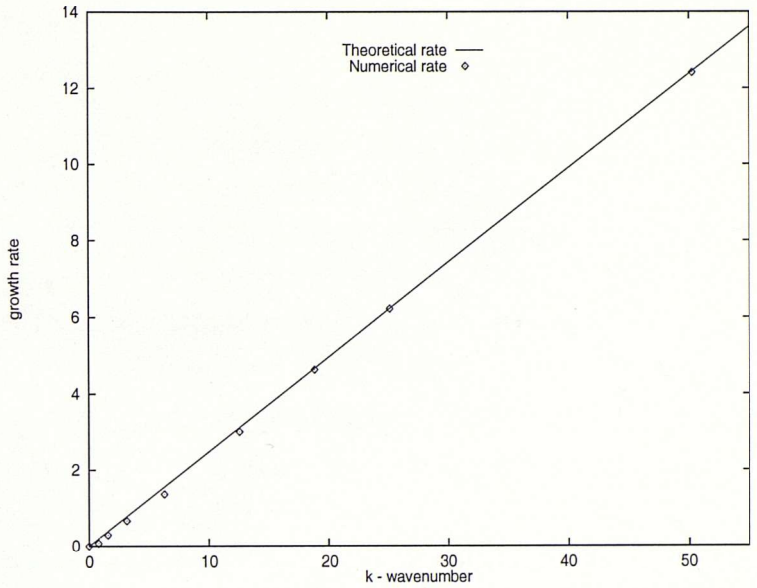


Figure 3.23: Comparison of the linear numerical growth rate with the theoretically predicted growth rate ($\hat{\kappa} = 10^{-4}$). Theory and numerics agree well for large and moderate values of k.

Of course, in reality, the thermal diffusion coefficient κ is independent of the wavenumber k (in the analysis and Figures 3.22, 3.23 $\kappa \sim \frac{1}{k}$). Figure 3.24 shows the numerically obtained growth rates for various *fixed* values of κ and shows, reassuringly, that a large enough diffusion coefficient does indeed inhibit the growth of the high wavenumber modes (that is, fine scales *are* damped). A finite cutoff for small $k < 1.5$ (see also Figure 3.23) is also observed. This is in agreement with the linear-gradient baroclinic analysis of §3.3.1.

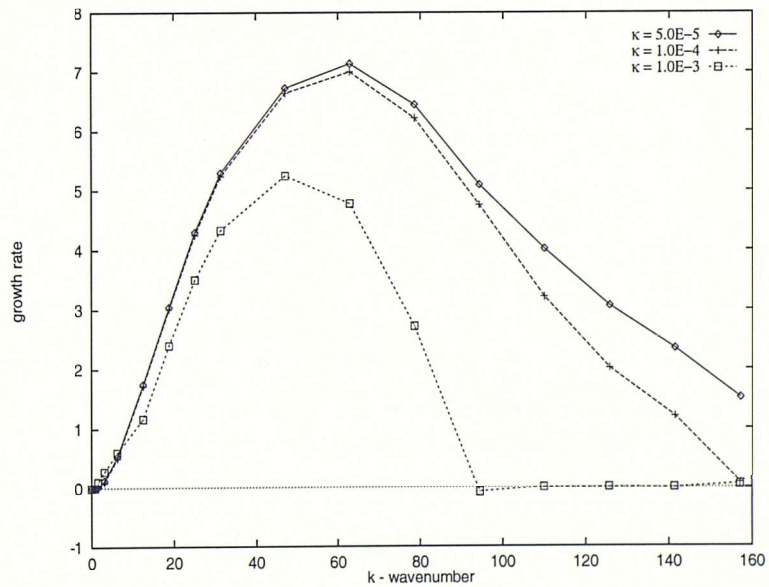


Figure 3.24: Numerical growth rate for fixed κ. A constant, finite value of κ damps the small-scale and very large-scale disturbances.

Nonlinear simulations. The full, nonlinear, time-dependent DIT equations (3.2, 3.4) were run starting from initial conditions corresponding to

$$T = \bar{T} + \text{small normal mode disturbances}, \quad \psi = \text{small normal mode disturbances}$$

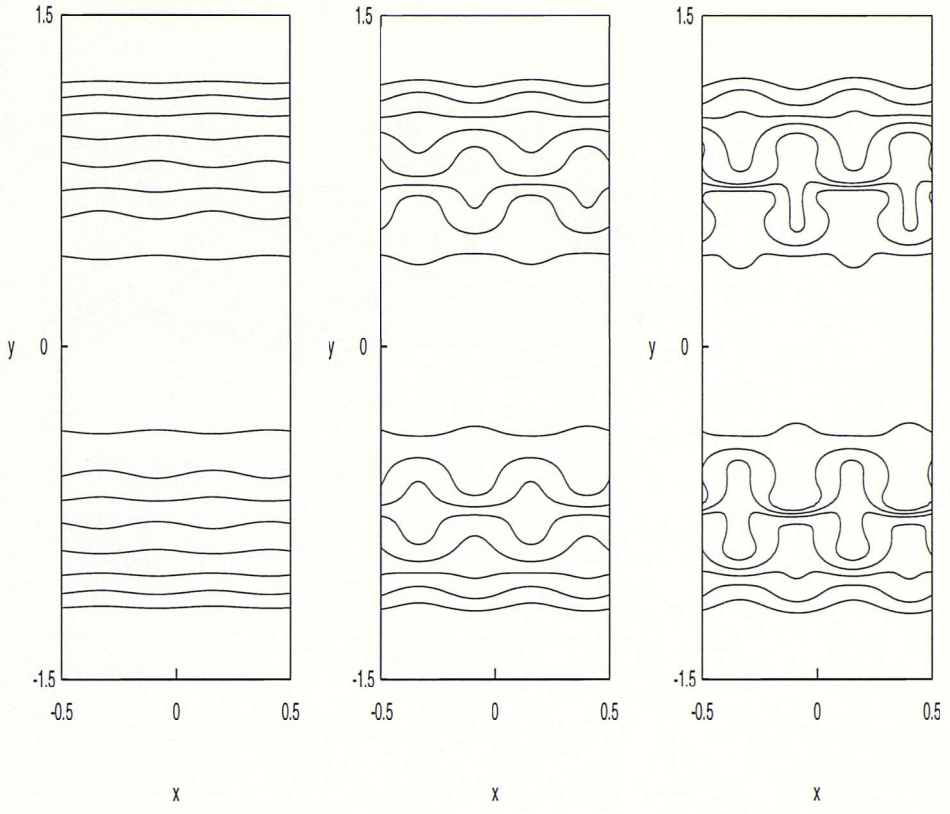
The results of a typical simulation are shown in Figures 3.25 - 3.27. Unlike the linear simulations, these figures show the whole temperature, $\bar{T} + \eta$, not just the disturbance. Snapshots of T are shown at (normalised) times of up to $t = 22.0$. These simulations are initialised from the linearly developed eigenmodes (in this case for $k = 4\pi$). As predicted by the analytics, the fastest growing waves are those with the largest wavenumber and so a lot of fine scale is seen in these nonlinear simulations[11]. Moreover, the nonlinear, secondary instabilities first develop (Figure 3.25(c, d, e) in the neighbourhood in which the thermal gradients are largest.

As in the case of the linear simulations, I also repeated the experiments with different values of thermal diffusion, κ and no discernible difference in the growth rate or qualitative nature of the solution could be observed. Larger κ corresponds to wider regions of instability. This is anticipated by the analysis, in particular, (3.79) in which it is shown that the phase component of the solution, $\eta \sim e^{\frac{1}{\sqrt{\kappa}}}$ in the region of greatest instability. Furthermore, since the numerics seem to confirm the linear analysis, diffusion of the basic state appears to have a negligible influence on the evolution for $\kappa \ll 1$.

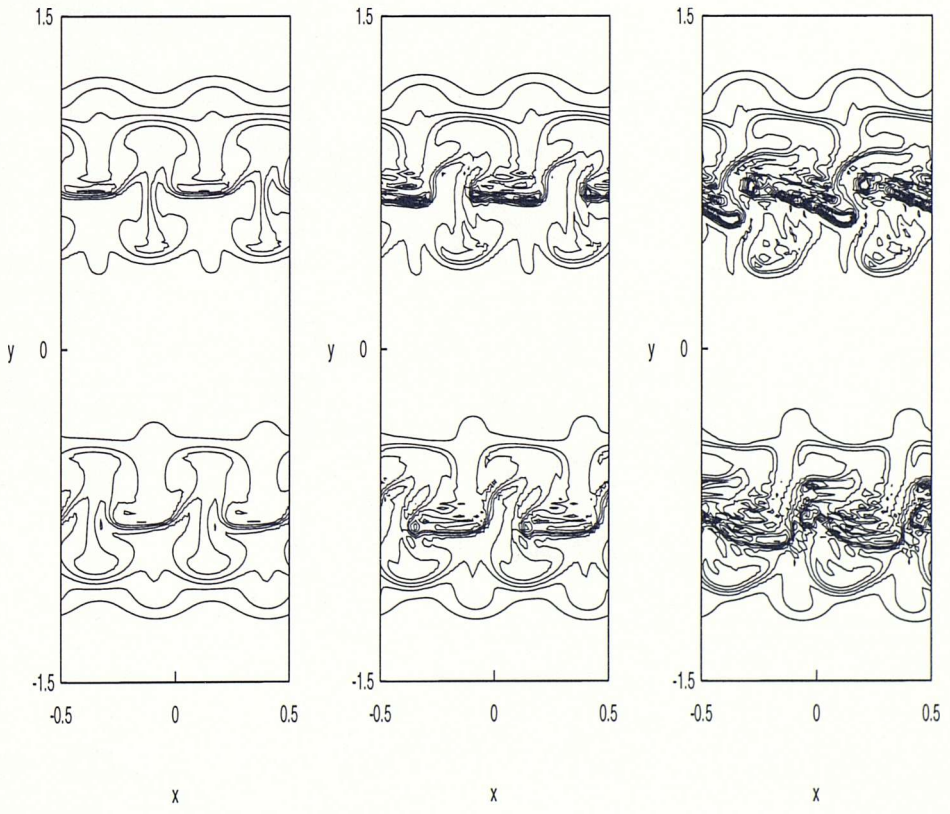
3.4.6 Summary

In §3.4 the baroclinic instability analysis of §3.3 is extended to the case in which the temperature anomaly is localised in its meridional extent. The motivation is that of a warm WBC flowing through a colder ocean. Since the solutions are no longer sinusoidal normal modes, the analysis is much less straightforward than in §3.3. A WKBJ solution for large wavenumbers, k, and small thermal diffusion coefficient, κ, reveals that the disturbance is localised and centred about the region in which the thermal gradients are highest. The instability dies away exponentially on either side. The width of the instability is characterised by κ. Numerical simulations (§3.4.5) confirm these qualitative predictions. The nonlinear simulations show that the formation of plumes similar in nature to those of §3.3.3. Such plumes can be thought of as the first stage in the development of rings (eddies) being shed from a WBC into the surrounding ocean (Figure 1.1).

[11] All the numerics were performed using a 257×257 grid resolution. Although some of the features look very small scale indeed, enlarging the images does appear to show that they *are* resolved by the model. Additionally, energy was conserved and the CFL number was maintained at about 0.1 throughout the simulation and at no point were more than five corrector steps needed at any time step. For more details of the numerics, see B.2.

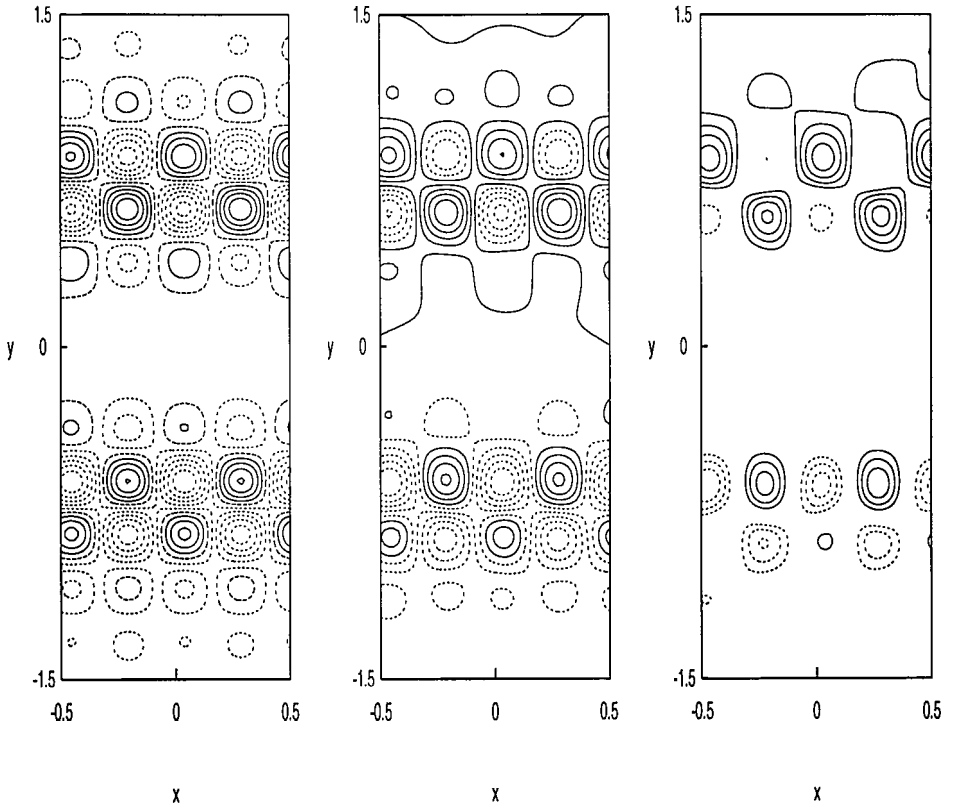


(a) t = 0.0 (b) t = 10.0 (c) t = 15.0

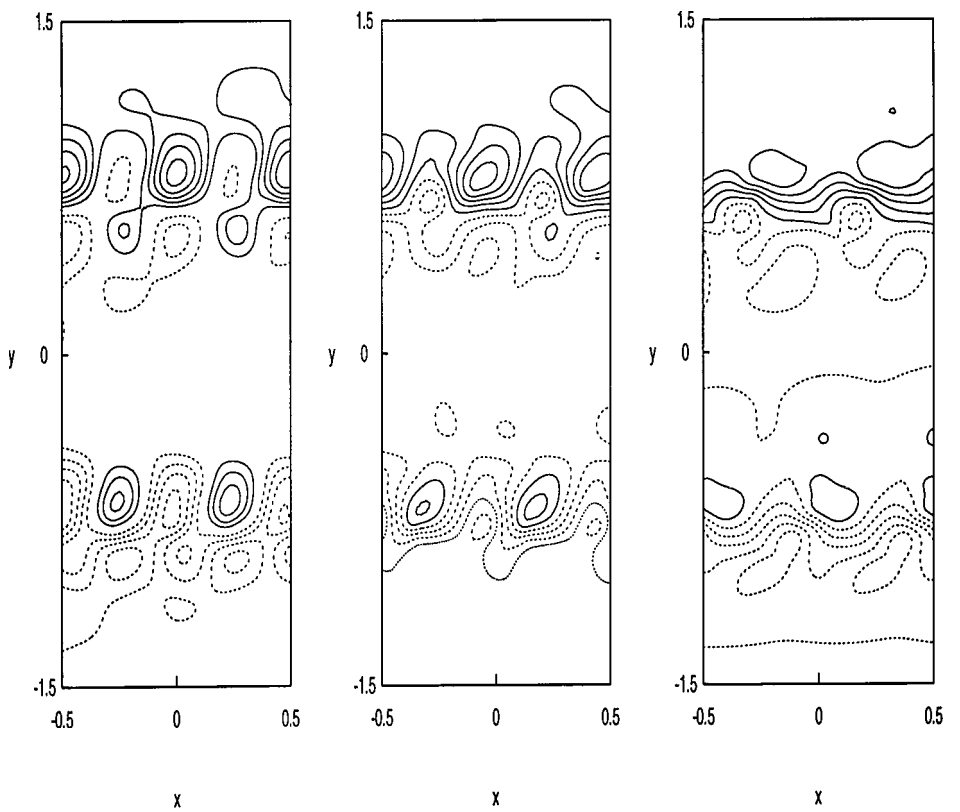


(d) t = 18.0 (e) t = 20.0 (f) t = 22.0

Figure 3.25: Nonlinear evolution of a Gaussian-strip temperature anomaly; T field.

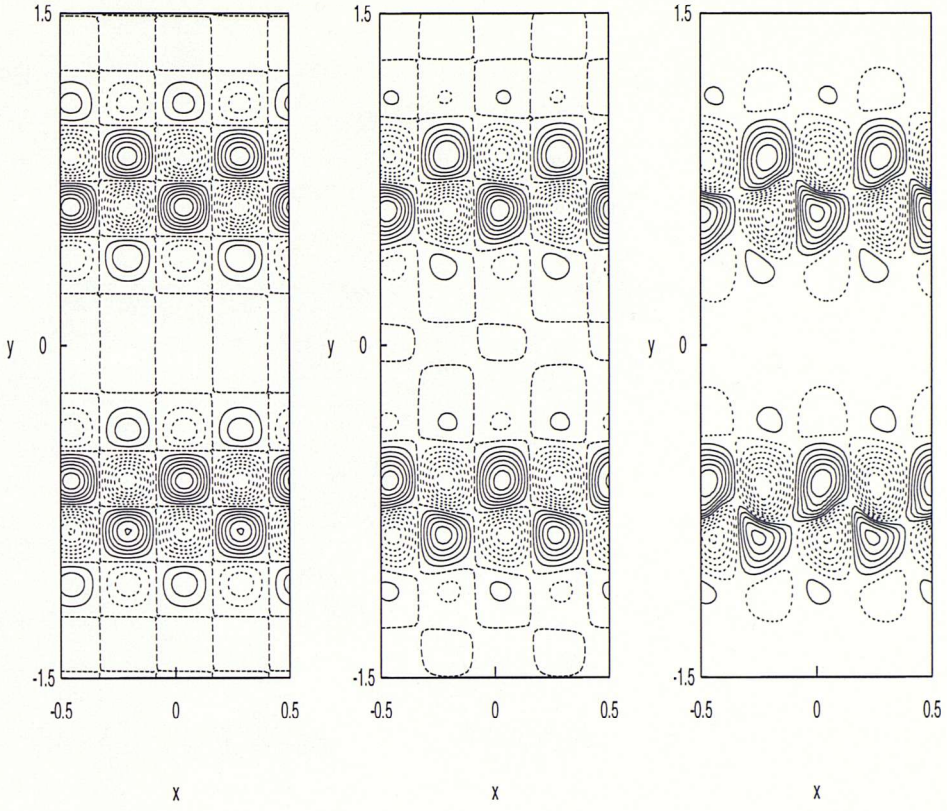


(a) t = 0.0 (b) t = 10.0 (c) t = 15.0

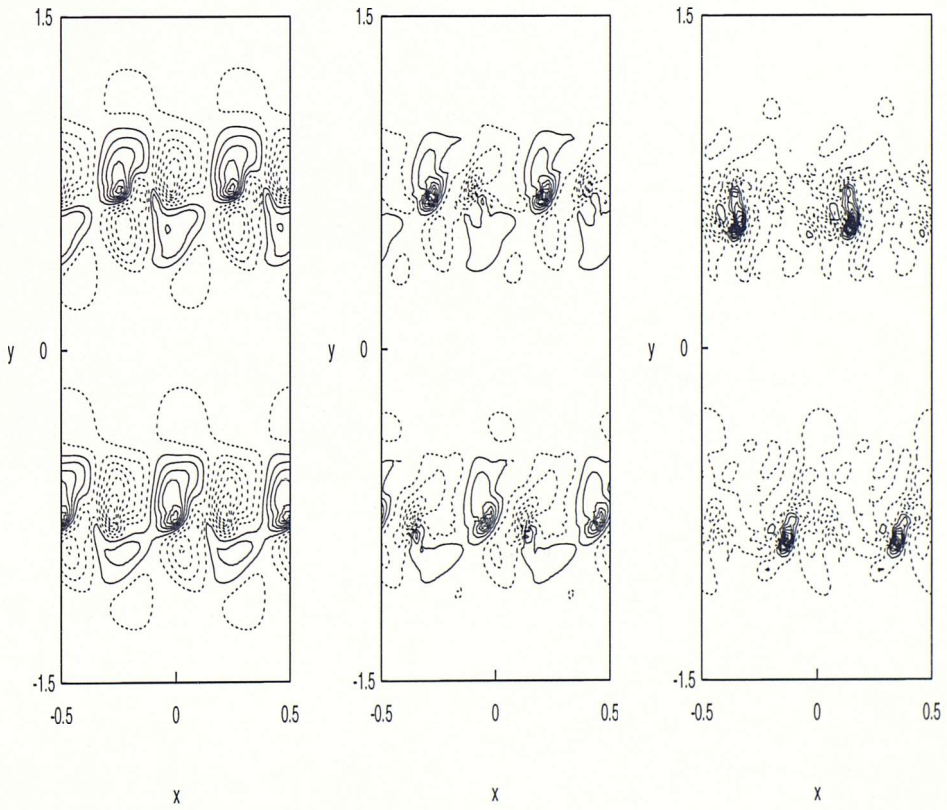


(d) t = 18.0 (e) t = 20.0 (f) t = 22.0

Figure 3.26: Nonlinear evolution of a Gaussian-strip temperature anomaly, ψ field.



(a) t = 0.0 (b) t = 10.0 (c) t = 15.0



(d) t = 18.0 (e) t = 20.0 (f) t = 22.0

Figure 3.27: Nonlinear evolution of a Gaussian-strip temperature anomaly; ζ field.

A disturbing aspect of the analysis is that it predicts that the largest wavenumbers grow most rapidly. This is a consequence of the scaling $\kappa \sim k^{-1}$ which is required for the analysis, but can be relaxed in the numerical experiments which then show, as expected, that a fixed, finite value of κ successfully damps the smaller scales.

3.5 Localised temperature anomalies and turbulence

In a typical study of turbulence in a new system of equations, an understanding of the problem is developed through building up the complexity of the problem from an isolated circular vortex, via pairs of interacting vortices and eventually leading to full turbulence studies (which can be thought of as a very large number of vortices all interacting with each other). In this section, I present such a series of simulations; instead of the fundamental element being a vortex, it is the DIT equivalent, namely a localised (usually elliptical) temperature anomaly (or, in other words, a *patch* of warm or cold water[12]), (3.107).

$$T(x, y, t = 0) = \exp\left(-\frac{(x - x_0)^2}{a^2} - \frac{(y - y_0)^2}{b^2}\right). \tag{3.107}$$

Turbulence is a well studied, although little understood, area of fluid dynamics. Even the definition of *turbulence* is a subject of disagreement. However, most people agree with some of the following characteristics (Salmon[74]): turbulence is associated with vorticity; turbulent flow has complex structure; turbulent flow appears to exhibit a high degree of disorder but coherent structures are often to be found within the flow fields; turbulent flow rapidly mixes passive tracers; turbulence is chaotic and unpredictable.

Despite this unpredictability, many attempts have been made to develop statistical or qualitative models of turbulence which have proved successful in explaining many of its characteristics. Another approach, made possible with the availability of powerful computational resources, has been that of direct simulation. In particular, many studies have been performed looking at whether a particular system displays two-dimensional characteristics (in which the long time vortex field contains well defined structures of a finite scale, see McWilliams[48]) or three-dimensional characteristics (in which everything cascades to smaller and smaller scales). A recent example of such a study is that of Held *et al.*[33] who examine the Surface-Quasi-Geostrophic (SQG) equations. SQG describes three-dimensional QG flow in which the potential vorticity is assumed to be uniform

[12]Localised regions of anomalously warm water have been proposed as a source of energy for hurricanes. The dramatic increase in strength of *Hurricane Brett* on 22^{nd} August 1999 from winds of $75mph$ to over $140mph$ within 24 hours has been attributed to Brett passing directly over a warm eddy shed from currents in the Gulf of Mexico.

throughout the domain. Contrast this with the derivation of the DIT in which the potential vorticity $\frac{f+\epsilon\zeta}{H}\frac{\partial\theta}{\partial z}$ is assumed to be zero, by virtue of the fact that θ is independent of z. Hence, the DIT have a similar relationship with the LSGE to that which SQG have with QG. Moreover, SQG flow is entirely driven by a surface temperature distribution; DIT flows are also driven by T in the initial stages of evolution. SQG, however, requires only one evolution equation for the (surface) temperature and the streamfunction is determined by a three-dimensional Laplace equation. Many of the characteristics of SQG are exposed within [33] via a series of numerical experiments. Briefly, SQG exhibits the generation of secondary instabilities (compare this with the appearance of secondary instabilities in §3.3.3.) and a generic cascade to smaller and smaller scales.

Turbulence within the two-layer quasi-geostrophic system is examined by Salmon[64], [65]. Frontal geostrophic turbulence is the subject of a study by Cushman-Roisin & Tang[21] (for the one-layer shallow-water version) and Tang & Cushman-Roisin[83] (for the two-layer shallow-water version). The frontal geostrophic regime is of interest here (see §2.1) because the main characteristic is that the vertical displacement of isopycnals is large; in order to maintain a small Rossby Number, the length scales must be large in comparison with the internal deformation radius. This is precisely the assumption of the LSGE. The main results of these (and other) studies are that:

- for length scales larger then the deformation radius, baroclinic instability leads to a cascade to small scales.
- the conversion of baroclinic to barotropic energy results in a barotropisation of the flow.
- for small-scale barotropic motions outside the stable regime (that is, of sufficiently large magnitude) the energy cascades towards larger scales until it reaches the *Rhines Scale* ($L_R^3 = \frac{\lambda_{int}^2 f_0}{\beta_0}$). In this section we only consider solid body rotation so $L_R = \infty$.

In the two-layer QG model, Salmon[64] shows that for scales smaller than the deformation radius, there is a cascade to larger scales. This halts the small-scale cascade of the long waves and leads to a well defined equilibrium. However, the DIT model does not include the sub-deformation-radius-scale terms so it must rely upon diffusion to achieve an equilibrium. This is somewhat unsatisfactory, but diffusion *is* included in models in order to parametrise small-scale effects. If the non-conservative DIT are able to reproduce the results of more complicated models in which small-scale effects are explicitly included then this is an argument in favour of their use, especially as a theoretical tool.

This section is the most numerical of the thesis. The aim is to show how isolated anomalies and buoyancy-driven, turbulent flow fields evolve and to gain further insight into generic

characteristics of DIT dynamics. The evolution is compared to barotropic and SQG dynamics and interpreted in terms of the two-layer QG interpretation of the DIT (§3.1.1). The effects of incorporating topography into the model are investigated in §3.6.2.

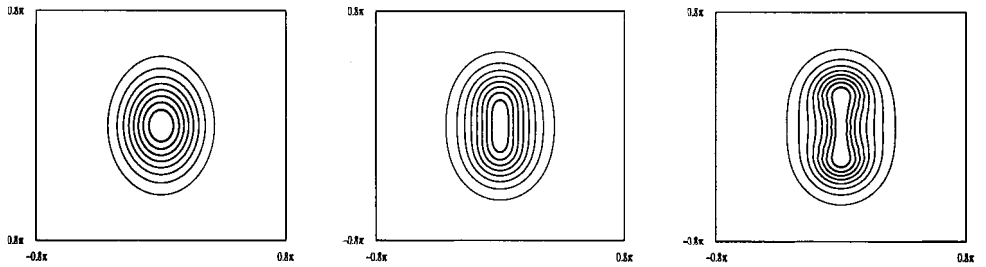
3.5.1 An isolated temperature anomaly

The simplest possible case to consider is an isolated circular anomaly sitting in a quiescent flow field. This is a stationary solution of the DIT because initially $\psi = 0$ and $J(T, \nabla^2 T) = 0$. Consequently, $\frac{\partial T}{\partial t} = \frac{\partial}{\partial t}\nabla^2\psi = 0$.

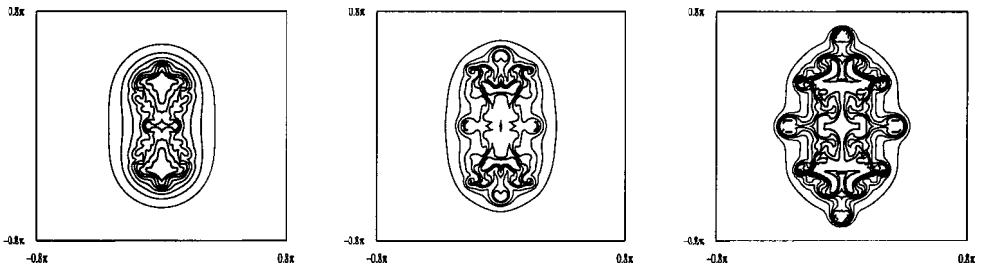
The obvious generalisation of a circular anomaly is an elliptical anomaly. A standard elliptical vortex rotates about its origin and sheds filaments as it settles into a more circular shape (Figure 3 of [33]). There is no sign of any secondary instability. An SQG vortex also rotates and sheds filaments but a small-scale, secondary instability develops on these filaments and the central vortex retains much of its eccentricity (Figure 2 of [33]). The evolution of an elliptical temperature anomaly, on the other hand, is shown in Figures 3.28, 3.29, 3.30.

The behaviour of the temperature anomaly clearly differs from that of an elliptical vortex. The most obvious difference is that there is no rotation. The dynamics are harder to understand than standard vortex dynamics because it is no longer a trivial matter to determine what the streamlines will be induced simply by placing a vortex into a fluid otherwise at rest. If a vortex is placed in a quiescent fluid then (by the definition of a vortex) the streamlines are elliptical and so the vortex rotates. However, if a temperature anomaly is placed into the fiuid, then this sets up barotropic vortex quadrapole (Figures 3.29(a), 3.30(a)) and the initial evolution of the flow can be understood upon consideration of the flow driven by this vortical configuration.

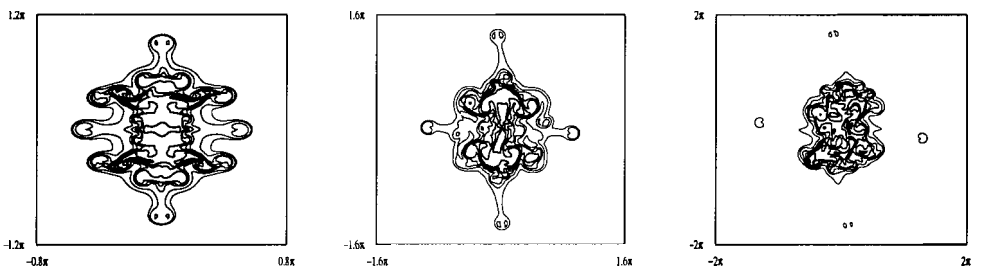
The initial stages of evolution (Figures 3.28(c-f)–3.30(c-f)) show baroclinic instability creating small scales within the structure. This behaviour is similar to the secondary instability observed in SQG. The symmetry of the problem is well preserved for a reasonable length of time. The magnitude of the barotropic streamfunction rapidly increases (particularly between times $3.3 < t < 5.8$) until by $t \approx 10$ the barotropic and baroclinic terms are of equal importance. Eventually (Figure 3.28(j, k)) plume-like structures are observed within the flow. This is reminiscent of the numerical simulations in §3.3.3.



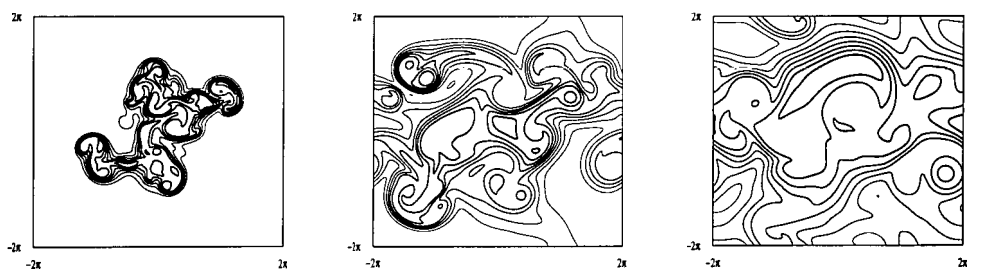
(a) $t = 0.0$,CI=0.125 (b) $t = 3.3$,CI=0.125 (c) $t = 4.6$,CI=0.125



(d) $t = 5.8$,CI=0.125 (e) $t = 6.8$,CI=0.125 (f) $t = 7.6$,CI=0.125

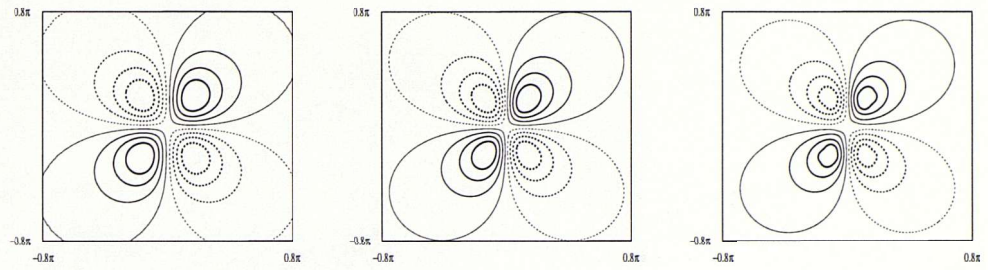


(g) $t = 8.6$,CI=0.125 (h) $t = 10.2$,CI=0.125 (i) $t = 12.6$,CI=0.12

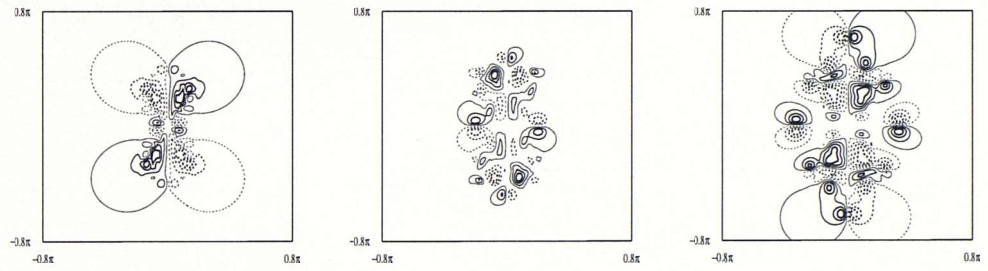


(j) $t = 20.5$,CI=0.10 (k) $t = 63.3$,CI=0.025 (l) $t = 116.4$,CI=0.013

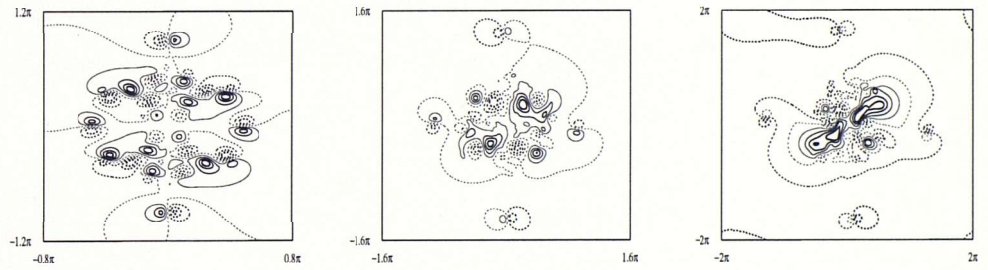
Figure 3.28: Evolution of an isolated elliptical temperature anomaly; T field. $\mathsf{Re}^{-1} = \kappa = 2 \times 10^{-3}$. Note different domain sizes and contour intervals (CI).



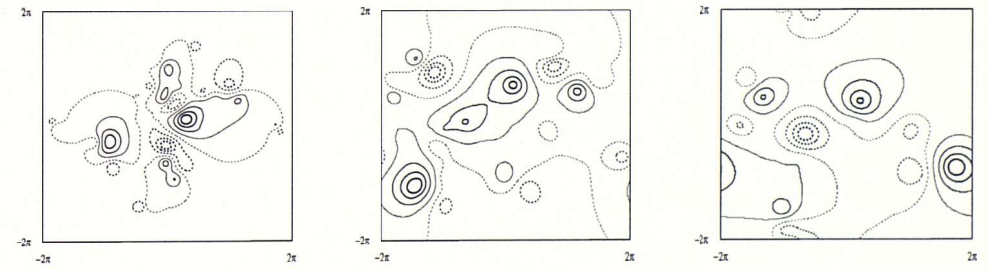
(a) $t = \Delta t$,CI = 0.001 (b) $t = 3.3$,CI = 0.003 (c) $t = 4.6$,CI = 0.006



(d) $t = 5.8$,CI = 0.012 (e) $t = 6.8$,CI = 0.015 (f) $t = 7.6$,CI = 0.018

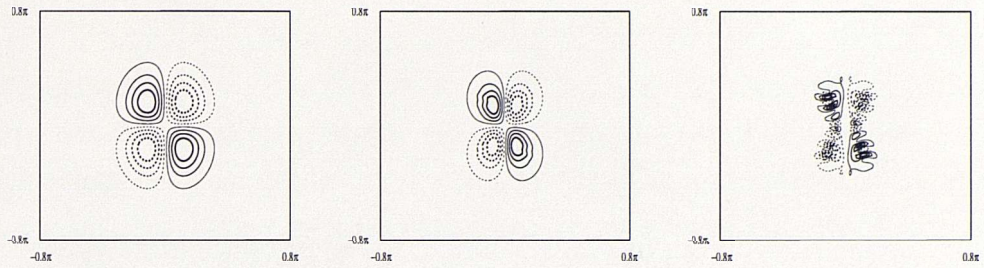


(g) $t = 8.6$,CI = 0.031 (h) $t = 10.2$,CI = 0.058 (i) $t = 12.6$,CI = 0.074

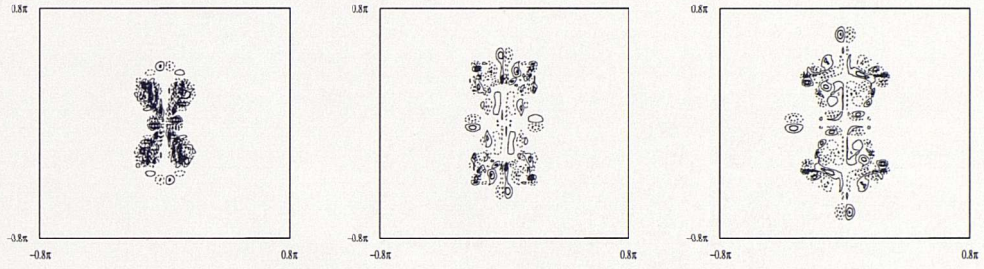


(j) $t = 20.5$,CI = 0.083 (k) $t = 63.3$,CI = 0.078 (l) $t = 116.4$,CI = 0.073

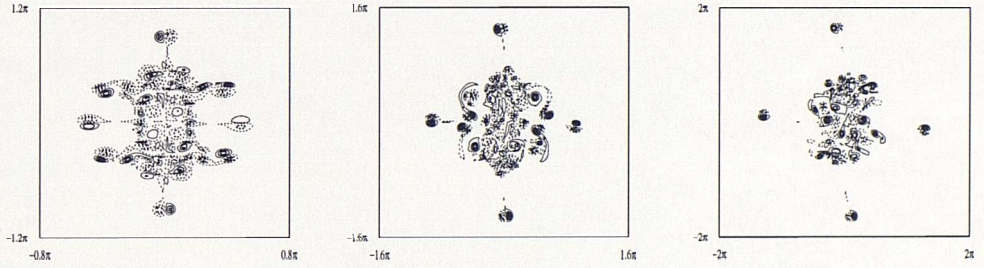
Figure 3.29: Evolution of an isolated elliptical temperature anomaly; ψ field. $\mathsf{Re}^{-1} = \kappa = 2 \times 10^{-3}$. Note different domain sizes and contour intervals (CI).



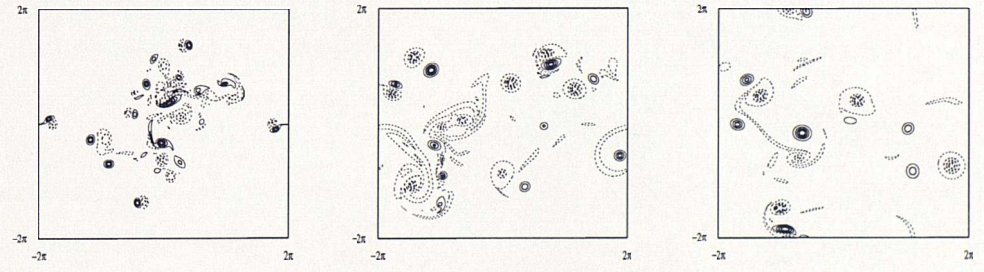
(a) $t = \Delta t$,CI = 0.047 (b) $t = 3.3$,CI = 1.8 (c) $t = 4.6$,CI = 6.9



(d) $t = 5.8$,CI = 7.2 (e) $t = 6.8$,CI = 14 (f) $t = 7.6$,CI = 13



(g) $t = 8.6$,CI = 9.6 (h) $t = 10.2$,CI = 15 (i) $t = 12.6$,CI = 23



(j) $t = 20.5$,CI = 14 (k) $t = 63.3$,CI = 9.6 (l) $t = 116.4$,CI = 5.3

Figure 3.30: Evolution of an isolated elliptical temperature anomaly; ζ field. $\mathsf{Re}^{-1} = \kappa = 2 \times 10^{-3}$. Note different domain sizes and contour intervals (CI).

3.5.2 A pair of temperature anomalies

A useful pedagogical tool in vortex dynamics is the consideration of point vortices. A simple explanation of the difference between two- and three- dimensional turbulence is that in the former, a point vortex produces velocities of order r^{-1} (where r is radial distance form the point vortex) whereas in the latter, a point vortex produces velocities of order r^{-2}. Consequently three-dimensional vortices have a shorter interaction range than two-dimensional vortices. Thus, in three-dimensions, two close vortices will tend to interact (that is, merge or diverge) and will be little affected by anything slightly further away.

The analogous problem in the DIT setup is a point temperature anomaly. However, this initial value problem is ill posed; mathematically because three derivatives of a *Dirac Delta function* are required and physically because, within the two-layer QG framework, an anomaly of dimension zero (or even one) corresponds to a discontinuity in the interface height. A more tractable (and more realistic) situation is an elliptic T anomaly in which $T \sim r^{-1}$. At $t = 0$ the only non-zero term in the DIT (3.2, 3.4) is the $J(T, \nabla^2 T)$ term. This has magnitude of order r^{-6} suggesting a very short interaction range. The conclusion drawn from this scaling is that if two anomalies are placed in a flow a significant distance apart then they will not affect each other. Simulations (not shown) demonstrate this result to be true if the peaks are more than (roughly) $2.5r$ apart where r is the radius at which the strength of the anomaly has fallen to 5% of its peak value. However, there are many factors involved such as the effective Rayleigh Number which have not been fully investigated.

The short r^{-6} interaction range of DIT also suggests that, when temperature anomalies are sufficiently close to interact, this interaction is particularly violent. This is hinted at in Figures 3.28(h, i) in which it appears that the collision has been so violent, four anomalies have been flung away from the centre of the disturbance and form *satellite anomalies*. A similar phenomenon is reported in Held *et al.*[33] for turbulent SQG dynamics.

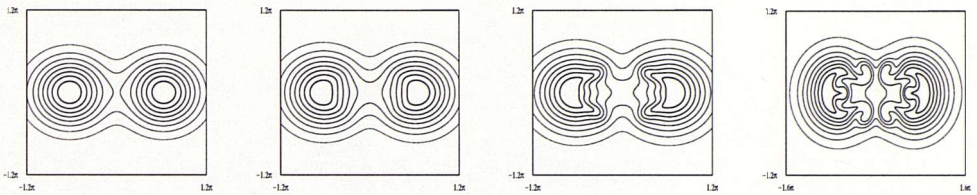
The evolution of two circular anomalies placed close together with their centres separated by $\frac{4}{3}r$ is shown in Figures 3.31-3.33 for the case in which both anomalies have the same sign (positive, PP) and in Figures 3.34-3.36 for the case in which they have have opposing signs (PM). In both simulations the anomalies are placed into quiescent flow (that is, $\psi = \zeta = 0$ at time $t = 0$).

Both dipolar configurations result in the production of a vortex quadrapole (Figures 3.33(a), 3.36(a)). The initial stages of evolution can then be understood in terms of the flow driven by these quadrapoles. In the PP case fluid is drawn from neighbouring zonal regions and pushed laterally. The temperature field is advected by the barotropic flow and

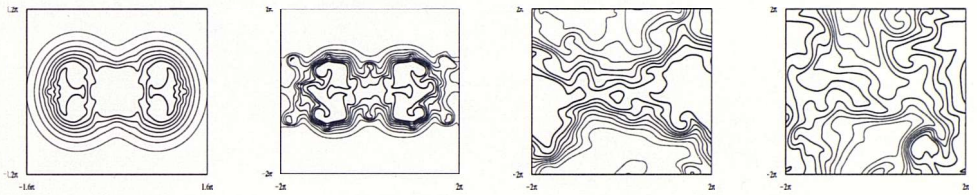
this causes the perceived *implosion* of the anomalies (Figures 3.31(b-e)). Conversely, the quadrapole configuration in the PM case has the opposite effect and the portions of the temperature field closest to the centre of the domain are drawn into attracting proboscides (Figure 3.34(b-e)). This is easily remembered with the phrase *like anomalies repel, opposites attract.* This behaviour is quite unlike classical one-layer dynamics in which like vortices merge together and un-like vortices typically pair up and "elope". However, it is consistent with our intuition (§3.2) that the DIT dynamics act in such a way as to increase thermal gradients.

The PM simulations illustrate two further important features. The short range of interaction is emphasised (as it is also in the PP case) by the fact that only a small proportion (that in which the T isarithms are not radially symmetric) of the T anomalies are affected (at least in the initial stages of development). Additionally, in the PM case when the two proboscides are drawn towards each other, it may seem possible for them to merge and annihilate each other (Figure 3.34(c,d)). In QG terminology, they represent an elevation and a depression in the layer interface and, from a physical standpoint, there is nothing to prevent a merger. Such a merger can occur in the two-layer QG model but the event is presumably controlled by the sub-deformation-radius terms. The thermal diffusion of the DIT, which is parametrising such fine-scale terms, acts in a similar manner, attempting to effect the merger. However, as in §3.3, if the thermal gradients are large enough, then thermal diffusion is insufficiently strong to maintain a steady flow. Consequently, the two proboscides are twisted around each other by advection. This process breaks the symmetry thus far retained and leads to baroclinic instability. The PP symmetry is preserved for a longer period.

The eventual fate of both the PP and the PM configurations is similar. The break in symmetry leads to instability and all the original structure is lost. Small vortex pairs radiate energy away from the centre of the domain (Figures 3.33,3.36(f-h)) and disrupt the radial symmetry of the T field (Figures 3.31(f-h), 3.34(f-h)).

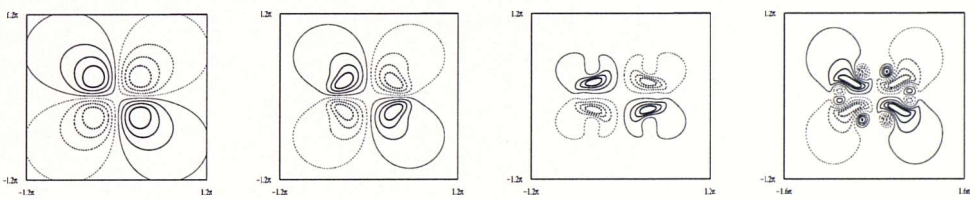


(a) t = 0.0,CI = 0.13 (b) t = 5.0,CI = 0.13 (c) t = 8.0,CI = 0.13 (d) t = 11.0,CI = 0.13

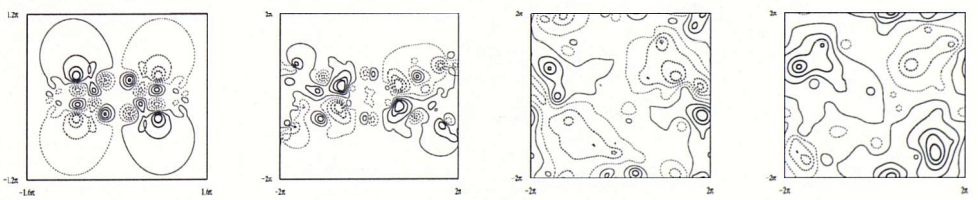


(e) t = 15.0,CI = 0.11 (f) t = 31.0,CI = 0.10 (g) t = 66.0,CI = 0.08 (h) t = 100.0,CI = 0.05

Figure 3.31: Evolution of a pair of positive circular temperature anomalies (PP); T field. $\mathsf{Re}^{-1} = \kappa = 2 \times 10^{-3}$. Note different domain sizes and contour intervals (CI).

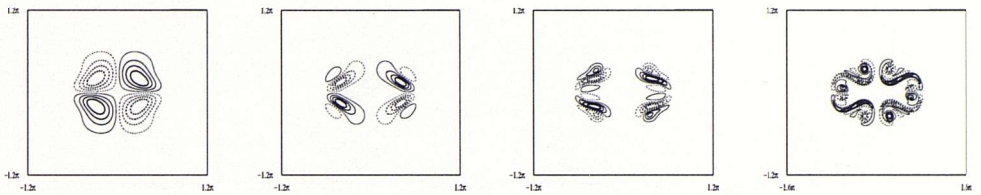


(a) $t = \Delta t$,CI = 0.001 (b) t = 5.0,CI = 0.003 (c) t = 8.0,CI = 0.009 (d) t = 11.0,CI = 0.014

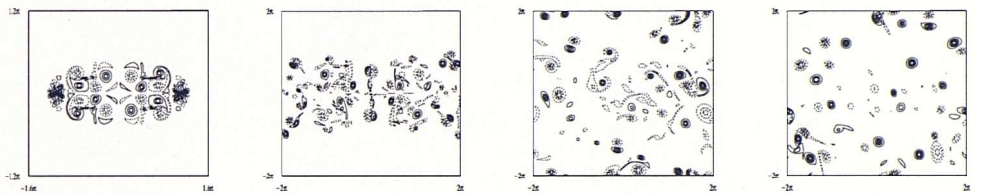


(e) t = 15.0,CI = 0.026 (f) t = 31.0,CI = 0.04 (g) t = 66.0,CI = 0.04 (h) t = 100.0,CI = 0.04

Figure 3.32: Evolution of a pair of positive circular temperature anomalies (PP); ψ field. $\mathsf{Re}^{-1} = \kappa = 2 \times 10^{-3}$. Note different domain sizes and contour intervals (CI).

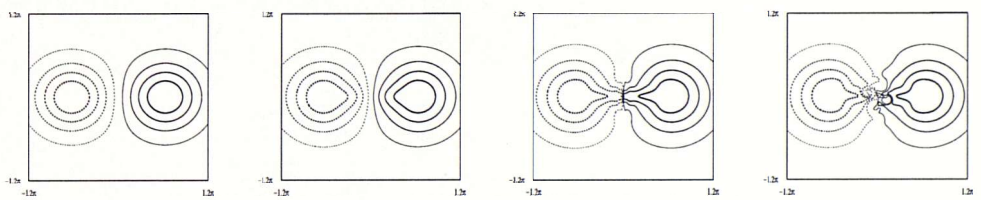


(a) $t = \Delta t$,CI = 0.020 (b) $t = 5.0$,CI = 0.15 (c) $t = 8.0$,CI = 1.0 (d) $t = 11.0$,CI = 2.3

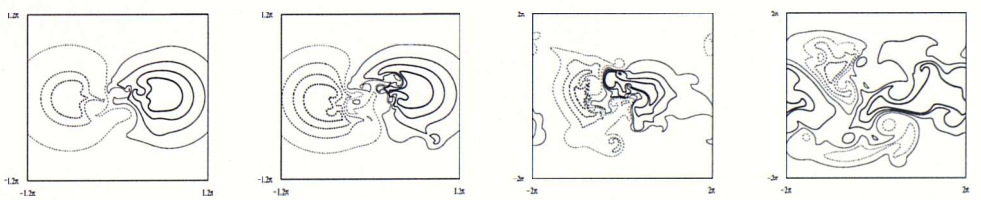


(e) $t = 15.0$,CI = 3.3 (f) $t = 31.0$,CI = 3.0 (g) $t = 66.0$,CI = 1.5 (h) $t = 100.0$,CI = 1.0

Figure 3.33: Evolution of a pair of positive circular temperature anomalies (PP); ζ field. $\mathsf{Re}^{-1} = \kappa = 2 \times 10^{-3}$. Note different domain sizes and contour intervals (CI).

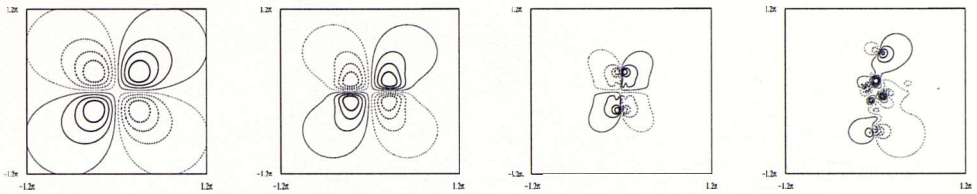


(a) $t = 0.0$,CI = 0.25 (b) $t = 5.0$,CI = 0.25 (c) $t = 7.0$,CI = 0.24 (d) $t = 9.0$,CI = 0.24

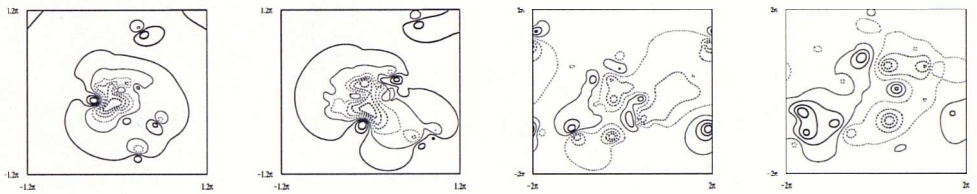


(e) $t = 11.0$,CI = 0.23 (f) $t = 15.0$,CI = 0.22 (g) $t = 30.0$,CI = 0.13 (h) $t = 68.0$,CI = 0.10

Figure 3.34: Evolution of a pair of circular temperature anomalies of opposite sign (PM); T field. $\mathsf{Re}^{-1} = \kappa = 2 \times 10^{-3}$. Note different domain sizes and contour intervals (CI).

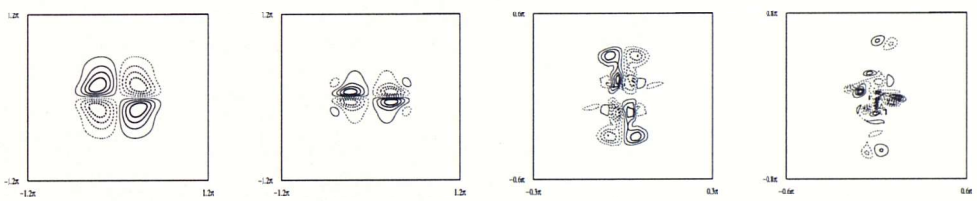


(a) $t = \Delta t$,CI = 0.001 (b) $t = 5.0$,CI = 0.004 (c) $t = 7.0$,CI = 0.034 (d) $t = 9.0$,CI = 0.049

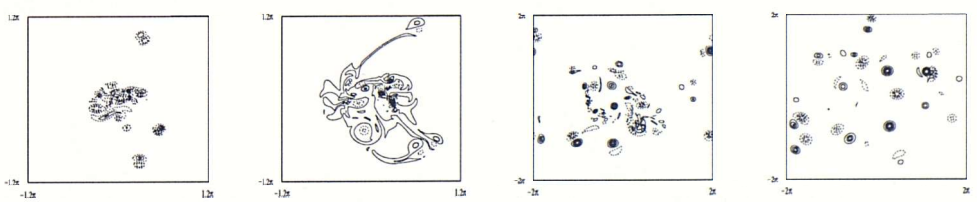


(e) $t = 11.0$,CI = 0.062 (f) $t = 15.0$,CI = 0.076 (g) $t = 30.0$,CI = 0.090 (h) $t = 68.0$,CI = 0.090

Figure 3.35: Evolution of a pair of circular temperature anomalies of opposite sign (PM); ψ field. $\mathsf{Re}^{-1} = \kappa = 2 \times 10^{-3}$. Note different domain sizes and contour intervals (CI).



(a) $t = \Delta t$,CI = 0.023 (b) $t = 5.0$,CI = 0.24 (c) $t = 7.0$,CI = 20 (d) $t = 9.0$,CI = 21



(e) $t = 11.0$,CI = 19 (f) $t = 15.0$,CI = 8.2 (g) $t = 30.0$,CI = 5.14 (h) $t = 68.0$,CI = 5.14

Figure 3.36: Evolution of a pair of circular temperature anomalies of opposite sign (PM); ζ field. $\mathsf{Re}^{-1} = \kappa = 2 \times 10^{-3}$. Note different domain sizes and contour intervals (CI).

3.5.3 Turbulence

Spin down. Many initial studies of turbulence in a new model (for example, McWilliams[48], Tang & Cushman-Roisin[83], Held *et al.*[33]) start from some random initial conditions and simply let the flow evolve. Such a simulation is shown in Figures 3.37-3.39. The initial conditions for this and other similar simulations were constructed as follows:

$$(T, \psi) = \mathbb{R}\left\{\Sigma_{K=1}^{K=N}(T_K(k), \psi_K(K))e^{i\mathbf{k}.\mathbf{x}}\right\} \tag{3.108}$$

where the total wavenumber, $K = |(k, l)|$ is the magnitude of the wavenumber vector. (T_K, ψ_K) is a random amplitude vector. A typical simulation uses

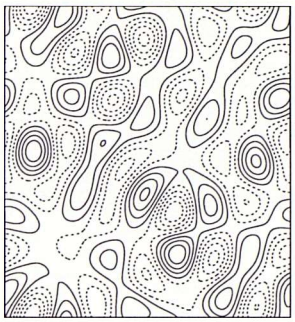
$$(T_K, \psi_K) = (T_0, \psi_0)\frac{1}{(K - K_0)^3}\Phi \tag{3.109}$$

where T_0, ψ_0 and K_0 are prescribed, positive[13] constants and Φ is a sample drawn from the random Gaussian distribution $N(0, 1)$. This results in a smooth spectrum with a peak at $K = K_0$ and which decays like $T_K \sim K^{-3}$ for large K. However, experimentation (not shown) has shown that the precise functional form of the initial distribution of (T, ψ) is unimportant. In particular, the value of K_0 and the exponent in (3.109) have little influence on the qualitative aspects of the evolution or the final state of the simulation. All simulations in this section are performed on a grid of size $[0..2\pi] \times [0..2\pi]$

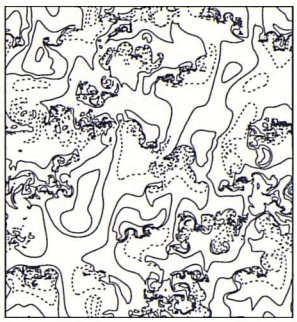
The energy conversions which occur during the simulation are most easily visualised via the barotropic energy time-series, Figure 3.40. Due to the choice of initial conditions (see above), the potential energy vanishes at all times and initially, $\psi = 0$ so the barotropic energy also vanishes. During the early stage of evolution, baroclinic instability causes small scales to grow (see Figures 3.37(b, c)-3.39(b, c)). This means that the barotropic fields (ψ, ζ) become non-zero and the barotropic energy grows. As the strength of the barotropic field increases, the strength of the baroclinic field decreases and the flow adopts the characteristics of two-dimensional flow. Specifically, the direction of the cascade reverses, and the ψ field develops progressively larger scales (Figure 3.38(c, d, e)). The baroclinic temperature field is reduced to the role of a passive tracer and is simply advected around by the barotropic flow. The vorticity field evolves in a typical barotropic manner ([48]). Note that the location of the vortices in Figure 3.39(f) coincides with the location of the temperature anomalies in Figure 3.37(f). This is indicative of the passive nature of T at later times ([46]). Since there is no β effect to arrest the cascade towards larger scales, the ultimate length scales of the barotropic fields (Figures 3.38(f), 3.39(f)) are determined by the domain width.

In the flat-bottomed, solid-body-rotation case under consideration, the only baroclinic feedback on the barotropic flow is given by $J(T, \nabla^2 T)$. The importance of this baroclinic

[13] ψ_0 is allowed to take the value 0.



(a) $t = 0$,CI $= 0.25$



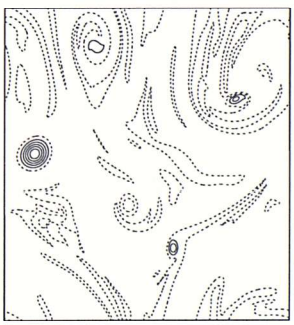
(b) $t = 4.8$,CI $= 0.20$



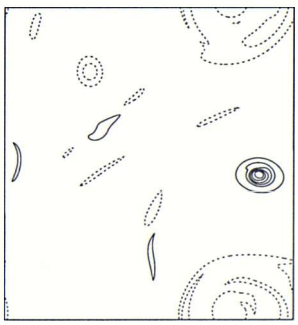
(c) $t = 12.2$,CI $= 0.15$



(d) $t = 30.9$,CI $= 0.10$

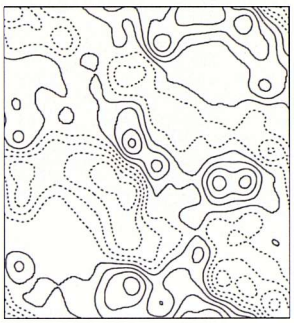


(e) $t = 57.0$,CI $= 0.05$

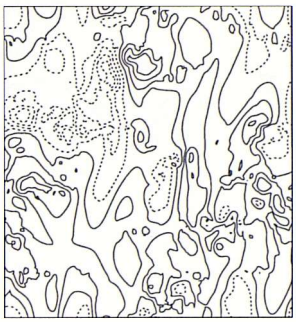


(f) $t = 76.8$,CI $= 0.03$

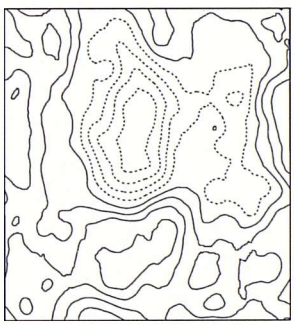
Figure 3.37: Un-forced evolution of a turbulent flow; T field. Note different contour intervals (CI).



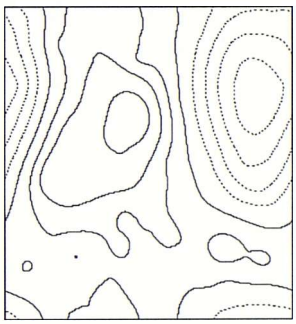
(a) $t = \Delta t$,CI = 0.001



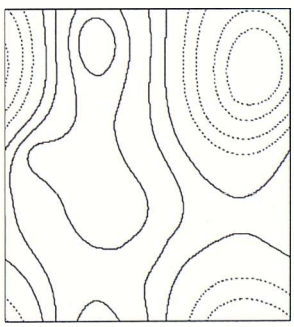
(b) $t = 4.8$,CI = 0.004



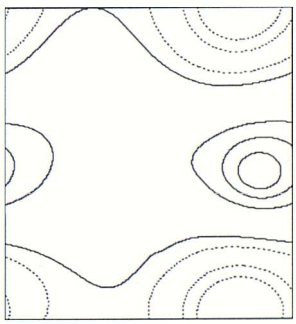
(c) $t = 12.2$,CI = 0.07



(d) $t = 30.9$,CI = 0.075

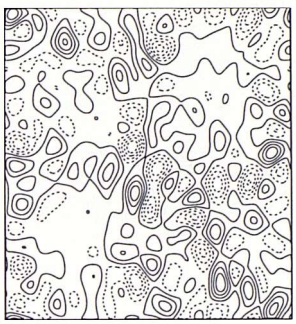


(e) $t = 57.0$,CI = 0.07

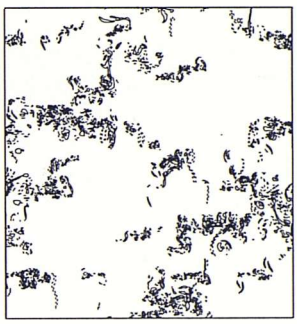


(f) $t = 76.8$,CI = 0.07

Figure 3.38: Un-forced evolution of a turbulent flow; ψ field. Note different contour intervals (CI).



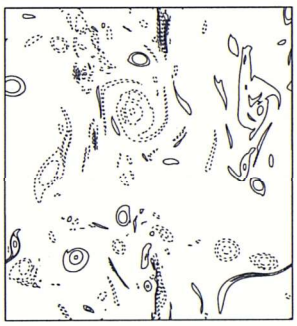
(a) $t = \Delta t$,CI = 0.023



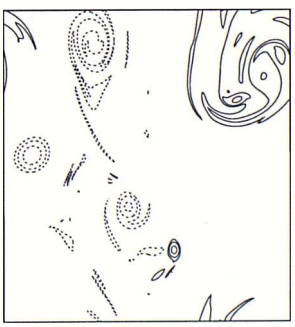
(b) $t = 4.8$,CI = 8.2



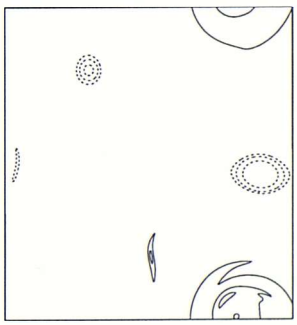
(c) $t = 12.2$,CI = 12.1



(d) $t = 30.9$,CI = 5.0



(e) $t = 57.0$,CI = 1.0



(f) $t = 76.8$,CI = 1.0

Figure 3.39: Un-forced evolution of a turbulent flow; ζ field. Note different contour intervals (CI).

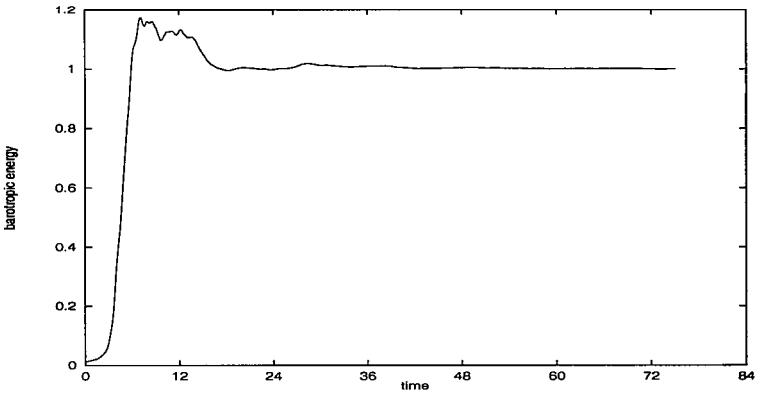


Figure 3.40: Barotropic kinetic energy time series for turbulent spin down experiment. The rapid initial increase is due to baroclinic instability.

term in the turbulence simulations is shown in Figure 3.41. Initially, there is a rapid increase in $\nabla^2 T$ as baroclinic instability initiates rapid growth in the small scales. This obviously results in the Jacobian feedback term increasing in influence. However, at later times, the trend is reversed. The baroclinic field loses all its energy to the barotropic field and so $\nabla^2 T$, and hence $J(T, \nabla^2 T)$, wane. Notice that the Jacobian decays more rapidly than does $\nabla^2 T$. This is a result of the stirring by the barotropic flow which strains the temperature field into long, thin strands. Some of these strands roll up to form the coherent, vortex-like, radially symmetric eddies. We have earlier noted that if T is exactly radially symmetric then isopleths of $\nabla^2 T$ and of T coincide and so the Jacobian vanishes. This also happens when T is considered to be one-dimensional (that is, long thin strands). Thus, as a result of *both* the reduction in strength of the baroclinic field *and* the nature of the structures left behind, the influence of the baroclinicity rapidly declines and the flow becomes barotropic.

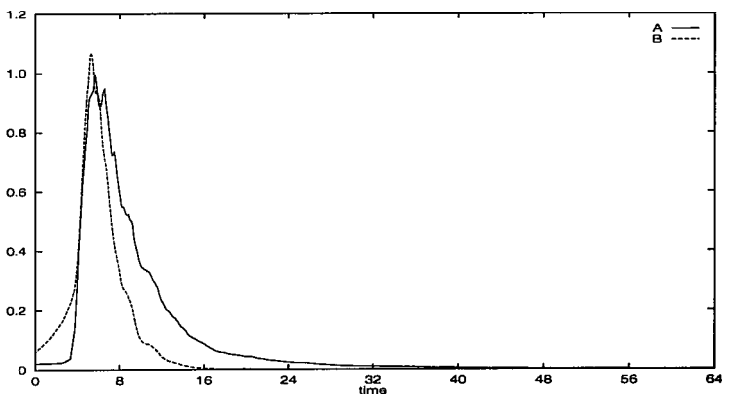


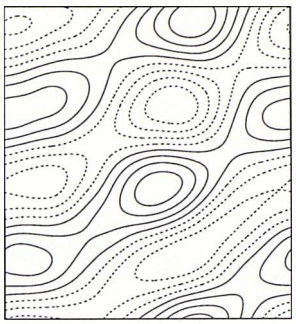
Figure 3.41: Time series of (A, solid line) $\nabla^2 T$; (B, dashed line) $J(T, \nabla^2 T)$ for turbulent spin down experiment (suitably scaled).

The value of thermal diffusion in this simulation is not particularly small: $\kappa = 10^{-2}$. This is necessary because if κ is insufficiently large, baroclinic instability occurs on even smaller

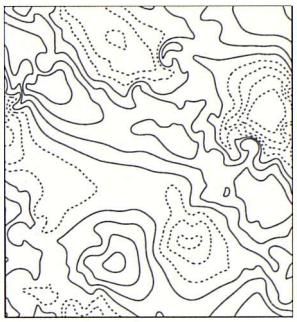
scales than in Figure 3.37(b,c) (see §3.3). It is important to prevent instabilities occurring on an un-resolvable, sub-grid scales. However, this results in the T field dissipating relatively rapidly for a turbulence simulation. This phenomenon is one drawback of the DIT for use in numerical simulations. In practice, the problem is not great because in the ocean basin simulations of §4.2 external thermal forcing attempts to relax the temperature field to a prescribed value.

Spin up. The DIT revert to standard barotropic two-dimensional behaviour because the temperature field, as it cascades to small scales, becomes too weak to have any appreciable effect and that which is left is configured in such a way that the baroclinic feedback term vanishes. However, it is perhaps more realistic to assume that there is some external, large-scale force to "top up" the temperature. In the ocean, surface heating by the sun has precisely this effect. We now examine the case in which both the temperature and the vorticity fields initially vanish everywhere. The flow is forced by a turbulent heating term, $\mathsf{Q}(x, y)$. At any instant of time, Q is generated by a formula similar to (3.108) but at any fixed location, the time-series of Q is white-noise (see Saravanan & McWilliams[77]). Heating of the ocean by the sun occurs on a planetary scale which is therefore characterised by a very low wavenumber. Hence, in these simulations, Q contains only modes $K = 1...8$. That is, $N = 8$ in (3.108) ([77] suggests the use of only one spatial scale). The evolution of the flow is shown in Figures 3.42-3.44.

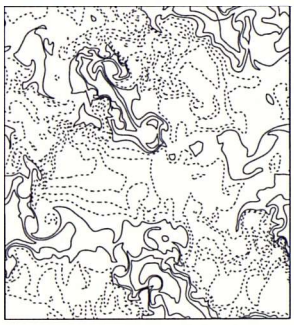
Initially (Figure 3.42(a)), the magnitudes of all fields are small so the dynamics are completely determined by the $O(1)$ thermal forcing. Eventually, by $t = 40$, the strength of the temperature field increases to the point at which baroclinic instability is triggered (Figure 3.42(b)). This is shown clearly by the dramatic increase in $J(T, \nabla^2 T)$ in Figure 3.5.3. Baroclinic instability dominates thermal forcing for a period (Figures 3.42(c)–3.44(c)) and the flow evolves similarly to the un-forced simulation (Figures 3.37-3.39). The difference between the un-forced and forced cases lies in the long-term behaviour. In the latter instance, thermal forcing is continually feeding energy into the low wavenumber baroclinic modes. Consequently, there is a constant source of available potential energy for the baroclinic instability. Hence, the baroclinic flow is not diminished as drastically as in the un-forced case. Since barotropisation is less complete, the cascade back to low wavenumbers is less striking; baroclinic instability continues to produce fine-scale barotropic structure. This can be seen by observing that there are many small vortices in the present case (Figure 3.44(f)) whereas there are fewer, but larger, vortices in the freely evolving case (Figure 3.39(f)). Comparison of Figures 3.42(f), 3.44(f) demonstrates, because of the lack of correlation, that T is not simply a passive tracer. This is also demonstrated by the non-zero equilibrium valus of $\nabla^2 T$ and $J(T, \nabla^2 T)$ in Figure 3.5.3.



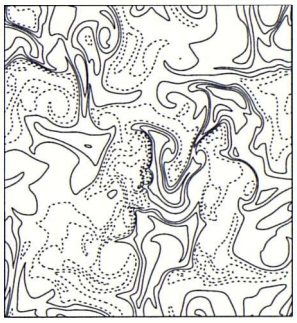
(a) $t = 2$,CI $= 0.03$



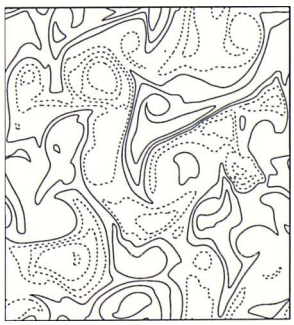
(b) $t = 43$,CI $= 0.07$



(c) $t = 60$,CI $= 0.1$



(d) $t = 80$,CI $= 0.05$



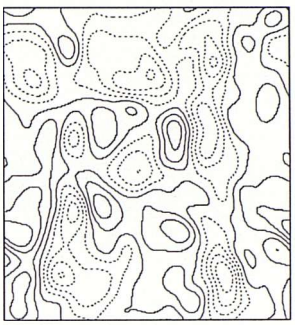
(e) $t = 100$,CI $= 0.05$



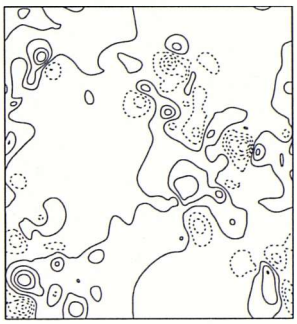
(f) $t = 120$,CI $= 0.05$

Figure 3.42: Evolution of a turbulently forced flow; T field. Note different contour intervals (CI).

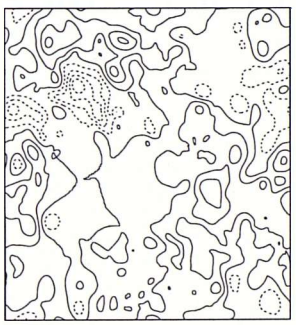
It is clear that thermal forcing has a big impact on DIT dynamics. It prevents the barotropic field from dominating. Notice that, towards the end of the simulation, the



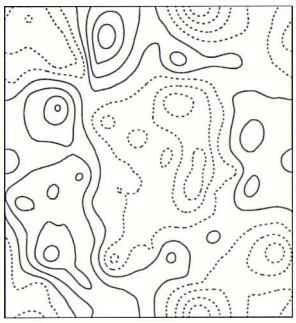
(a) $t = 2$,CI $= 0.00005$



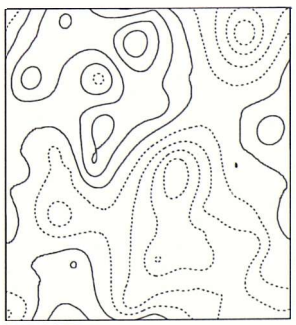
(b) $t = 43$,CI $= 0.01$



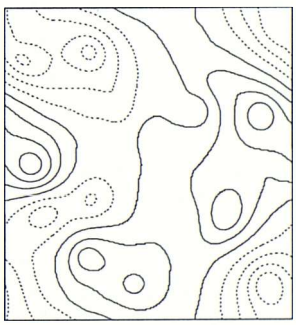
(c) $t = 60$,CI $= 0.07$



(d) $t = 80$,CI $= 0.1$

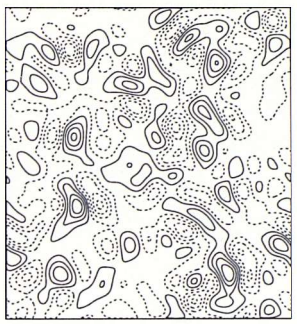


(e) $t = 100$,CI $= 0.1$

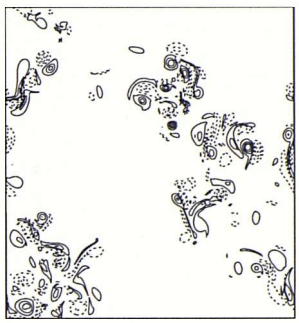


(f) $t = 120$,CI $= 0.1$

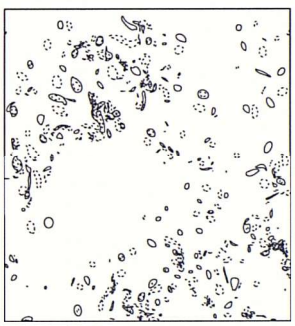
Figure 3.43: Evolution of a turbulently forced flow; ψ field. Note different contour intervals (CI).



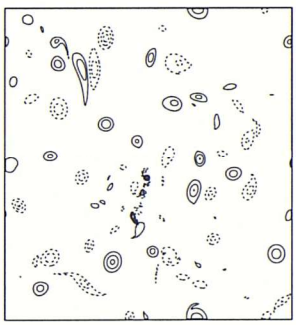
(a) $t = 2$,CI $= 0.0002$



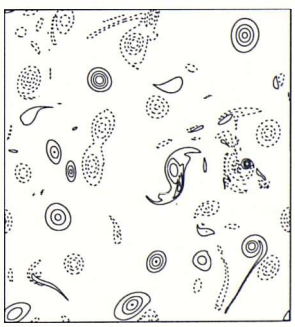
(b) $t = 43$,CI $= 1.8$



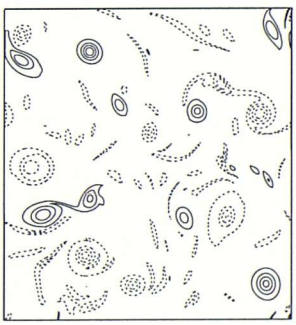
(c) $t = 60$,CI $= 12$



(d) $t = 80$,CI $= 5.3$



(e) $t = 100$,CI $= 2.8$



(f) $t = 120$,CI $= 2.7$

Figure 3.44: Evolution of a turbulently forced flow; ζ field. Note different contour intervals (CI).

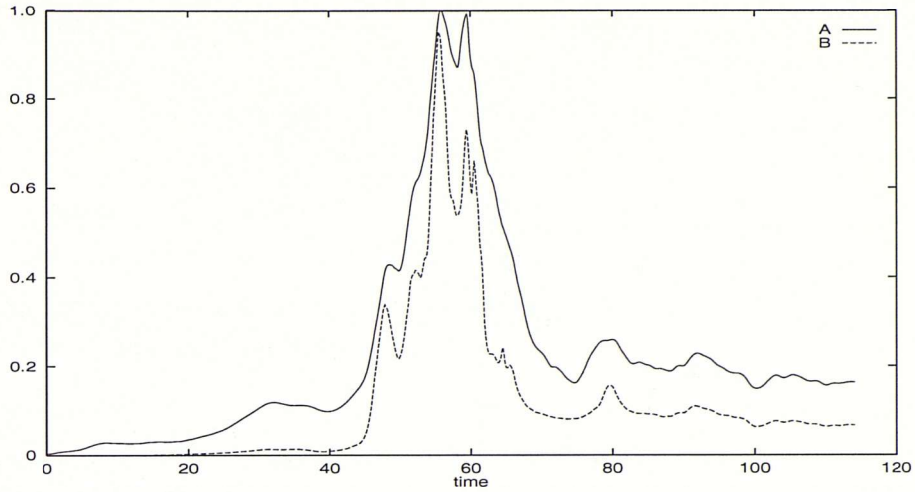


Figure 3.45: Evolution of (A, solid line) $\nabla^2 T$, (B, dashed line) $J(T, \nabla^2 T)$ with an initial condition of vanishing T, ζ but thermally forced by a turbulent Q.

temperature (Figure 3.42) and the streamfunction (Figure 3.43) tend towards equilibrium values of the same order of magnitude. This result motivates a detailed investigation of the thermal forcing, Q, in the ocean basin simulations of §4.2.

3.5.4 Summary

In §3.5 a series of numerical simulations has been presented. The simulations range in complexity from a solitary elliptical thermal anomaly to turbulence. Taken as a whole, the series shows that the interaction range of such anomalies is small. Furthermore, when the flow is buoyancy-driven, the dynamics differ significantly from two-dimensional, barotropic dynamics and a series of secondary instabilities is observed. However, in the absence of any external imposition of a large-scale thermal structure, baroclinic instability causes a cascade to small scales. This converts baroclinic energy to barotropic energy and culminates in the role of the temperature being reduced to that of a passive tracer. The long term behaviour is barotropic. The direction of the cascade then reverses; barotropic flow transfers the energy towards lower wavenumbers. External forcing modifies this behaviour by providing a constant source of large-scale baroclinic energy. This means that the baroclinic feedback term $J(T, \nabla^2 T)$ is important at all times. This behaviour is consistent with theories of two-layer QG and frontal turbulence. The role of thermal diffusivity, κ, to parametrise all sub-deformation-radius-scale terms is highlighted in this section. In the absence of thermal diffusivity, or if $\kappa \ll 1$, then baroclinic instability occurs on the finest scales and no structure is left behind.

3.6 Topography

In this section the effects of topography on the DIT (3.2, 3.4) are considered. The most important difference between this section and §§3.3-3.5 is the retention of the $J(\psi, \frac{1}{H})$ and $J(T, H)$ terms in (3.2). Since we are primarily concerned with buoyancy driven flows, it is the second term which is of more interest to us here. This is the *JEBAR* term; its influence on simple oceanic basin flows is examined in Salmon & Ford[75]. In this section, we consider the effect of *JEBAR* (and the other topographic terms) on the problems of the earlier sections.

In the presence of a variable basin depth, potential energy in the form $-\int zT\mathbf{dx}$, is not conserved by the DIT (see §3.2). As a result, there is a further mechanism for potential energy to be converted into kinetic energy in addition to the *tilting columns* mechanism of §3.2. This is illustrated in Figure 3.46. Potential energy is released by moving, via advection (3.4), warm fluid particles from deep regions of the basin to shallower regions. This is a *JEBAR* related effect; it also applies if inertia is completely neglected.

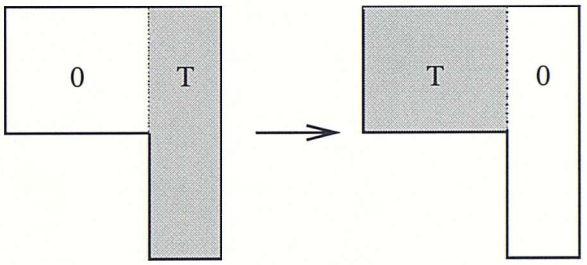


Figure 3.46: $T > 0$. If the initial configuration is such that the warm (shaded) fluid is in deep regions then potential energy $= -\int zTdxdz$ can be released by rearranging the fluid particles so that the warm, buoyant water lies in the shallow regions. This is a source of energy which can feed an instability.

3.6.1 Linear thermal gradient

We return to the simplest possible (non-trivial) thermal structure; that of a linear gradient on an f-plane (§3.3). In the case of a flat bottom (§3.3) all wavenumbers are unstable in the absence of any diffusion. The extra factor here is that of a linearly sloping floor:

$$H = H_0 + H_1 y, \quad T = T_1 y + \hat{\eta}(y)e^{(ikx - i\omega t)}, \quad \psi = \hat{\phi}(y)e^{(ikx - i\omega t)}$$
$$-1 \leq y \leq 1, \quad H_0 > |H_1|, \quad \hat{\eta}, \hat{\phi} \ll 1. \tag{3.110}$$

Substitution of (3.110) into the DIT (3.2, 3.4) and linearising, leads, in the usual way, to a pair of coupled eigenvalue equations for $\hat{\eta}, \hat{\phi}$. After eliminating $\hat{\phi}$ from this pair we are

left with

$$\begin{aligned}\epsilon H\omega^2(H\hat{\eta}'' + H_1\hat{\eta}' - Hk^2\hat{\eta}) - \epsilon H_1\omega^2\hat{\eta} + HH_1\omega k\hat{\eta} - \frac{1}{2}H_1H^2T_1k^2\hat{\eta} \\ + \frac{1}{12}\epsilon H^4T_1^2k^2(\hat{\eta}'' - k^2\hat{\eta}) + \frac{1}{4}\epsilon H^2H_1T_1^2k^2(H\hat{\eta}' - H_1\hat{\eta}) = 0.\end{aligned} \tag{3.111}$$

This can be solved numerically, subject to boundary conditions of no normal flow[14] and no stress at both ends:

$$\hat{\eta} = \hat{\eta}'' = 0 \text{ at } y = \pm 1. \tag{3.112}$$

In order to make progress analytically, we consider the limit of small topographic gradients ($H_1 \ll 1$). There is an additional small parameter because the Rossby Number, $\epsilon \ll 1$. Consequently, we neglect terms of $O(\epsilon H_1, H_1^2)$ in (3.111). This procedure yields

$$\epsilon H_0^2\omega^2\left(\hat{\eta}'' - k^2\hat{\eta}\right) + H_0H_1\omega k\hat{\eta} - \frac{1}{2}H_1T_1k^2\hat{\eta} + \frac{1}{12}\epsilon H_0^4T_1^2k^2(\hat{\eta}'' - k^2\hat{\eta}) = 0. \tag{3.113}$$

It is clear that the solution of (3.113) is given by

$$\hat{\eta}(y) = \mathbb{R}\left[e^{ily}\right], \qquad l = (2n+1)\frac{\pi}{2}. \tag{3.114}$$

Substituting (3.114) into (3.113) gives the dispersion relation

$$\omega = \frac{H_1k \pm k\sqrt{H_1^2 - 4\epsilon K^2\left(\frac{1}{12}\epsilon T_1^2H_0^4K^2 + \frac{1}{2}H_0^2H_1T_1\right)}}{\epsilon H_0K^2} \tag{3.115}$$

where $K^2 = k^2 + l^2$. This relation (3.115) predicts that if the topography is aligned such that the colder water is in the deeper part of the domain ($T_1H_1 < 0$) then it does indeed have a stabilising influence on the flow. However, if the topography is aligned such that the colder water is in the shallower part of the domain ($T_1H_1 > 0$) then (3.115) suggests that there is initially an increase in the growth rate but that after the slope becomes sufficiently steep, the topography again acts to stabilise, rather than destabilise, the flow. Indeed, the maximum growth rate is attained when $H_1 = \epsilon K^2T_1$.

The full eigenvalue problem is solved numerically using the Newton-Raphson relaxation scheme described in B.4. Figure 3.47 shows that for $H_1T_1 < 0$ the growth rate of the instability rapidly decreases from the flat-bottom value. Recall that there is no diffusion in the present case. This confirms the predictions of the linear analysis (3.115) and of the qualitative argument illustrated in Figure 3.46. The instability is completely killed at a moderate value of H_1. The linear analysis predicts that the instability disappears completely at a value of $H_1 = \left(2 - \frac{4}{\sqrt{3}}\right)\epsilon K^2T_1$. Considering the $T_1 = 0.4$ curve, the

[14] $\hat{\phi} = \frac{H\omega}{kT_1}\hat{\eta}$ and no normal flow corresponds to $\frac{\partial\hat{\phi}}{\partial x} = 0$.

cutoff slope in Figure 3.47 is approximately $H_1 = -0.125$. This compares favourably with a predicted cutoff slope of $H_1 = -0.1236....$

Figure 3.48 shows the growth rates for the opposite orientation of the topography. As predicted by the linear analysis, the growth rate increases for small topographic slopes but reaches a maximum and as the slope becomes steeper, the disturbance becomes *less* unstable. Although the numerics agree qualitatively with the analysis, the quantitative agreement is less good. The maximum growth rate predicted by (3.115) should occur at $H_1 = \epsilon K^2 T_1$ and the cutoff at $H_1 = \left(2 + \frac{4}{\sqrt{3}}\right) \epsilon K^2 T_1$. Considering the same $T_1 = 0.4, k = 10$ case again yields values of 0.4 and 1.6 respectively. This is clearly a long way from the numerically obtained values in Figure 3.48. However, if we consider the $T_1 = 0.1, k = 10$ curve, the values are 0.1 and 0.4 respectively. The maximum growth rate (of $H_1 = 0.11$ in Figure 3.48) is thus well predicted. Therefore, it seems that the linear analysis is a good qualitative model in general and a good quantitative model for $H_1 \lesssim 0.1$. This small value is not surprising considering the drastic approximations required to derive (3.115). In particular, we have neglected $O(H_1^2)$ terms while retaining $O(\epsilon)$ terms. Since $\epsilon = 0.01$ in all simulations in this subsection, this is a valid approximation for $H_1 \lesssim 0.1$.

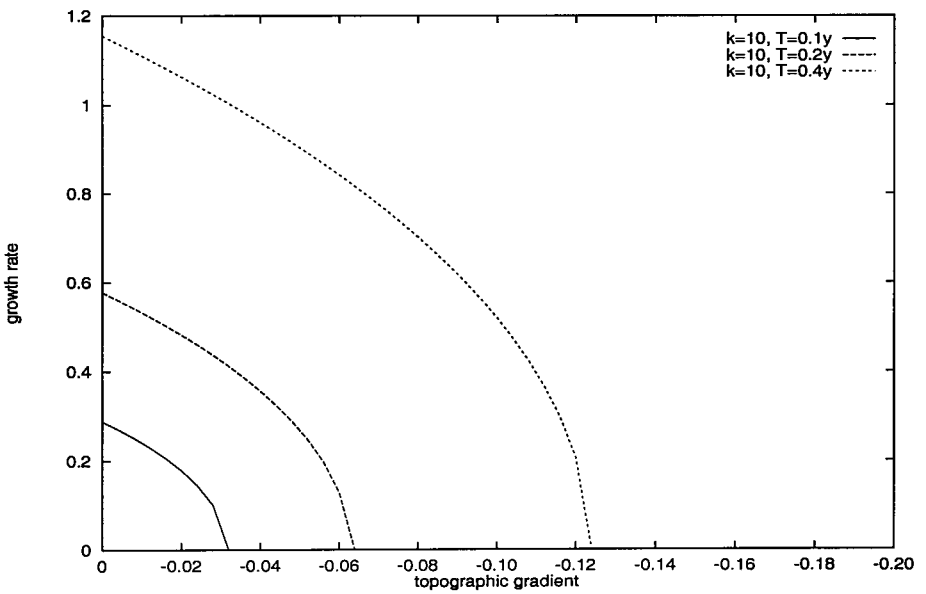


Figure 3.47: Growth rate of instability when $H_1 T_1 < 0$; $\epsilon = 0.01$; $l = 1$.

The dispersion relation for fixed values of H_1 is shown in Figures 3.49, 3.50 for the real and imaginary parts respectively. The qualitative behaviour predicted by the linear (3.115) of $w_{Re} \sim \frac{1}{k}$ and $\omega_{Im} \sim k$ for large k are clearly shown for small topographic gradients. However, the quantitative predictions correlate poorly with the numerics. In the light of earlier comments, this is not unexpected.

Note also that for steeper topographic gradients, the growth rate appears to increase less rapidly than the linear prediction of $w_{Im} \sim k$. However, this is difficult to verify because

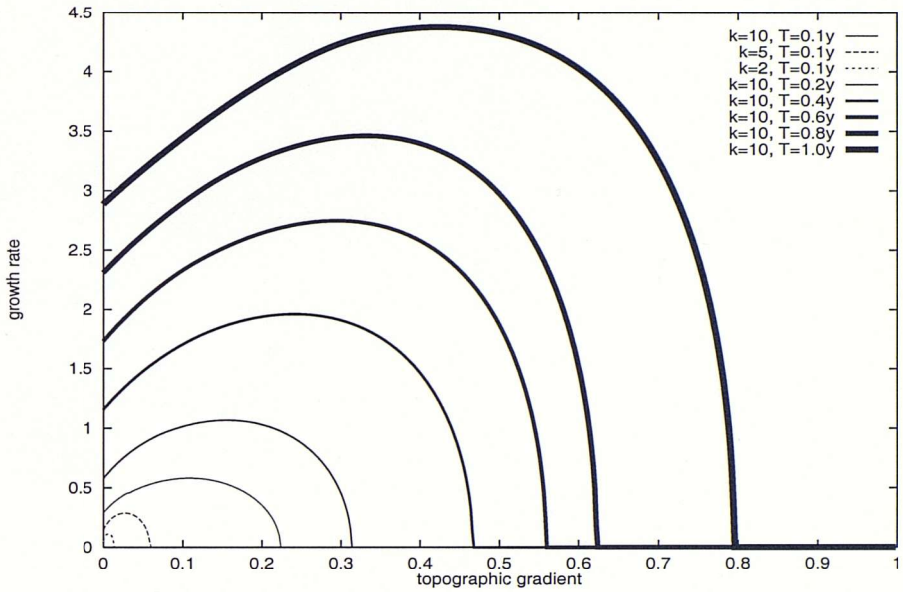


Figure 3.48: Growth rate of instability when $H_1 T_1 > 0$; $\epsilon = 0.01$; $l = 1$.

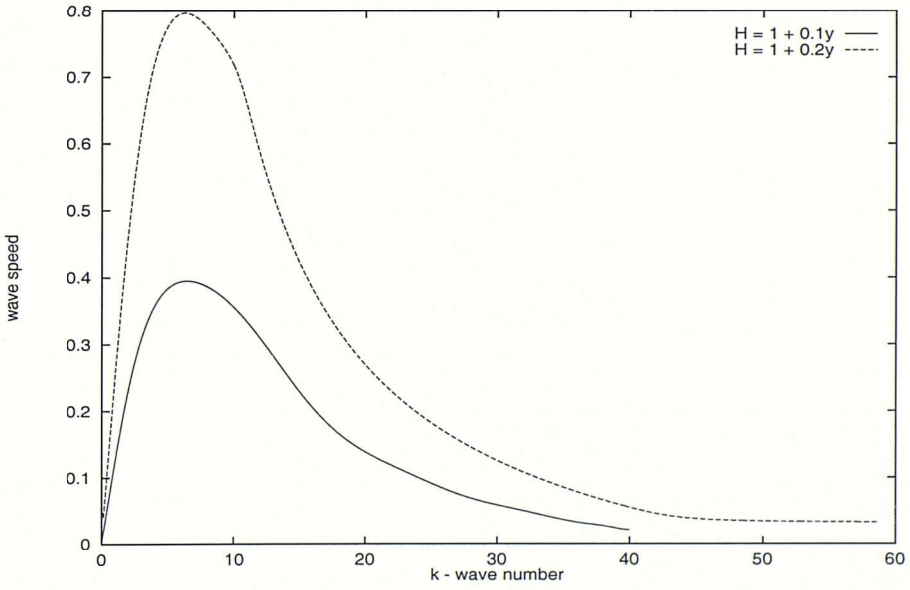


Figure 3.49: Dispersion relation for fixed topographic gradient $\mathbb{R}(\omega)$; $\epsilon = 0.01$.

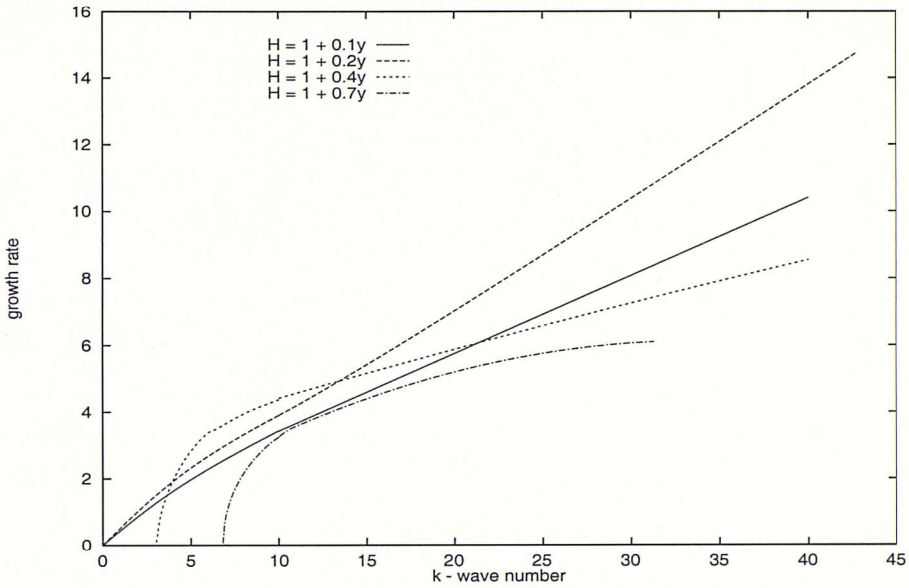


Figure 3.50: Dispersion relation for fixed topographic gradient $\mathbb{I}(\omega)$; $\epsilon = 0.01$.

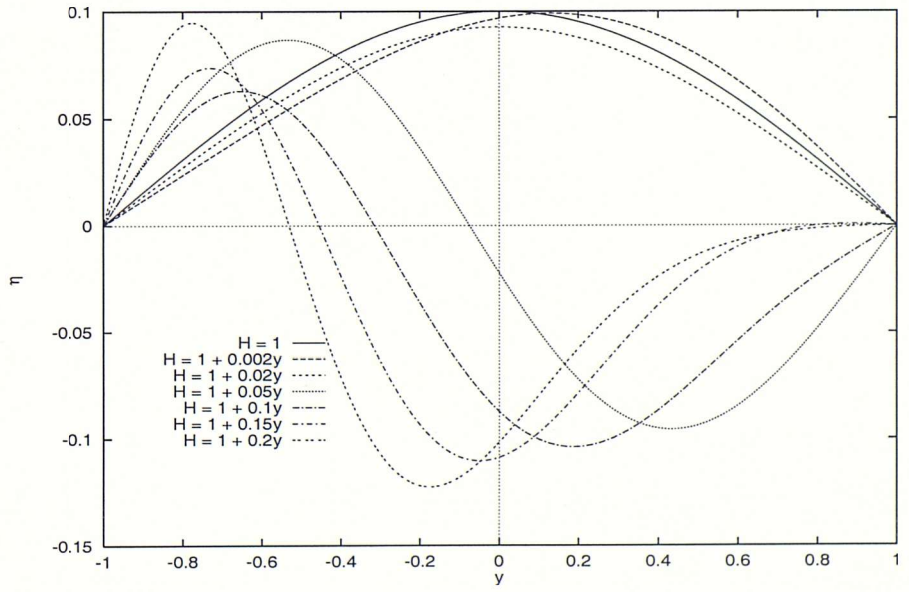


Figure 3.51: Eigenmodes for $T_1 = 1.0, k = 10$, varying H_1, (part I : $H_1 \ll 1$); $\epsilon = 0.01$.

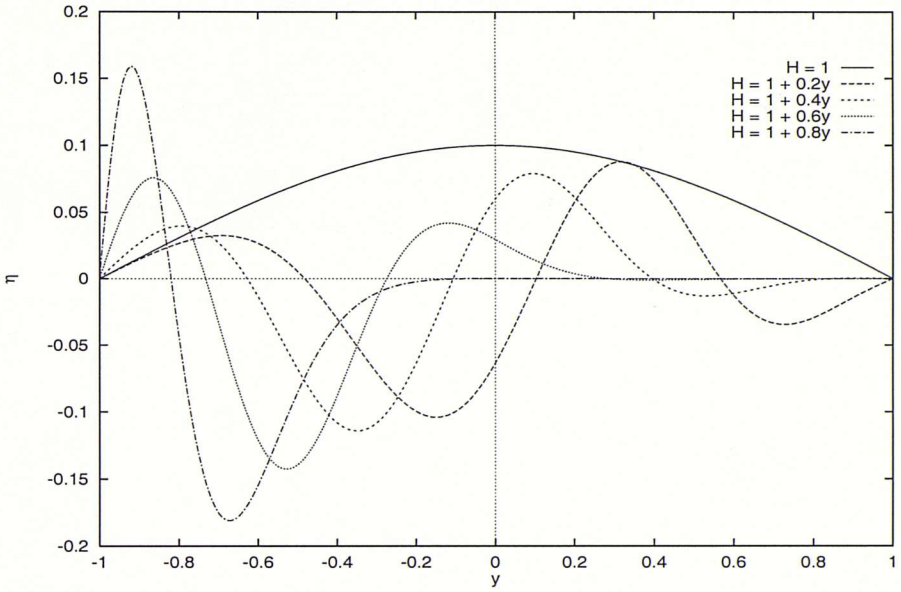


Figure 3.52: Eigenmodes for $T_1 = 1.0, k = 10$, varying H_1 (part II : $H_1 \sim 1$); $\epsilon = 0.01$.

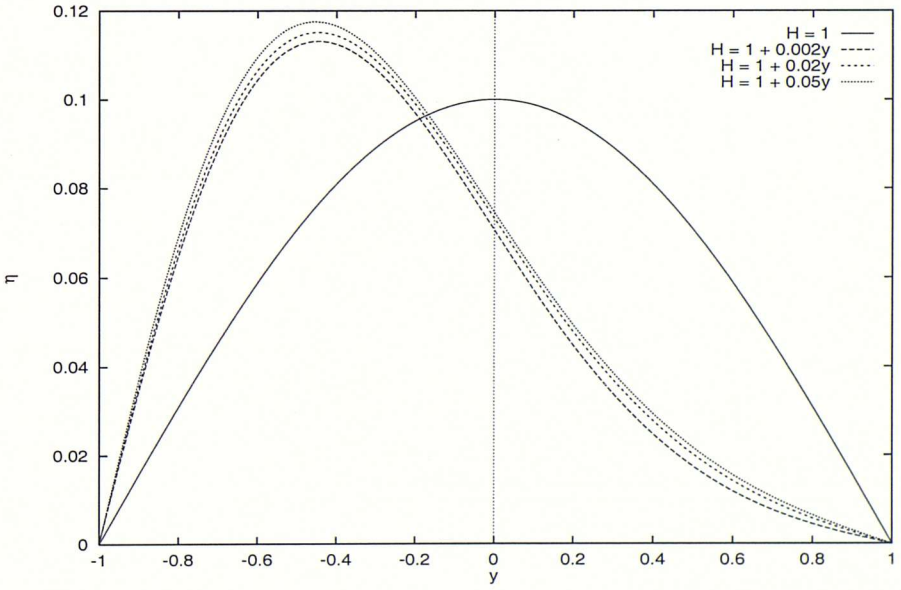


Figure 3.53: Eigenmodes for $T_1 = -1.0, k = 10$, varying H_1; $\epsilon = 0.01$. These are stable modes.

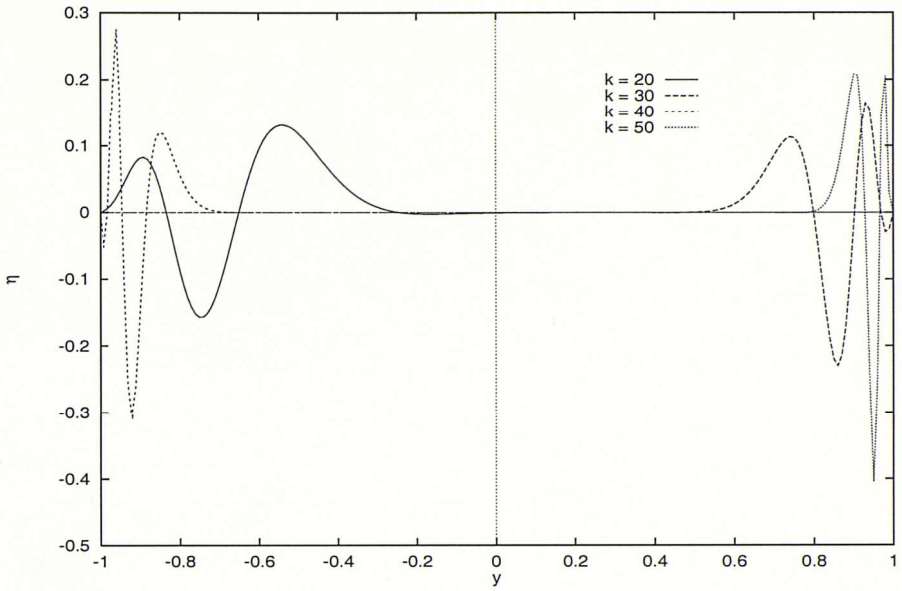


Figure 3.54: Eigenmodes for $T_1 = 1.0, H_1 = 0.2, k \gg 1$; $\epsilon = 0.01$. The $k = 20, k = 40$ wave modes have been reflected in $y = 0$ to aid clarity.

it becomes increasingly difficult to locate the eigenmode at higher wavenumbers. It is perhaps worth noting that in all instances in which a quantitative prediction is made on the basis of (3.115), this prediction over-estimates the actual growth rate. From this fact, we deduce that the net effect of the terms neglected in proceeding from (3.111) to (3.113) is to further stabilise the flow. From a practical viewpoint it is perhaps more reassuring to have an upper, rather than a lower, bound on the growth rate of an instability.

There is a trend clearly displayed in the behaviour of the eigenmodes as the slope steepens (Figures 3.51 – 3.54): the peak disturbance moves towards $y = -1$. This is where the domain is shallowest. Also, note that as $k \to \infty$ in Figure 3.54 the width of the disturbance becomes very narrow indeed. This explains why it becomes more difficult to find the eigenmodes as the wavenumbers increase. Such behaviour is predicted by a WKBJ analysis in which, to leading order, the eigenmodes are concentrated within a region of thickness ϵ and outside this region there is exponential decay. The behaviour is similar to that seen in the case of the Gaussian-strip temperature anomalies (§3.4) and is further evidence of the DIT's characteristic tendency for all the dynamics occur within localised regions.

A qualitative explanation of the topographical effects can be deduced from consideration of the origin of the terms in the dispersion relation (3.115). We first note that the instability is due to the last two terms. The first of these, $(\epsilon T_1^2 H_0^4 K^2)$ represents the flat-bottom baroclinic instability of §3.3 which was revealed to be caused by *JEBAI*. Although *JEBAI* contains terms involving ∇H, such terms do not influence the leading order behaviour. The second "unstable" term, $\frac{1}{2} H_0^2 H_1 T_1$, derives from the *JEBAR* term. It is this term which is responsible for the leading order behaviour for small slopes, namely that if $H_1 T_1 > 0$

then the flow is more unstable than the flat-bottom case and that if $H_1T_1 < 0$ then the opposite is true. The physical explanation of this is illustrated in Figure 3.46.

The final term of (3.115) to influence the stability of the flow is the H_1^2 term. This originates in the advective $J(\psi, T)$ term of (3.4). If topographic gradients are non-zero, this term always acts to stabilise the flow. In the case when $H_1T_1 < 0$, it re-enforces the *JEBAR* effect. However, in the case when *JEBAR* is attempting to destabilise the flow, the advective term opposes it. Consider swapping the two fluid columns shown in Figure 3.46. If topographic gradients are large then one column is very short and fat and the other is very long and thin. Because both temperature and mass are conserved by the DIT, the hot (shaded) column must be deformed from the thin to the fat configuration. This process requires a dramatic rearrangement of the fluid particles and requires a lot of kinetic energy. The potential energy released by the rearrangement of Figure 3.46 is not sufficient to compensate for the amount of kinetic energy required to achieve this rearrangement. Consequently, the net result of the topography is to stabilise the wave.

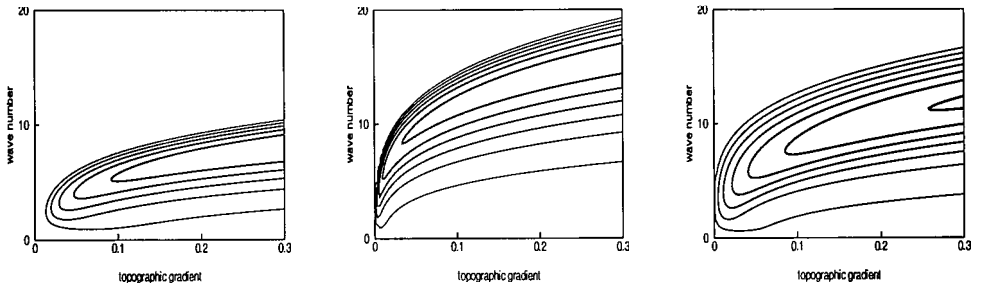
Diffusion Viscous and diffusive effects can be incorporated into the dynamics, as in the flat-bottomed case §3.3. However, we are now faced, in general, with a sixth-order linear ODE with non-constant coefficients to solve. It is not clear that any further insight can be gained from solving this eigenvalue problem numerically. If we make the same "small slope" approximation that was made in the inviscid case (that is, neglecting terms of magnitude $O(H_1^2, \epsilon H_1, \nu H_1, \kappa H_1)$) then all the non-constant-coefficient terms vanish, the solution is the familiar normal-mode solution and the dispersion relation is given by the solutions of

$$\begin{aligned}\omega^2 \epsilon K^2 H_0^2 + \omega\left[iK^4 H_0^2(\epsilon\kappa + \nu) - H_1 H_0 k\right] \\ + \left[\frac{1}{2} H_1 H_0^2 T_1 k^2 + \frac{1}{12}\epsilon T_1^2 k^2 H_0^4 K^2 - \nu\kappa K^6 H_0^2\right] = 0.\end{aligned} \tag{3.116}$$

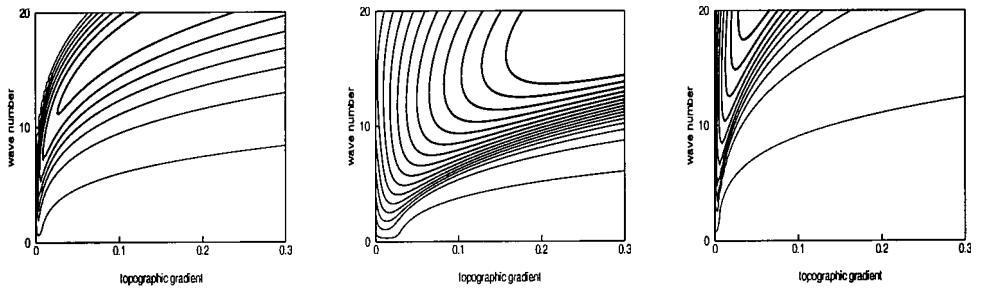
In the limit of $H_1 = 0$ (3.116) reduces to (3.35) and in the limit $\nu = \kappa = 0$ (3.116) reduces to (3.115). Accordingly, the solutions have a nature incorporating both these limits. Isopleth plots demonstrating how the behaviour varies with k and H_1 for various values of the parameters ν, ϵ, κ are shown in Figure 3.55. As in §3.3 there is a multi-dimensional parameter regime[15]; it is infeasible to examine all of it so we restrict attention to $\sigma = 1$.

The behaviour of the flat-bottomed model is captured in Figure 3.55 by the left vertical axis. Only positive topographic gradients are shown; in all calculations $H_0 = T_1 = 1$ so $H_1 > 0$ corresponds to the more interesting scenario in which there exists the possibility of a greater degree of instability than in the flat-bottomed case. The six cases shown

[15]There now exists one extra dimension, being the topographic gradient, H_1.



(a) $\nu = 10^{-4}, \epsilon = 10^{-3}, \kappa = 10^{-1}$ (b) $\nu = 10^{-5}, \epsilon = 10^{-4}, \kappa = 10^{-1}$ (c) $\nu = 4.472 \times 10^{-5}, \epsilon = 10^{-3}, \kappa = 4.472 \times 10^{-2}$



(d) $\nu = 4.472 \times 10^{-6}, \epsilon = 10^{-4}, \kappa = 4.472 \times 10^{-2}$ (e) $\nu = 10^{-5}, \epsilon = 10^{-3}, \kappa = 10^{-2}$ (f) $\nu = 10^{-6}, \epsilon = 10^{-4}, \kappa = 10^{-2}$

Figure 3.55: Isopleth plots of wavenumber k against topographic gradient H_1 showing growth rate of unstable mode, $\mathbb{I}(\omega)$; $T_1 = 1$. (a, b) are subcritical; (c, d) are marginally supercritical; (e, f) are supercritical for the flat-bottomed case. The influence of topography is more noticeable at smaller values of ϵ. Isopleths are equally spaced. Darker isopleths represent greater instability. See text for further details.

correspond to (a, b) $\mathsf{Ra} < \mathsf{Ra}_c$; (c, d) $\mathsf{Ra} \gtrsim \mathsf{Ra}_c$; (e, f) $\mathsf{Ra} > \mathsf{Ra}_c$. In all cases, it is observed that for any given wavenumber, k, there exists a finite topographic gradient which maximises the growth rate for that k. Furthermore, the most unstable wavenumber increases with increasing H_1. This means that when there is a topographic slope, the instabilities ought to occur on smaller scales than in the flat-bottomed case (§3.3.2).

The effect is more pronounced for smaller values of the Rossby Number, ϵ. That is, increasing ϵ diminishes the influence of topography. A similar result is found by Özgökmen *et al.*[56] who were concerned with determining what influences the Gulf Stream separation at Cape Hatteras.

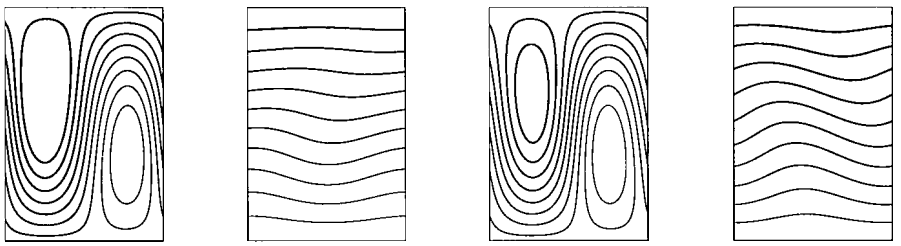
Nonlinear simulations. The preceding linear analysis suggests that variable topography has a stabilising influence on the flow (unless gradients are very small) and that, when dissipative effects are incorporated, the most unstable wavenumber is higher than in the flat-bottom case. These qualitative predictions are now tested in the nonlinear regime, where H_1 is not necessarily small, via a series of numerical simulations similar to those of §3.3.3. Our aim is to compare the behaviour with the flat-bottomed simulations in which the behaviour is characterised by the value of the Rayleigh Number, $\mathsf{Ra} \equiv \frac{\epsilon T_1^2}{\kappa \mathsf{Re}}$ and $\mathsf{Ra}_c = 48\pi^2$ is the critical value above which the flow is unstable. In the present instance, we continue to characterise the flow with reference to Ra_c of the flat-bottomed DIT. Furthermore, we use the same domain size as in the flat-bottomed case of $[0..2] \times [0..1]$. The domain width is chosen because in §3.3 the most unstable wavenumber is $k = \pi$. Consequently, in a domain of width 2, we see one whole wavelength (see, for example, Figure 3.8). We anticipate that the topography will reduce the wavelength of the most unstable wave and so we should observe more than one wavelength.

Figures 3.56, 3.57 show the nonlinear evolution of the flow at $\mathsf{Ra} = 1.05\mathsf{Ra}_c$ with a topographic gradient specified by $H_1 = \pm 0.5$. The simulations are initialised with the linear solution ($T = T_1 y + \sin(\pi y)\cos(\pi x)$) with a small amount of an additional mode $\sin(\pi y)\sin(4\pi x)$. The inclusion of this second mode allows wave-triad interactions to create further modes within the flow. Snapshots of the temperature field are shown in Figure 3.56 and the Nusselt number times series are shown in Figure 3.57[16]. Both figures demonstrate, as predicted by the linear analysis, that there is *no* instability, regardless of the orientation of the topographic gradient relative to the thermal gradient. (In both simulations, $\partial_y T > 0$).

Figures 3.58, 3.59, 3.61 show the evolution of a flow which *does* exhibit instability. They represent, respectively, the temperature field, T, the vorticity field, ζ, and the Nusselt Number, Nu. The choice of $\mathsf{Ra} = 20\mathsf{Ra}_c \approx 10,000$ corresponds to the values of ν, ϵ, κ in Figure 3.55(f). A Fourier analysis indicates that the most unstable wavenumber is the $k = 6\pi$ mode. This is lower than the prediction of Figure 3.55(f) which is presumably due to the neglect of several nonlinear terms in (3.116). The numerical eigenvalue calculations (Figures 3.48, 3.50) also suggest that the linear analysis (3.115) over-estimates growth rates even in the absence of any dissipation.

The cases of $H_1 = 0.2, 0.4$ are similar to the $H_1 = 0.1$ case. Qualitative linear predictions that the most unstable number will increase and that the growth rate will decrease are

[16] As with the energy profiles, for example, Figure 4.4, I have offset the vertical coordinate to enable both series to be shown on the same graph. In this case, as with the energy profiles, the specific long-time value of Nu (energy) to which the solution asymptotes, is unimportant; what *is* important is the manner in which they get there. In Figure 3.57 both series should asymptote to $\mathsf{Nu} = 1$.



(a) $H = 1 + 0.5y; t = 0$ (b) $H = 1 + 0.5y; t = 10$ (c) $H = 1 - 0.5y; t = 0$ (d) $H = 1 - 0.5y; t = 10$

Figure 3.56: Evolution of the T field in Rayleigh Bénard convection simulations on a topographic slope. (a, b) $H_1 = 0.5$; (c, d) $H_1 = -0.5$. In all simulations, $\mathsf{Ra} = 1.05\mathsf{Ra}_c$ where Ra_c refers to the critical Rayleigh number in the flat-bottomed domain. Therefore, the $H_1 = 0$ case is unstable. Here, both flows are stable.

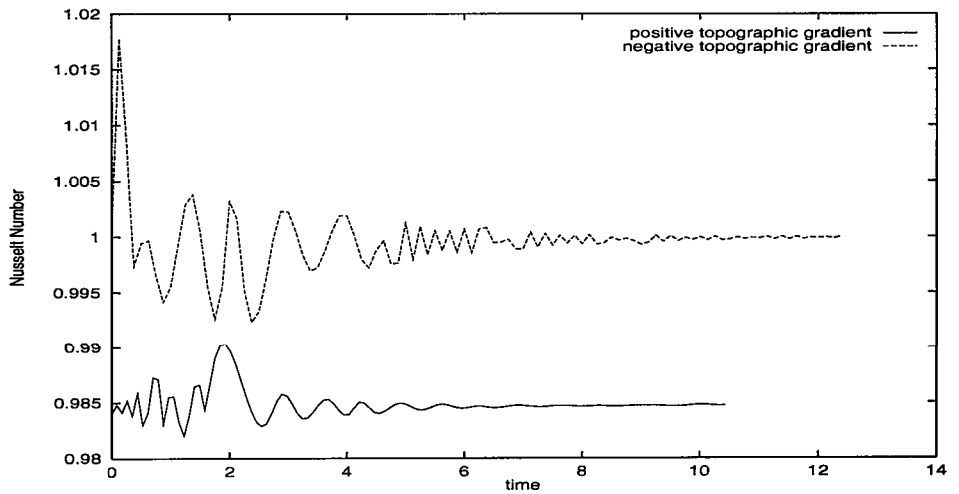
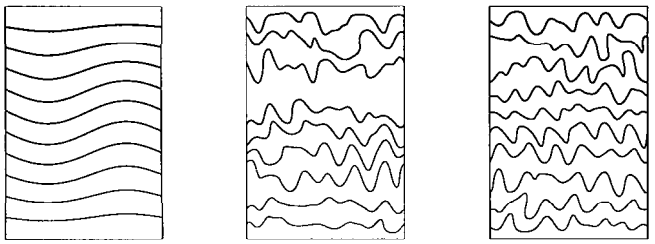


Figure 3.57: Time series of Nusselt number for $\mathsf{Ra} = 1.05\mathsf{Ra}_c, H = 1 \pm 0.5y$. Solid line series ($H = 1 + 0.5y$) is offset vertically to aid clarity. It actually asymptotes to $\mathsf{Nu} = 1$. Hence, both flows are stable.

confirmed by Figure 3.60 and by the Nusselt Number time series, Figure 3.61 which shows that, for a fixed value of Ra, Nu decreases as the topographic gradient increases. The *spikes* at $t = 0.5$ in Figure 3.61 do not appear to be very significant. The flow fields at $t = 0.5$ (not shown) are very similar to the long time flow fields (Figure 3.60). The spike occurs because it is at this time that nonlinear wave-triad-interactions create the first unstable modes. The simulations are initialised with only $k = \pi$ and a small amount of $k = 4\pi$ modes, both of which are stable modes.



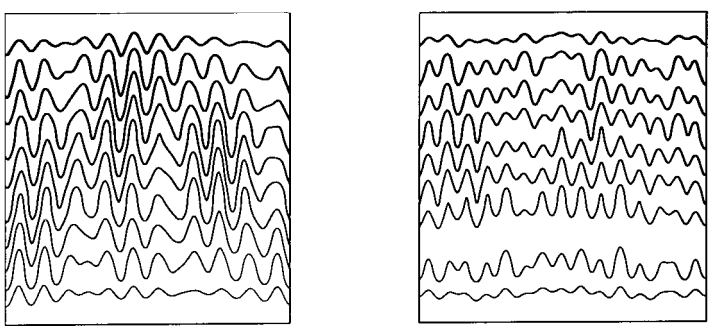
(a) $t = 0$ (b) $t = 2.0$ (c) $t = 4.0$

Figure 3.58: Evolution of an initially sinusoidal disturbance on a linear thermal gradient ($T = y$) and a topographic gradient ($H = 1 + 0.1y$); $\mathsf{Ra} = 20\mathsf{Ra}_c$; T field.



(a) $t = 0$ (b) $t = 2.0$ (c) $t = 4.0$

Figure 3.59: Evolution of an initially sinusoidal disturbance on a linear thermal gradient ($T = y$) and a topographic gradient ($H = 1 + 0.1y$); $\mathsf{Ra} = 20\mathsf{Ra}_c$; ζ field.



(a) $H_1 = 0.2$ (b) $H_1 = 0.4$

Figure 3.60: Snapshots of T field in a simulation initialised as in Figure 3.58 on a topographic gradient ($H = 1 + H_1 y$), $\mathsf{Ra} = 20\mathsf{Ra}_c$. Increasing gradients shift the most unstable wavenumber higher. In (a) most unstable mode is $k = 10\pi$. In (b) most unstable mode is $k = 15\pi$.

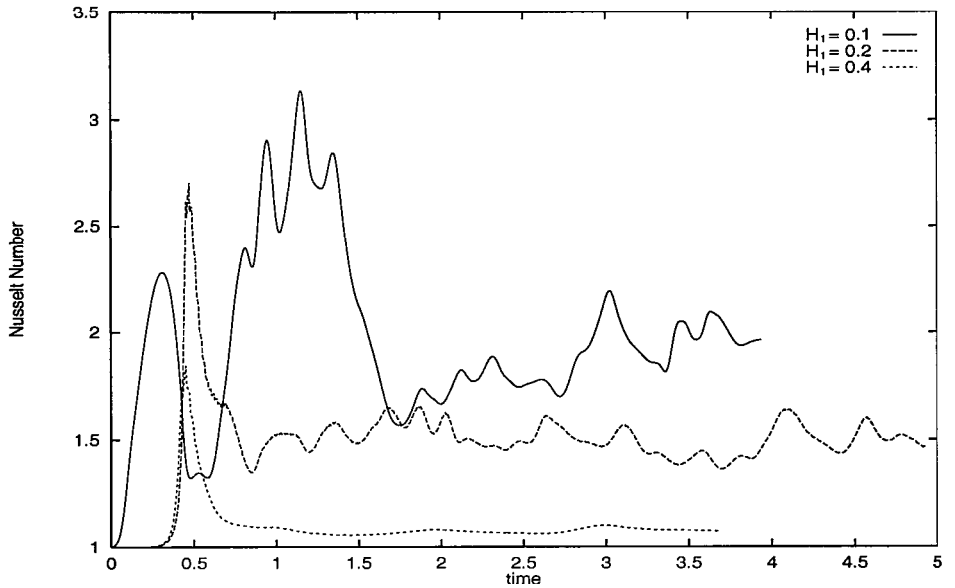


Figure 3.61: Time series of Nusselt Number for $\mathsf{Ra} = 20\mathsf{Ra}_c$, $H = 1 + H_1 y$. As H_1 increases, the statistical mean of Nu decreases. This signifies less efficient mixing in the domain and reduced instability.

3.6.2 Turbulence

A series of numerical experiments, similar to those of §3.5.3, is executed. The only difference between the simulations of this section and those of §3.5.3 is the inclusion of a radially symmetric Gaussian topographic anomaly in the centre of the doubly periodic domain[17].

$$H = 1 + A\exp(-\mu\left[(x - x_0)^2 + (y - y_0)^2\right]). \tag{3.117}$$

A and $\mu > 0$ are $O(1)$ constants. The numerical domains have non-dimensional size $[-\pi..\pi]\times[-\pi..\pi]$. Together with the condition of double-periodicity, this imposes a restriction on A, μ, that the Gaussian anomaly must be sufficiently small at the edge of the domain that the depth of the basin may be regarded as constant. That is, $A\exp(-\mu\pi^2) \ll 1$. This condition ensures that the topography varies smoothly from one cell to the next. Experimentation has shown that if ∇H is discontinuous then anomalously large gradients of ψ, in particular, are produced in the neighbourhood of the discontinuity.

The evolution of a typical, un-forced turbulent simulation is shown in Figures 3.63-3.65. The Gaussian anomaly is characterised by $A = -0.8, \mu = 1$. Therefore, the anomaly is a rise rather than a dip. Initially, the behaviour is dominated by baroclinic instability just as in the flat-bottomed case (Figures 3.37-3.39). However, the long-time behaviour is

[17] A doubly periodic domain is necessary now because no normal flow cannot be satisfied on vertical side-walls unless $T = const.$ on that wall. Consequently, the topography must be consistent with this so we are limited in the choice available. In particular, turbulence on a sloping plane cannot be simulated.

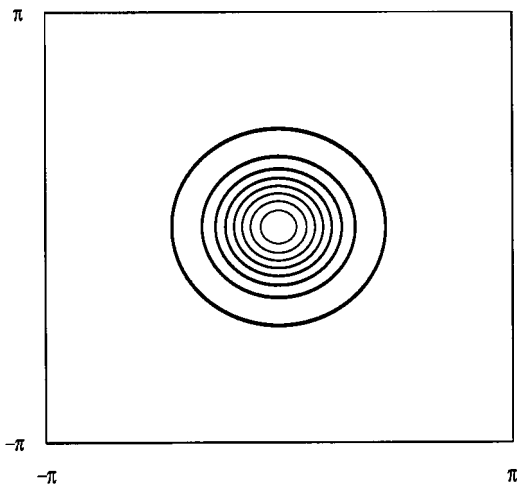


Figure 3.62: Gaussian topographic anomaly. Contours are equally spaced from $H = 0.25$ (innermost) to $H = 0.95$ (outermost).

clearly very different from the flat-bottomed case. The most striking feature is that the temperature field has aligned itself very strongly with the topography. The warmest water is located in the centre, in the shallowest part of the domain. This is precisely the configuration predicted by the non-inertial theory in which the potential energy $\int_A \frac{1}{2}H^2 T dx dy$ is minimised.

The Rayleigh Number, $\mathsf{Ra} \equiv \frac{T_0^2}{\kappa \mathsf{Re}^{-1}} = 2.5 \times 10^5$ is identical[18] to the value of Ra in Figures 3.37-3.39 (the flat-bottomed case). One effect of the topography is to hinder the baroclinic instability. The radius of the bump sets a horizontal length scale and the result is then in agreement with §3.6.1 in which the instability growth rate of a fixed wavenumber decreases with increasing topographic gradient. Of course, after some time period, the temperature field organises itself into the stabilising configuration (warm fluid in shallow regions); this further hinders any instability. The temperature field does not stop evolving completely. Figs3.63(d, e, f) show evidence of a mode one periodic oscillation moving azimuthally around the centre of the domain.

For comparative purposes, the long-time flow fields of the barotropic dynamics ($T = 0$) is shown in Figure 3.66. An important feature of this flow is the trapping of the anticyclone by the topography. The barotropic flow conserves potential vorticity $\frac{f+\epsilon\zeta}{H}$. The rotation is constant so as fluid flows over the topography (where H is anomalously low), PV conservation requires that the relative vorticity, ζ, is reduced. Such anticyclonic trapping is observed (Dewar[24] and references therein) in the vicinity of sea-mounts in the ocean

[18] T_0 is a typical magnitude of the initial temperature field. For the simulations in this subsection, $T_0 = 0.5$.

such as the *Azores Plateau* in the North Atlantic and the *Zapiola Drift* in the South Atlantic.

The DIT vorticity field (Figure 3.65(f)) shows evidence of a trapped anticyclone but it is much weaker than in the barotropic case. Moreover, the vorticity in the barotropic simulation is spread over the whole region of topography whereas in the DIT simulation, there is a small anticyclone in the centre, a strong ring of activity around the edge of the bump (centred on $r \approx \frac{\pi}{2}$) and noticeably more activity over the flat bottom. In particular, there is very little activity over the area where the topography is steepest. Recall that the highest gradients of this particular Gaussian bump are concentrated on $r = \frac{1}{\sqrt{2}}$. This is further evidence of the stabilising influence of topography, especially in this orientation, when the warm, buoyant fluid is concentrated in the shallowest regions.

Finally, the joint effect of topography and forcing is considered. Clearly a more detailed study than is presented below would demonstrate that the details of the behaviour depend on the relative magnitudes of the forcing and the topography. In fact, only a small parameter window offers any interesting behaviour. If the forcing is too weak, the magnitude of the T field does not grow sufficiently to create any baroclinic instability. In this instance, the *JEBAR* term dominates and there is a slow evolution leading to a state in which all the warm water is located over the anomaly in the centre of the domain (see Figure 3.63(f)). Conversely, if the forcing is too strong, it completely dominates the topographic influence and the evolution resembles that of the flat-bottom case (Figures 3.42-3.44).

The thermal forcing must be modified somewhat to account for the fact that the amount of "heat" in the system is HT rather than T. If we use the prescribed formula of §3.5.3 (namely Q = (3.108)) then the initial behaviour is governed by $\frac{\partial T}{\partial t} = \frac{\mathsf{Q}}{H}$. Over the topography, H is less than elsewhere so T will be larger. This sets up a warm anomaly over the topography which is a stable solution of the problem (indeed, it is the stable attractor of the freely evolving turbulent flow, see Figure 3.63(f)). Simulations (not shown) demonstrate that this is the dominant feature of the flow for all time. Consequently, we modify the forcing via $\mathsf{Q} \leftarrow H\mathsf{Q}$.

Figures 3.67-3.69 show the stages of evolution for a simulation with this modified thermal forcing with a magnitude of 5.0 which allows *both* topographic *and* baroclinic processes to affect the flow[19]. As in the flat-bottom case (§3.5.3), not much activity occurs in the flow for a long period (until $t \sim 48$). This is to enable the magnitude of the T field to grow to values at which baroclinic instability can occur. The influence of topography is clearly not

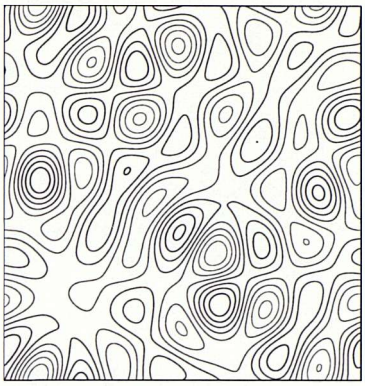
[19] I also tried magnitudes of 1.0 which proved too weak and no baroclinic instability ever occurred, and of 10.0 which proved too strong and did not allow any topographic influence to be felt. In the ocean basin simulations of §4.2.2, in which topographic gradients are slightly greater than here, we employ a thermal forcing term of magnitude $\mathsf{Q} \sim 5 - 50$.

as great here as in the freely evolving case. The random forcing prevents the thermal field aligning itself completely with the topography. This means, that, as in the flat-bottom case, the baroclinic instability is never switched off. The influence of topography is clearly shown by the radial nature of the ψ (Figure 3.68) and ζ (Figure 3.69) fields. However, the trapping of the anticyclone observed in the un-forced case (Figure 3.65(f)) is not apparent here. As in the flat-bottom case, when there is a continuous source of large-scale baroclinic energy, barotropisation does not occur. The T and ψ fields attain approximately equal magnitudes in Figures 3.67(e,f), 3.68(e,f).

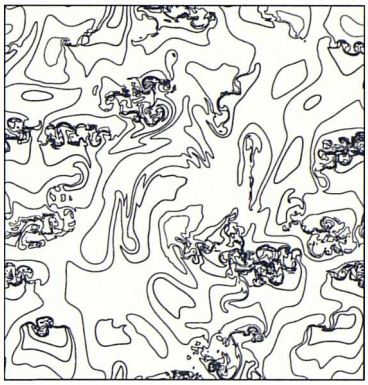
As in the freely evolving case above, the corresponding barotropic problem is also briefly summarised (Figure 3.70) because the case of large amplitude topography has not been extensively studied. However, since there is no thermal forcing in the problem, the barotropic simulation is forced via a wind-like term ($\mathsf{W}(x,y)$) in (4.1)). This takes exactly the same form as the thermal forcing in the DIT problem. The resemblance between the forced and un-forced barotropic case is less than the corresponding difference in the DIT model. Specifically, the anticyclonic trapping by the topography remains evident in Figure 3.70(d), even though it is not as striking as in the freely evolving case. As in the freely evolving simulations, the vorticity in the barotropic case is distributed relatively evenly over the topography in comparison to the DIT case in which the most active dynamics avoids the areas where the topographic gradients are steepest.

3.6.3 Summary

In §3.6 the effect of topography on the results of §§3.3, 3.5.3 has been studied. There are two alignment cases to consider. When the topography is oriented such that warmer water is in shallower regions, then the effect is stabilising. When the converse is true, the situation is more complicated. For small slopes the effect is to increase the growth rate of the disturbances. However, if the slope becomes sufficiently steep, a maximum growth rate is attained and then the effect reverses and a further steepening causes increased stability. Furthermore, the most unstable wavenumber increases with increasing topographic gradient. The leading order balance is between the *JEBAR* term which tries to move warm water to shallow regions and the temperature advection term which is unwilling to swap long, thin columns with short, fat ones. In turbulent simulations the initial behaviour exhibits baroclinic instability as in the flat-bottom case. However, the *JEBAR* effect, which occurs over a longer time scale, eventually moves all the warm water into the shallowest regions. The alignment of the thermal and topographic fields switches off *JEBAR* ; this means that the behaviour is similar to the barotropic case and we observe a weak trapped anticyclone over the topography.



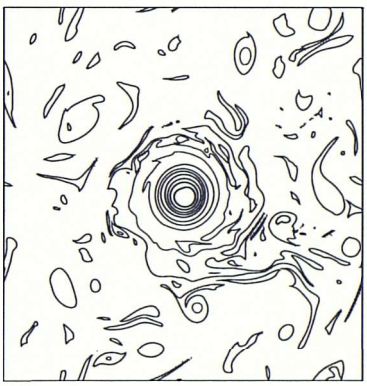
(a) $t = 0.0$,CI $= 0.25$



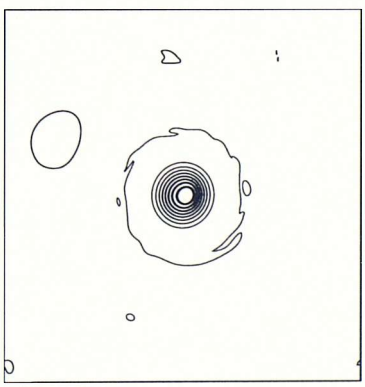
(b) $t = 4.4$,CI $= 0.21$



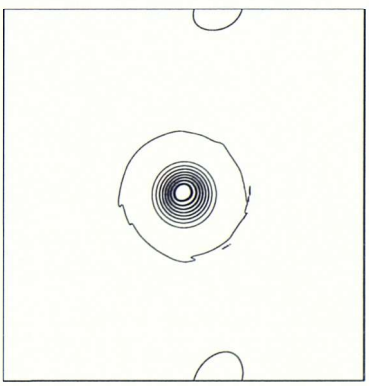
(c) $t = 8.2$,CI $= 0.17$



(d) $t = 24.9$,CI $= 0.10$

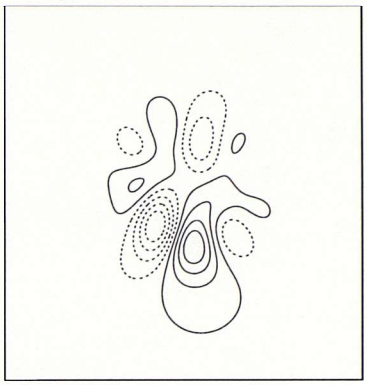


(e) $t = 46.2$,CI $= 0.07$

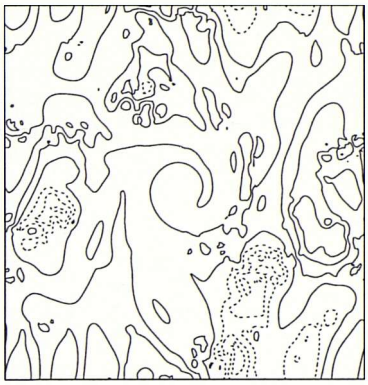


(f) $t = 71.6$,CI $= 0.05$

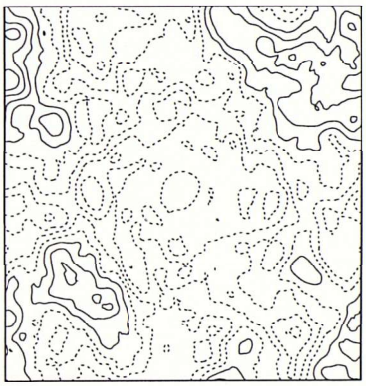
Figure 3.63: Un-forced evolution of an initially turbulent DIT flow over an isolated Gaussian topographic anomaly; T field. $\mathsf{Re}^{-1} = \kappa = 2 \times 10^{-3}$. Note the different contour intervals (CI).



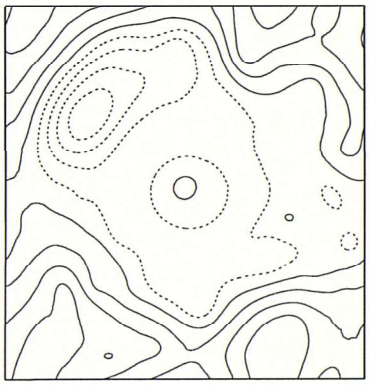
(a) $t = \Delta t$,CI = 0.001



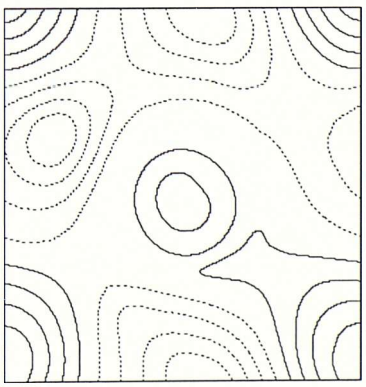
(b) $t = 4.4$,CI = 0.004



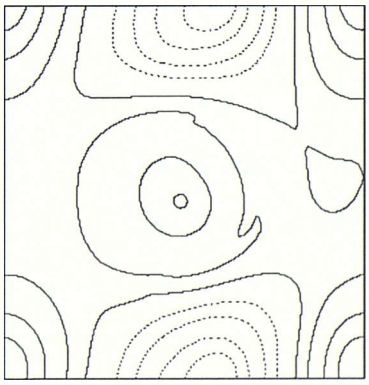
(c) $t = 8.2$,CI = 0.08



(d) $t = 24.9$,CI = 0.07

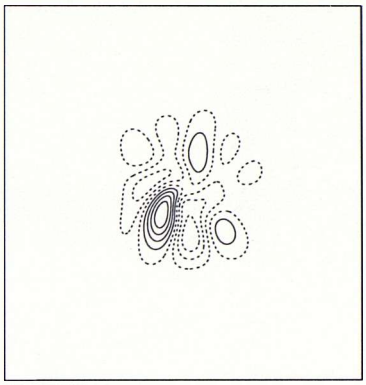


(e) $t = 46.2$,CI = 0.07

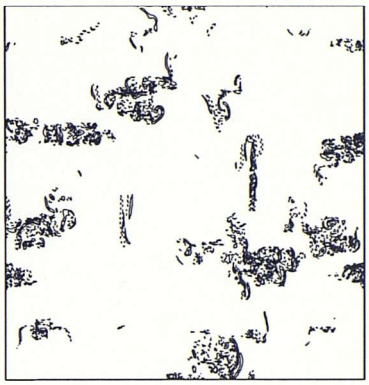


(f) $t = 71.6$,CI = 0.06

Figure 3.64: Evolution of an initially turbulent DIT flow over an isolated Gaussian topographic anomaly; ψ field. $\mathsf{Re}^{-1} = \kappa = 2 \times 10^{-3}$. Δt refers to time after one numerical time step. Initially, $\psi(x, y) = 0$. Note the different contour intervals (CI).



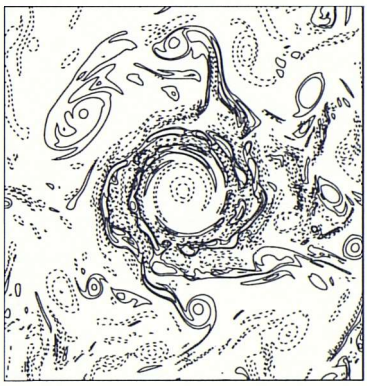
(a) $t = \Delta t$,CI = 0.023



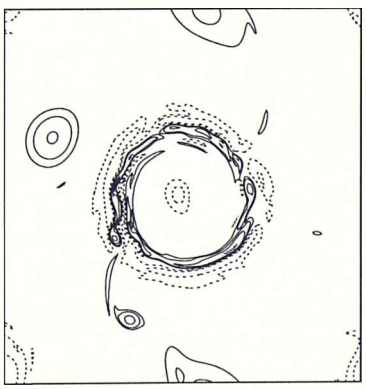
(b) $t = 4.4$,CI = 5.4



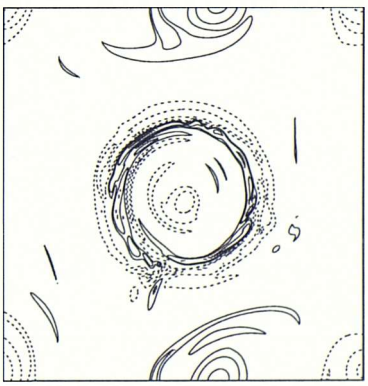
(c) $t = 8.2$,CI = 8.0



(d) $t = 24.9$,CI = 2.1

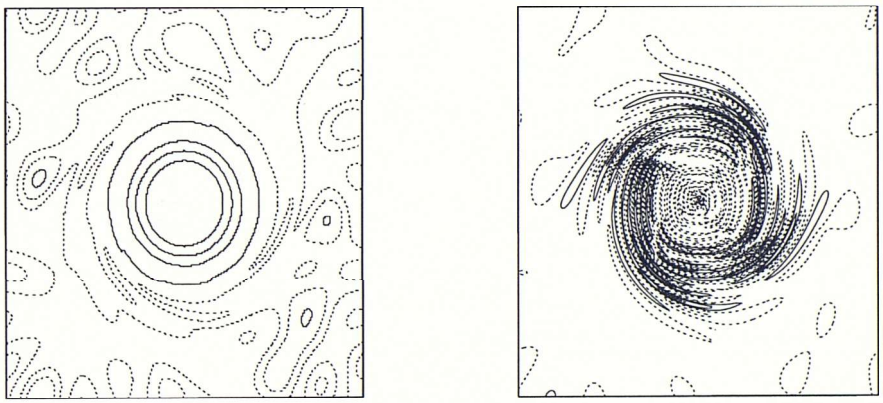


(e) $t = 46.2$,CI = 1.2



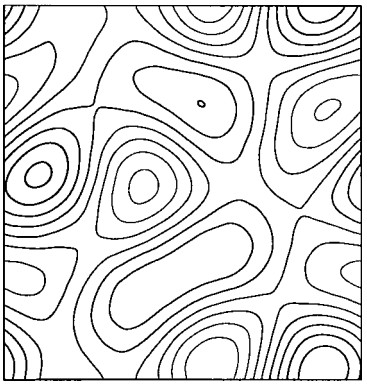
(f) $t = 71.6$,CI = 1.2

Figure 3.65: Un-forced evolution of an initially turbulent DIT flow over an isolated Gaussian topographic anomaly; ζ field. $\mathsf{Re}^{-1} = \kappa = 2 \times 10^{-3}$. Δt refers to time after one numerical time step. Initially, $\zeta(x, y) = 0$. Note the different contour intervals (CI).

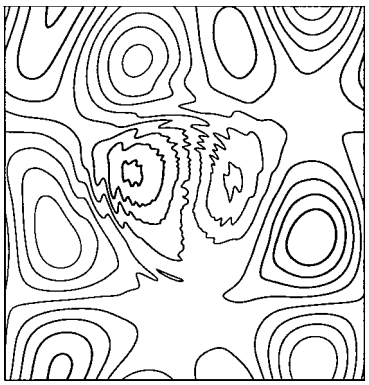


(a) ψ,CI = 0.20 (b) ζ,CI = 4.0

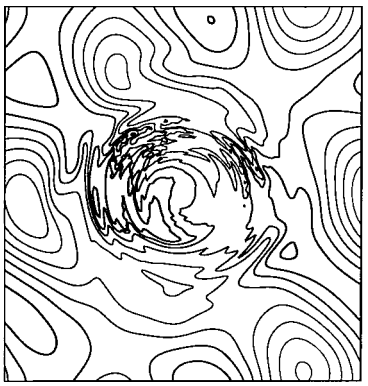
Figure 3.66: Long time behaviour ($t = 30$) of an initially turbulent **barotropic** flow over an isolated Gaussian protuberance. A strong anticyclone is trapped by the topography.



(a) $t = 3.2$,CI $= 0.002$



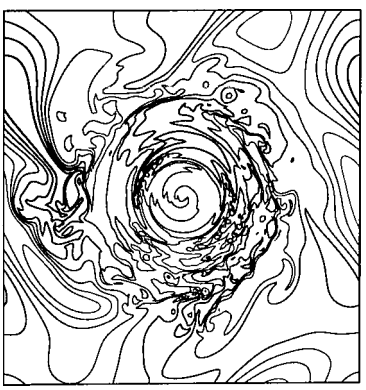
(b) $t = 32$,CI $= 0.12$



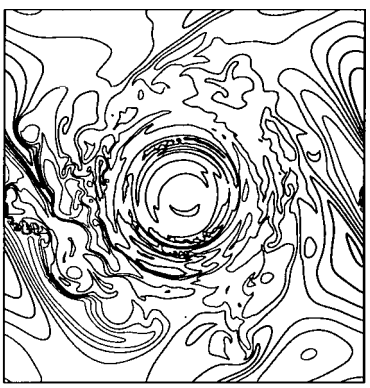
(c) $t = 48$,CI $= 0.125$



(d) $t = 64$,CI $= 0.125$

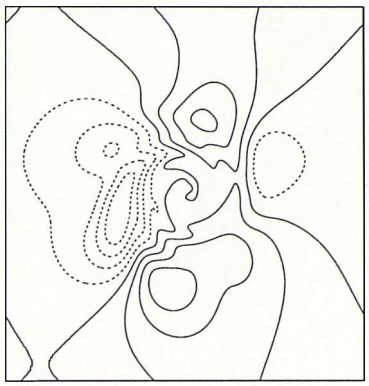


(e) $t = 80$,CI $= 0.135$

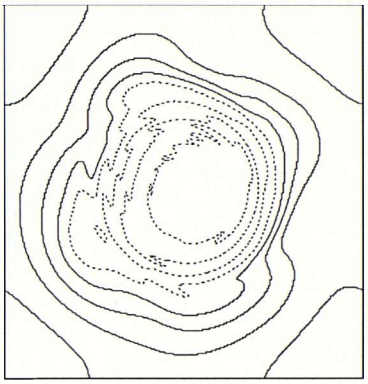


(f) $t = 96$,CI $= 0.125$

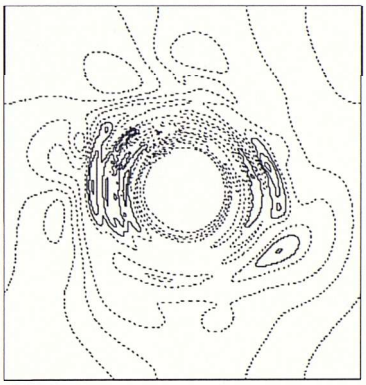
Figure 3.67: Evolution of a turbulently forced DIT flow over an isolated Gaussian topographic anomaly; T field. $\mathsf{Re}^{-1} = \kappa = 2 \times 10^{-3}$. Note the different contour intervals (CI).



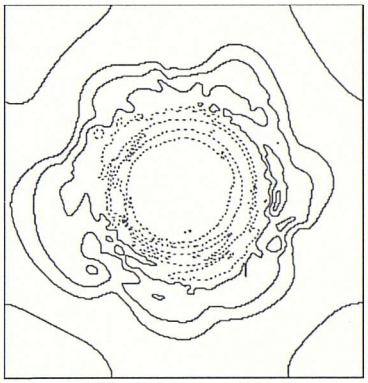
(a) $t = 3.2$,CI $= 0.002$



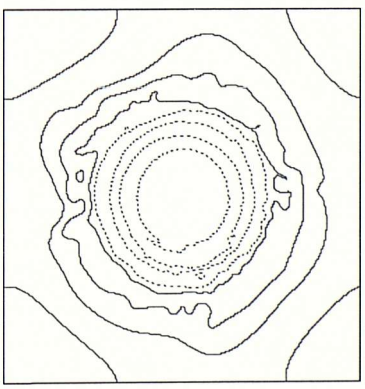
(b) $t = 32$,CI $= 0.11$



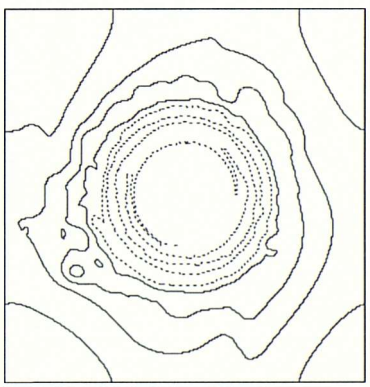
(c) $t = 48$,CI $= 0.11$



(d) $t = 64$,CI $= 0.11$

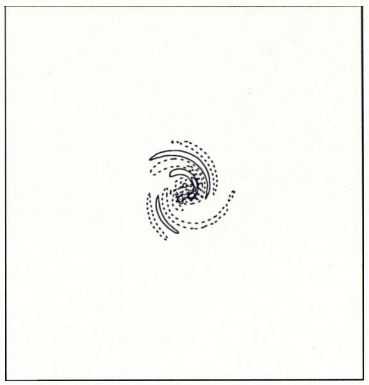


(e) $t = 80$,CI $= 0.11$

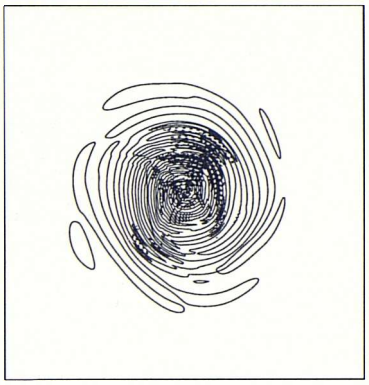


(f) $t = 96$,CI $= 0.11$

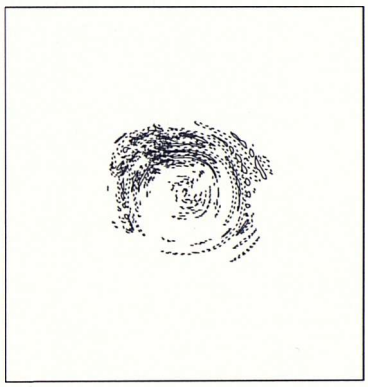
Figure 3.68: Evolution of a turbulently forced DIT flow over an isolated Gaussian topographic anomaly; ψ field. $\mathsf{Re}^{-1} = \kappa = 2 \times 10^{-3}$. Note the different contour intervals (CI).



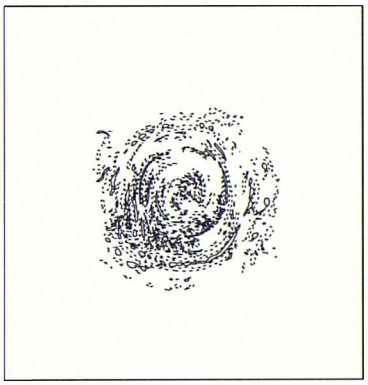
(a) $t = 3.2$,CI $= 0.03$



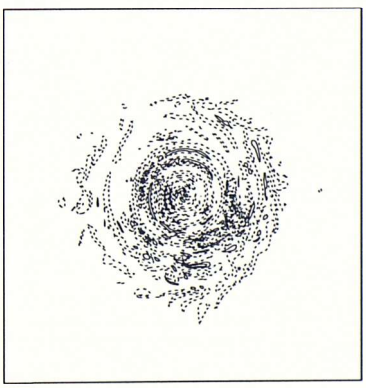
(b) $t = 32$,CI $= 3.4$



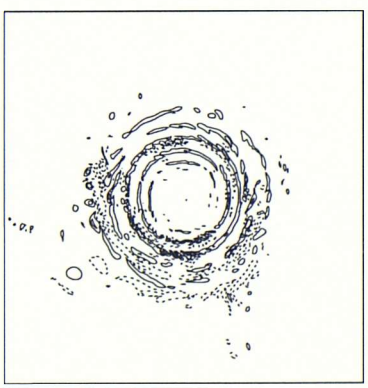
(c) $t = 48$,CI $= 5.2$



(d) $t = 64$,CI $= 5.7$

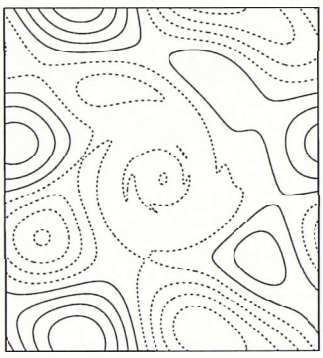


(e) $t = 80$,CI $= 6.2$

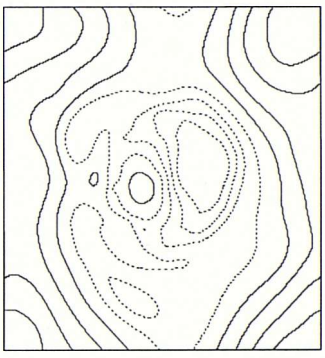


(f) $t = 96$,CI $= 6.2$

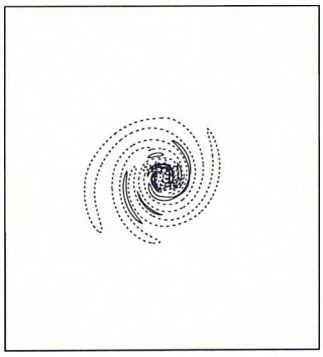
Figure 3.69: Evolution of a turbulently forced DIT flow over an isolated Gaussian topographic anomaly; ζ field. $\mathsf{Re}^{-1} = \kappa = 2 \times 10^{-3}$. Note the different contour intervals (CI).



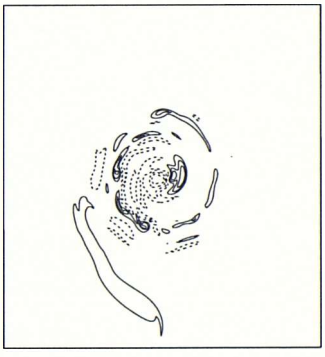
(a) $\psi, t = 15$,CI $= 0.22$



(b) $\psi, t = 30$,CI $= 0.19$



(c) $\zeta, t = 15$,CI $= 4.2$



(d) $\zeta, t = 30$,CI $= 4.1$

Figure 3.70: Long time behaviour of a turbulently forced barotropic flow, initially at rest, over an isolated Gaussian protuberance.

Chapter 4

Ocean Basins

In this chapter we use the understanding of the LSGE developed in Chapters 2 and 3 to explain the dynamics in global ocean basins. Previous chapters have studied various processes, such as baroclinicity, and the roles of topography and forcing, in isolation. We now address the question of what happens when all these factors act simultaneously to influence the circulation. Sheremet *et al.*[79] stress that the answer to this question is not well understood and this provides much of the motivation behind the development of simple models such as the DIT. The barotropic ocean is investigated in §4.1 and the baroclinic DIT ocean is investigated in §4.2.

Our aim is to reproduce and interpret some of the typical features of ocean circulation described in the opening paragraphs of the thesis. Our strategy is to take as our starting point the barotropic basins of [7]. For various technical reasons, this basin is unsuitable for studying DIT ocean dynamics. We therefore make a series of modifications, changing one factor at a time to arrive, by the end of §4.1.6, at an ocean basin which is identical in every respect to the DIT ocean basin used throughout §4.2, except for the inclusion of baroclinicity in the latter. In §4.2 we consider the influence of the baroclinicity.

4.1 Barotropic ocean basins

In this section we neglect the effect of baroclinicity and model an ocean which consists of one homogeneous layer of fluid. This restriction is a very great simplification and is clearly an unrealistic assumption for the real ocean. However, it allows us to gain some understanding of the model. Additionally, since the barotropic ocean is a well studied problem, it enables a large portion of the computer code to be verified in comparing our results with those of other authors.

The wind-driven, barotropic problem is a well known one in oceanography. Stommel[82]

and Munk[52] found exact, steady state solutions to the geostrophic equations with a flat bottom. Since these two pioneering studies, many other steady states have been discovered by varying the boundary conditions, viscosity and initial conditions. Instabilities of these steady state solutions have also been studied. Berloff & Meacham[11] (and references therein) suggest several possible causes of instability in the ocean. They include oscillations of the thermohaline overturning cycle, response of the ocean to stochastic forcing by the atmosphere and shear instabilities in barotropic jets. In the barotropic ocean of this section, there is no thermohaline circulation and the wind forcing is steady so only the last mechanism can be responsible for instability. Meacham & Berloff[50] performed a detailed analysis of a flat-bottomed, barotropic, closed basin with a single-gyre wind-forcing. They find steady state solutions for a range of Re and find that as Re is increased, an instability is associated with a standing meander of the WBC after it has left the boundary and rejoined the interior flow. Moreover, they show that the instability is not a wholly localised process; the eastern boundary has a role to play in determining the marginal value of Re.

In comparison to the flat-bottomed problem, oceans with varying bathymetry are poorly understood. Holland[35] was perhaps the first person to look at the effect of topography of $O(1)$ extent. He pointed out that, in the limits of vanishingly small viscosity and inertia, the flow follows streamlines of $\frac{f}{H}$. Other studies have been performed by Welander[85] who looked at the how the structure of the WBC is affected by the meridional derivative of $\frac{f}{H}$. Nishigaki[55] performed an analytic study of how the topography controls the path of the WBC. Nishigaki compared his results to the actual path of the Kuroshio current and found (qualitative) agreement. Even in these studies, however, researchers have remained shy of including ocean depths that vanish smoothly at the coastlines. This is despite the fact that the equations (4.1, below) are hardly any more complicated with the inclusion of such topography.

This section reprises many of the results of Becker & Salmon[7] which *does* model coastal depths that vanish at the western coast. In a study similar to that of Meacham & Berloff[50], they find that the steady state solution of low Ro loses stability as Ro is increased. The western coastal slope is found to reduce the stability of the steady state; the critical Ro when a slope is present is much lower than when it is not. The difference between the present section and [7] is that in this section (and again in §4.2) we study an ocean with slopes on the western, eastern and northern boundaries. There is a solid vertical wall at the southern boundary which represents the equator. See Figure 4.3(a). The reason for this is that the DIT[1] *require* the depth to be zero at all boundaries (except when $f = 0$, namely, the equator) in order to preserve no normal flow. In order to ensure

[1]The GTLE, (Appendix A, [73]) also have this requirement.

that the *only* difference between §4.1.6 and §4.2 is the baroclinicity, the same topography *must* be used in both cases.

4.1.1 The barotropic vorticity equation

In a homogeneous ocean all the fluid possesses the same temperature. The simplest way to derive the equations is to insist that $h = 0$ in the two-layer model (or to insist that $T = 0$ in the DIT model). This immediately reduces the equation for the interface depth (2.31) to the trivial identity $0 = 0$ and also reduces the equation for the barotropic streamfunction (2.22) to

$$\epsilon\frac{\partial\zeta}{\partial t} + J\left(\psi, \frac{f}{H}\right) + \epsilon J\left(\psi, \frac{\zeta}{H}\right) = -\nu\zeta + \mathsf{W}(x, y). \tag{4.1}$$

Here ϵ is the Rossby number and so we use the symbol ν to represent Rayleigh friction.

Equation (4.1) is called the **Barotropic Vorticity Equation**. It can easily be derived directly from the primitive equations (1.1a-e) after making the assumption of a barotropic flow. In this instance the fundamental assumption of the LSGE does not lead to any approximation at all. This is because, in a barotropic ocean, there is no internal Rossby radius; a one-layer ocean can be regarded as a two-layer ocean with deformation radius $\lambda_{int} = 0$. Since *all* positive scalars are very much bigger than zero, the restriction to length scales bigger than the deformation radius is vacuous. Therefore the BVE (4.1) derived from the LSGE is exactly the same equation that is derived from the primitive equations.

Since the ocean is barotropic, $\mathbf{u} = \bar{\mathbf{u}}$, $\hat{\mathbf{u}} = 0$, so the semi-geostrophic co-ordinates (1.11a-c) coincide exactly with the Cartesian co-ordinates.

The wind-forcing is always constant and, with one exception (Figure 4.14), takes the form of a purely zonal, sinusoidal double gyre:

$$\mathsf{W}(x, y) = \begin{cases} 0 & 2 > y > 2 - \delta_w \\ -\sin\left[\frac{\pi}{1-\delta_w}(y - \delta_w)\right] & 2 - \delta_w > y > \delta_w \\ 0 & \delta_w > y > 0 \end{cases} \tag{4.2}$$

Becker & Salmon[7] use the same basic form but it is concentrated over the middle half of the basin. This corresponds to $\delta_w = 0.5$ in (4.2). The wind-forcing is not applied over the whole basin because there are numerical difficulties at the northern and southern boundaries. I have also experienced similar difficulties if the wind-forcing is applied over the whole basin but, after a period of some experimentation, I have discovered that applying it over 80% ($\delta_w = 0.1$ in (4.2)) is sufficient to prevent these problems occurring. The strategy adopted in this section is to perform some simulations (§§4.1.3-4.1.5) with $\delta_w = 0.5$, so that the results may be compared with those of [7] and then to use $\delta_w = 0.1$

thereafter (§4.1.6). This is because the wind-driven gyres are confined to the portion of the basin with a non-zero forcing. Consequently, $\delta_w = 0.1$ yields bigger gyres and hence the features within them are better resolved. The double-gyre wind is selected for simplicity. Observations (e.g. Hellerman & Rosenstein[34]) suggest that a triple-gyre form more accurately represents the true wind structure over the North Atlantic (see Figure 4.14).

Throughout this chapter, we confine attention to an *equatorial beta plane*: $f = \beta y$.

4.1.2 Scaling of parameters

The Atlantic ocean is approximated (very roughly indeed!) by a cubic basin of width $L = 4000km$ and depth $H_0 = 4km$. A typical ocean velocity, U, is chosen in such a way that the Sverdrup transport, $H_0 LU = 30Sv$. This ensures that a typical Sverdrup transport through the Gulf Stream corresponds to a non-dimensional transport of $O(1)$. This scaling yields $U = 2mm\ s^{-1} \approx 0.2km\ day^{-1}\ s^{-1}$, which, in turn, gives a value for $\epsilon \equiv \mathsf{Ro}$, the Rossby Number $= \frac{U}{f_0 L}$ of $\epsilon = \mathsf{Ro} \approx 0.08 \times 10^{-4}$.

Having arrived at this value, we then proceed to use a value of $\mathsf{Ro} \approx 2.0 \times 10^{-4}$ which is an order of magnitude larger than our derived value. The justification for this is based upon consideration of the width of the western continental slope. In order to resolve all the dynamics occurring in this region, the width of slope is relatively wide compared to the width of the ocean basin (Figure 4.3(a)). In fact, the slope occupies approximately one quarter of the basin yielding a width of $1000km$ which is at least one order of magnitude too wide. A typical continental slope might be only $50-100km$ wide. We therefore imagine shrinking the width of the wind-driven gyres by a factor of $10 - 20$ whilst retaining the same transport. This means that the velocities in the gyres outside the WBC are $10 - 20$ faster than in reality but, more importantly, the velocities, transport and width of the WBC are now the same magnitude as in the Atlantic.

We choose an advective time scale of $T = \frac{1}{\mathsf{Ro} f_0} = 5 \times 10^7 s \approx 600$ days. This is an interannual time scale. The ultimate motivation behind the development of the DIT is to use it as the oceanic component of a coupled atmosphere-ocean model. Interaction between the two climatic components occurs on an interannual to interdecadal time scale so the above scaling is appropriate to this. A longer (that is, interdecadal) time scale is less justifiable because of the neglect of salinity in the model.

The smallness of Ro can be misleading; this is a *global* Rossby Number. In fact, the inertia is important in relatively narrow boundary currents which have much smaller horizontal length scales. A typical WBC may be $40 - 80km$ wide, giving a *local* Rossby Number of $O(10^{-2})$.

Finally, we consider the value of the Rayleigh frictional parameter, ν. There is considerable

variation in the value of frictional and viscous parameters used by authors. Moreover, some authors (e.g. Özgökmen *et al.*[56]) regard $-\nu\zeta$ terms to represent *bottom friction* and others (e.g. Jiang *et al.*[38]) regard them to represent *Rayleigh friction.* Numerical values vary from $5 \times 10^{-9}s^{-1}$ (Dewar[24]) to $2 \times 10^{-7}s^{-1}$ (Özgökmen *et al.*[56]). Based on our time scale of $T \sim 10^8$ yields values of $\nu \sim 0.1 - 10$. On the other hand, many authors also use some form of *lateral friction* in addition to bottom/Rayleigh friction. There is considerable variation here as well (see Berloff & Meacham[9] and references therein) with values ranging from $50m^2s^{-1}$ to $400m^2s^{-1}$. A common choice ([38], [56]) is $200m^2s^{-1}$ which corresponds to $\nu = 2 \times 10^{-3}$. Numerical and physical issues are of equal importance in choosing a value. Dewar[24] derives a value of $D = 2 \times 10^{-7}s^{-1}$ for the bottom friction based on an estimate of $10m$ for the bottom Ekman layer and then proceeds to use $D = 10^{-9}s^{-1}$ in the numerical simulations.

In this chapter, we use the "smallest value that we can get away with numerically". For the flat-bottomed model it is easy to show (Stommel[82]) that there is a frictional boundary layer on the western boundary of width ν. This boundary layer *must* be resolved and so $\nu > \Delta x$ where Δx is the width of the numerical grid spacing. The grids in §§4.1.3–4.1.5 are 129×257 in extent and so $\nu > \frac{1}{129}$. To maintain consistency with Salmon[72] and Becker & Salmon[7] we choose $\nu = 0.01$ in most cases. Interestingly, even though there is no western boundary layer in the continental slope solutions (see e.g. Figure 4.1(a)), this value of ν still appears to be the smallest value that prevents the solution from blowing up numerically. The friction *is* important in the southwestern corner of these solutions.

4.1.3 Numerical solution of the BVE

The BVE is solved by an Adams-Bashforth-Moulton predictor-corrector time-stepping scheme (see B.2) for the relative vorticity, ζ. At each time step a new ζ is calculated and a multigrid algorithm (see B.3) is used to obtain the streamfunction, ψ, from the vorticity.

The nonlinear $J(\psi, \frac{\zeta}{H})$ term is evaluated using Leonard's Third Order Upwinding Scheme. This is equivalent to a standard, centred difference Jacobian plus an implicit hyperdiffusion term. This hyperdiffusion damps down the very fine scales of the flow (see B.1).

The case for using upwinding rather than an explicit lateral diffusion or hyperdiffusion term is made by Hecht *et al.*[32]. Furthermore, and perhaps more convincingly, Figures 4.1(a)-(c) show that there is very little qualitative (or quantitative) difference between the results of the three schemes. In particular, the upwinding(a, d) and hyperdiffusive(c, f) cases are very similar. Hyperdiffusion is more scale-selective than lateral diffusion and so permits slightly sharper features. This is most evident at the point where the WBC dismounts the western slope. I have found that, of the three schemes, upwinding has

proved the most reliable in terms of converging quickly at a wide range of parameter values.

In all cases within §§4.1.3–4.1.5 I used a numerical grid of size 129×257[2]. In many cases I started off with a 65×129 grid. This can be stepped forward in time much more rapidly but tends not to converge with the parameters chosen (see §4.1.2). I proceeded as far as possible on the coarse grid and then interpolated to the fine grid and refined the solution there[3].

4.1.4 Flat bottom

The flat-bottomed case with vertical side-walls has been extensively investigated. The flow is shown in Figure 4.2. It is symmetrical about the point of zero WSC and is relatively stable at comparatively large values of Ro. Cessi & Ierley[15] and Ierley & Sheremet[37] have shown that multiple steady states, some of which are asymmetric, can exist for particular parameter regimes even when the forcing is the same antisymmetric, two-gyre wind used here. There is a well defined viscous boundary layer of width ν at the western boundary, but away from this region, the flow follows the zonal $\frac{f}{H}$ contours. The effect of increasing Ro is simply to push the mid-latitude jet further and further towards the eastern boundary. Eventually, as found by Becker & Salmon[7], the flow does become asymmetric and instability does set in. This occurs when the jet hits the eastern boundary.

4.1.5 Coastal slopes

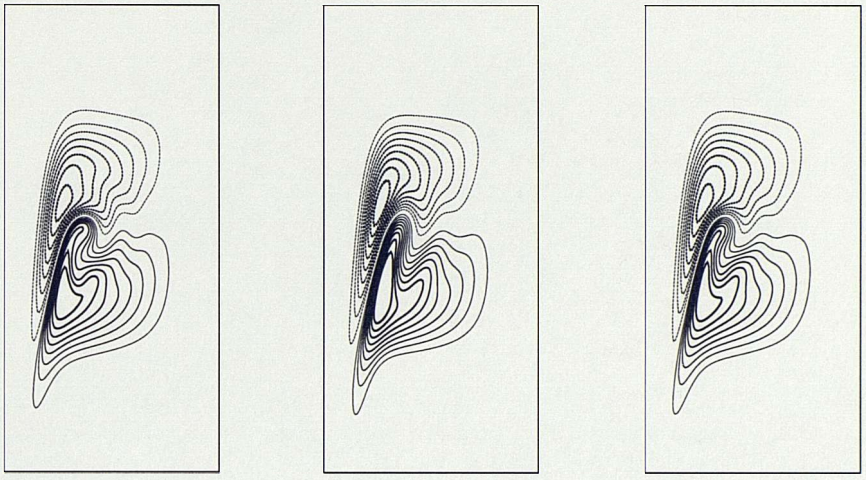
We now introduce a bathymetry that varies smoothly to zero at three of the coastlines (Figure 4.3(a)). This is similar, if not identical, to the bathymetry of [72].

The resulting contours of $\frac{f}{H}$ are shown in Figure 4.3(b) and a stable, steady state flow configuration is shown in Figure 4.1(a). It is clear, that in the main body of the flow, the $\frac{f}{H}$ contours are driving the flow. The flow is qualitatively different to the flat-bottomed case (Figure 4.2(a)) which renders it surprising that so few studies have included a variable topography. The fact that the WBC flows approximately northwards, parallel to the western boundary, far more closely resembles the path of the Gulf Stream (Figure 1.1) than the zonal WBC of the flat-bottomed model.

The destabilising effect of increasing Ro is shown by the oscillating energy profiles of Figure 4.4. For $\mathsf{Ro} = 2 \times 10^{-4}$ the energy achieves a stable steady value whereas for more inertial simulations, the energy is no longer steady. Snapshots of a single oscillation are presented

[2] One disadvantage of using a multigrid scheme is that the mesh size is required to be of the form $2^n + 1$ for some integer n.

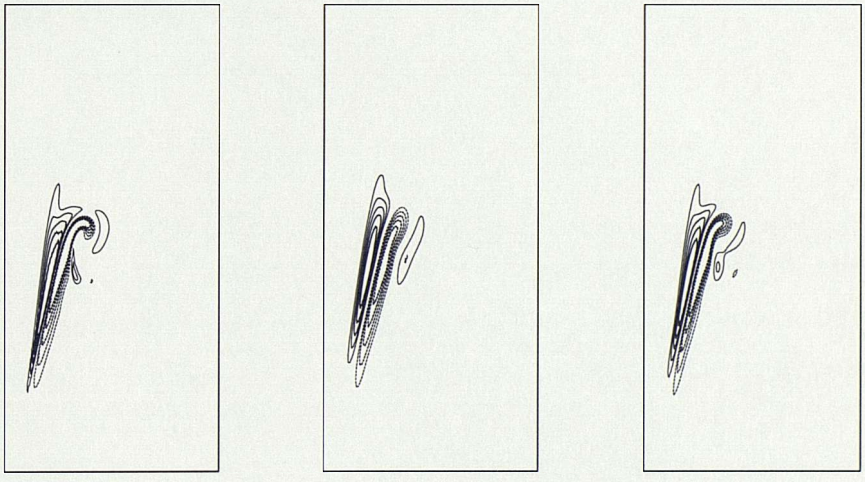
[3] An *advantage* of the multigrid scheme is that this conversion from coarse grid to fine grid is trivial.



(a) Rayleigh Friction + upwinding

(b) Laplacian Diffusion, free slip

(c) HyperDiffusion, free slip, free hyperslip

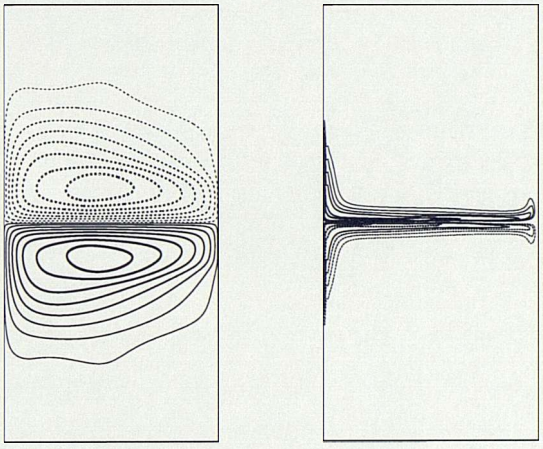


(d) Rayleigh Friction + upwinding

(e) Laplacian Diffusion, free slip

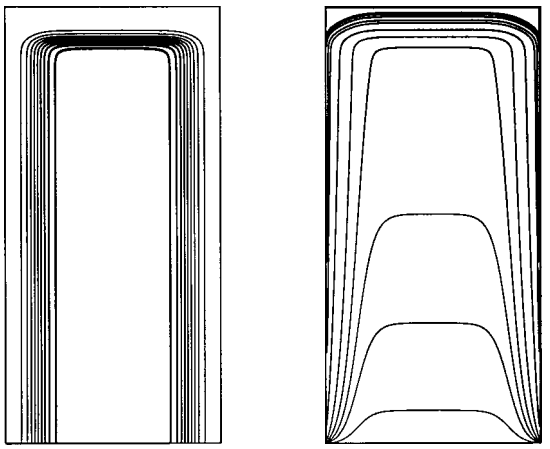
(f) HyperDiffusion, free slip, free hyperslip

Figure 4.1: Comparison of (top) the streamfunction, ψ, and (bottom) the relative vorticity, $H\zeta$, using three different numerical schemes for the dissipative terms. Note the great similarity of all three schemes. $-0.85 < \psi < 0.85$, $-800 < H\zeta < 765$. The negative vortex sheet is stronger than the positive sheet. Unless otherwise stated, the ranges of ψ and $H\zeta$ apply to all plots in §§4.1.3–4.1.5. We present plots of $H\zeta$ rather than ζ because of the large values of vorticity that occur in the southwestern corner of the basin.



(a) ψ (b) ζ

Figure 4.2: (a) The streamfunction and (b) the relative vorticity in a basin with a flat bottom and vertical side-walls. $\mathsf{Ro} = 12 \times 10^{-4}$ which is relatively large in comparison to other simulations in this chapter. This is the maximum Ro that leads to a stable steady state solution as can be seen by the fact that the vorticity jet has stretched all the way to the eastern boundary. Ranges are $-0.89 < \psi < 0.89, -842 < \zeta < 843$; the vortex sheets are of equal strength and it is this equality which contributes to the stability of the flat-bottomed solutions.



(a) bathymetry (b) $\frac{f}{H}$ isarithms

Figure 4.3: (a)The bathymetry used in all coastal slope basins. (b)The resulting $\frac{f}{H}$ isarithms which control flow in the limit of vanishing Ro and Ekman number.

in Figures 4.5, 4.6 showing an eddy-shedding event from the WBC. As shown in Figure 4.4, the steady state solution of low Ro loses its stability to a periodic solution at about $\mathsf{Ro} = 4 \times 10^{-4}$. There is a further bifurcation around $\mathsf{Ro} = 8 \times 10^{-4}$ when a period four orbit emerges. However, this is not exactly a straightforward period-doubling bifurcation; the dominant spectral peak decreases slightly as Ro increases. A further consequence of Ro increasing is that the harmonic content of the energy spectra increases until at about $\mathsf{Ro} = 12 \times 10^{-4}$ we are left with a chaotic attractor. Although this simulation was left running for a very long time[4], it showed no signs of settling into a periodic orbit.

In [7], Becker & Salmon find that even at this value of Ro there is a stable periodic orbit. This suggests that the difference is due to the effect of the topography at the eastern boundary. The streamfunction, ψ, in Figure 4.5 suggests that the northern coastal slope has a negligible part to play in the dynamics. This is primarily due to the choice of wind stress which is concentrated in the middle half of the domain. However, as the Rossby Number is increased, the WBC is pulled further and further towards the eastern boundary (as it is in the flat-bottomed case) and must eventually begin to interact with it. It is this interaction which breaks up the stability of the periodic solutions.

The onset of unsteadiness seems to be signalled by the formation of closed contours of

[4]Figure 4.4 shows only the latter stages of the simulation, after the energy had settled to a statistically average state.

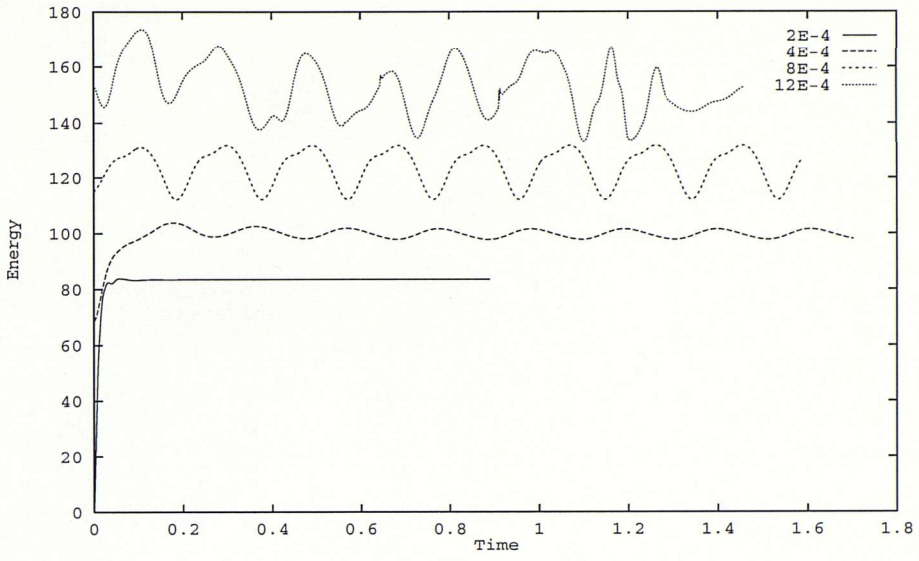


Figure 4.4: Energy profiles at different Ro. Unsteadiness corresponds to eddy formation and shedding near to the point of separation from the western continental slope. Time series have been vertically offset by an arbitrary amount to aid clarity. Time is scaled on $\mathsf{Ro} = 2 \times 10^{-4}$. Therefore, a non-dimensional time of $t = 1$ corresponds to 600 days. This applies to all energy profile plots in this chapter.

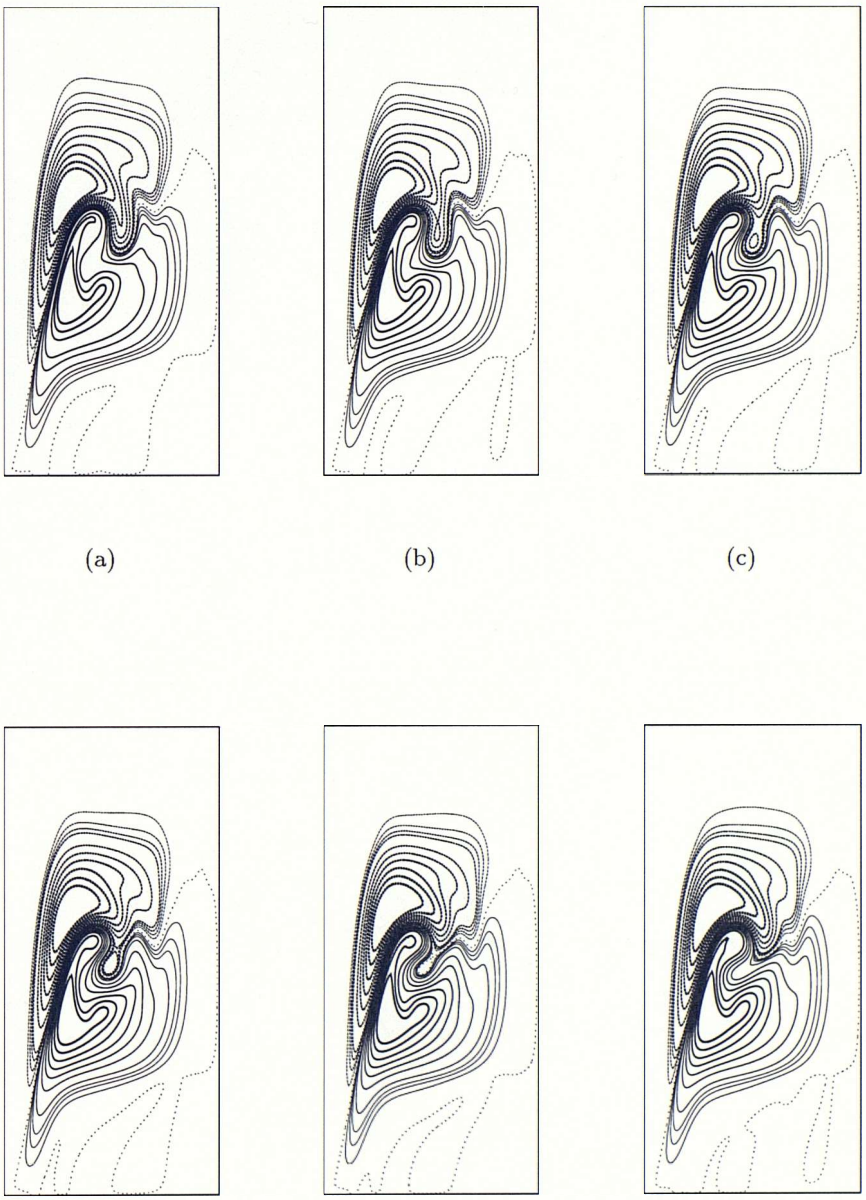
potential vorticity

$$Q \equiv \frac{\mathsf{Ro}\zeta + f}{H} \tag{4.3}$$

At small values of Ro where the flow is steady, the Q field appears on the verge of overturning but there are no closed isopleths (corresponding to local maxima and minima) until the flow becomes unsteady.

The explanation of why the coastal slope solutions are more unstable than their flat-bottomed counterparts is given in Becker & Salmon[7]. The key lies in the strength and orientation of the two vortex sheets. Consider the $\mathsf{Ro} = 0$ case; in the flat-bottomed model, the two sheets are of equal strength. One is located in the northern half of the basin on the western boundary and the other is in the southern half of the basin, also on the western boundary (see Figure 4.2(b)). Each vortex sheet exerts only a weak force on the other and so, as Ro increases, the effect is to pull the other sheet eastwards. Each sheet exerts an equal and opposite force on the other and so the configuration remains symmetrical and the two sheets remain separate (Figure 4.2(b)).

In the coastal slope solution, however, both the vortex sheets are located in the southern half of the basin and are side-by-side (Figure 4.1(d)). Both vortex sheets exert a northwards influence on each other and so as Ro increases, the sheets move further away from



(a) (b) (c)

(d) (e) (f)

Figure 4.5: The streamfunction, ψ, at subsequent time slices of a complete oscillation. $\mathsf{Ro} = 8 \times 10^{-4}, \nu = 0.01$, $0.92 < t < 1.08$. The dimensional lifetime of the eddy is approximately $4 - 5$ months.

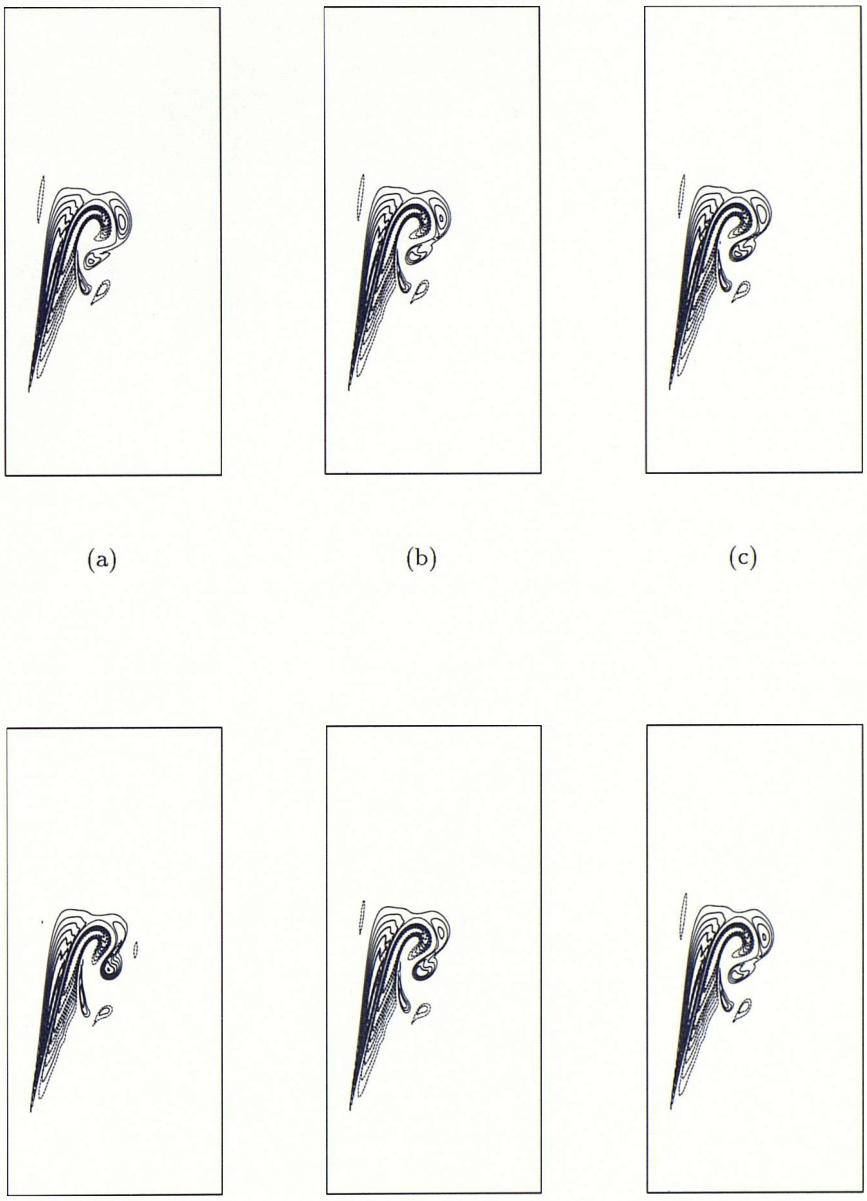
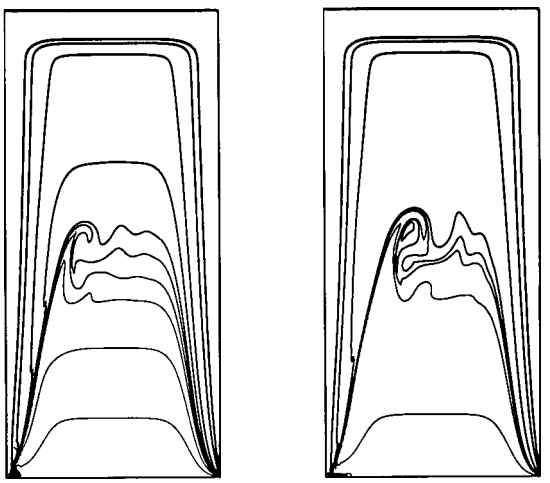


Figure 4.6: The relative vorticity, $H\zeta$, at subsequent time slices of a complete oscillation. $\mathsf{Ro} = 8 \times 10^{-4}, \nu = 0.01$, $0.91 < t < 1.08$. The strong negative vortex sheet wraps the weaker positive vortex sheet around its tip and rips off a cyclonic eddy. The vortex sheets extend much further east than in the lower Ro simulations of Figure 4.1.



(a) $\mathsf{Ro} = 2 \times 10^{-4}$ (b) $\mathsf{Ro} = 4 \times 10^{-4}$

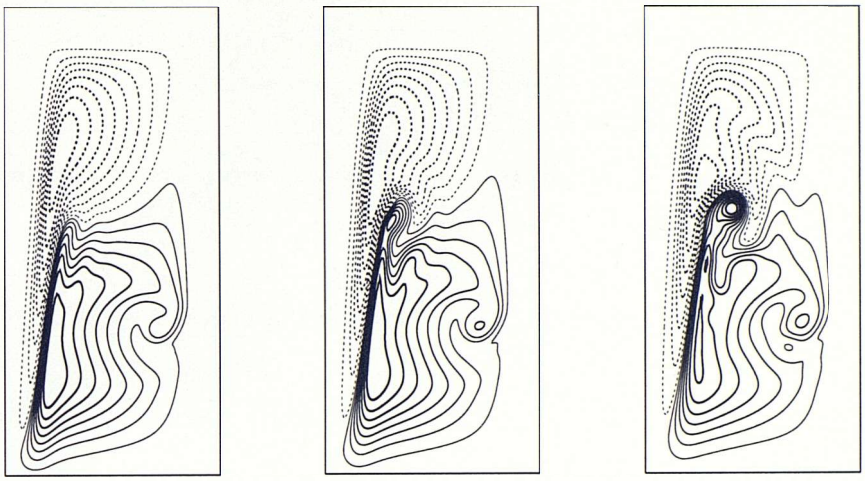
Figure 4.7: Snapshots of the potential vorticity, Q, (a) for the steady case at $\mathsf{Ro} = 2 \times 10^{-4}$ and (b) for the unsteady case at $\mathsf{Ro} = 4 \times 10^{-4}$. In (b) there are closed contours.

the southern, equatorial boundary. As this happens, the eastern vortex begins to wrap the western one around its northern tip. Instability occurs as pieces of the western sheet are torn off and are surrounded by the eastern vortex (Figure 4.6).

4.1.6 80% wind gyre

This subsection comprises results of simulations in a basin in which the setup is identical to the previous two sections, but in which the wind forcing is only switched off in the top and bottom 10% of the domain. Figure 4.8 shows snapshots of the streamfunction for three values of the Rossby Number. The corresponding energy time-series are shown in Figure 4.9.

Both the streamfunction plots and the energy profiles look qualitatively similar to their respective counterparts in §4.1.5. However, the gyres in Figure 4.8 are larger, and hence better resolved, than in Figure 4.5. In Figure 4.9 we have also included the $\mathsf{Ro} = 3 \times 10^{-4}$ profile. This narrows the range in which the first bifurcation occurs to $3 \times 10^{-4} < \mathsf{Ro} < 4 \times 10^{-4}$. A careful comparison of Figures 4.4, 4.9 reveals that the 80% wind case is slightly less stable than the 50% wind case. This is most easily seen from the $\mathsf{Ro} = 8 \times 10^{-4}$ profile. The reduced stability is due to the increased influence of the eastern slope in the 80% wind case. It is clear to see in Figure 4.8 that the eastern slope is having a significant effect on



(a) Ro $= 2 \times 10^{-4}$ (b) Ro $= 4 \times 10^{-4}$ (c) Ro $= 8 \times 10^{-4}$

Figure 4.8: Snapshots of the streamfunction, ψ, for a barotropic ocean with wind-forcing over 80% of the domain at three values of Rossby Number. The eastern boundary has an increasing influence on the flow as Ro increases and the gyres move slightly further away from the south-western corner of the domain. $-0.70 < \psi < 0.70$.

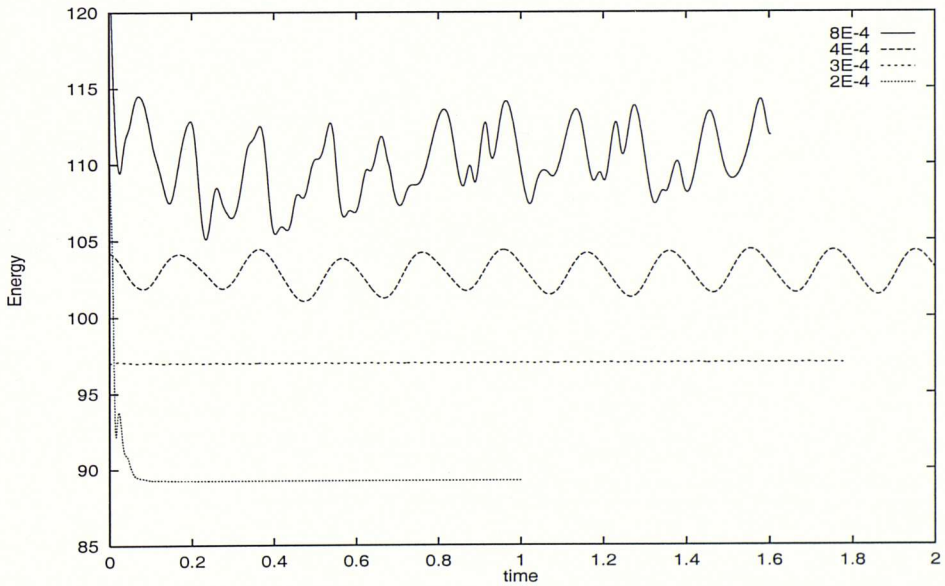


Figure 4.9: Energy profiles at different Ro. Wind forcing is over 80% of the domain. Increasing Ro causes greater instability. The unsteadiness corresponds to eddy formation and shedding near to the point of separation from the western continental slope. Time series have been vertically offset by an arbitrary amount to aid clarity.

the flow; *per contra*, the northern slope still does not appear to be affecting the dynamics to any great degree.

In §4.2, I find that this forcing in this basin geometry leads to numerical difficulties near the equator. The wind forcing does not have sufficient time to build up a strong enough gyre structure (the *fetch* is insufficiently great) to withstand the destructive inertial forces in the neighbourhood of the south-western corner. This results in the main gyre circulation being destroyed and a strong cyclonic vortex moving eastwards from the south-west corner along the equator[5]. This difficulty is removed by doubling the width of the basin whilst retaining the width of the coastal slopes. This produces a domain with a much wider central region (Figure 4.10) and this yields a big enough fetch for the wind to build up a self-sustaining double-gyre structure. In order to examine the effect of baroclinicity alone, I reproduce here some of the results for a basin of width $2L$ (numerically it now has 257×257 grid points). If the horizontal length scale of the ocean is doubled, then this means that the Rossby Number, Ro should be halved (see §4.1.2). Thus, $\mathsf{Ro} = A$ in these wide basin simulations should be compared with the $\mathsf{Ro} = 2A$ in the narrow basin simulations.

Doubling the width of the ocean so that the basin is now square ($2L \times 2L$) has both benefits and drawbacks: on the negative side, it is less faithful to the actual dimensions of the North Atlantic which has an approximate aspect ratio of two. A square basin, on the other hand, is more representative of the North Pacific. A great advantage of the new domain, however, is that the eastern and western coastal slopes are further apart. Even in the new, square domain, they are much closer together than in the actual Atlantic (see §4.1.2). but the greater distance apart prohibits the eastern slope from interacting too strongly with the WBC (Figures 4.8(c), 4.11(d)). Finally, note that the double-width simulations proceed only $\frac{1}{4}$ as rapidly as the regular-width domains. This is because there is twice the number of grid-points[6] and, because of the CFL criterion (see B.2), the maximum time-step allowed must also be halved.

Snapshots of the streamfunction are shown in Figure 4.11. The relative vorticity, $H\zeta$, in western-most $\frac{2}{5}$ of the basin is shown in Figure 4.12. Figure 4.11 seems to suggest that the influence of the eastern boundary is much less than in the narrow basin simulations. This impression is confirmed by the energy time series (Figure 4.13). The wide (narrow) basin yields a stable steady solution for $\mathsf{Ro} = 1 \times 10^{-4}$ ($\mathsf{Ro} = 2 \times 10^{-4}$), and a periodic orbit for $\mathsf{Ro} = 2 \times 10^{-4}$ ($\mathsf{Ro} = 4 \times 10^{-4}$). The main difference is observed between $\mathsf{Ro} = 4 \times 10^{-4}$

[5]The streamfunction looks similar to the case in which the equatorial parameter δ_{eq} is too small. See Figure 4.32.

[6]The cost of the principal numerical routines, including the multigrid algorithm, the time-stepper and all the auxiliary routines such as calculating derivatives, all vary linearly with the number of grid points. See Appendix B.

wide basin simulation, which is very close to a periodic orbit, and the $\mathsf{Ro} = 8 \times 10^{-4}$ narrow basin simulation which appears to be on a chaotic attractor.

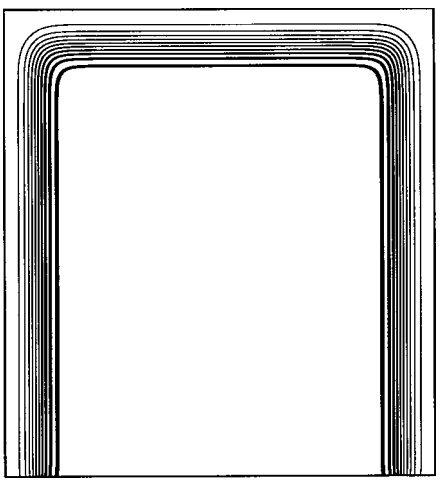


Figure 4.10: Bathymetry of wide basin. Central, deep region is now much wider than Figure 4.3(a) allowing for greater wind fetch.

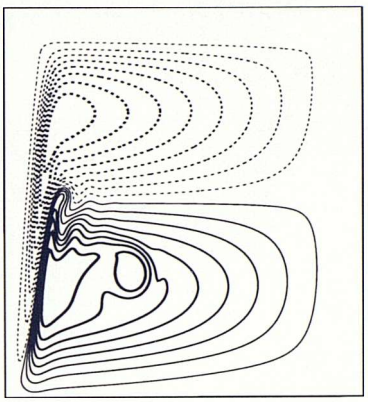
Finally in this section, a simulation with three-gyre wind forcing is presented (Figure 4.14). Three-gyre wind forcing is perhaps more realistic for the North Atlantic ([34]). However, apart from the obvious fact that there is now an extra gyre in the ocean, the qualitative aspects, in particular the stability, of the circulation appear to be unaffected by the different wind-forcing. Consequently, we concentrate on the two-gyre case which is simpler and leads to larger, better resolved features.

4.1.7 Summary

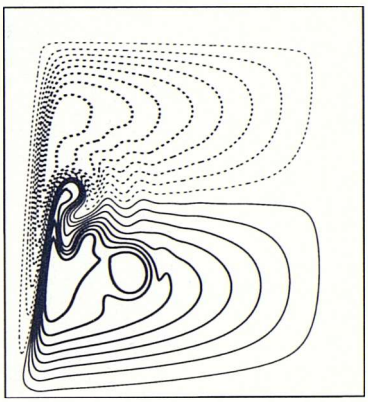
The main purpose of §4.1 is that the dynamics of the Depth-Independent-Temperature Ocean (§4.2) may be compared with the dynamics of a barotropic ocean. Starting from the ocean of Becker & Salmon[7], we change one element at a time to arrive at an ocean which is identical in every respect to the DIT ocean of §4.2 except for the baroclinicity.

In the process of examining the barotropic ocean, the following points were established:

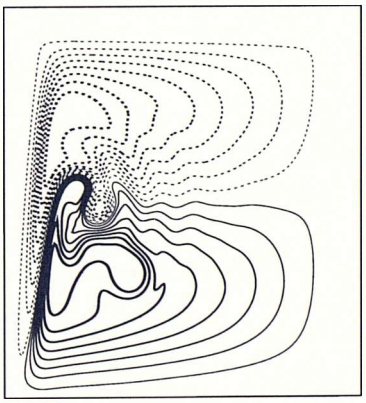
- The precise form of viscosity used in the simulations is unimportant. From a fluid dynamical viewpoint, the Laplacian, ∇^2 is the correct term. However, I found that the easiest way to perform numerical experiments was to use a linear drag and to augment this with an implicit numerical hyperdiffusion which derives from a third-order upwinding method. This removes the requirement for an extra boundary



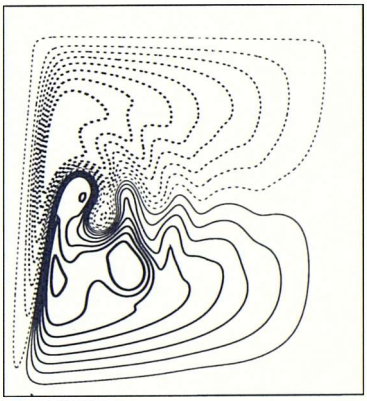
(a) $\mathsf{Ro} = 1 \times 10^{-4}$



(b) $\mathsf{Ro} = 2 \times 10^{-4}$

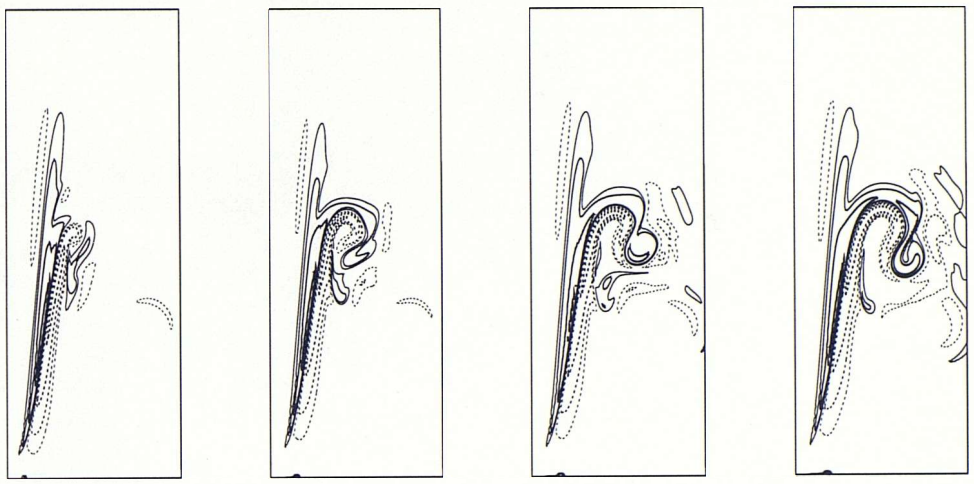


(c) $\mathsf{Ro} = 3 \times 10^{-4}$



(d) $\mathsf{Ro} = 4 \times 10^{-4}$

Figure 4.11: Snapshots of the streamfunction, ψ, for a wide barotropic ocean with wind forcing over 80% of the domain at four values of Rossby Number. The eastern boundary has a smaller effect than in the narrow basins. $-1.45 < \psi < 1.49$. The radius of the eddy increases with Ro.



(a) Ro $= 1 \times 10^{-4}$ (b) Ro $= 2 \times 10^{-4}$ (c) Ro $= 3 \times 10^{-4}$ (d) Ro $= 4 \times 10^{-4}$

Figure 4.12: Snapshots of the relative vorticity, $H\zeta$, for a wide barotropic ocean with wind forcing over 80% of the domain at four values of Rossby Number. Only the westernmost $\frac{2}{5}$ of the domain is shown. $-1400 < H\zeta < 1200$. In all cases, the negative vortex sheet is stronger than the positive vortex sheet.

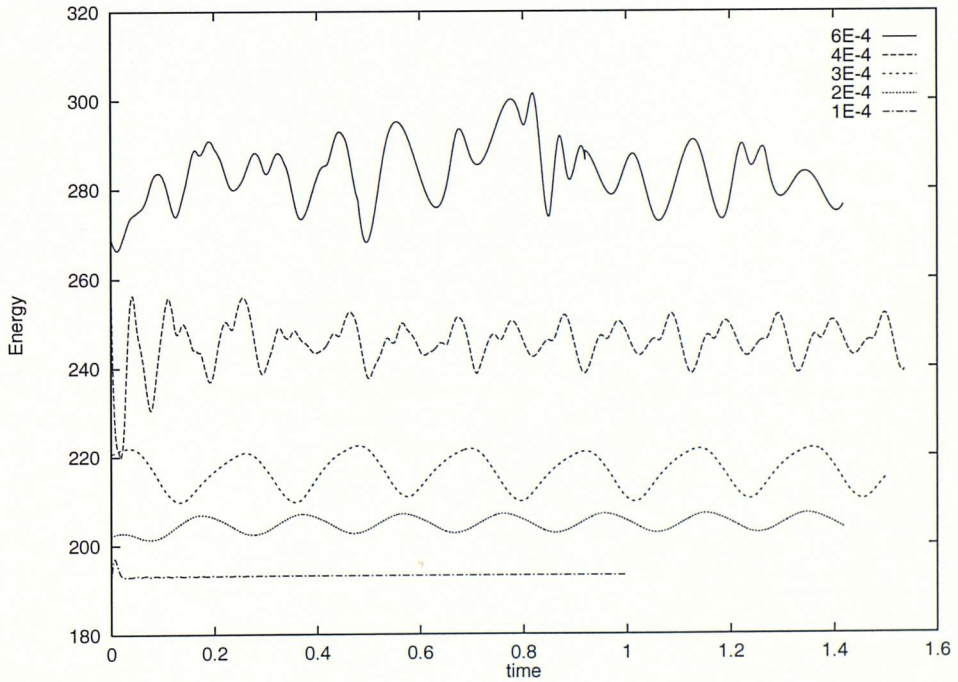
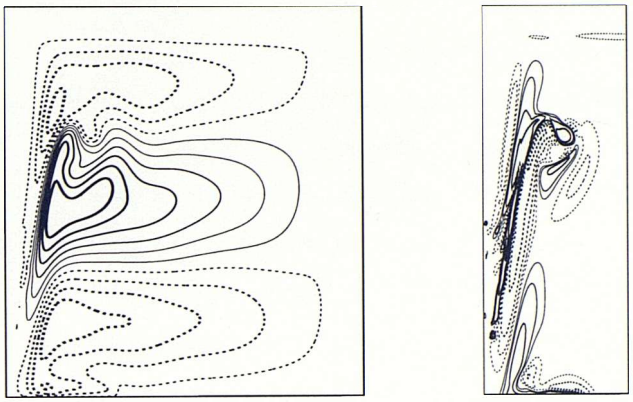


Figure 4.13: Energy profiles at different Ro for a square basin. Same as Figure 4.9 except basin is twice as wide.



(a) ψ (b) $H\zeta$

Figure 4.14: Stable steady state streamfunction and relative vorticity for a barotropic ocean with three-gyre wind-forcing. $\mathsf{Ro} = 1 \times 10^{-4}, \nu = 0.01$. Only the westernmost $\frac{2}{5}$ of vorticity basin is shown. Isarithms of ψ are equally spaced, isarithms of $H\zeta$ are log-equally spaced.

condition. The insensitivity of the dynamics to the form of the viscous term is because there is no western boundary layer.

- A sloping western boundary has a profound impact on the dynamics. A sloping northern boundary has no discernible influence. A sloping eastern boundary has a small but noticeable effect. This is slightly problematic because, using a length scale based on the width of these coastal slopes, the eastern boundary is far too close to the western boundary to realistically represent the North Atlantic Ocean. However, the eastern slope is required because the depth of the ocean must vanish smoothly at boundaries in the DIT ocean.

4.2 DIT ocean basins

In this section we perform an analogous study to that of §4.1 but for a DIT, rather than a barotropic, ocean. Our aim is to understand how the baroclinicity modifies the barotropic flow. The full DIT equations (3.2, 3.4) involve many parameters. In addition to the wind-forcing, Ro and ν of the barotropic ocean, values must be chosen for thermal forcing, Q, thermal diffusivity κ, and the equatorial parameter, δ_{eq}. It is infeasible to cover the entire parameter space of these parameters. We therefore concentrate on the manner in which Ro influences the dynamics. This is the subject of §4.2.4.

Prior to examining the Ro bifurcation sequence, it is necessary to examine the generic effects of baroclinicity and to decide upon values for all the other parameters outlined above. Probably the most important of these is the thermal forcing, Q. It has been shown in §§3.5.3, 3.6.2 that the existence of external forcing has a striking influence of the flow. Details of the thermal forcing terms are considered in §4.2.2. The Rossby Number of these initial studies is held constant at $\mathsf{Ro} = 1 \times 10^{-4}$. This value yields a steady state in the barotropic ocean (see Figure 4.13). Consequently, any instability detected in the DIT ocean can be attributed to the influence of baroclinicity.

It has been argued strongly throughout §4.1 that the explicit viscous terms (ν) are relatively unimportant because of the use of upwinding (B.1). Consequently, we continue to use the same frictional terms as in the barotropic case. In particular, we retain linear Rayleigh friction in preference to the lateral diffusion of (3.2). A brief investigation into the effect of varying κ, δ_{eq} and the wind-forcing is conducted in §4.2.3.

An overview of all the numerical experiments of this section is given in table 4.1. Unless stated otherwise in the *other params* column of table 4.1, $\kappa = 0.1, \nu = 0.01, \delta_{eq} = 0.1$ and wind forcing is double gyre, over 80% of the domain (4.2). In all experiments, the sphericity of the Earth is approximated by a β plane ($f = \beta y$). The bathymetry is always that of Figure 4.10. The boundary conditions are those of no normal heat flux and no normal flow at all boundaries.

4.2.1 Coastal slopes and the SG co-ordinate transformation

The DIT (3.2, 3.4) *require* that the depth of the ocean vanish at the boundaries[7] because it is not possible to satisfy no normal flow at vertical boundaries at all depths. To see this, note that, at vertical boundaries, the thermal wind equations (1.13) impose a condition of

$$u_{normal} = \frac{2z + H}{\tilde{f}} \frac{\partial T}{\partial s} \tag{4.4}$$

[7]This restriction is relaxed in certain special cases, see §3.3.

where $\frac{\partial}{\partial s}$ refers to the derivative tangential to the boundary. It is not reasonable (nor realistic) to enforce a boundary condition that the temperature along the boundary be constant. For example, this would require the temperature at the equator to be the same as that at the North Pole. Consequently, (4.4)$\Rightarrow u_{normal} \neq 0$. Even the depth at the equator (the southern boundary of the basin) should be made to vanish. However, the equator poses additional problems such as the singularity in (3.2) due to the division by $\tilde{f}$. This problem is dealt with in §2.1.3. Furthermore, the equator is the *one* boundary where the required condition of a constant T may almost be justified. See, for example, Figure 4.17(a) below. Closing the basin with a sloping boundary at the equator would not only be unrealistic for a model of the North Atlantic, it results in qualitatively different behaviour (see Kawase[42]) because the $\frac{f}{H}$ isopleths would then be closed. Bearing all this in mind, we elect to relax the condition of no normal flow *at all depths* to a condition of no normal *vertically averaged* flow. This is automatically satisfied by the DIT since $\psi = 0$ at all boundaries and $\int_{-H}^{0} \hat{\mathbf{u}} dz = 0$ by construction.

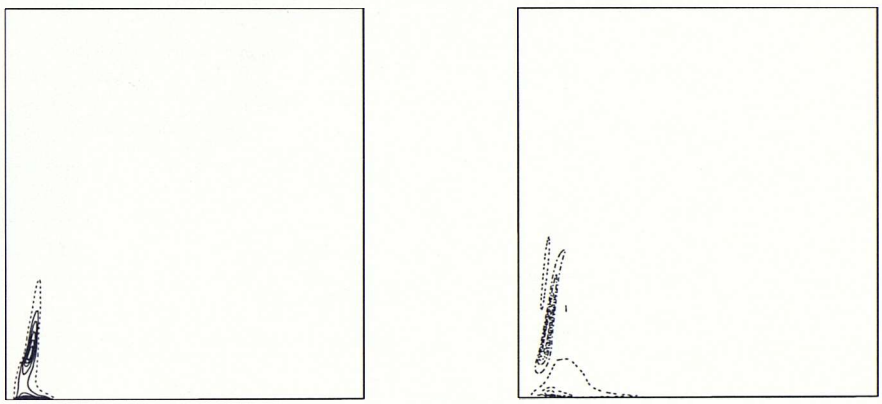
The sloping side-walls bring an extra consideration; since $\frac{\partial T}{\partial z} = 0$, the boundary condition of no normal heat flux through the bottom of the ocean cannot be satisfied

$$\frac{\partial T}{\partial n} \neq 0 \tag{4.5}$$

where n is the normal to the ocean floor $z = -H(x, y)$. This means that it is possible to lose (or gain) heat through the base of the ocean. Such heat flux is affected only by the diffusive term $\kappa H \nabla^2 T$ because the fluid velocity *is* tangential to the ocean floor; thus heat cannot be advected through this surface. We automatically compensate for any possible heat loss via the imposed heating at the surface. Since the heat flux at $z = 0$ attempts to relax the temperature to a climatological mean state (see §4.2.2 below), if heat is lost at the bottom then it will be replaced by extra heating at the top. We might expect a short time lag between the loss of heat through the bottom and its subsequent replacement at the top. However, the time-scale for the surface heating is chosen to be small in comparison to the advective time scale which should minimise any time lag. Nevertheless, it is possible, in principle, that this mechanism is responsible for some part of the high frequency small amplitude fluctuations in the potential energy (see, for example, Figure 4.34(b)). To test, and disprove, this hypothesis, I conducted a small series of simulations (not shown) in which the diffusive term in (3.4) is replaced by $\kappa \nabla.(H \nabla T)$. This term, whilst being a somewhat *ad hoc* modification to the equations, has the benefit of precluding any diffusive heat flux through $z = -H$. As such, some authors, (for example, Salmon[72]) use $\kappa \nabla.(H \nabla T)$ *a priori* in preference to $\kappa H \nabla^2 T$. However, the choice of term appears academic, since no discernible difference in the flow fields or any of the energy time series is observed between simulations using different terms.

At this stage, it is worth noting that all the Figures presented in this section represent the

flow in Semi-Geostrophic co-ordinates (1.11a,b). These differ from physical co-ordinates by $O(\epsilon) \sim 10^{-4}$. Given the small size of ϵ it is not surprising that there is virtually no visible difference between the Figures presented here and those in physical co-ordinates. Figure 4.15 shows the differences between the two flows. The important point is that the magnitudes of the differences are very small compared to the $O(1)$ magnitudes of T and ψ.



(a) $-2.4 \times 10^{-5} < \Delta T < 6.4 \times 10^{-3}$ (b) $-8.9 \times 10^{-4} < \Delta\psi < 4.4 \times 10^{-3}$

Figure 4.15: Difference between flows in physical and semi-geostrophic space for simulation **A**. The magnitude of the difference is very small.

In the case of the DIT, where the surface values of T and ψ are calculated, the relationship between the two co-ordinate frames is given by

$$x_c = x_s - \epsilon T_x \frac{H}{2\tilde{f}^2}. \tag{4.6}$$

Consequently, we would expect the biggest differentials to occur in the fast flowing WBC and near the equator where $f^2 \ll 1$. This is indeed seen to be the case in Figure 4.15. However, the equatorial parameter, δ_{eq}, prevents the error blowing up at the equator.

The co-ordinate transformation also implies that terms which are constant in physical space are not constant in SG space. For example, Taylor's Theorem yields $f(x_s, y_s) = f(x_c, y_c) + \epsilon \frac{\partial f}{\partial x}\left(\frac{\hat{v}}{f}\right) - \epsilon \frac{\partial f}{\partial y}\left(\frac{\hat{u}}{f}\right) + O(\epsilon^2)$. The question arises of what value of z to use when applying the co-ordinate transformation. Since we may consistently neglect $O(\epsilon^2)$ terms, the transformation need only be applied to $O(1)$ terms involving f. There is only one of these; $J(\psi, \frac{f}{H})$. Since ψ represents a vertically integrated quantity, it is appropriate to take a vertical integral of the transformation. Because, $\int_{-H}^{0} \hat{\mathbf{u}} dz = 0$, all the $O(\epsilon^2)$ terms vanish and it is consistent to use $f_s = \beta y_s$ in the $J(\psi, \frac{f}{H})$ term.

sim.	Ro $\equiv \epsilon$	$\mathcal{T}$	λ	other params	comments
A	1×10^{-4}	5	5	-	thermal forcing too weak
B	1×10^{-4}	5	10	-	acceptable forcing
C	1×10^{-4}	5	20	-	acceptable forcing
D	1×10^{-4}	5	50	-	thermal forcing too strong
E	1×10^{-4}	10	10	-	acceptable forcing
F	1×10^{-4}	10	20		complex chaotic flow
G	1×10^{-4}	10	50	-	thermal forcing too strong
H	0.5×10^{-4}	5	10	-	steady state
I	0.5×10^{-4}	10	10	-	steady state
J	2×10^{-4}	5	10	-	quasi-periodic (period 2)
K	2×10^{-4}	10	10	-	quasi-periodic
L	4×10^{-4}	5	10	-	quasi-periodic (period 4)
M	4×10^{-4}	10	10	-	chaotic flow, WBC weakened
N	4×10^{-4}	5	10	$\kappa = 0.01$	similar to **L**, more energetic
O	4×10^{-4}	5	10	$\kappa = 0.05$	similar to **L**, more energetic
P	4×10^{-4}	5	10	$\kappa = 0.2$	similar to **L**, less energetic
Q	4×10^{-4}	5	10	$\delta_{eq} = 0.2$	similar to **L**, more energetic
R	4×10^{-4}	5	10	$\delta_{eq} = 0.05$	equatorial bdy layer not resolved
S	1×10^{-4}	5	10	three gyre wind	similar to two gyre
T	4×10^{-4}	5	10	no *JEBAI*	less baroclinic instability

Table 4.1: Summary of numerical simulations. Defaults for *other params* is $\kappa = 0.1, \nu = 0.01, \delta_{eq} = 0.1$, wind-forcing is double gyre (4.2, $\delta_w = 0.1$).

We now consider the forcing terms: W, Q. These are both applied at the surface. Hence, $z = 0$ is the appropriate value to use in the transformation. However, both wind-forcing (4.2) and the thermal forcing (4.7, below) take highly idealised forms which differ from reality by a factor much greater than ϵ. Consequently, in order to preserve as much simplicity as possible, no transformation is made to W or Q either.

Finally, consider the bathymetry. It is shown in Salmon[73] that $z_c = 0, -H_c$ correspond to $z_s = 0, -H_s$ respectively where $H_c = H(x_c, y_c)$ and $H_s = H(x_s, y_s)$. Therefore, no transformation is required for the bathymetry. This is not very important in the present investigation because we can argue, as above, that the topography is so idealised, that executing an $O(\epsilon)$ transformation at every time step would be churlish. However, if the DIT were to be used in a model with realistic bathymetry, then repeatedly having to modify H_s would impose severe limitations on the speed and usefulness of any algorithm.

4.2.2 Thermal forcing

Our ocean is thermally forced by attempting to relax the surface temperature to a prescribed steady state. In accordance with a model of the North Atlantic this prescribed temperature is warm (zero) at the equator (bottom of the model domain) and cold (negative) at the North Pole (top of the domain). It is independent of the longitude. Recall that absolute values are irrelevant; we are only concerned with thermal gradients. Thus,

$$\mathrm{Q}(x,y) \equiv \lambda\left[T(x,y,t) + \mathcal{T}y\right]. \tag{4.7}$$

We have two parameters under our control. λ is an inverse time-scale specifying how rapidly the SST is relaxed to $T = -\mathcal{T}y$. This time-scale should be chosen such that it is smaller than the advective time-scale (specified by ϵ) and the diffusive time-scales (specified by ν and κ). $\mathcal{T}$ is a positive[8] constant specifying the global temperature difference between the northern and southern boundaries of the domain.

The buoyancy scales like $\theta \sim \frac{f_0 UL}{H_0}$ and it is related to the temperature via $\theta \equiv \alpha_T g T$ where $\alpha_T \approx 2.5 \times 10^{-4}(^oC)^{-1}$ is the coefficient of thermal expansion for water and $g \approx 10ms^{-2}$ is, as usual, the acceleration due to gravity. The observed large scale thermal gradient of the SST is ([87]) about 4^oC[9] over a longitudinal distance of $1000km$. This yields an observed buoyancy gradient of $\frac{\Delta\theta}{\Delta y} \approx 10^{-8}s^{-2}$. The SST is not the same as the vertically averaged temperature over the whole depth of the ocean. Therefore, in our non-dimensionalisation of buoyancy, it is appropriate to consider H_0 to be the depth of the mixed layer ($H_0 = 100m - 200m$) rather than the depth of the entire ocean ($4km$). We retain the values of $U = 2 \times 10^{-3}ms^{-1}$, $f_0 = 10^{-4}s^{-1}$, $L = 4 \times 10^6 m$ that were used in the scalings for the barotropic ocean. This gives a temperature scale of $10^{-9} - 2 \times 10^{-9}s^{-2}$. Dividing the observed buoyancy range by the buoyancy scale gives the magnitude of the non-dimensional buoyancy, that is, of $\mathcal{T}$, to be $\mathcal{T} = 5 - 10$. The manner in which these figures are derived may seem somewhat *ad hoc*. However, it agrees (roughly speaking) with the value of the mixed layer buoyancy used by Salmon[72] of $\theta = 100$. Salmon & Ford[75] then argue that the buoyancy range of the entire ocean is "an order of magnitude less" than that of the mixed layer and so use a value of $\mathcal{T} = 2 - 5$ in their simulations which are similar to those of this section. I have found that a value of $\mathcal{T} = 2$ does not seem to attach enough weight to the baroclinic terms; the simulations appear to show that the temperature is simply being advected around by the barotropic flow (3.4) and the nonlinear feedback terms of (3.2) do not modify the circulation.

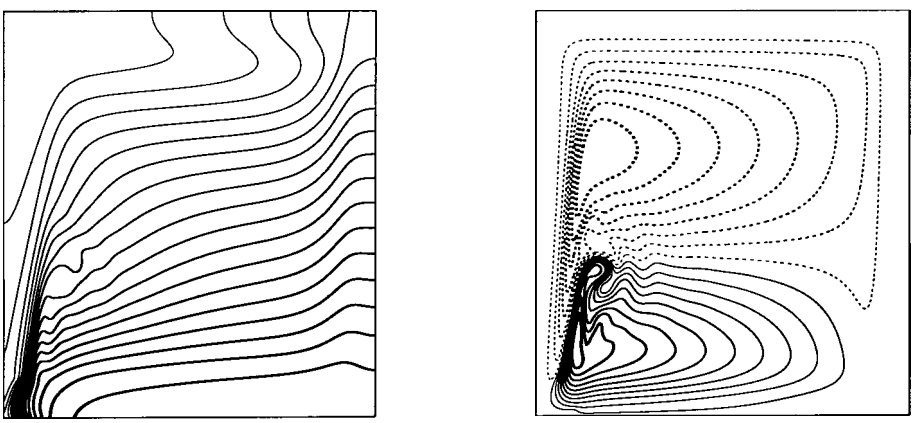
Salmon & Ford[75] have no thermal relaxation parameter, λ. Young[86], however, derives the whole mixed layer approximation based on using a relaxation parameter (τ^{-1} in the

[8] $\mathcal{T}$ is positive to ensure that it is hotter at the equator ($y = 0$) than at the North pole ($y = 2$).

[9] The same author also uses a value of 3^oC in an earlier paper, [86].

notation of [86]). The model is derived by expanding all the dynamic variables in a small parameter $\epsilon_\tau \equiv \frac{\tau}{t_0}$[10] which scales like $\epsilon_\tau = \mathcal{R}\sqrt{\mathsf{Ro}}$ where $\mathcal{R}$ is an (unspecified) $O(1)$ constant. We adopt this scaling and using the values of $\mathsf{Ro} \approx 10^{-4} - 10^{-3}$ obtained in §4.1.2 yields $\lambda \approx 30 - 100$. However, experimentation has shown that this value seems to enforce the climatological conditions too strongly. Figures 4.23–4.26 show the circulation patterns for $\lambda = 20, 50$. We therefore choose to concentrate, initially on $\lambda = 10$. This corresponds to $\mathcal{R} \approx 10$ in the scaling of Young[86].

Influence of $\mathcal{T}$. A value of $\lambda = 10$ corresponds, in dimensional units, to a time frame of 60 days for the relaxation. This is a seasonal time scale which is acceptable if we consider Q to parametrise atmospheric effects. Before a discussion of the influence of λ, we first consider the effects of baroclinicity (that is, of non-zero $\mathcal{T}$). The temperature and streamfunction for $\mathcal{T} = 5, 10$ are shown in Figures 4.16, 4.17. The corresponding relative vorticities are shown in Figure 4.28(a, d). Figures 4.18, 4.19 show the contribution near the western slope of the four conservative Jacobian terms in the barotropic equation (3.2) for the $\mathcal{T} = 5$ case.

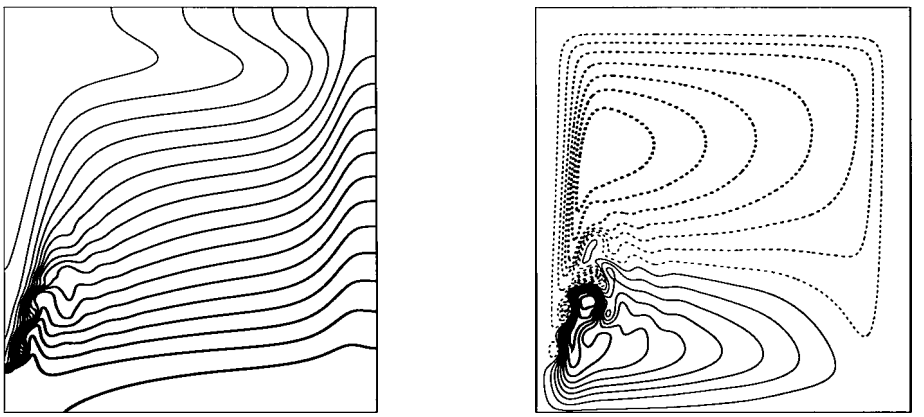


(a) T (b) ψ

Figure 4.16: $\lambda = 10, \mathcal{T} = 5$. Simulation **B**. $-1.45 < \psi < 1.60$, positive values are solid, negative values are dashed; $-2\mathcal{T} < T < 0$; darker isopleths represent larger magnitudes. Unless otherwise indicated, the ranges of ψ, T and isopleth conventions apply to all figures in this section.

Apart from on the western coastal slope, the temperature fields appear very similar. In the deep, flat interior of the ocean, the isotherms are approximately zonal. For a specific

[10] [86] refers to this variable as ϵ. I have appended the subscript to avoid confusion with ϵ of this thesis which is the Rossby Number.

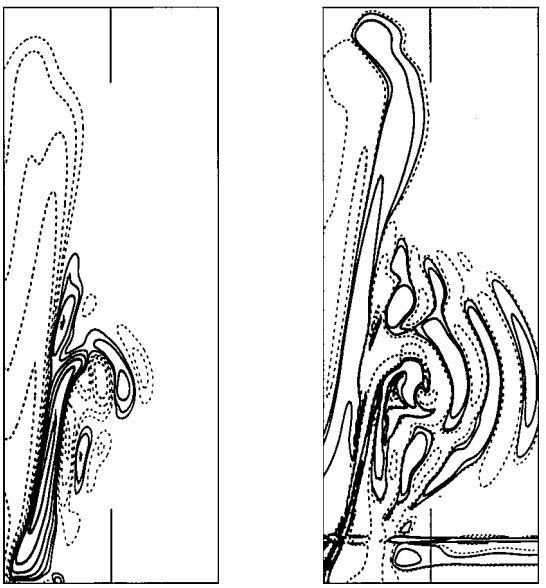


(a) T (b) ψ

Figure 4.17: $\lambda = 10, \mathcal{T} = 10$. Simulation **E**.

latitude, the eastern edge is slightly warmer than the western edge. This is also true of the North Atlantic. The temperature in this region is rather passive. *JEBAR* can have no influence because of the flat bottom and *JEBAI* is negligible because Ro is small and the thermal gradients are not great. On the eastern and northern slopes, T is advected strongly in an anticlockwise direction. This is due to a combination of the wind-forcing (which dominates the advection of ψ along f/H isolines, Figure 4.3(b)) and *JEBAR* . Both these terms contribute cyclonic rotation to the flow. To see that this is true of the *JEBAR* term note that, on the eastern slope, $J(T,H) = -\partial_y T \partial_x H$. Both derivatives are negative so $J(T,H) > 0$. The final step is to recall that $\frac{\partial \zeta}{\partial t} = -\frac{1}{2}J(T,H) + ...$ Consequently, a negative *JEBAR* corresponds to a more positive (that is, cyclonic) relative vorticity. *JEBAR* is very much weaker than the barotropic effect as can be observed by the fact that the T fields are so similar on the eastern and northern slopes, yet *JEBAR* is approximately twice as large in the $\mathcal{T} = 10$ case.

The temperature fields differ most notably in the southern half of the basin on the western slope. This region is shown in more detail in Figure 4.20. Both $\mathcal{T} = 5, 10$ simulations exhibit very strong thermal gradients. This is expected because the barotropic flow is vigorously advecting cold water southwards towards $y = 0$. However, the sub-tropical gyre is recirculating warm water northwards. A temperature *front* therefore forms where the two gyres meet. The most striking difference between Figure 4.20 (a) and (b) is that in the $\mathcal{T} = 5, (a)$ case, the front curves towards the south-western corner. This path is analytically obtained, for the asymptotic limit $\mathsf{Ro} = 0$; $\nu, \kappa \ll 1$, by Ford[27]. It is also shown that as $\mathcal{T}$ increases, the front moves progressively closer to the western boundary,

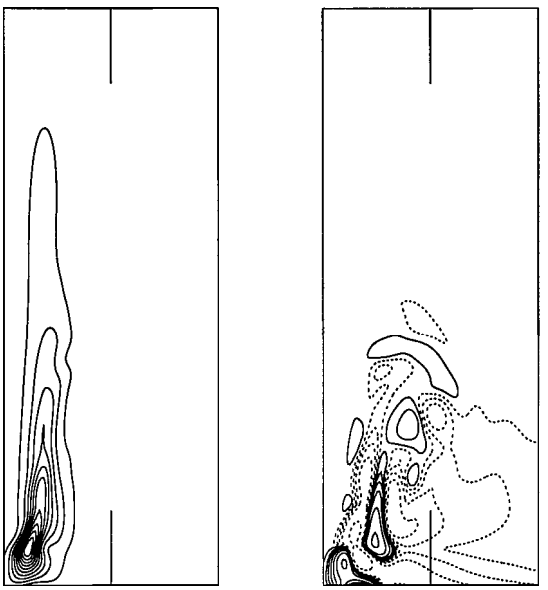


(a) $J\left(\psi, \frac{f}{H}\right)$ (b) $\epsilon J\left(\psi, \frac{\zeta}{H}\right)$

Figure 4.18: $\lambda = 10, \mathcal{T} = 5$, simulation **B**. Contributions of the Jacobian terms in the DIT to the dynamics; (a) $-10^4 < J\left(\psi, \frac{f}{H}\right) < 10^4$, isopleths are log-equally spaced; (b) $-6 < \epsilon J\left(\psi, \frac{\zeta}{H}\right) < 7$, isopleths are equally spaced. The extent of the western continental slope is indicated by vertical bars at the North and South of the domain.

until at some critical value of $\mathcal{T}$ the solution breaks down. Figure 4.17(a) reveals that front attaches itself to the western boundary. That the point of attachment to the boundary moves clockwise with increasing $\mathcal{T}$ can be attributed to the increasing magnitude of the *JEBAR* term. On the western slope, the *JEBAR* effect is opposite to that on the eastern slope. That is, $J(T, H) > 0$ (Figure 4.19(a)) and it contributes an anticyclonic component to the relative vorticity. Consequently, a strong *JEBAR* effect will rotate the temperature field in a clockwise manner.

This effect is also observed at the south-west corner of the ψ field. (Figures 4.16(b), 4.17(b)). In this respect *JEBAR* acts to oppose the barotropic topographic driving of the f/H isopleths by attempting to align the gyre boundary with lines of constant latitude. That is, the southern tail of the vortex sheets is moved northwards, away from the troublesome south-western corner. Welander[85] compares results from barotropic and two-layer models to suggest that the barotropic model greatly over-estimates the importance of bottom topography. The result here, however, is that the barotropic model *slightly* over-

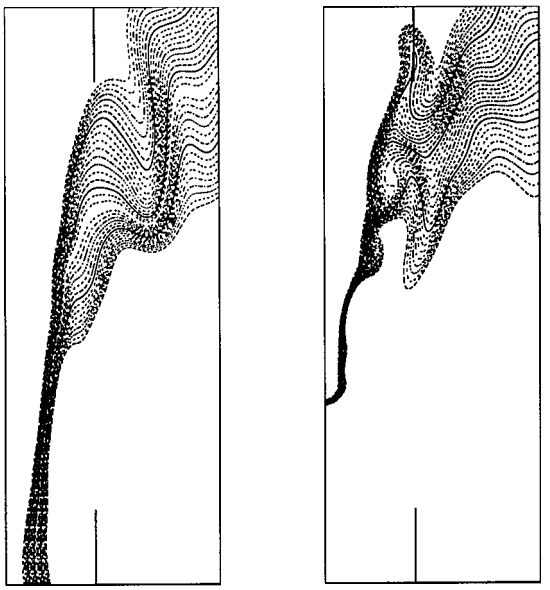


(a) $\frac{1}{2}J(T,H)$ (b) $\epsilon J(T,\Gamma)$

Figure 4.19: $\lambda = 10, \mathcal{T} = 5$, simulation **B**. Contributions of the Jacobian terms in the DIT to the dynamics, (a) $0 < \frac{1}{2}J(T,H) < 58$, isopleths are equally spaced; (b) $-3 < \epsilon J(T,\Gamma) < 7$, isopleths are equally spaced.

estimates its importance since Figures 4.16(b), 4.17(b) bear a greater similarity to Figure 4.11(a) than to Figure 4.2(a). Welander's result depends on the topography not outcropping above the lower layer. This precludes the vanishing coastal slopes of this thesis which is one of the drawbacks of traditional two-layer models.

The intense thermal gradients present on the western slope suggest that baroclinic instability may occur in this region. Figure 4.19(b) shows that *JEBAI* takes its largest values here. The time series of baroclinic and barotropic kinetic energies (Figures 4.29(b, c), 4.30(b, c)) indicate the presence of high-frequency, small amplitude oscillations. These are clearly not related to the barotropic eddy being shed from the off-shore meandering WBC (Figure 4.11(d)) of which there is no evidence in Figures 4.16(b), 4.17(b). It appears that the energetic oscillations are caused by instabilities in the neighbourhood of the thermal front. Close inspection of Figure 4.17(b) reveals the presence of two small cyclonic eddies in this region. These eddies are more clearly visible in the relative vorticity (Figure 4.28(d)). The baroclinic instability is caused by a combination of *JEBAI* and *JEBAR* . The influence of *JEBAI* is revealed by the appearance of the two eddies in Figure 4.19(b).



(a) $\mathcal{T} = 5$, range is $(-1.8 \ldots -6.6)$

(b) $\mathcal{T} = 10$, range is $(-8.4 \ldots -13.2)$

Figure 4.20: Temperature gradients on the western slope are very sharp. $\lambda = 10, \mathsf{Ro} = 1 \times 10^{-4}$. Only a small range of isotherms is visible.

To see that *JEBAR* also contributes to the instability, note that the cold water advected down from the North is located further inshore than the warm, equatorial water. This is the correct configuration for *JEBAR* to create instability (see §3.6.1).

A further influence of *JEBAR* is to shift the boundary between the sub-tropical and sub-polar gyres in a southerly direction. Inspection of the relative magnitudes in Figures 4.18, 4.19 reveals that the leading order behaviour is

$$J\left(\psi, \frac{f}{H}\right) = \mathsf{W}(x,y) - \frac{1}{2}J(T,H) < \mathsf{W}(x,y). \tag{4.8}$$

The right hand side of (4.8) can be regarded as a modified wind-stress-curl (MWSC). The point of zero MWSC occurs at a more southerly latitude than the point of zero WSC. As one would expect, the *JEBAR* effect becomes more significant with increasing $\mathcal{T}$ and the gyre boundary is pushed further south. See Figures 4.16(b), 4.17(b). The anticyclonic vorticity that *JEBAR* contributes to the flow is further illustrated by a comparison of the relative vorticity in the barotropic (Figure 4.12) and present (Figure 4.28(a)) cases.

In the DIT ocean, the cyclonic vortex sheet is rotated much further around the northern tip of the anticyclonic sheet. In fact, the cyclonic sheet is pulled so far around that a

portion of the negative vorticity is pinched off. This causes a recirculation gyre to form on the southern flank of the WBC. Figure 4.21 shows, in more detail, the streamfunction of simulation **E** in the separation region. In fact, there also appears to be another recirculation gyre on the northern flank of the WBC. This seems to be related to the eddies which are being generated by baroclinic instability further down the western slope so this is a *JEBAI* related effect. Moreover, in contrast to the southern recirculation gyre which is visible in every simulation in this section, the northern recirculation gyre is a much less robust feature.

The recirculation gyres are responsible for the dramatic increase in transport from of the Gulf Stream as it leaves the continental slope from $30Sv$ at Florida to $100Sv$ at the Grand Banks (see Chapter I, Johns *et al.*[39]). Earlier studies (Özgökmen *et al.*[56], Chao *et al.*[16]) have suggested that these gyres are an inertial, rather than a baroclinic, effect. There is some evidence of the southern recirculation gyre in the barotropic oceans of Figure 4.11 but it seems apparent that *JEBAR* has a significant role to play in enhancing this gyre. Moreover, the formation of barotropic, inertial recirculation gyres seems to be dependent on the choice of boundary condition at the western extremity of the ocean; no-slip conditions lead to the formation of a viscous sub-layer on the boundary, which in turn, is conducive to the formation of a recirculating gyre. On the other hand, if free-slip conditions are applied on the western boundary, there is no viscous sub-layer and hence the jet is more likely to penetrate eastwards. In this chapter, due to the continental slope, there is no viscous sub-layer and so the barotropic circulation does not include any recirculation gyre.

It is unclear whether *JEBAI* contributes to the formation of the southern gyre. Although the positive regions are stronger than the negative regions in Figure 4.19(b), the latter are more widespread and the mean value of *JEBAI* is negative.

Influence of λ. We now examine the response of the ocean to variations in the thermal forcing parameter, λ in (4.7). Figures 4.22 – 4.26 illustrate the temperature fields for $5 \leq \lambda \leq 50$. The corresponding relative vorticities are shown in Figure 4.27, 4.28. Increasing the strength of the relaxation parameter has two clearly visible, related effects on the temperature field: isotherms depart from isolines of latitude by a decreasing amount, and cold, Arctic water is advected less far south down the western boundary. These two effects are most striking upon comparison of the extremal values of $\lambda = 5, 50$ (Figures 4.22(a), 4.26(a) respectively). This influence is easily understood by noting that as λ increases, the forcing term, Q of (3.4), increases in importance relative to the advective term, $J(\psi, T)$.

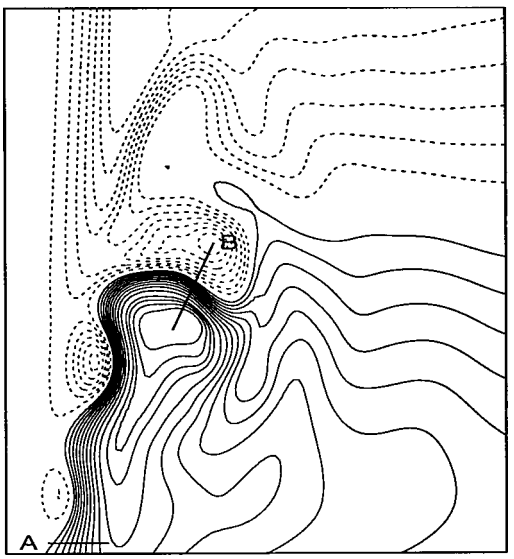
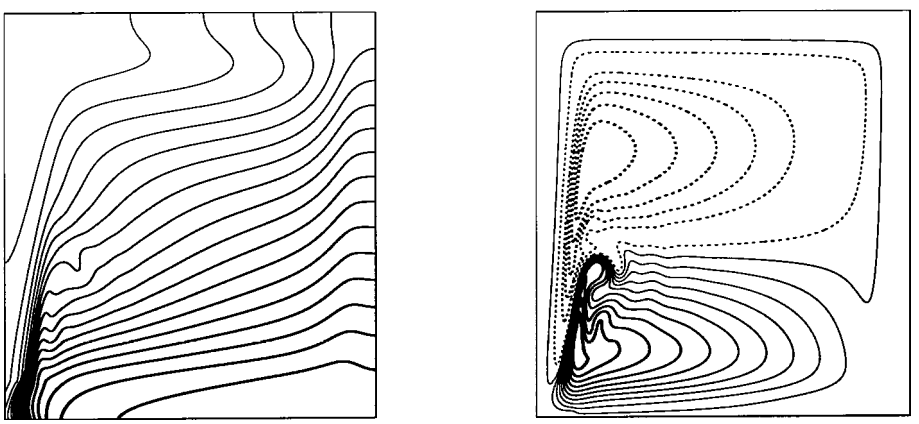


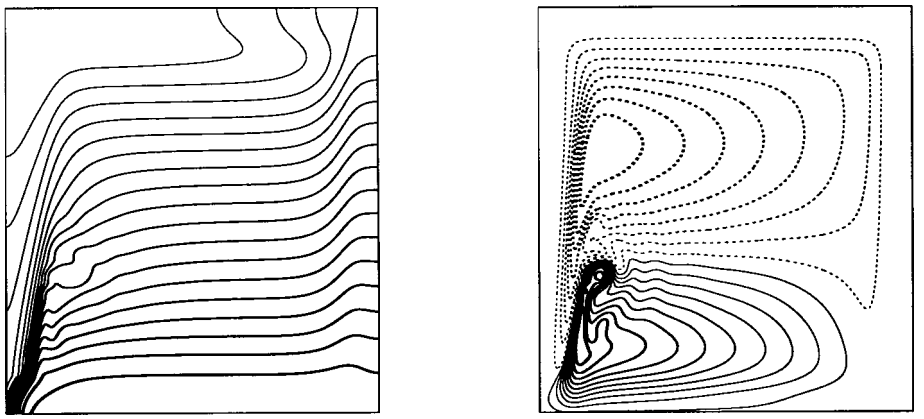
Figure 4.21: The streamfunction, ψ, in the neighbourhood in which the WBC dismounts the continental slope; simulation **E**. There are strong recirculation gyres on both flanks of the WBC. If the mass-transport at **A** is assumed to be $30Sv$, then the transport at B is approximately $83Sv$. The meanders of the WBC on the continental slope are clearly visible.



(a) T (b) ψ

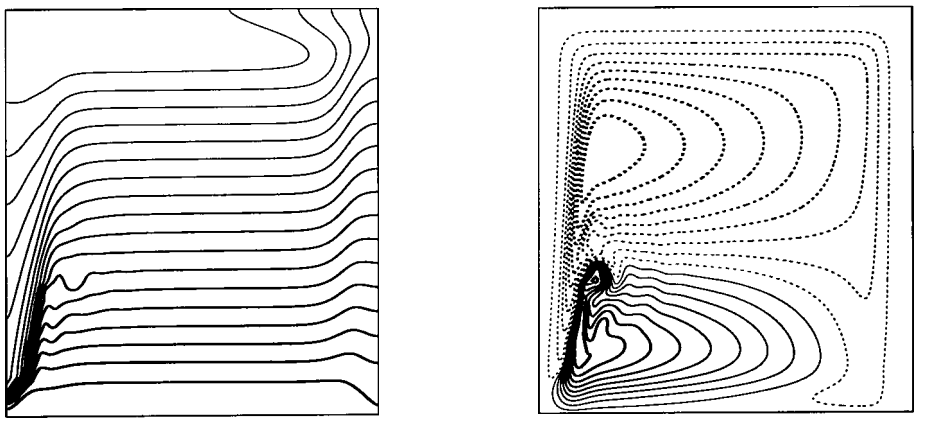
Figure 4.22: $\lambda = 5, \mathcal{T} = 5$. Simulation **A**.

Energy time-series. Finally in this subsection, we examine the energy time series for simulations **A-G**. Recall that for $\mathsf{Ro} = 1 \times 10^{-4}$ the barotropic ocean has a stable steady



(a) T (b) ψ

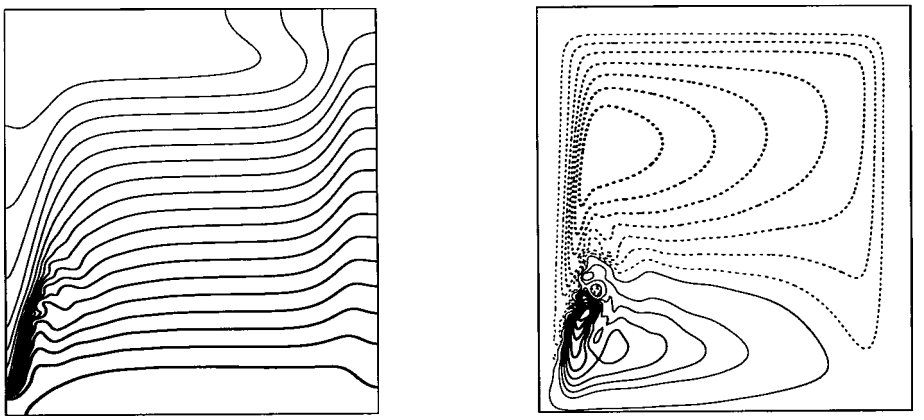
Figure 4.23: $\lambda = 20, \mathcal{T} = 5$. Simulation **C**.



(a) T (b) ψ

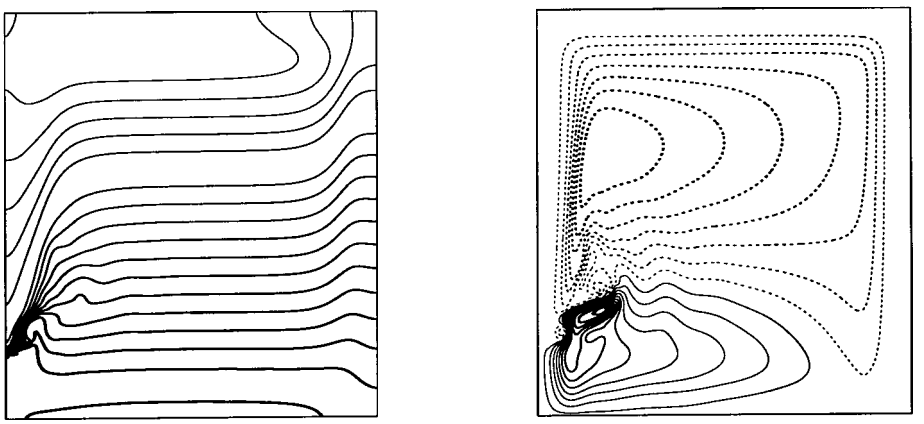
Figure 4.24: $\lambda = 50, \mathcal{T} = 5$. Simulation **D**.

state. It appears from the total energy profiles (Figures 4.29(a), 4.30(a)) that the DIT ocean is also steady. However, the total energy is dominated by potential energy, most of which is unavailable for conversion into kinetic energy. Consideration of the baroclinic (Figures 4.29(b), 4.30(b)) and barotropic (Figures 4.29(c), 4.30(c)) kinetic energies shows that the flow is *not steady.* Instead, its evolution is characterised by high frequency, small amplitude oscillations. Comparison of the relative magnitudes of the kinetic and total energies confirms that the potential energy is much greater than the kinetic energy and



(a) T (b) ψ

Figure 4.25: $\lambda = 20, \mathcal{T} = 10$. Simulation **F**.



(a) T (b) ψ

Figure 4.26: $\lambda = 50, \mathcal{T} = 10$. Simulation **G**.

reveals why these oscillations are not visible in the total energy. It has already been noted that the oscillations are related to small baroclinic eddies in the neighbourhood of the sharp temperature contrast on the western slope.

An interesting feature illustrated by the kinetic energy (KE) time series is the relatively small amplitude of the oscillations in the $\lambda = 50$ simulations. This is more noticeable in the $\mathcal{T} = 10$ series. Figure 4.30(c) also shows that the mean barotropic KE of simulation **G** is significantly less than in simulations **E, F**. The corresponding result for $\mathcal{T} = 5$ is also

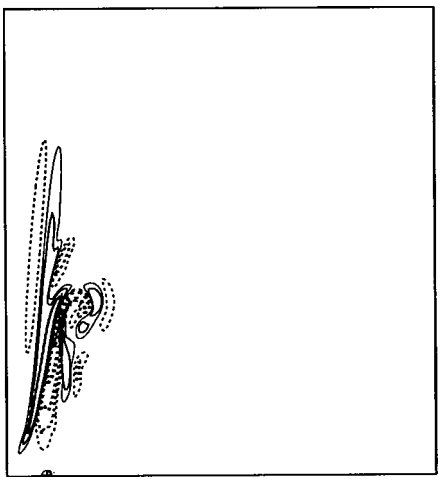
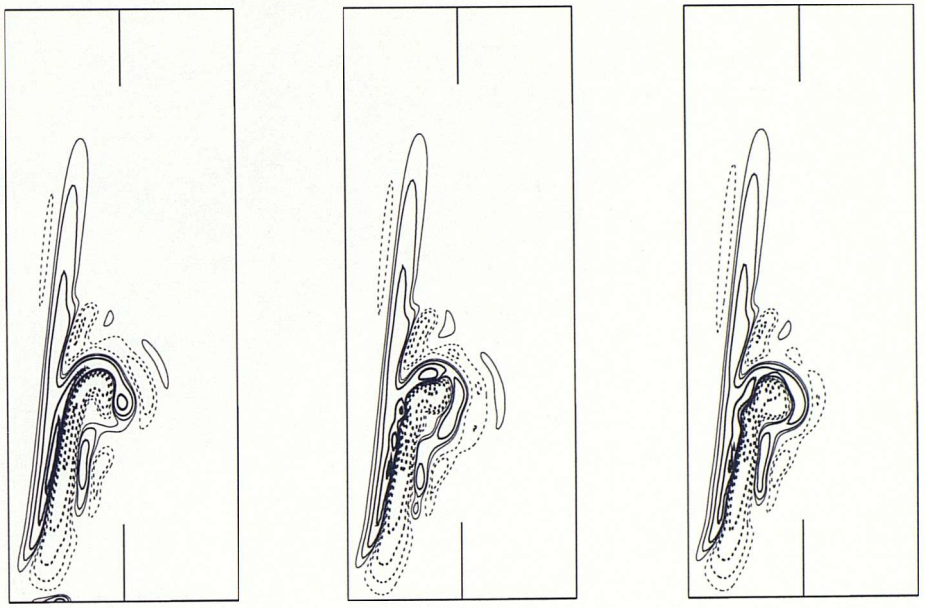


Figure 4.27: The relative vorticity, $H\zeta$ for the entire basin, $\lambda = 5, \mathcal{T} = 5$, simulation **A**. All the activity is confined to the western $\frac{2}{5}$ of the domain. $-1700 < H\zeta < 1300$. The negative vortex sheet is stronger than the positive sheet by a larger margin than in the barotropic simulations. Isopleths are log-equally spaced. Negative values are dashed and positive values are solid. Unless otherwise stated, this range and isopleth convention applies to all relative vorticity plots in this section.

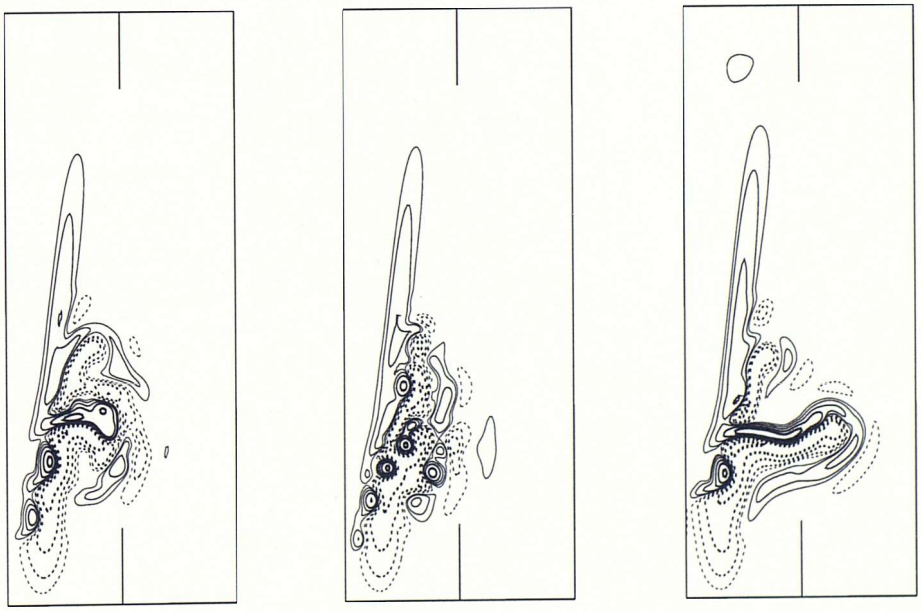
shown to be true in Figure 4.29(c). This suggests that Q is too domineering. The thermal structure is *so* rigidly determined by Q that large thermal gradients are never built up. Hence, baroclinic instability is reduced. Consequently, both the number of eddies shed from the WBC and the amount of energy converted into barotropic KE are reduced. At the other end of the spectrum, the oscillatory behaviour of simulation **A** is also weak. In this case, the thermal forcing is too weak and advection dominates. The intermediate cases of $\lambda = 10, 20$ (simulations **B**, **C**, **E**, **F**) are the most active. There seems to be a balance between the advective and the forcing terms.

Clearly, we expect the $\mathcal{T} = 10$ simulations to be more active than their $\mathcal{T} = 5$ counterparts since temperature gradients are approximately twice as great. Thus, it is no surprise that the mean baroclinic KE, and total energy, and the amplitude of the oscillations are all larger in the former case. Increased baroclinic instability also results in more barotropic KE being produced.

A final noteworthy feature of the total energy profiles is the speed at which the circulation reaches an equilibrium. Larger values of λ correspond to shorter time-scales for the thermal forcing and so one would expect equilibrium to be reached more rapidly. This is borne out by Figures 4.29(a), 4.30(a).

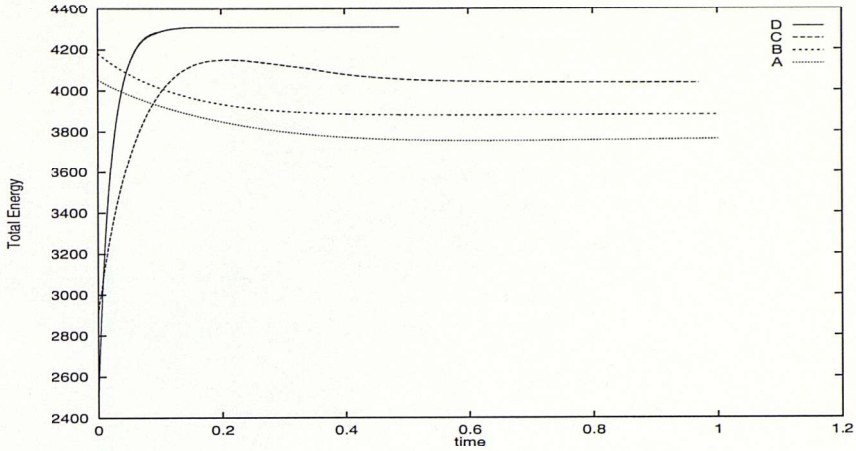


(a) $\lambda = 10, \mathcal{T} = 5$ (b) $\lambda = 20, \mathcal{T} = 5$ (c) $\lambda = 50, \mathcal{T} = 5$

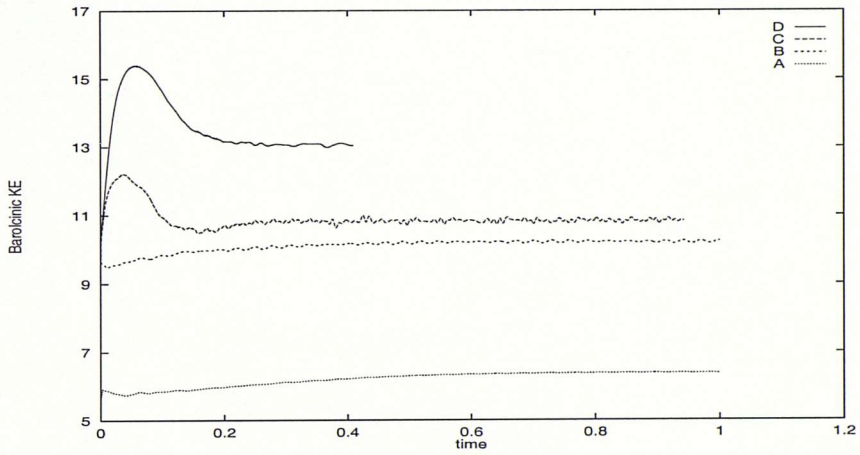


(d) $\lambda = 10, \mathcal{T} = 10$ (e) $\lambda = 20, \mathcal{T} = 10$ (f) $\lambda = 50, \mathcal{T} = 10$

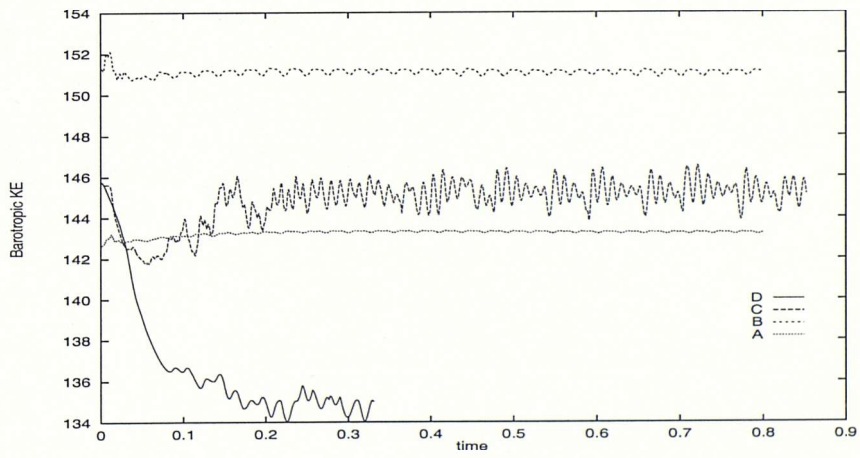
Figure 4.28: The relative vorticity, $H\zeta$ for the western-most $\frac{2}{5}$ of the domain, simulations **B–G**.



(a) Total Energy

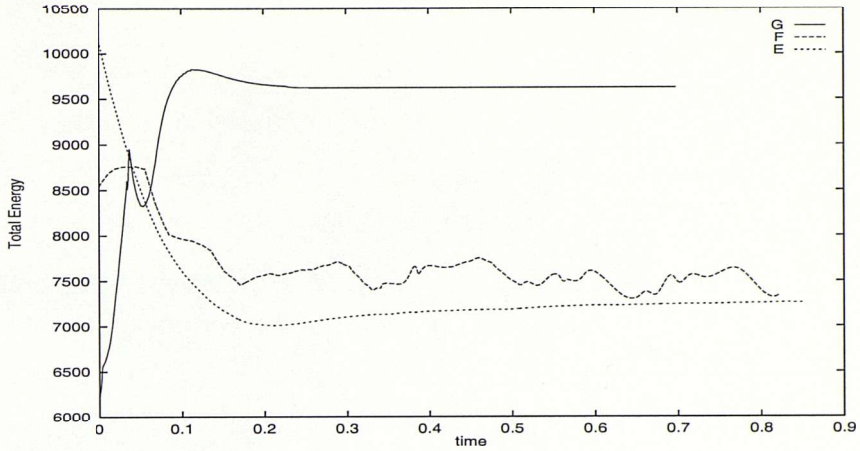


(b) Baroclinic KE

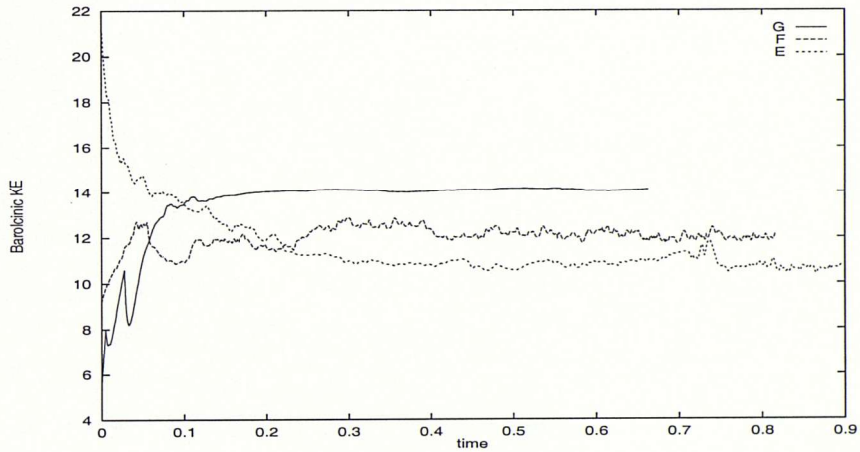


(c) Barotropic KE

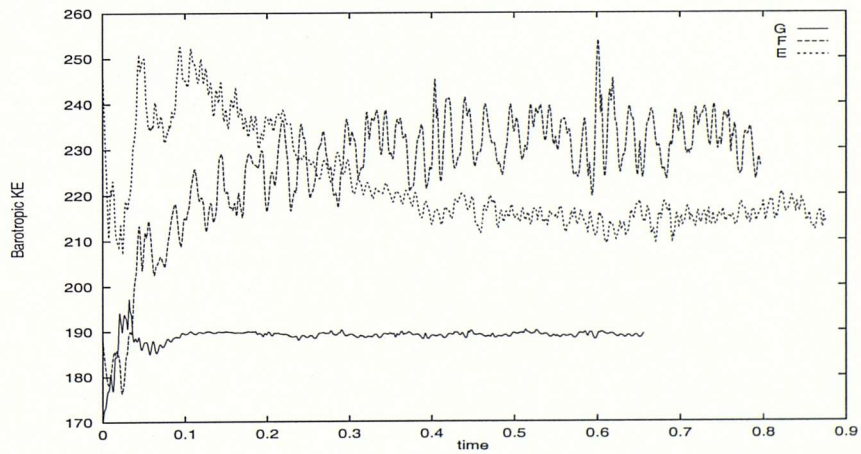
Figure 4.29: Energy profiles for simulations with varying thermal parameter λ; $\mathsf{Ro} = 1 \times 10^{-4}, \nu = 0.01, \kappa = 0.1, \mathcal{T} = 5$. Experiments **D, C, B, A**. In all energy plots within this section, time is scaled on $\mathsf{Ro} = 2 \times 10^{-4}$ so a non-dimensional time of $t = 1$ corresponds to 600 days. In contrast to most other energy plots, time-series are *not* vertically offset.



(a) Total Energy



(b) Baroclinic KE



(c) Barotropic KE

Figure 4.30: Energy profiles for simulations with varying thermal parameter λ; $\mathsf{Ro} = 1 \times 10^{-4}, \nu = 0.01, \kappa = 0.1, \mathcal{T} = 10$. Experiments **G, F, E**. In contrast to most other energy plots, time-series are *not* vertically offset.

4.2.3 Additional parameters

In addition to the two thermal forcing parameters (§4.2.2) and the Rossby Number (§4.2.4), there exist a further four parameters to be studied: friction, ν; thermal diffusivity, κ; the equatorial parameter δ_{eq} (see §2.1.3) and the wind-forcing, $\mathsf{W}(x,y)$. This section investigates the effect of varying these parameters.

Energy time-series for simulations **N–R** are shown in Figure 4.31. The most important point to take from this Figure is that, with the exception of simulation **R**, the nature (that is, the magnitude, frequency and variance) of the oscillations is remarkably similar.

Diffusion. Experiments in the barotropic case suggest that the frictional parameter, ν, has a minimal effect on the dynamics. This is because of the numerical upwinding (B.1) which controls the flow. In all simulations, I continue to use the same value as in the barotropic simulations, that is, $\nu = 0.01$. The numerical solution of the temperature advection-diffusion equation, (3.4), does not include any upwinding and so the possibility exists that the magnitude of κ will have an appreciable effect on the flow. However, Figure 4.31 shows that this is not the case. As expected, a smaller value of κ results in a slightly higher mean potential and total energy state. The frequency and variability of the oscillations in both forms of kinetic energy (Figure 4.31(c,d)) remains unchanged, although the magnitude of the oscillations does increase slightly. The results of §3.4 suggest that the radius of those eddies which are produced by baroclinic instability (that is, the eddies shed over the continental shelf) should be related to κ. However, this is impossible to determine at the resolution used here. Since the value of κ is chosen somewhat arbitrarily, it is reassuring to observe that varying it by one order of magnitude does not have a big qualitative influence on the circulation. The highest thermal gradients occur on the continental slope and the results of §3.6.1 show that the stabilising influence of topography helps to reduce the importance of the dissipative terms.

Equatorial parameter. The equatorial constant, δ_{eq}, is a numerical constant included to prevent the singularity at the equator (see §2.1.3, §3.1). It results in the formation of a boundary layer in the neighbourhood of $y = 0$ of width δ_{eq}. There exists the potential that this boundary layer (which we *do* resolve numerically) will affect the interior flow. This possibility is briefly investigated and found, fortuitously, not to be the case. Clearly, from a physical point of view, we would prefer δ_{eq} to be as small as possible since it has no

physical meaning. On the other hand, from a numerical point of view, narrow boundary layers are harder to resolve and are more likely to contain large velocities (which will slow the simulation down via the CFL criterion (see B.2)). Consequently, from a numerical view point, we would like δ_{eq} to be as large as possible.

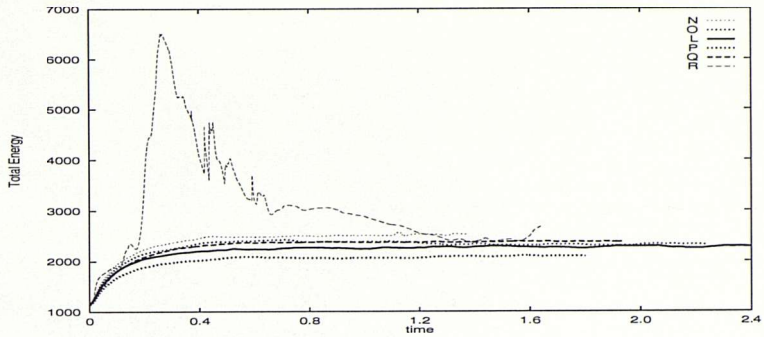
In the only other study to employ an equatorial parameter, Salmon[72] proposes a value of $\delta_{eq} = 0.5$. The majority of simulations in this section use a value of $\delta_{eq} = 0.1$. This coincides with the decision to switch the wind-forcing off in the bottom 10% of the basin. The energy profiles of simulations **L**, **Q** in Figure 4.31 show that the differences between the case $\delta_{eq} = 0.1, 0.2$ are small. The principal effect of δ_{eq} appears to be in broadening the temperature front as it is approaches the southwestern corner (see, for example, Figure 4.20(b)). In the asymptotic limit of $\mathsf{Ro}, \nu, \kappa \ll 1$ one might expect the width of the front to continue to decrease as T is advected towards the corner.

However, the $\delta_{eq} = 0.05$ simulation (**R**) displays remarkably different behaviour to that at larger values of δ_{eq}. After an initial, notable increase, the potential energy subsequently decreases approximately to its original value (Figure 4.31(b)). Snapshots of the stream-function (Figure 4.32) reveal the cause to be a train of cyclonic vortices which are torn off the bottom of the westernmost vorticity strip (Figure 4.32(b)). These eddies are then advected along the equator (Figure 4.32 (c, d, e)) in the opposite direction to the prevailing flow there. Once the eddies reach the eastern boundary, they are rapidly swept by the f/H isopleths around the boundary (Figure 4.32(f, g)). Observe that the cyclonic (western-most) vortex sheet is dramatically weakened by the initial tearing. This prevents more eddies from following the path around the boundary of the domain. Eventually, the cyclonic eddies are re-absorbed back into the sub-polar gyre and vortex sheet and the familiar gyre, intense WBC pattern is temporarily restored (Figure 4.32(h)). However, the re-vitalised cyclonic vortex sheet is short-lived as it provides the source of another train of eddies moving along the equator (Figure 4.32(i)).

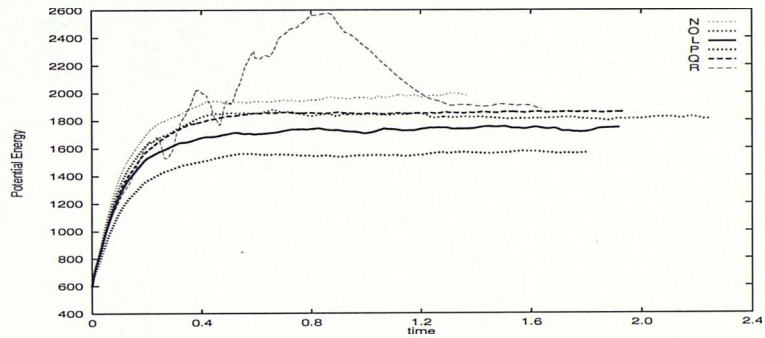
Wind forcing. In most simulations the wind-forcing takes a constant, antisymmetric, double-gyre form (4.2). This form is chosen for its simplicity. Becker & Salmon[7] reported numerical difficulties if the wind-forcing is applied over the entire domain. Their solution was to squeeze the double-gyre into the middle half of the ocean. I have found difficulties with applying the wind over 100% of the basin. However, they appear to vanish when the forcing is applied over 80% of the basin. In fact, there is very little qualitative difference between a wind-forcing over 50% or 80% of the ocean. I therefore use the latter alternative because the gyres are larger. Consequently, the features are more clearly resolved.

In Figure 4.33 a simulation with a three-gyre wind-forcing is presented (simulation **S**). This should be compared with barotropic ocean (Figure 4.14). The energy profiles (not shown) demonstrate that, as in the two-gyre case (Figures 4.29, 4.30), this is not quite a steady state; rather, there are small amplitude, high frequency oscillations in both the barotropic and baroclinic kinetic energies. These are associated with small eddies in the WBC above continental slope. In essence, the qualitative nature of the three-gyre case is the same as the two-gyre case. Consequently, we henceforth confine attention to the simpler, latter alternative even though it may be physically less relevant.

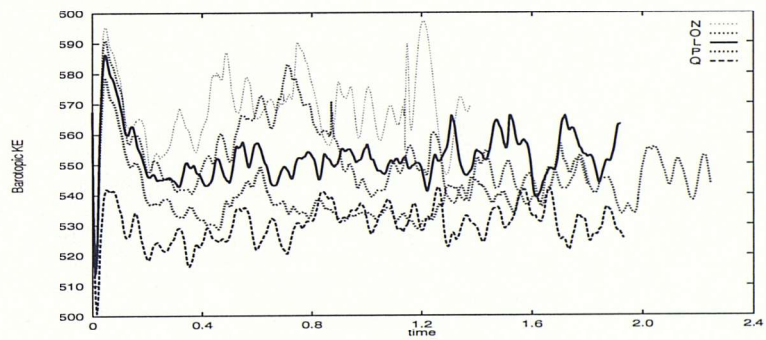
We briefly note here that a comparison of Figures 4.14, 4.33 highlights the effect of the *JEBAR* term on the western slope. The sub-polar gyres of the barotropic and DIT oceans occupy virtually exactly the same proportion of the basin. However, the DIT sub-tropical gyre occupies a smaller proportion of the basin than its barotropic counterpart. This is because the *JEBAR* term shifts the zero-wind-stress-curl-line southwards (4.8). The *JEBAR* term is much stronger in the southern half of the basin than in the northern half (Figure 4.19(a)). Thus, the sub-tropical gyre is affected to a much greater degree than the sub-polar gyre.



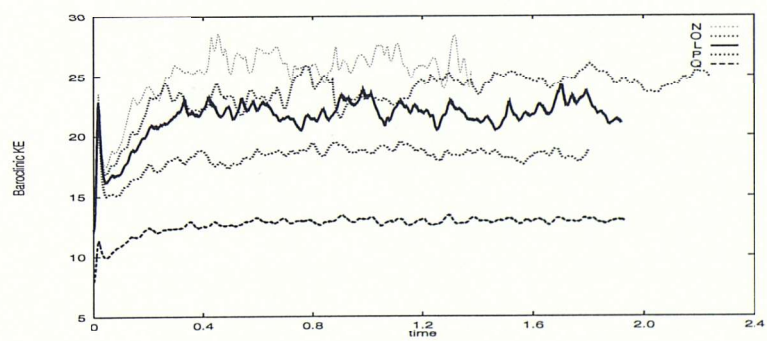
(a) Total Energy



(b) Potential Energy

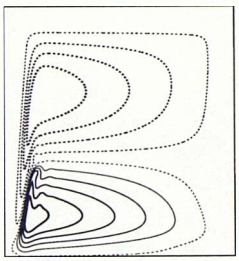


(c) Barotropic KE

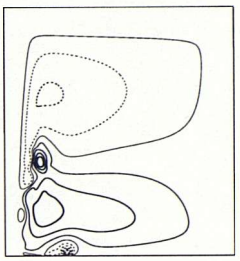


(d) Baroclinic KE

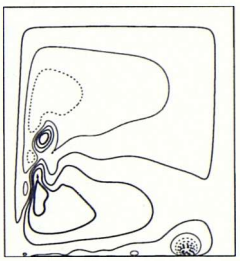
Figure 4.31: Energy profiles for simulations with varying κ and δ_{eq}. Refer to Table 4.1 for details of parameter values. With the exception of $\mathbf{R}$, all energy profiles appear remarkably similar.



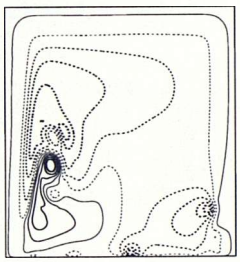
(a) $t = 0.0$



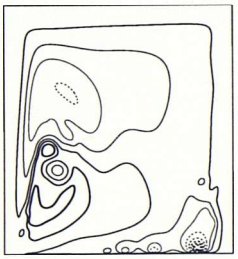
(b) $t = 0.01$



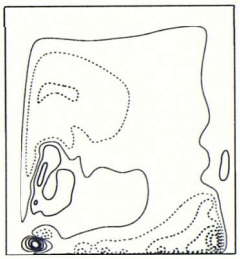
(c) $t = 0.03$



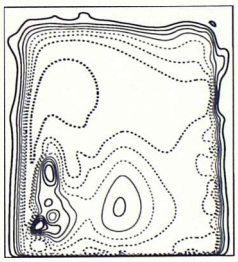
(d) $t = 0.05$



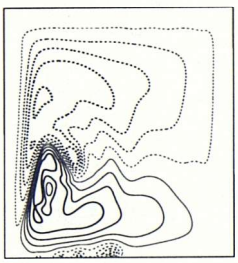
(e) $t = 0.07$



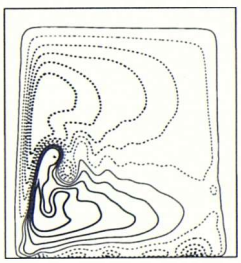
(f) $t = 0.10$



(g) $t = 0.15$

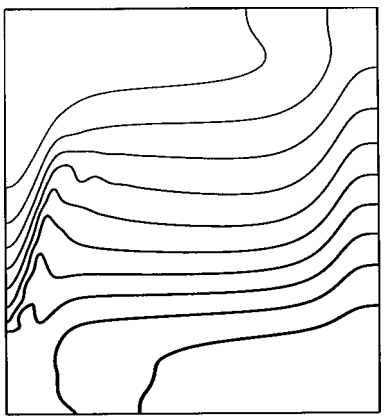


(h) $t = 0.50$

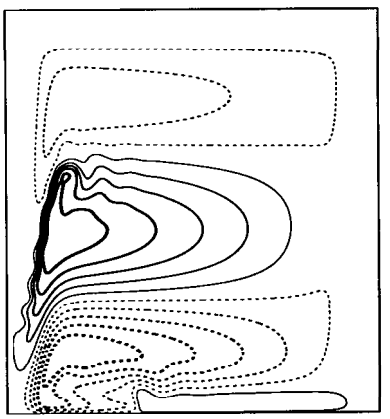


(i) $t = 0.80$

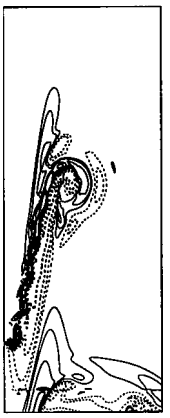
Figure 4.32: Snapshots of the streamfunction, ψ, for simulation **T**. $\delta_{eq} = 0.05$. The equatorial boundary layer is not sufficiently well resolved by δ_{eq}; this leads to eddies travelling eastwards along the equator. They are then swept around the basin and destroy the double-gyre structure of the flow.



(a) T



(b) ψ



(c) $H\zeta$

Figure 4.33: Response of the DIT ocean to three-gyre wind-forcing; simulation **S**. The qualitative aspects are the same as in the two-gyre case. In particular, we observe a thermal front (a) on the western slope. This leads to baroclinic instability and small meanders in the WBC (b, c).

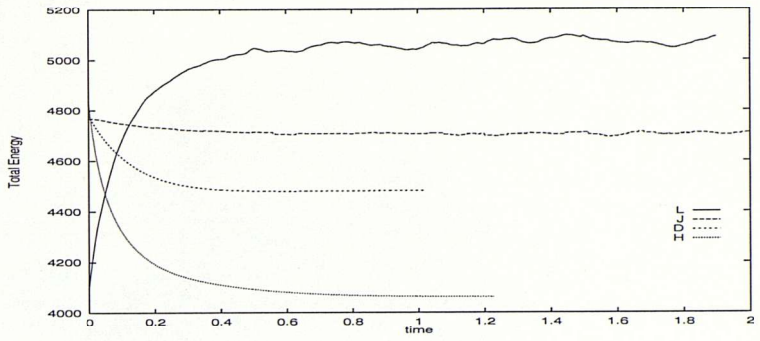
4.2.4 Inertia

Increasing Ro in the barotropic ocean has two easily identifiable effects. The WBC is drawn towards the eastern edge of the domain (Figure 4.11) and the flow becomes more unstable (Figure 4.13). The instability is associated with a large, cyclonic eddy which propagates in a southerly direction and is eventually re-absorbed by the WBC.

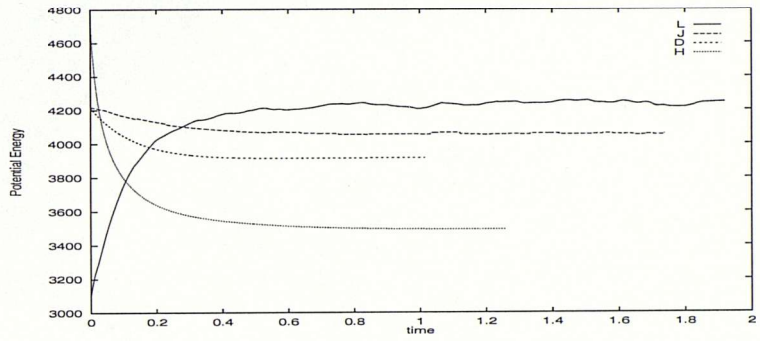
In this section, the effects of increasing Ro in a DIT ocean are investigated. We fix all the other parameters at $\kappa = 0.1, \nu = 0.01, \delta_{eq} = 0.1, \lambda = 10, \mathcal{T} = 5, 10$ and the wind-forcing is steady state, double gyre over 80% of the basin (4.2, $\delta_w = 0.1$). The energy profiles are shown in Figures 4.34, 4.35 for the $\mathcal{T} = 5, 10$ cases respectively.

We have seen in §4.2.2 that baroclinicity causes the steady barotropic solution to lose stability at $\mathsf{Ro} = 1 \times 10^{-4}$. In §3.3.1 it is shown that there exists a critical $\mathsf{Ra} \equiv \frac{\mathsf{Ro}\mathcal{T}^2}{\kappa\nu}$ (for the flat-bottomed case) below which baroclinic instability is prohibited. Consequently, one might conclude that a steady state can be achieved in the DIT ocean if Ro is reduced sufficiently. In fact, a steady state for both $\mathcal{T} = 5, 10$ cases is attained at $\mathsf{Ro} = 0.5 \times 10^{-4}$. The $T, \psi, H\zeta$ fields are shown in Figures 4.36, 4.37, 4.38 respectively. Notice that the recirculation gyre on the southern border of the WBC is present in the $\mathcal{T} = 10$ case but not in the $\mathcal{T} = 5$ case. There is even some evidence of the northern recirculation gyre in the former case. This emphasises the importance of the baroclinic terms in the formation of this gyre.

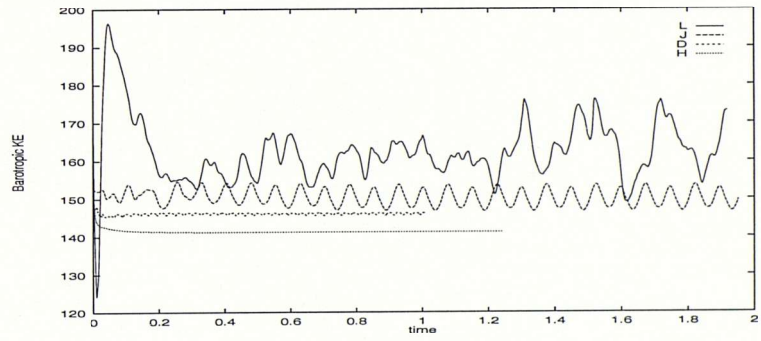
Increasing Ro from 1×10^{-4} causes a large eddy shedding event from the WBC after it has left the continental slope; this is similar to the barotropic behaviour. However, whereas this eddy-shedding is, for moderate values of Ro, periodic in the barotropic case (Figure 4.13), the same cannot be said of the DIT simulations (Figures 4.34, 4.35). One complete period of the temperature, streamfunction and relative vorticity fields for the case $\mathcal{T} = 5, \mathsf{Ro} = 4 \times 10^{-4}$ is shown in Figures 4.39, 4.40, 4.41, 4.42. Clearly, the flow structure is much more complicated than in the barotropic case (Figures 4.5, 4.6). In addition to the large, cyclonic eddy which is shed from the south of the WBC and the ever-present anticyclonic recirculation gyre on the southern flank of the WBC, there exists a collection of other, smaller eddies. In particular, there is evidence of an anticyclonic eddy being shed from the northern edge of the WBC. This is most clearly visible in Figures 4.39(e), 4.42(b-e). I have been unable to locate any evidence of such a feature in the barotropic ocean. It seems apparent, therefore, that this is a result of baroclinic instability. Recall that in §3.4.5 plume-like structures are ejected both North and South from the Gaussian-strip idealised WBC. Figure 1.1 shows that eddies, known as *warm core rings*, are indeed shed from the northern edge of the meandering Gulf Stream shortly after it has left the coast.



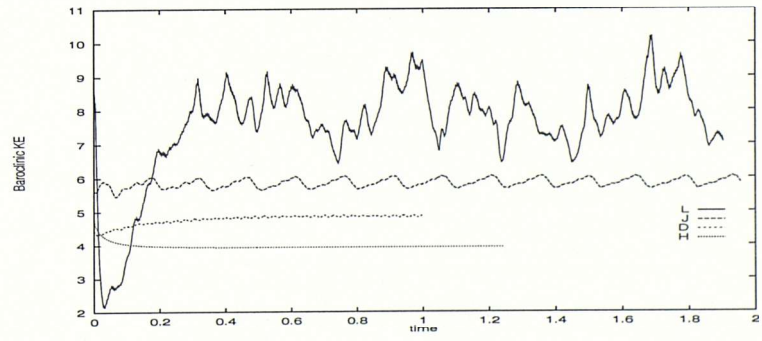
(a) Total Energy



(b) Potential Energy

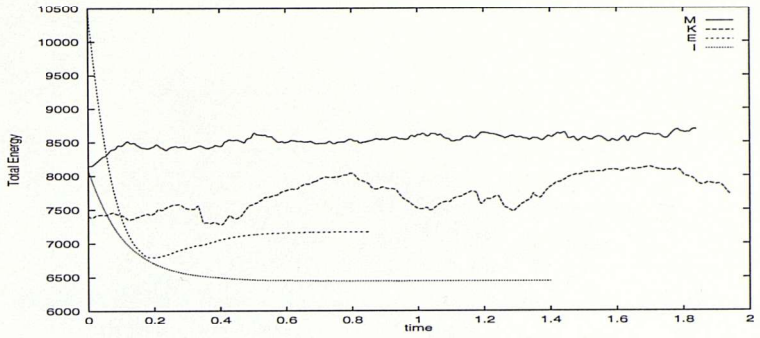


(c) Barotropic KE

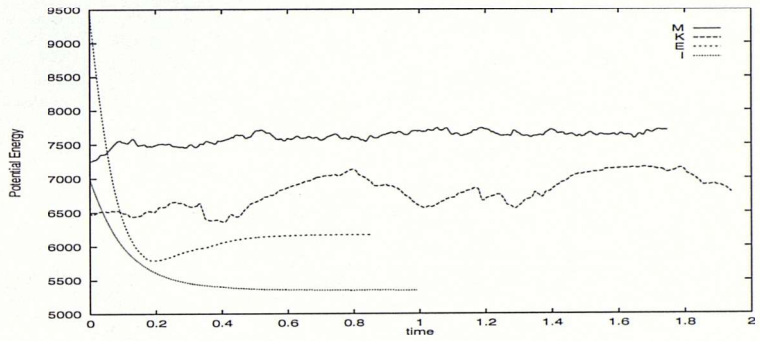


(d) Baroclinic KE

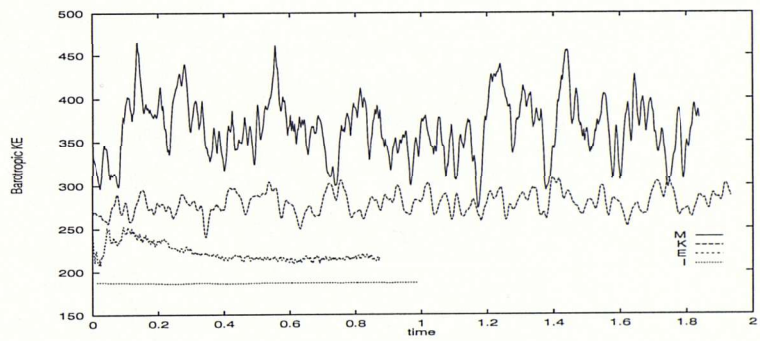
Figure 4.34: Energy profiles for $\mathsf{Ro} = 4, 2, 1, 0.5 \times 10^{-4}$; $\mathcal{T} = 5$. Experiments **L, J, D, H**. Unsteadiness corresponds to eddy shedding as in the barotropic simulations and also to baroclinic instabilities forming smaller eddies. Time series have been vertically offset by an arbitrary amount to aid clarity.



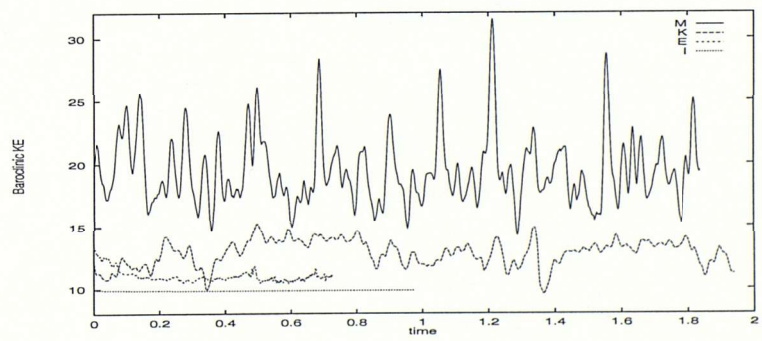
(a) Total Energy



(b) Potential Energy

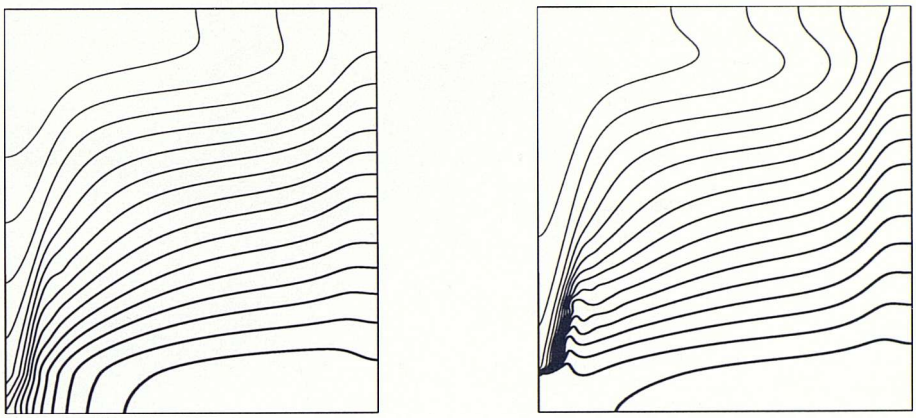


(c) Barotropic KE



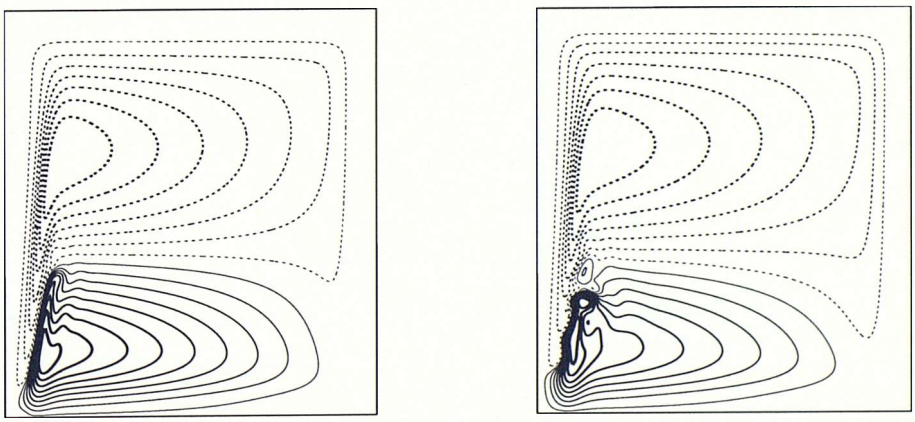
(d) Baroclinic KE

Figure 4.35: Energy profiles for $\mathsf{Ro} = 4, 2, 1, 0.5 \times 10^{-4}$; $\mathcal{T} = 10$. Experiments **M**, **K**, **E**, **I**. Unsteadiness corresponds to eddy shedding as in the barotropic simulations and also to baroclinic instabilities forming smaller eddies. Time series have been vertically offset by an arbitrary amount to aid clarity.



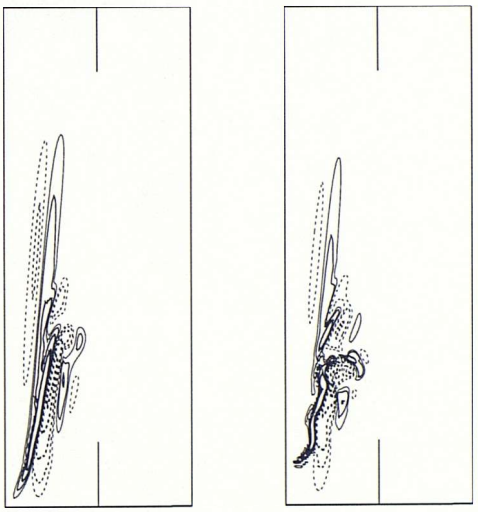
(a) $\mathcal{T} = 5$ (b) $\mathcal{T} = 10$

Figure 4.36: Steady state of DIT ocean; T field; $\mathsf{Ro} = 0.5 \times 10^{-4}, \lambda = 10$; simulations **H**, **I**.



(a) $\mathcal{T} = 5$ (b) $\mathcal{T} = 10$

Figure 4.37: Steady state of DIT ocean; ψ field; $\mathsf{Ro} = 0.5 \times 10^{-4}, \lambda = 10$; simulations **H**, **I**. There is a recirculation gyre on the southern flank of the WBC in the more baroclinic case (*b*).



(a) $\mathcal{T} = 5$ (b) $\mathcal{T} = 10$

Figure 4.38: Steady state of DIT ocean; $H\zeta$ field; $\mathsf{Ro} = 0.5 \times 10^{-4}, \lambda = 10$; simulations **H, I**. In the more baroclinic case (*b*), the tail of the cyclonic vortex has been pulled northwards, away from the south-west corner and the head of the sheet is more strongly rotated clockwise in mid-latitudes. Both vortex sheets are confined to the westernmost $\frac{1}{5}$ of the basin. Contrast this the more inertial circulations (for example, Figure 4.42) in which the vorticity extends much further east.

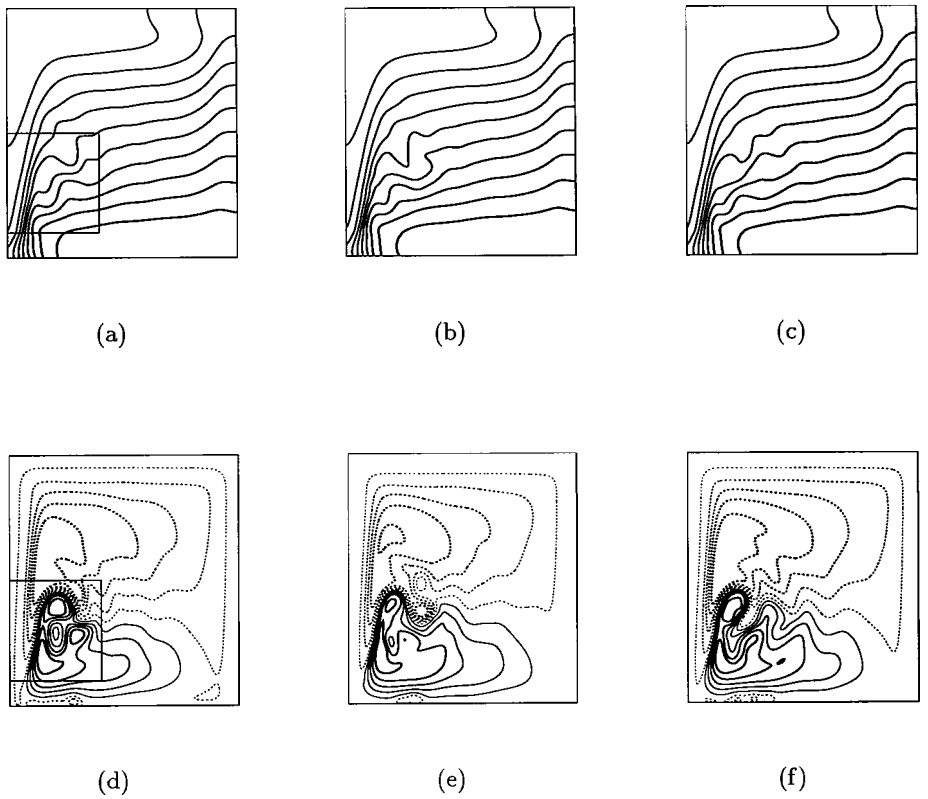


Figure 4.39: One eddy-shedding event period of the DIT ocean; $1.323 < t < 1.503$; (a-c) T field; (d-f) ψ field; $\mathrm{Ro} = 4 \times 10^{-4}, \lambda = 10, \mathcal{T} = 5$; simulation **L**. Boxed region of (a, d) is shown in more detail in Figures 4.40, 4.41.

We observe that this warm core ring is shed from the WBC *after* it has left the coastal slope (Figure 4.42(b, c)), the eastern limit of the slope is indicated by vertical lines at the top and bottom of the domain). This would appear to suggest that *JEBAR* cannot be responsible for its presence. On the other hand, the influence of *JEBAR* is not necessarily confined to the slope. This is clearly demonstrated in the non-inertial simulations of Salmon & Ford[75] where *JEBAR* is the *only* baroclinic term but its impact is felt throughout the whole basin. To address this issue, I ran a simulation (**T**) with *JEBAI* removed. Although *JEBAI* is always small in magnitude, there is no formal limit in which *JEBAR* and $\epsilon J\left(\psi, \frac{\zeta}{H}\right)$ may be retained when *JEBAI* is neglected. Hence the results of simulation **T** must be treated with caution. The temperature, streamfunction, relative vorticity and energy profiles are shown in Figures 4.43 – 4.45. The warm core ring is visible in Figures 4.43(e, f), 4.44(b, c). This indicates that the influence of *JEBAR* is being felt even in the deep flat basin although it does not prove that *JEBAI* has no role to play in the formation of this eddy. The recirculation gyre on the southern flank of the WBC is present in Figures 4.43(d, e, f), 4.44. However, it does not appear to be as strong a feature as in Figures 4.41, 4.42.

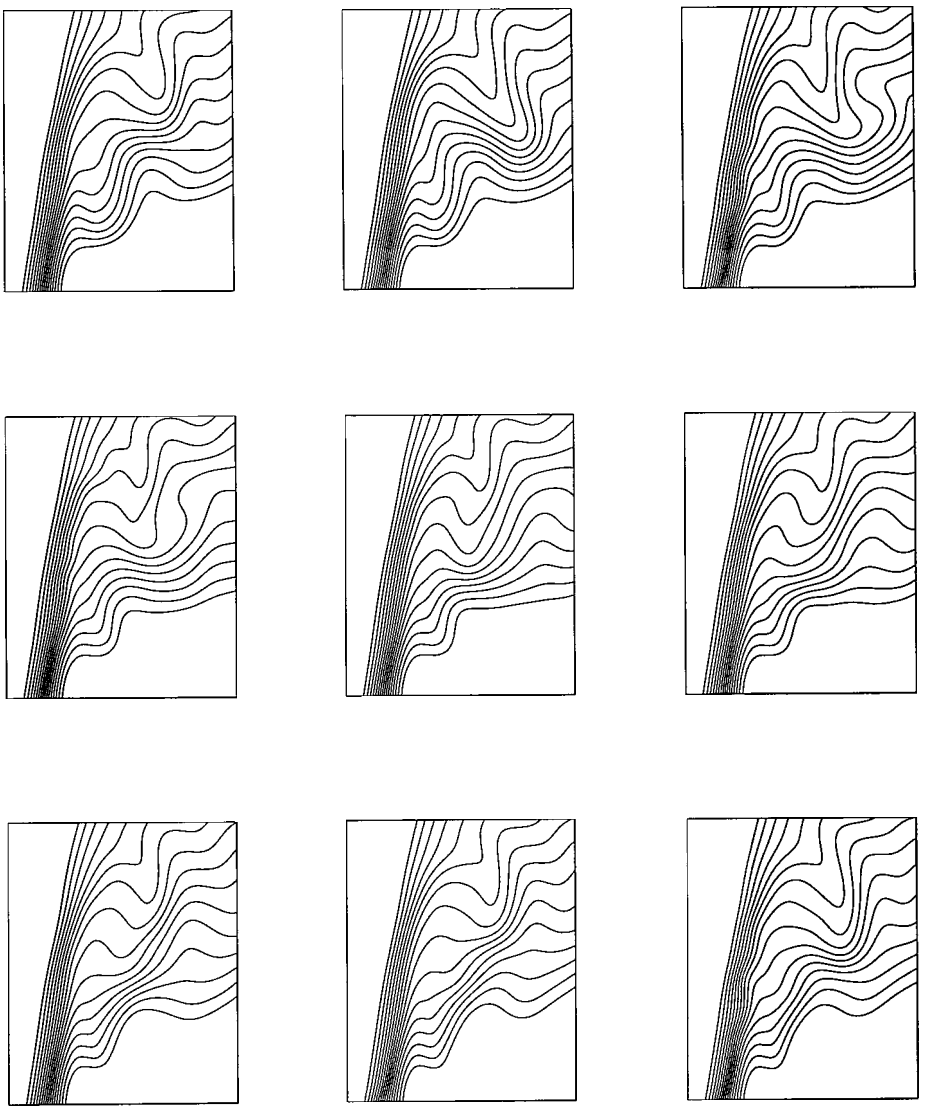


Figure 4.40: One eddy-shedding event period of the DIT ocean; $1.323 < t < 1.503$; T field; $\mathsf{Ro} = 4 \times 10^{-4}, \lambda = 10, \mathcal{T} = 5$; simulation **L**.

This suggests that *JEBAI* contributes to the creation of this gyre. This seems to confirm that baroclinicity *and* inertia are both important to the recirculation gyre. Notice also, that the high frequency energetic oscillations have disappeared. Figure 4.45 shows that the majority of the total energy variability is due to fluctuations in the barotropic energy. This is because the neglect of *JEBAI* has removed the main source of baroclinic instability. In Figure 4.43(d-f) the WBC is free of meanders when it is above the coastal slope. In §3.2 it is argued that *JEBAI* frees potential energy for baroclinic instability by increasing thermal gradients. Figures 4.39(a-c), 4.43(a-c) show, respectively, the temperature fields with and without *JEBAI* present. The two figures are very similar; the only noticeable

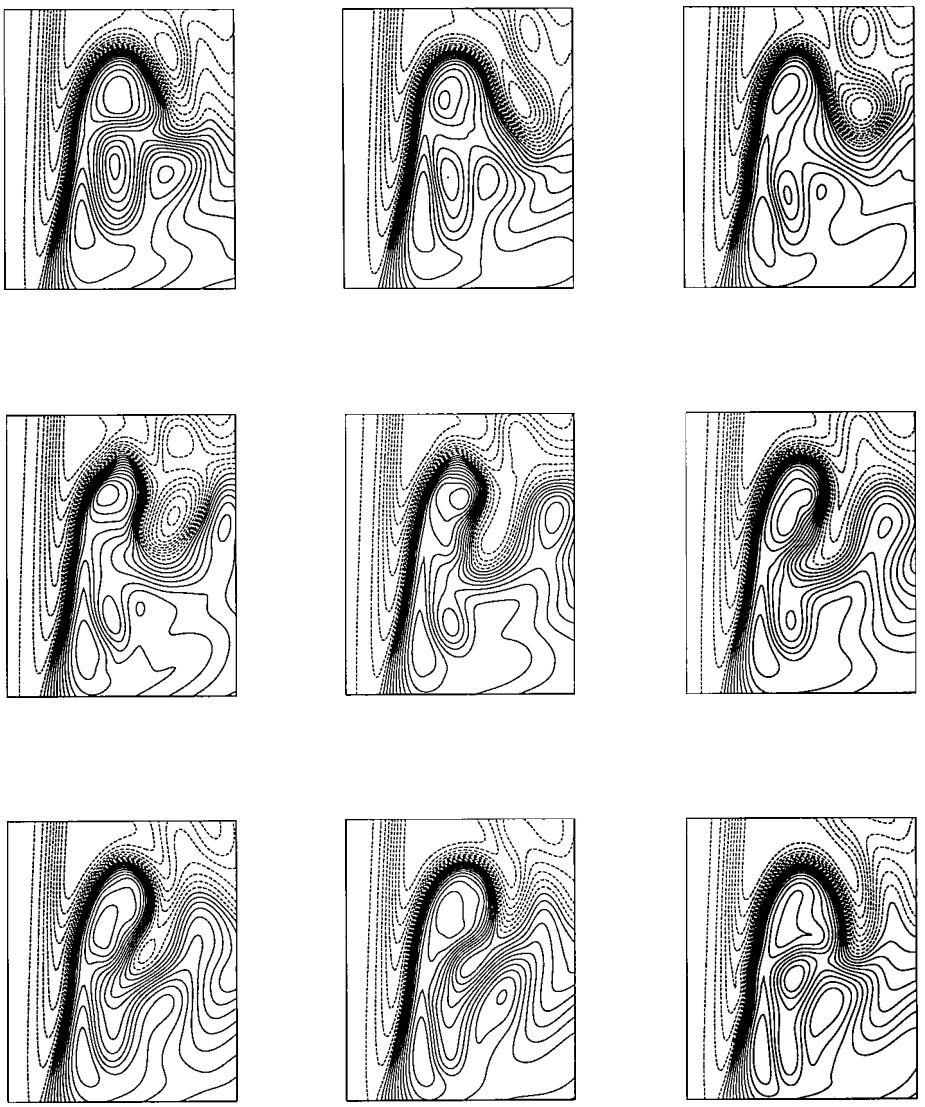


Figure 4.41: One eddy-shedding event period of the DIT ocean; $1.323 < t < 1.503$; ψ field; $\mathsf{Ro} = 4 \times 10^{-4}, \lambda = 10, \mathcal{T} = 5$; simulation **L**.

difference lies in the strength of the front on the western slope which is stronger in the former case when *JEBAI* is present.

Retaining the same value of Ro but increasing the baroclinicity, $\mathcal{T}$, has a further destabilising influence on the dynamics. Snapshots from the entire length of the simulation are shown in Figures 4.47, 4.48, 4.49 for $T, \psi, H\zeta$ respectively. The barotropic eddy is present at times $t = 0.0, 0.4, 1.6$ but not at the other times shown. There is little evidence of the warm core ring of simulation **L** except perhaps in Figure 4.48(d). The relative vorticity field in Figure 4.49 is significantly more complex than that of Figure 4.42 rendering it hard to identify specific features. The majority of eddies present in the northern gyre of

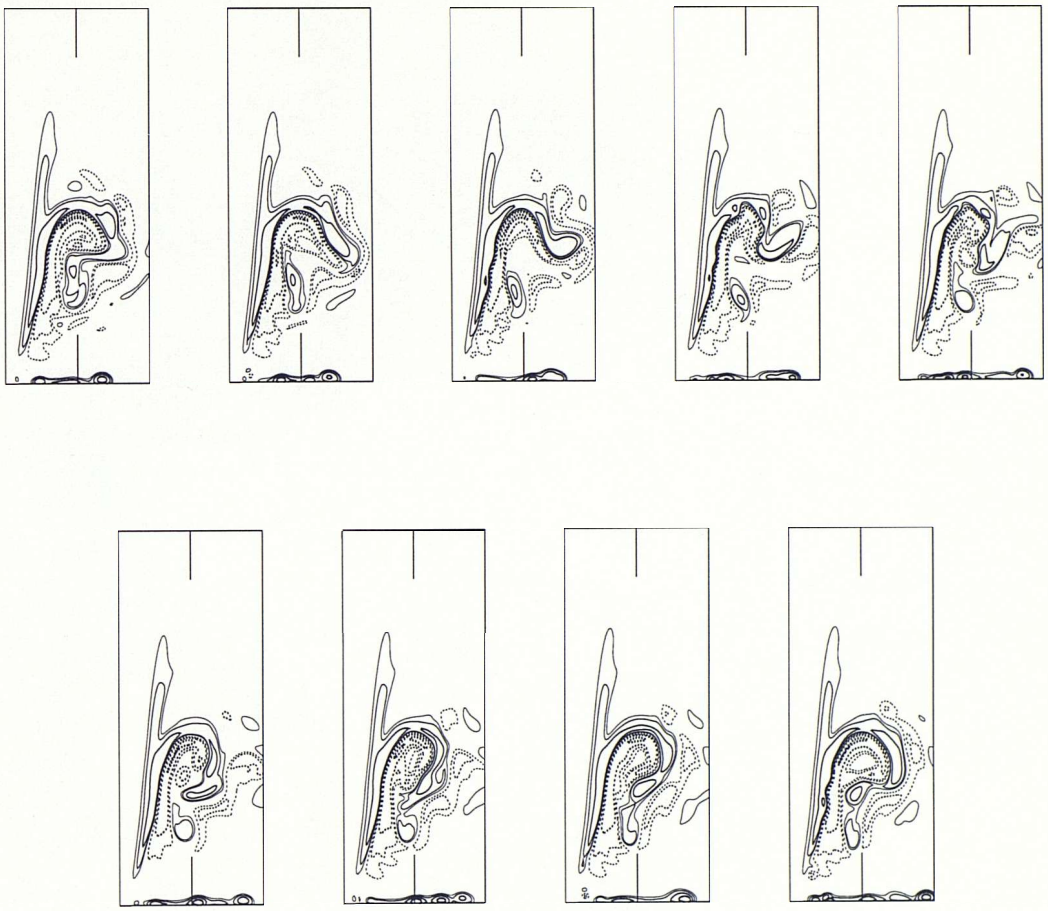
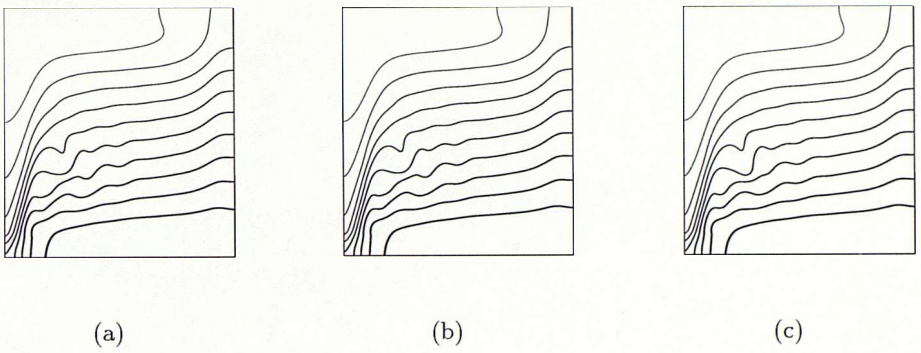
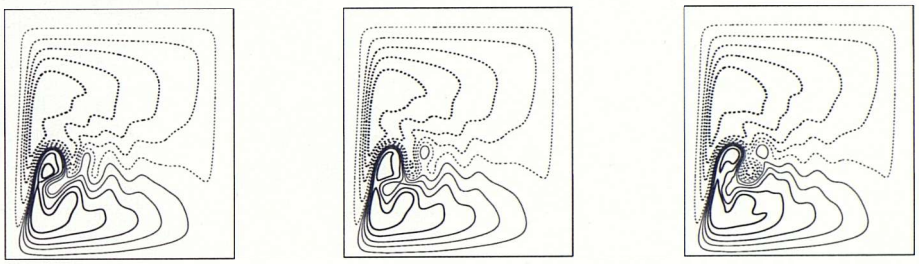


Figure 4.42: One eddy-shedding event period of the DIT ocean; $1.323 < t < 1.503$; $H\zeta$ field; $\mathsf{Ro} = 4 \times 10^{-4}, \lambda = 10, \mathcal{T} = 5$; simulation **L**.

Figure 4.48 appear to have originated on the western slope in the neighbourhood of the temperature front rather than from the off-shore meandering WBC. This is most clearly seen in Figure 4.49(a) in which there is a stream of cyclonic vortices emanating from this region (left side of figure). The fact that most of these eddies are cyclonic, rather than anticyclonic, suggests that their origin is different from that of the warm core ring of simulation **L**.

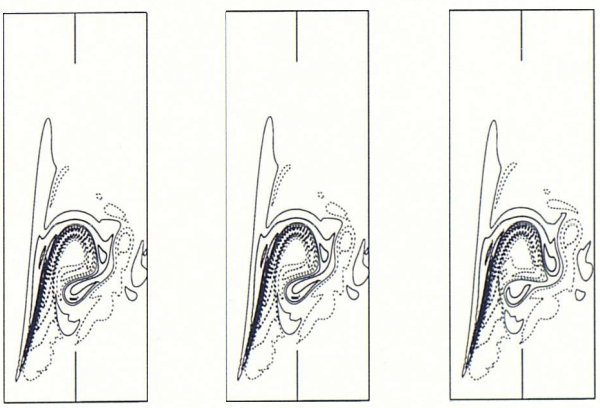


(a) (b) (c)



(d) (e) (f)

Figure 4.43: Half an eddy-shedding event period of the DIT ocean; $1.59 < t < 1.71$; (a-c) T field; (d-f) ψ field; $\mathsf{Ro} = 4 \times 10^{-4}, \lambda = 10, \mathcal{T} = 5$; simulation **T**. The *JEBAI* term is removed from equations.



(a) (b) (c)

Figure 4.44: Half an eddy-shedding event period of the DIT ocean; $1.59 < t < 1.71$; $H\zeta$ field; $\mathsf{Ro} = 4 \times 10^{-4}, \lambda = 10, \mathcal{T} = 5$; simulation **T**. The *JEBAI* term is removed.

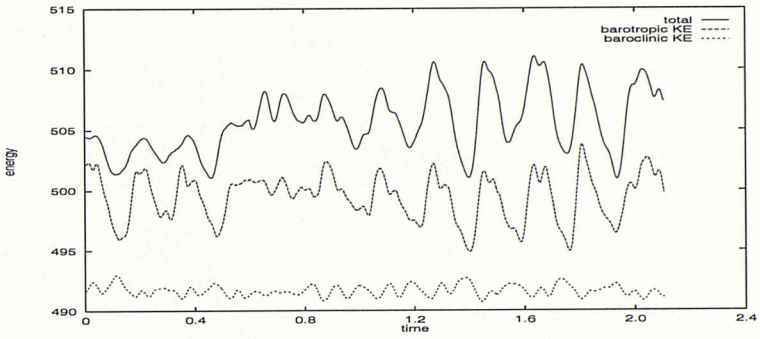
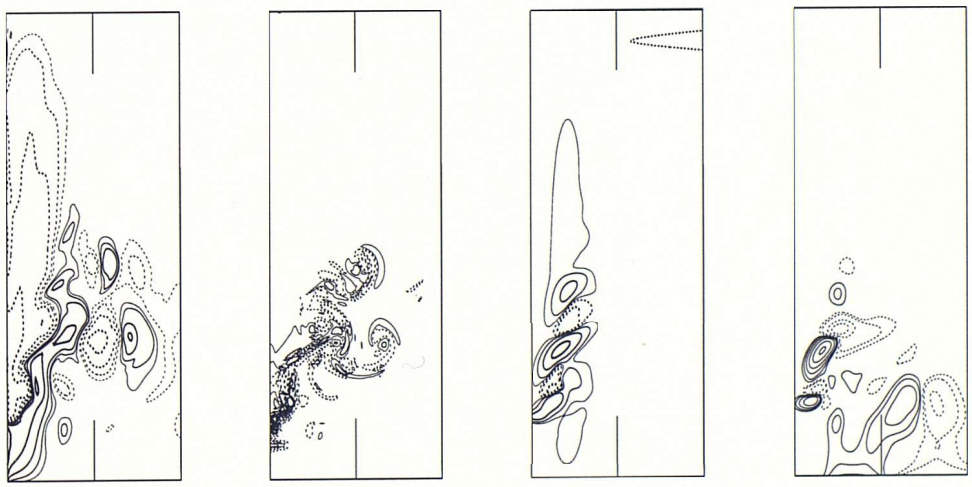


Figure 4.45: Energy profiles for simulation **T**. Total and baroclinic energy profiles have been shifted vertically towards barotropic energy profile for clarity. Because *JEBAI* has been neglected, baroclinic instability is much less prevalent than in other simulations of this section. Therefore, most of the variation in the total energy is due to variation in the barotropic kinetic energy and instabilities are associated with barotropic shear.



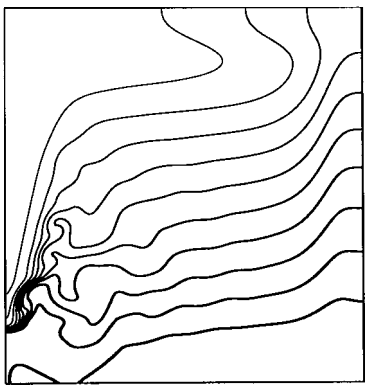
(a) $J\left(\psi, \frac{f}{H}\right), (-4 \times 10^4, 4 \times 10^4)$

(b) $\epsilon J\left(\psi, \frac{\zeta}{H}\right), (-10^3, 10^3)$

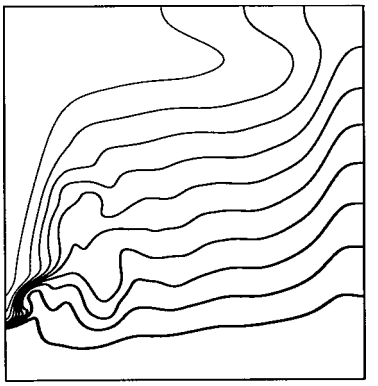
(c) $\frac{1}{2} J(T, H), (-60, 300)$

(d) $\epsilon J(T, \Gamma), (-17, 45)$

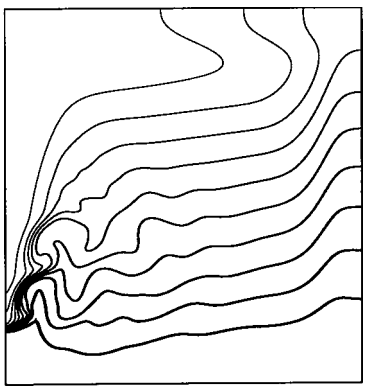
Figure 4.46: Conservative terms of DIT, for $\mathsf{Ro} = 4 \times 10^{-4}, \lambda = 10, \mathcal{T} = 10, t = 1.6$, simulation **M**; all contours are log-equally spaced, magnitudes are indicated in parentheses.



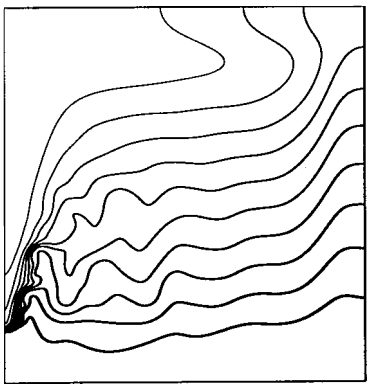
(a) t=0.0



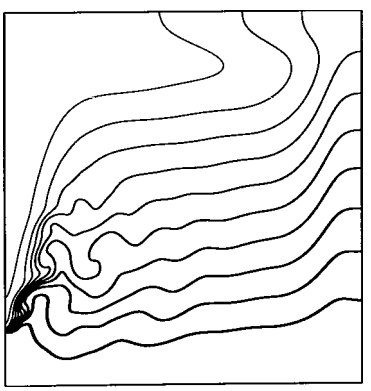
(b) t=0.4



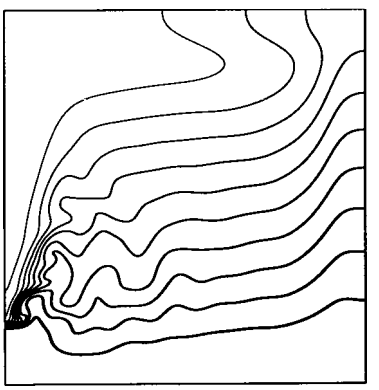
(c) t=0.8



(d) t=1.2

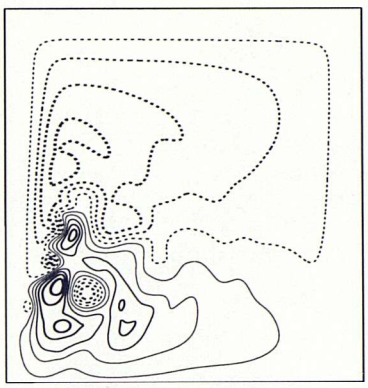


(e) t=1.6

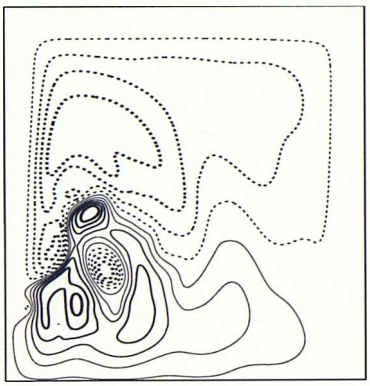


(f) t=2.0

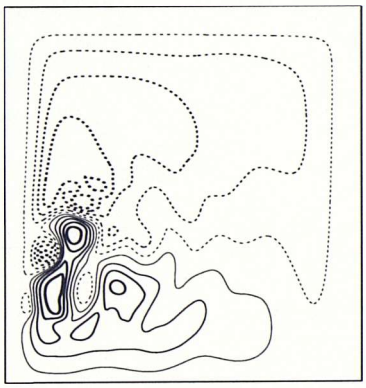
Figure 4.47: Snapshots of T field; $\mathsf{Ro} = 4 \times 10^{-4}, \lambda = 10, \mathcal{T} = 10$; simulation **M**.



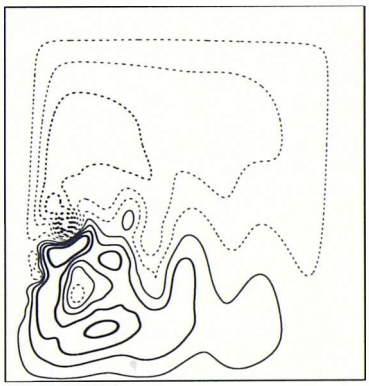
(a) t=0.0



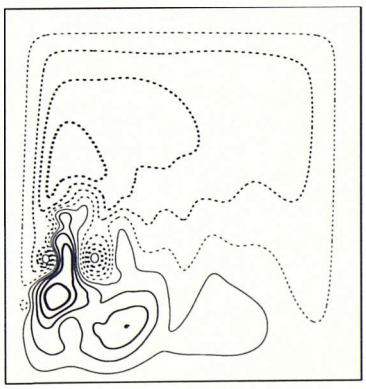
(b) t=0.4



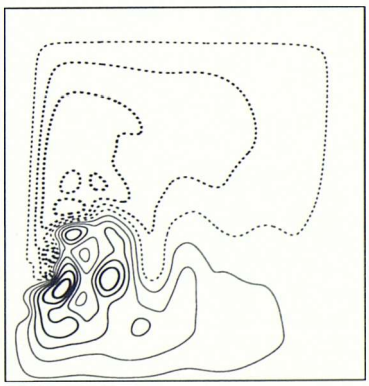
(c) t=0.8



(d) t=1.2

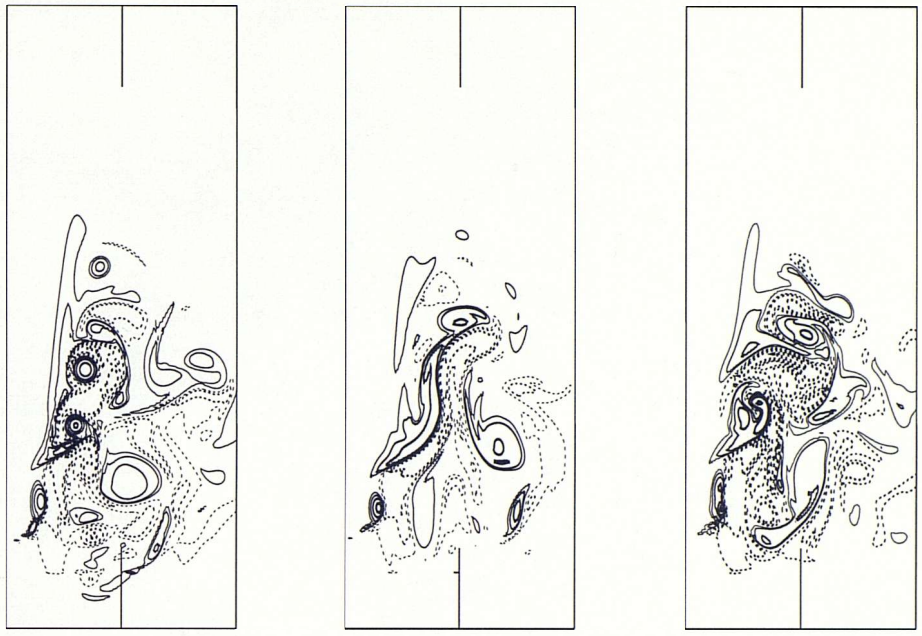


(e) t=1.6

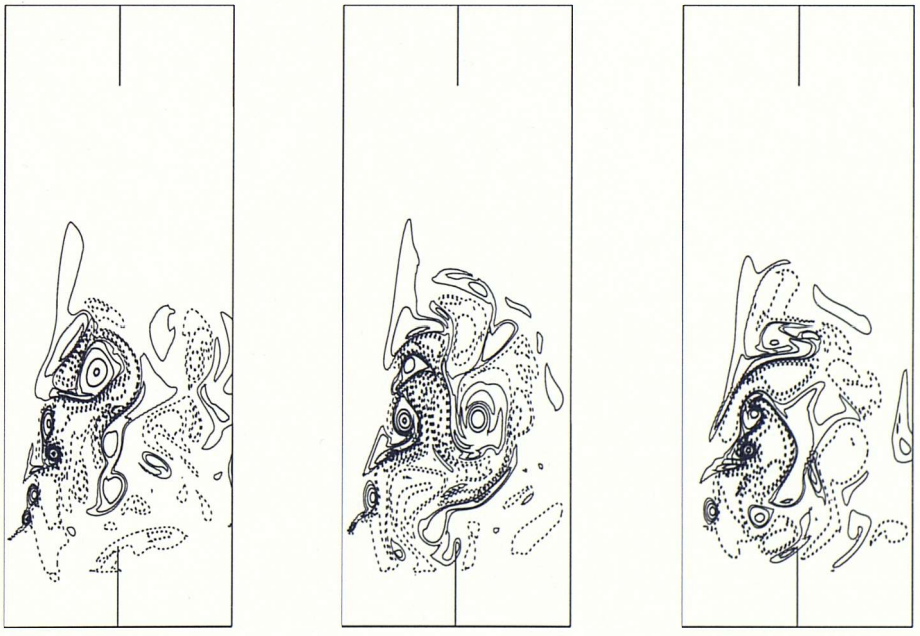


(f) t=2.0

Figure 4.48: Snapshots of ψ field; $\mathsf{Ro} = 4 \times 10^{-4}, \lambda = 10, \mathcal{T} = 10$; simulation **M**. Range is $-1.6 < \psi < 1.9$, isopleths are equally spaced.



(a) t=0.0 (b) t=0.4 (c) t=0.8



(d) t=1.2 (e) t=1.6 (f) t=2.0

Figure 4.49: Snapshots of $H\zeta$ field; $\mathsf{Ro} = 4 \times 10^{-4}, \lambda = 10, \mathcal{T} = 10$; simulation **M**. Range is $-2300 < H\zeta < 2500$, isopleths are log-equally spaced. The positive vortex sheet has been broken up and intense, cyclonic vortices have replaced it.

The individual conservative terms of the DIT (3.2) for simulation M are shown in Figure 4.46. Although the details of these terms obviously vary over time, many points of interest are raised upon consideration of this solitary time slice. Figure 4.46 should be compared with Figures 4.18, 4.19 from simulation **B** which is both less inertial and less baroclinic than simulation M.

The most dramatic difference occurs in the magnitude of the terms. The inertial barotropic term, $J\left(\psi, \frac{\zeta}{H}\right)$, has increased by a factor of 10^2 whereas Ro has only increased by a factor of four. This suggests that the majority of the increase is due to the emergence of finer length scales (L_c) in the flow which has the effect of increasing $J\left(\psi, \frac{\zeta}{H}\right) \sim \frac{\psi^2}{L_c^4}$. This impression is confirmed by contrasting the relatively large, smooth, wave-like features of Figure 4.18(b) with the much more compact, vortex-like structures of Figure 4.46(b). We have already noted that increasing Ro extends the WBC in an easterly direction. The point is clearly highlighted by comparing the leading order term, $J\left(\psi, \frac{f}{H}\right)$ term in both simulations; for $\mathsf{Ro} = 1 \times 10^{-4}$ it is almost completely confined to the slope whereas for $\mathsf{Ro} = 4 \times 10^{-4}$ there is a lot of activity over the flat bottom.

The most notable effect of the increased baroclinicity is that for simulation M, the *JEBAR* term is not positive definite on the western slope (Figure 4.46(c)). It remains true that $J(T, H) = -\partial_y T \partial_x H$ and that $\partial_x H > 0$ so the negative regions of *JEBAR* are due to $\partial_y T > 0$. This, in turn, is due to baroclinic instability on the slope leading to meandering of the WBC and small eddies being shed. *JEBAI* (Figures 4.19, 4.46(d)) has increased by a factor of approximately ten. Since $\mathcal{T}$ has increased by a factor of two and $J(T, \Gamma) \sim \frac{T^2}{L_{cT}^4}$ we conclude that the length-scale of the thermal structures, L_{cT}, has decreased, but nowhere near as much as has the barotropic length-scale, L_c. This is probably because that the thermal diffusivity, κ, is greater than the Rayleigh friction, ν. As expected, in both simulations, *JEBAI* takes its largest values where the thermal gradients are highest. The structures within the *JEBAI* field, as in the $J\left(\psi, \frac{\zeta}{H}\right)$ field, are more compact in the more inertial simulation.

4.2.5 Summary

In this section we have examined the dynamics within a Depth-Independent-Temperature ocean basin. The circulations differ from those of §4.1.6 because of the inclusion of baroclinicity. A brief investigation reveals that the flow is relatively insensitive to the value of the arbitrary constants κ, δ_{eq} provided that $\delta_{eq} \geq 0.1$. Thermal forcing imposes a global temperature structure and a scaling analysis yields approximate values for the cross-basin temperature gradient and the time-scale for the relaxation. It is then shown that:

- The inclusion of baroclinicity has a destabilising influence. At values of Ro for which the barotropic ocean has a stable stationary solution, the DIT ocean exhibits small amplitude, high frequency oscillations.

- These small oscillations are associated with meandering of the WBC on the western continental slope. Eddies can be shed from this region. This is due to baroclinic instability caused by a combination of both baroclinic feedback terms of (3.2).

- Very high temperature gradients are found on the western slope. For small values of $\mathcal{T}$ this thermal front is advected towards the south-western corner under the influence of the barotropic flow. For larger values of $\mathcal{T}$, the jet attaches itself to the western boundary. The high thermal gradient explains the presence of baroclinic instability in this region.

- For small Ro, *JEBAR* contributes an anticyclonic component to the barotropic vorticity on the western continental slope. In the neighbourhood of the south-western corner, this moves the two vortex sheets northwards, away from the corner. Also, the latitude at which the WBC separates from the slope is shifted southwards. Since the coldest water is located on the shallowest parts of the shelf, *JEBAR* attempts to move it into deeper regions and therefore contributes to destabilising the flow. For larger Ro, the effect is less clear because *JEBAR* is no longer positive deflnite.

- *JEBAI* is everywhere small but leads to baroclinic instability where thermal gradients are large. This causes eddies to be shed from the WBC on the western coastal slope. Furthermore, in combination with *JEBAR* , it causes eddies to be shed from both the southern and northern edges of the meandering WBC after it has dismounted the slope. These are interpreted as cold and warm core rings, respectively. The two baroclinic terms are also responsible for increasing the magnitude and eastern extent of the off-shore WBC meanders.

- A further impact of the baroclinic terms is to create the anticyclonic recirculation gyre on the southern flank of the WBC as it dismounts the coastal slope. The gyre is formed because the negative vortex is strengthened by *JEBAR* . Consequently, it pulls the positive vortex sheet right around its northern tip and pinches off an anticyclonic eddy. It seems that *JEBAI* also has a supplementary role to play in strengthening this recirculation gyre. The highly baroclinic circulations also include a recirculation gyre on the northern flank of the WBC. This appears to be formed by eddies which are created by baroclinic instability caused, primarily, by *JEBAI* .

- As in the barotropic case, the main effects of increasing Ro are to destabilise the flow and to extend the WBC in an easterly direction.

- An important parameter in characterising the flow seems to be the Rayleigh Number, $\mathsf{Ra} = \frac{\mathsf{Ro}\mathcal{T}^2}{\kappa\nu}$. Instabilities, meanders, small scales, eddies, gyres and vortex-like structures become more prevalent when Ra is large. Furthermore, the WBC extends less far into the south-western corner since both inertia and baroclinicity act to move the tail of the vortex sheets northwards. When Ra is small, the flow is dominated by the wind-forcing and topographic stretching; circulations are comparatively stable and the WBC extends right into the south-western corner of the domain.

Chapter 5

Conclusions and further work

5.1 Conclusions

This thesis has examined the behaviour of the Large-scale Semi-Geostrophic Equations (LSGE)(1.17a-e) and their applicability to modelling large-scale features of ocean circulation. These equations were developed in Salmon[73] as an alternative to other balanced systems of equations such as the quasi-geostrophic (QG) equations.

The approach taken here has been both analytical and numerical. I have tried to highlight where these two approaches agree and where they differ and to show where the results of this thesis fit into the work of other studies. A discussion of the accuracy, efficiency and applicability of the numerical algorithms can be found in Appendix B.

The principal results of the thesis are :

- Derivation of a two-layer model based on the LSGE (§2.1).
- Investigation of baroclinic instability in the two-layer model (§2.2). It is demonstrated that QG over-estimates the instability growth rate for finite interface heights. An intermediate stratified layer has a small stabilising effect. This is explained by a parcel-instability argument. In the light of results from Chapter 3, this shows that the ultra-violet catastrophe exhibited in the DIT baroclinic instability problem is *not* a generic feature of the LSGE.
- Derivation of the Depth-Independent-Temperature (DIT) model based on the LSGE (§3.1). The DIT model is arguably the simplest model of rotating flow to include the effects of baroclinicity, topography and inertia. I also prove conservation of energy and explain how potential energy can be released, even in a flat-bottomed model. It is shown in §3.1.1 that the flat-bottomed model has an interpretation as the large-scale terms of two-layer QG.

- Analysis of baroclinic instability in the DIT model (§3.3). *Both* thermal diffusivity and viscosity are required to avoid an ultra-violet catastrophe. The dependence on dissipative terms to prevent such a catastrophe is probably the biggest disadvantage of the DIT as a theoretical tool. Growth rates are proportional to thermal gradients. Linear analysis of the no-slip and free-slip cases highlights the big difference in stability of the two cases and adds weight to the argument in favour of studying ocean basins in which the depth of the ocean vanishes. A weakly nonlinear analysis of the free-slip problem reveals the existence of a stable finite amplitude solution for marginally supercritical flows. Analogies with Rayleigh-Bénard convection are drawn. Nonlinear simulations are presented and compared with the analysis. They show that a secondary instability breaks the stability of the weakly non-linear solution. At very high Rayleigh numbers, characteristics of hard turbulence are found. The analysis is extended to a localised thermal anomaly (§3.4) which represents an idealised western boundary current. A WKBJ analysis is performed and compared with numerical simulations. Instabilities are shown to be highly localised with the width dependent on the thermal diffusivity, κ. Furthermore, the global importance of κ is highlighted since a solution cannot be found if it is neglected outside the internal boundary layer.

- A series of numerical simulations of localised thermal anomalies and turbulence is presented (§3.5). The interaction range of anomalies is shown to be very small. The generation of secondary instabilities and cascade to small scales is observed once again. This behaviour is very distinct from two-dimensional flow and is perhaps more closely related to the behaviour of Surface-Quasi-Geostrophic dynamics. However, in turbulence simulations the behaviour is demonstrated to tend towards barotropic behaviour unless there is an external thermal structure imposed upon the flow. This is explained by analysing the magnitude of the *JEBAI* feedback term which shows an initial rapid increase due to generation of small scales by baroclinic instability and then declines as the baroclinic field weakens and the structures left behind do not contribute to *JEBAI* .

- The effects of topography are investigated (§3.6). Linear analysis and nonlinear simulations show that topography has a stabilising influence in the case in which it is oriented such that the warm water is located in shallow regions of a domain. This is explained in terms of potential energy release. If the topography is in the opposite orientation then the effect is more complicated. *JEBAR* acts as a destabilising influence by trying to release potential energy but the net effect of steep gradients is to stabilise the flow because the difficulty of deforming columns of constant temperature as they are advected up and down the slope opposes the *JEBAR* influence. A

further topographic effect is to increase the most unstable wavenumber.

- Investigation of barotropic ocean basins with coastal slopes (§4.1). This section mainly reprises the results of Becker & Salmon[7] and is used for comparative purposes with §4.2 in which it is shown that a western continental slope deflects the boundary between the two wind-driven gyres towards the south-western corner and destabilises the flow. However, in conjunction with the results of [7] it is shown here that the coastal slope on the northern boundary has a negligible effect but that the eastern slope has a small, but noticeable, destabilising influence. Additionally, it is demonstrated that the precise form of the viscous terms is unimportant. This is because there is no longer a boundary layer along the whole western boundary; the boundary region is now restricted to the south-western corner.

- Investigation of a DIT ocean basins with coastal slopes (§4.2). The results of all the earlier work of the thesis are brought together to study and explain the dynamics in the basin and how they differ from those of the barotropic ocean. There is greater instability in the WBC, induced by the high thermal gradients in this region. The separation from the coast occurs at lower latitudes due to the *JEBAR* term adding extra anticyclonic vorticity to the barotropic flow. *JEBAR* also reduces the stability of the WBC above the western continental slope. The principal effect of *JEBAI* is to create baroclinic instability in the neighbourhood of a strong thermal front on the western slope. The two baroclinic terms also act in conjunction to cause eddies to be shed from both edges of the WBC rather than just the southern edge as is the case in the barotropic ocean. Furthermore, they enhance the meandering of the WBC after it has dismounted the western slope and also lead to the development of a recirculation gyre on the southern flank of the WBC at the point of separation from the slope. In the highly baroclinic circulations there is also a recirculation gyre on the northern flank of the WBC. The two recirculation gyres cause a realistic increase in transport of the WBC as it separates from the continental slope.

- The results of Chapter IV suggest that instabilities can be caused by highly inertial or highly baroclinic flows. It is suggested that an important parameter in characterising the nature of the flow is the Rayleigh Number, $\mathsf{Ra} = \frac{\mathsf{Ro}\mathcal{T}^2}{\kappa\nu}$ which is introduced in §3.3. When Ra is small, the circulation is dominated by wind-forcing and topographic stretching; when Ra is large, we observe features such as meandering of the WBC, a recirculation gyre and shedding of warm and cold core rings.

To summarise, I believe that this thesis develops a simple model of rapidly rotating fluid and utilises it to provide a simple interpretation of many of the ubiquitous large-scale features of ocean circulation.

5.2 Further work

There are several directions in which the work of this thesis can be advanced. The investigations carried out in this thesis, even those of Chapter 4, have been highly idealised. The emphasis has been on identifying and understanding the fundamental characteristics of the DIT model rather than on reproducing in detail specific features observed in the Atlantic and other oceans. However, a more rigorous numerical study of the DIT ocean basin can be performed by using a finite-element code to construct realistic coastlines and bathymetry as well as more realistic thermal and wind forcing fields. It would be interesting to see how accurately the simple DIT model can reproduce the Atlantic circulation patterns.

In addition to the DIT and two-layer models discussed here, there are two further reductions of the LSGE which can be studied. The Generalised Two-Layer Equations (Appendix A) derive from a very general ansatz concerning the vertical structure of the ocean, although they do not include the DIT. However, the resulting equations are of such complexity that interpreting them is not straightforward. Furthermore, apart from in a few specific circumstances, a state of rest is not a solution of these equations. A more tractable problem would be to investigate a two-layer model with an active (DIT) upper layer (TLAUL). Such a model is obtained in exactly the same way as the two-layer and DIT models but we now start with the ansatz:

$$\theta \equiv T(x,y,t)\mathbb{H}(z+h(x,y,t))\,, \qquad -H(x,y) < z < 0 \tag{5.1}$$

where $\mathbb{H}$ is the Heaviside function.

TLAUL combines the two models studied in Chapters 2 and 3. Consequently, the behaviour of such a model should be explicable in terms of the behaviour of either a two-layer model or a DIT model. Furthermore, a TLAUL model would have the combined advantages of a (moderately) realistic vertical thermal structure *and* an active sea-surface temperature which is precisely what would be required by a coupled atmosphere-ocean model. Cushman-Roisin *et al.*[22] shows that the equivalent-barotropic model is a poor approximation to the two-layer model for horizontal length scales beyond the internal deformation radius. Consequently, TLAUL is arguably the next generalisation of the DIT that should be studied. Recall that the problem of baroclinic instability in a channel with no dissipation in the two-layer model (§2.2) exhibits a finite wavenumber cutoff whereas the corresponding DIT problem (§3.3.1) exhibits an ultra-violet catastrophe. Hence, I believe that it is very important to establish the behaviour of TLAUL in this situation.

From a mathematical standpoint, there is still a lot of work to be done in completing the multi-dimensional phase-space of the problem of baroclinic instability in a channel.

In §§3.3, 3.6.1 our main aim was to gain insight into the generic behaviour of the DIT. The influence of varying $\sigma \equiv \frac{\nu}{\kappa}$ and Ro was not examined. However, overall, this thesis has demonstrated that both inertia and diffusion have an important role to play in the DIT. Consequently, a detailed study into the parameter space of this problem may help to quantify the dependence.

One of the original motivations behind the development of the DIT was to construct a simple ocean that can be coupled to a simple atmospheric model in order to study a complete climate system. Other than the highly idealised and prescribed form of thermal and wind forcing of §4.2, no attempt has been made to study the influence of an atmosphere on the DIT ocean. There is some evidence in Figure 4.35 of interannual oscillations in the un-coupled DIT model. If the wind and thermal forcing were part of a closed system, the possibility exists of isolating variation on a longer time-scale as a paradigm for coupled oscillations such as ENSO. Discovery and interpretation of interannual and interdecadal oscillations within a simple model of the climate would be the ultimate vindication of the DIT.

Appendix A

Generalised Two-Layer Equations

As explained in the introduction it is beneficial to reduce the number of independent variables in the LSGE from four (namely, three spatial plus time) to three (two spatial variables plus time). This is usually achieved by specifying the vertical structure of the ocean. Most often it is assumed that the ocean consists of a finite number of immiscible layers of uniform density. Chapter 3 of this thesis assumes takes the orthogonal view point that the temperature of the ocean is independent of the vertical co-ordinate. However, these are not the only ways to achieve such a reduction. We could, instead, make the assumption that the surfaces of constant temperature and constant potential vorticity coincide. This is a considerably more general approach; it is applicable to the LSGE because temperature(θ) and the potential vorticity($\tilde{f}\frac{\partial\theta}{\partial z}$) take a simple form in these equations. In fact, because (1.17a–e) conserve both temperature and potential vorticity, we have

$$\frac{D\theta}{Dt} = \frac{D}{Dt}(\tilde{f}\theta_z), \tag{A.1}$$

(where subscripts denote differentiation)
so if at some initial time

$$\tilde{f}\theta_z = G(\theta) \tag{A.2}$$

for some *arbitrary* function G then (A.2) holds for all time. Solving for θ we find that

$$\theta = F''\left(\frac{z}{\tilde{f}} + S(x,y,t)\right) \tag{A.3}$$

where F is another arbitrary function related to G and the primes(denoting differentiation) are for later convenience as we shall require F' and F.

This idea was first introduced by Salmon[72] which dealt with reductions of the planetary geostrophic equations on a beta-plane in which the potential vorticity is $y\theta_z$. In [72], Salmon shows that if we make the choice of a Heaviside function $\mathbb{H}$ for F'' then the resulting

equations are those of a conventional two layer fluid where $h = yS$ is the depth of the upper layer. Hence the coining of the phrase *Generalised Two-Layer Equations* (GTLE). One advantage of the GTLE over the conventional two-layer equations is that we can choose F to represent a more realistic ocean in which the density is not discontinuous. An appropriate choice might be a smooth approximation to $\mathbb{H}$.

In [73] Salmon proposes that the LSGE be analysed using the same techniques and this was the original aim of the thesis. The derivation of the GTLE follows in a similar manner to the derivation of the other models.

A.1 Derivation of the GTLE

F is a prescribed function which determines the vertical temperature structure of the ocean. We need to derive an equation governing $S(x, y, t)$, and, as usual, another equation for the barotropic stream function, ψ.

As might be expected, the individual terms of this model are very much more complex than in any of the other models studied in this thesis. It is this additional complexity which hinders attempts at any analytical study of these equations and makes their behaviour difficult to understand.

$$\begin{aligned}\nabla.\mathbf{A} =&\nabla^2 S\left[F' - F'_T\right] + |\nabla S|^2\left[F'' - F''_T\right] - \frac{2z}{\tilde{f}^2}\nabla S.\nabla\tilde{f}F'' \\ &+ 2\left(\frac{\nabla^2\tilde{f}}{\tilde{f}} - \frac{|\nabla\tilde{f}|^2}{\tilde{f}^2}\right)\left[F - F_T\right] + \frac{2\nabla S.\nabla\tilde{f}}{\tilde{f}}\left[F' - F'_T\right] \\ &- \frac{z\nabla^2\tilde{f}}{\tilde{f}^2}F' + \frac{z^2|\nabla\tilde{f}|^2}{\tilde{f}^4}F'' - \frac{z}{\tilde{f}^2}\nabla\tilde{f}.\mathbf{M} + \frac{z}{\tilde{f}}\nabla.\mathbf{M}\end{aligned} \tag{A.4}$$

where

$$\begin{aligned}\mathbf{M} = \frac{1}{H}\Bigg(&\tilde{f}S_x\left[F'_B - F'_T\right] + 2\tilde{f}_x\left[F_B - F_T\right] + \frac{H\tilde{f}_x}{\tilde{f}}F'_B, \\ &\tilde{f}S_y\left[F'_B - F'_T\right] + 2\tilde{f}_y\left[F_B - F_T\right] + \frac{H\tilde{f}_y}{\tilde{f}}F'_B\Bigg)\end{aligned} \tag{A.5}$$

and we have introduced the notation $F_T \equiv F(x, y, z = 0), F_B \equiv F(x, y, z = -H)$ etc.

In this model the singularity at the equator is more explicit than in the DIT. In addition to the singularity in the co-ordinate transformation, there is also a singularity in the fundamental ansatz (A.3) where $\tilde{f} = 0$. This singularity can be avoided by replacing the ansatz with

$$\theta = F''\left(\frac{z}{\tilde{f}_{eq}} + S(x, y, t)\right) \tag{A.6}$$

where

$$\tilde{f}_{eq} = \sqrt{\tilde{f}^2 + \delta_{eq}^2} \tag{A.7}$$

as in §2.1.3.

Wind forcing and other non conservative effects are dealt with in the same manner as all other models. We again opt to use linear Rayleigh Friction (again, with the same justification as in §2.1.1). The modified equation is the same as (2.12):

$$\epsilon\nabla.\left(\frac{1}{H}\nabla\frac{\partial\psi}{\partial t}\right) = J\left(\frac{\tilde{f}}{H},\psi\right) + J\left(\frac{1}{H},\gamma\right) + \\ + \epsilon\left\{J\left(\frac{1}{H},\sigma_z\right) - \frac{\partial}{\partial x}\left[\frac{1}{H}\sigma_y\right] + \frac{\partial}{\partial y}\left[\frac{1}{H}\sigma_x\right]\right\} - \nu\zeta + \mathsf{W}(x,y)$$

where $\gamma, \sigma_z, \sigma_x, \sigma_y, W(x,y), \zeta$ are given by (2.13, 2.14, 2.15, 2.16, 2.17, 2.19) respectively. (A.1) is the generalisation Salmon's(1994)[72] vorticity equation[1] to include inertia.

To obtain an equation for the baroclinic part of the flow, namely S, we require that the vertical integral of the Temperature equation (1.17e) vanish. Note that in this case we cannot insist that (1.17e) hold at every vertical level of the ocean basin. This is because, where non-conservative effects are present, even the fundamental ansatz (A.3) does not hold exactly because neither the temperature, θ, nor the potential vorticity, $\theta_z\tilde{f}$ is conserved on fluid parcels.

$$\frac{\partial}{\partial t}\int_{-H}^{0}\theta dz + \nabla.\left[\int_{-H}^{0}\mathbf{u}\theta dz\right] = \nabla.\left[\int_{-H}^{0}\kappa\nabla\theta dz\right] + \mathsf{Q}. \tag{A.8}$$

Q represents a prescribed surface heat flux and we assume that there is no heat flux through the ocean floor.

We can proceed using the same method as in previous cases, the only difference here is that the algebra is just a little more involved. Eventually an equation for the evolution of

[1] (4.4) of [72].

S can be derived.

$$
\begin{aligned}
A_T\Bigg\{ & H\frac{\partial S}{\partial t} + J\left(\psi, S\right) + \tilde{c}_{Ro} J\left(S, \tilde{f}\right) \\
& + \frac{\epsilon}{\tilde{f}_{eq}}\left[HJ\left(S, \sigma_{z1}\right) + J\left(S, \sigma_{z2}\right) + \frac{\partial S}{\partial x}\sigma_y - \frac{\partial S}{\partial y}\sigma_x\right]\Bigg\} \\
+A_B\Bigg\{ & H\frac{\partial}{\partial t}\left(S - \frac{H}{\tilde{f}_{eq}}\right) + J\left(\psi, S - \frac{H}{\tilde{f}_{eq}}\right) + \tilde{c}_{Ro} J\left(S - \frac{H}{\tilde{f}_{eq}}, \tilde{f}\right) + \tilde{c}_H J\left(S - \frac{H}{\tilde{f}_{eq}}, \tilde{f}\right) \\
& + \frac{\epsilon}{\tilde{f}_{eq}}\left[J\left(S - \frac{H}{\tilde{f}_{eq}}, \sigma_{z2}\right) + \frac{\partial}{\partial x}\left(S - \frac{H}{\tilde{f}_{eq}}\right)\sigma_y - \frac{\partial}{\partial y}\left(S - \frac{H}{\tilde{f}_{eq}}\right)\sigma_x\right]\Bigg\} \\
& + c_{eq1} + \epsilon c_{eq2} \\
& = \nabla.\left[\nu\left(D\nabla S + E\nabla\tilde{f}\right)\right] + \nabla.\left[\kappa\left(\mu\nabla S + \alpha\nabla\tilde{f}\right)\right] \\
& \quad + \mathsf{Q}(x, y) + \mathsf{W}_s(x, y).
\end{aligned}
\tag{A.9}
$$

where

$$
sigma_{z2} = \int_{-H}^{0} z^2 \frac{\partial\theta}{\partial z} dz \tag{A.10}
$$

and

$$
A_T \equiv \frac{\tilde{f}_{eq}}{H}\left(\theta_T - \bar{\theta}\right) \qquad A_B \equiv -\frac{\tilde{f}_{eq}}{H}\left(\theta_B - \bar{\theta}\right) \tag{A.11}
$$

are weighting factors for the top and bottom layers;

$$
\tilde{c}_{Ro} \equiv \frac{\tilde{f}^2}{\tilde{f}^2 + \nu^2}\left[2\left(F_T - F_B\right) - \frac{H}{\tilde{f}_{eq}}\left(F_T' + F_B'\right)\right] \tag{A.12}
$$

corresponds to the Rossby wave speed;

$$
\tilde{c}_H \equiv \frac{\tilde{f}H}{\tilde{f}^2 + \nu^2}\left(\bar{\theta} - \theta_B\right) \tag{A.13}
$$

corresponds to the topographic wave speed; and

$$
c_{eq1} \equiv \frac{\left(\delta_{eq}^2\nu^2 + 2\nu^2\tilde{f}^2 - \delta_{eq}^2\tilde{f}^2\right)}{\tilde{f}_{eq}(\tilde{f}^2 + \nu^2)^2} J\left(\tilde{f}, S\right)\int_{-H}^{0}(\theta - \bar{\theta})^2 dz. \tag{A.14}
$$

$$
\begin{aligned}
c_{eq2} \equiv \frac{\left(\delta_{eq}^2\nu^2 + 2\nu^2\tilde{f}^2 - \delta_{eq}^2\tilde{f}^2\right)}{\tilde{f}_{eq}(\tilde{f}^2 + \nu^2)^2}\Big[& \theta_T J\left(\tilde{f}, \sigma_{z1}\right) + \theta J\left(\tilde{f}, \sigma_{z2}\right) + \tilde{f} J\left(\tilde{f}, \sigma_{z3}\right) \\
& - \frac{\partial\tilde{f}}{\partial x}\sigma_y - \frac{\partial\tilde{f}}{\partial y}\sigma_x\Big]
\end{aligned}
\tag{A.15}
$$

are the equator-correction terms. They are small everywhere except near the equator where they contribute approximately an eastward propagation tendency to S.

The diffusion coefficients of (A.9) are defined by

$$\begin{aligned} D &\equiv \frac{\tilde{f}_{eq}}{\tilde{f}^2+\nu^2}\int_{-H}^{0}(\theta-\bar{\theta})^2 dz \\ &= \frac{\tilde{f}_{eq}^2}{\tilde{f}^2+\nu^2}\left[M(S)-M\left(S-\frac{H}{\tilde{f}_{eq}}\right)\right]-\frac{\tilde{f}_{eq}H}{\tilde{f}^2+\nu^2}\bar{\theta}^2 \end{aligned} \tag{A.16}$$

and

$$\begin{aligned} E &\equiv \frac{\tilde{f}}{\tilde{f}_{eq}^2(\tilde{f}^2+\nu^2)}\int_{-H}^{0} z(\theta-\bar{\theta})^2 dz \\ &= \frac{\tilde{f}}{\tilde{f}^2+\nu^2}\Bigg[(N_B-N_T)+S(M_T-M_B) \\ &\quad +(F_T'-F_B')\left(\frac{3}{2}F_B'+\frac{1}{2}F_T'+2\frac{\tilde{f}_{eq}}{H}(F_B-F_T)\right)\Bigg] \end{aligned} \tag{A.17}$$

where

$$M(\xi)\equiv\int_0^{\xi}F''(\eta)^2 d\eta \qquad N(\xi)\equiv\int_0^{\xi}\eta F''(\eta)^2 d\eta \tag{A.18}$$

As elsewhere in this thesis, Q is the prescribed surface heat flux and the wind-forcing term is

$$\mathrm{W}_s(x,y)\equiv\nabla.\left[H\bar{\mathbf{u}}_E\left(\theta_T-\bar{\theta}\right)\right]. \tag{A.19}$$

Interestingly, for *any* prescribed function, F, the equation can be expressed as a linear combination of "conservation of temperature at the surface" and "conservation of temperature on the basin floor" + non conservative effects. Note that the thinner layer receives the greater weighting in (A.9) as the potential vorticity of the thicker layer is more strongly influenced by the barotropic (depth averaged) flow.

It is also easy to see that in the non-inertial limit $\epsilon = 0$, (A.1) and (A.9) reduce to Salmon's non-inertial GTLE[2]. These have been shown to include the conventional two-layer geostrophic equations as a special case.

In the conservative limit, (A.1, A.9) reduce to equation (5.25) and (a corrected form of[3]) (5.33) of [73]. They also include the Two Layer Equations of Chapter 2 in the case where F'' = Heaviside Function and the modified two-layer model with a third stratified layer of §2.2.4 n the case where F'' =(2.52). However, because the solution (A.3) of (A.2) assumes $G(\theta)\neq 0$, the GTLE *do not* include the DIT equations of Chapter 3.

[2](4.4) and (4.31) of [72].

[3]Equation (5.33) of [73] is incorrect, even on dimensional grounds.

Appendix B

Numerical Methods

Much of the work presented in this thesis is very numerical in nature. The principal equations which we are trying to solve (3.2,3.4) are too complicated in general to permit an analytical solution to be found. Even the barotropic model (4.1) is time-dependent and nonlinear. A glance at some of the numerically obtained solutions, for example Figures 3.37, 4.5, 4.28, reveals that there is a lot of complicated structure to describe.

However, this work is not primarily a treatise on numerical analysis. The numerical methods employed are merely tools to achieve an end. In this appendix, we present an overview of some of the more complicated and lesser known of these methods[1].

B.1 Upwinding methods

In the solution of the DIT, (3.2, 3.4) and their barotropic simplification, the BVE, (4.1) we are required to evaluate the nonlinear Jacobian

$$J\left(\psi, \frac{\zeta}{H}\right) \tag{B.1}$$

where

$$\zeta = \nabla.\left(\frac{1}{H}\nabla\psi\right). \tag{B.2}$$

Now, since

$$\frac{\partial\psi}{\partial x} = Hv \qquad \frac{\partial\psi}{\partial y} = -Hu \tag{B.3}$$

[1] All the numerical routines used to solve the equations in their various forms were implemented in "c" by me during the course of the thesis. They can be obtained at `http://members.tripod.co.uk/James_Shepherd/`. All that is required is an ANSI c-compiler.

this Jacobian can be written as

$$v\frac{\partial\zeta}{\partial y} + u\frac{\partial\zeta}{\partial x}. \tag{B.4}$$

We may therefore think of this Jacobian as describing how the flow advects the relative vorticity, $\epsilon\zeta$, around the domain. It seems plausible that the value of the vorticity at a particular point, $\mathbf{x}$, is more likely to have a stronger effect on particles downstream of $\mathbf{x}$ than on particles upstream of $\mathbf{x}$. This is the rationale behind upwind differencing.

The particular scheme employed in this thesis is *Leonard's third order upwind differencing* [45]. It replaces $u\frac{\partial\zeta}{\partial x}$ by the finite difference approximation

$$u\left(\frac{\zeta_{i+1,j}-\zeta_{i-1,j}}{2\Delta x} - \frac{\zeta_{i+1,j}-3\zeta_{i,j}+3\zeta_{i-1,j}-\zeta_{i-2,j}}{6\Delta x}\right) \quad (u>0) \tag{B.5a}$$

and

$$u\left(\frac{\zeta_{i+1,j}-\zeta_{i-1,j}}{2\Delta x} - \frac{\zeta_{i+2,j}-3\zeta_{i+1,j}+3\zeta_{i,j}-\zeta_{i-1,j}}{6\Delta x}\right) \quad (u<0). \tag{B.5b}$$

Here $\zeta_{i,j}$ is the value of ζ at the (i,j)-th gridpoint and Δx is the horizontal grid spacing. Clearly there is an analogous expression for the other half of (B.4). It is easy to show that

$$\text{(B.5a, B.5b)} = u\left(\frac{\partial\zeta}{\partial x}\right)_{i,j} + \frac{|u|(\Delta x)^3}{12}\left(\frac{\partial^4\zeta}{\partial x^4}\right)_{i,j} + O\left((\Delta x)^4\right). \tag{B.6}$$

The second term of (B.6) corresponds to a hyperdiffusion term with diffusion coefficient proportional to the local fluid velocity. This can be thought of as hyperdiffusion along streamlines. It is this term which makes the scheme stable and hence suitable for use in numerical schemes. I tried using many other diffusion schemes including explicit Laplacian diffusion, explicit hyperdiffusion and first order upwinding. Leonard's third order scheme was the most flexible of all in terms of the range of parameters for which the solution converged to a steady state or periodic orbit. Hecht *et al.*[32] performed a more complete study of numerical diffusion terms and came to the same conclusion that third-order upwinding provides better results than first-order upwinding, Laplacian- or hyper-diffusion. Their study was for the advection of a *passive* tracer in a flat bottomed basin. Clearly, the relative vorticity is far from being passive and our ocean basin (4.3(a)) is not flat-bottomed. However, my investigations suggest that the conclusions of [32] are still valid with these modifications. The same upwind differencing scheme is also used in more complicated numerical models such as the NCAR ocean component model [29].

Third-order upwinding also has another (small) advantage over its explicit counterparts. If Laplacian- or hyper- diffusion terms are being employed, then extra boundary conditions, in addition to no normal flow, are required to evaluate $\nabla^2\zeta$ or $\nabla^4\zeta$ respectively.

Commonly chosen boundary conditions are *no slip* or *no stress*. However, it has been shown (Cummins, [19]) that (at least in flat–bottomed basins) the choice of boundary condition associated with explicit Laplacian diffusion has a big effect on the solutions of the BVE (4.1)[2]. Third-order upwinding, on the other hand, requires no extra boundary conditions because the velocity, at the boundaries, is tangential to those boundaries. This is due to the single condition of no normal flow. Since the implicit hyper-diffusion terms act only along streamlines (B.6), high-order derivatives normal to the boundary are no longer required.

A further argument in support of using Leonard's scheme, is that it does not seem to affect the physical solution. Figure 4.1 shows the different solutions obtained by using upwinding, Laplacian- and hyper- diffusion for parameters where all three schemes converge to a steady solution. All three solutions look remarkably similar. Indeed, it has been pointed out by Salmon[72] that the precise form of the non-conservative terms is relatively unimportant. This is because there is *no* boundary layer on the western boundary of basins in which the ocean depth vanishes smoothly.

There is an additional nonlinear term in the temperature advection equation of the DIT (3.4). The $J(\psi, T)$ term represents advection of temperature. I tried using third-order upwinding on this term as well. However, it did not seem to produce any improvements in the results. Moreover, (3.4) is sufficiently simple that it can be solved for a large range of κ without presenting any numerical difficulties.

B.2 Adams-Bashforth-Moulton methods

The DIT (3.2, 3.4) are time–dependent equations. Hence, we need a time-stepping routine to step ζ and T forward in time. Explicit methods, such as forward Euler time stepping, and higher order versions always failed to converge to any reasonable physical solution. Fully implicit methods, such as backward Euler time stepping, have proved too slow. This is because, although most derivatives are evaluated by second order centred-difference approximations, the upwinding terms (see B.1) require the use of $\zeta_{i+2,j}$ in order to evaluate $\zeta_{i,j}$. This means that tridiagonal factorisation methods cannot be used to solve the systems. We must resort to less efficient pentadiagonal schemes. This problem also prohibits the use of the semi–implicit Alternating Direction Implicit (ADI) method.

By far the easiest method to implement and the most reliable method, in terms of producing convergent solutions relatively rapidly, has been the *Predictor-Corrector*(PC) method. This involves making an initial guess of the value of a variable (namely ζ or T in the

[2]Since there is no boundary layer on the western boundary in basins with continental slopes, the solutions for such basins would be far less sensitive to the choice of boundary condition anyway.

case of the DIT) at the new time with a Predictor and then correcting this value with a Corrector.

The most popular PC methods are probably the Adams-Bashforth-Moulton schemes (see [59], [81]). The Adams-Bashforth part is the predictor (B.7) and the Adams–Moulton part is the corrector (B.8). After a period of experimentation, I discovered the third-order method to be optimal. That is, it is more efficient than the second-order method but no less so than higher order, slower versions.

$$\text{predictor} : \zeta_{n+1} = \zeta_n + \frac{\Delta t}{12}\left(23\zeta_n - 16\zeta_{n-1} + 5\zeta_{n-2}\right) + O\left((\Delta t)^4\right) \tag{B.7}$$

$$\text{corrector} : \zeta_{n+1} = \zeta_n + \frac{\Delta t}{12}\left(5\zeta_{n+1} + 8\zeta_n - \zeta_{n-1}\right) + O\left((\Delta t)^4\right). \tag{B.8}$$

Here Δt is the time step and the "n" subscript denotes the number of steps taken (that is, the time, t).

The predictor step (B.7) only requires the values of ζ at the current and earlier times[3]. Once we have a prediction for ζ at the new time, ζ_{n+1} is then fed into the corrector (B.8). This produces a better estimate of ζ_{n+1} which is then put back into (B.8) again. We can continue to perform this iteration as many times as we like. A fixed, finite number of iterations corresponds to an (extremely convoluted) *explicit* method. Instead, I continue iterating until the correction on a given cycle was less than 1% of the variable value on all grid points ($||\Delta\zeta_{n+1}||_\infty = 0.01$). This then becomes an *implicit* method (see [59]).

The big disadvantage of Predictor-Corrector methods in general is that it is difficult to implement step size control (although good methods such as Gear formulæ are known). The ability to modify the size of the time step taken is important; if it is too small then the program will take unreasonably large times to evolve the flow whereas if it is too large the algorithm becomes unstable. Furthermore, a "suitable time step" varies with time. When the scalar fields are relatively smooth (such as at the beginning of simulations initialised from rest) we can afford to take large time steps but when the fiow contains more small scale features we have to proceed with more care and take smaller time steps.

This concept is quantified, for linear wave equations, by the *Courant-Friedrich-Lewy*(CFL) criterion. This states that the time-step must be smaller than the time taken for the fastest wave to traverse one grid space.

$$\Delta t \leq |\mathbf{u}|\Delta x \tag{B.9}$$

where $|\mathbf{u}|$ is the speed of the fastest (linear) wave. Such a time-step is given a CFL number of 1 (CFL = 1). For linear simulations we might expect to be able to simulate with a

[3]For the first step, the first-order equivalent must be used because we do not have access to ζ_{n-1} etc. Similarly, for the second step, the second-order version is appropriate.

CFL number fairly close to 1. For nonlinear simulations a CFL number of $0.1 - 0.3$ is acceptable.

In all the time dependent simulations I monitored the CFL number of the system and attempted to keep it within such an acceptable range. For any given set of experiments I empirically determined an approximate maximum CFL number at which the algorithm could proceed. I then set a minimum of approximately $25\% - 50\%$ of this maximum. The maximum and minimum that I decided upon varied according the set of experiments. For example, in the homogeneous basin experiments $0.25 \leq CFL \leq 0.50$ whereas in the DIT temperature strip (§3.4.5) and vortex experiments (§3.5), where baroclinic instability and small scales tend to be a major feature, $0.05 \leq CFL \leq 0.15$.

In addition to trying to control the CFL number, I also monitored the number of corrector steps required for convergence. I insisted that at least one corrector step must be performed but tried to keep the maximum number of steps less than ten. If either the CFL number exceeded the maximum allowed value *or* the number of corrector steps exceeded ten then I reduced the time step (by a fixed multiplicative factor, usually 0.8) and re-performed the step. Alternatively, if the CFL number fell below the minimum allowed then I increased the time step (by another multiplicative factor, usually about 1.2). The exact factors by which I varied the time step varied from experiment to experiment and were based on what seemed to produce the fastest results.

In order to change the time step it is necessary to generate grids for the various scalar fields at previous times. This was done by a quadratic interpolation when the time step was to be decreased, or extrapolation when the time step was to be increased. See Figure B.1. Quadratic interpolation is appropriate because it requires knowledge of the dynamical grid values at two previous time steps. This is also the number of grid steps required by (B.7, B.8).

Extrapolation is, in general, much less reliable then interpolation (see [59], [81]). However, the use interpolation requires the storage of an extra set of grids (one grid for each dependent variable) and the copying of this grid at every time step. This slows the algorithm down and, after some experimentation, I discovered that the extrapolation step *never* resulted in the production of erroneous grids. This is mainly because, when the algorithm decides that an increase in time step is needed, it is because the CFL number is small. Consequently, there is not much variation in the dynamical fields over one time step.

This method of time-step modification, whilst somewhat *ad hoc*, did seem particularly successful. In almost all cases, after modifying the step length and generating new grids, the simulation returned to requiring only three or four corrector steps. Most importantly, it seemed to produce reliable results within an acceptable time frame. To determine whether

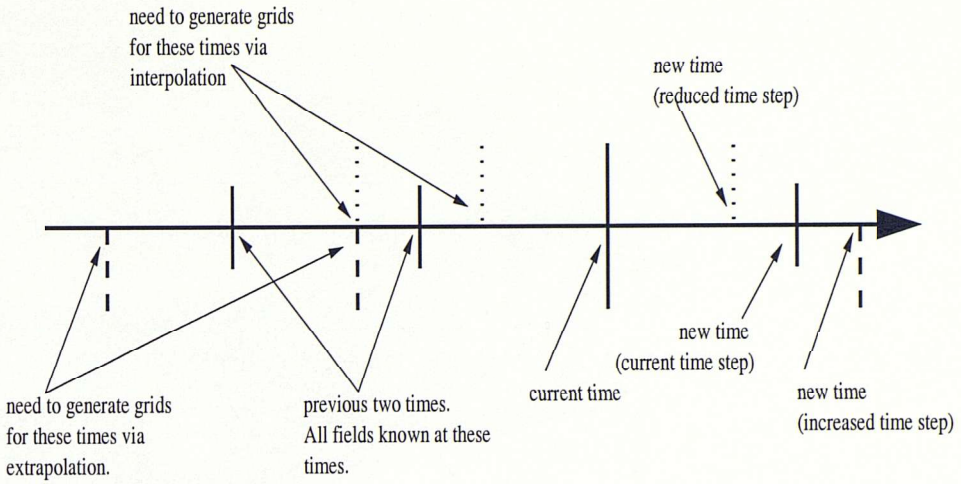


Figure B.1: If the time step changes then new grids must be generated at previous times. This is done by interpolating (or extrapolating) from currently existing grids at previous time steps.

or not this time step modification was affecting the results I performed simulations with several different values of CFL maximum, CFL minimum, step size modification factor etc. and no discernible difference was observed in any of the results.

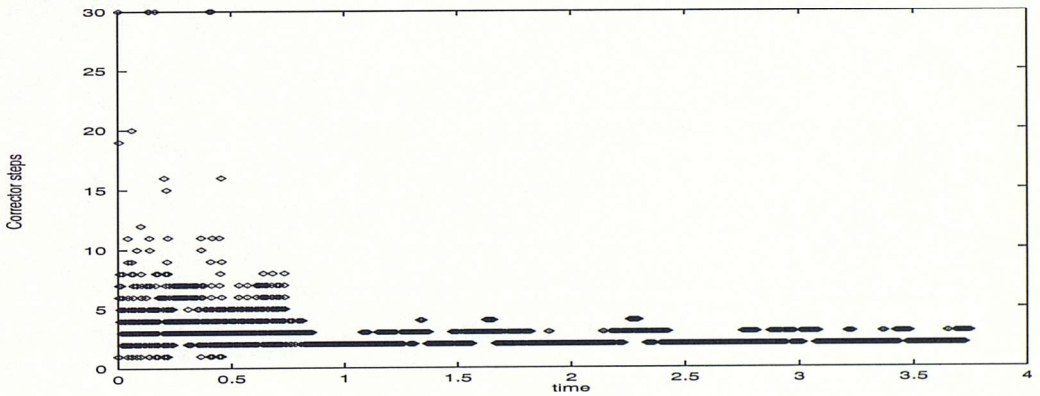


Figure B.2: Number of Corrector Steps for an entire simulation

Figures B.2, B.3 show respectively the number of corrector steps required and the CFL number (as a fraction of the ideal CFL number (B.9)) for one of the topographic DIT convection simulations §3.6.1(Figures 3.58, 3.59, 3.61). The topographic simulations were the harshest computational test. However, the CFL number is confined within the $0.1-0.2$ range for the majority of the simulation[4] The most frequent number of corrector steps required is two. The maximum allowed number of steps for this simulation was 30 and the

[4]The initial oscillation in Figure B.3 is artificial. Every time an entire time step failed due to the number of corrector steps being too great (in this case, 15), see Figure B.2, the CFL number is set equal to some (very) large number. This then tells the algorithm to reduce the step size. In order that the actual oscillations of the CFL number be visible, I have replaced this large number with zero in Figure B.3.

time-step was modified if the number of steps were greater than eight or less than two. The time step repeated if the number of steps was greater than 15 (which happened 11 times)[5]. After the simulation has been going for some time, it begins to settle down to a relatively constant CFL number with a constant number of time steps.

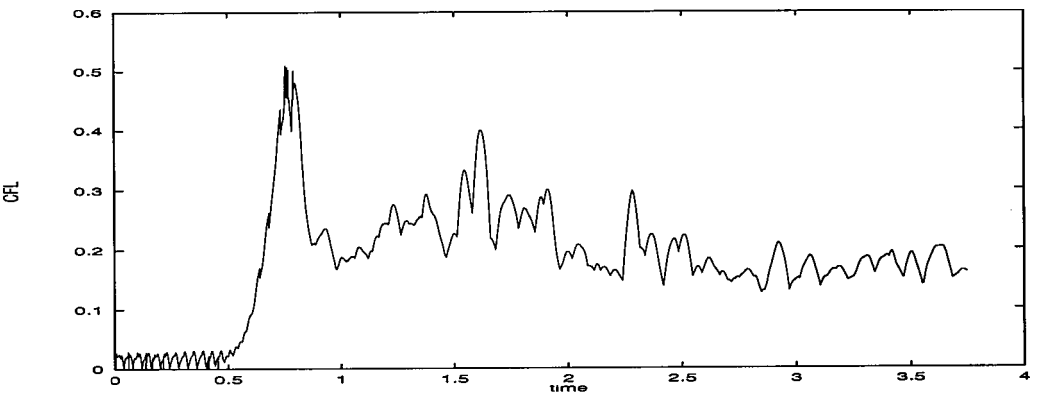


Figure B.3: CFL number as a fraction of maximum CFL time-step

B.3 Multigrid methods

All the models discussed in this thesis comprise one equation for the evolution of the barotropic flow and one evolution equation for the baroclinic flow. The former equation is expressed in the form $\frac{\partial \zeta}{\partial t} = ...$ where the relative vorticity, ζ, is given by

$$\zeta = \nabla . \left(\frac{1}{H} \nabla \psi \right) . \tag{B.10}$$

Since the streamfunction, ψ, is also required, it is necessary to invert the elliptic equation (B.10).

Since I used a Predictor-Corrector time stepper (see B.2), (B.10) must be solved several times in each time step and typically several thousand time steps were required per simulation. Thus, it is important to solve it as efficiently as possible. The most efficient way to solve elliptic PDE's is the multigrid method of Hackbusch[6] [30]. As the name suggests, this involves passing the solution between multiple grids of varying size. Fine grids quickly damp high–frequency errors but are very slow at damping low–frequency errors. Conversely, and fortuitously, coarse grids damp low–frequency errors rapidly but, clearly,

[5]This is clearly wasteful if the number of steps lies between 16 and 30, but since it only occurred 11 times out of 19189 time steps in this simulation, this inefficiency is not too damaging to the overall time taken by the simulation.

[6]Spectral methods are also very fast but they only work when H can be conveniently decomposed into spectral modes. In practice this means that the topography should be flat. Since much of this thesis is concerned with the effects of topography, spectral methods are non suitable. The multigrid method described here works, without modification, with *any* bathymetry.

cannot damp the higher frequency errors at all. Thus, using a variety of different grids damps all the errors rapidly enabling convergence after $O(N)$ operations where N is the number of grid points on the finest grid. This compares with $O(N^2)$ for the Gauss-Seidel iterative scheme and $O(N \log N)$ for optimal Successive Over Relaxation (SOR) [81].

In each simulation, the finest grid used was usually 257×257. One feature of the multigrid method is that, in order to generate the coarser grids, and determine the values on the new grid points, it is convenient if all dimensions are of the form $2^n + 1$, for some integer, n. This means that all points of all the coarse grids are also points of the finest grid. Thus, we can immediately populate each coarse grid with values of ζ from the finest grid.

In order to avoid a division by zero at the boundaries where $H = 0$, I used a 513×513 grid for the bathymetry. This means that the algorithm has access to the value of H at "half-grid points". I then approximated $\nabla.\left(\frac{1}{H}\nabla\psi\right)$ by

$$\frac{\partial}{\partial x}\left[\frac{1}{H}\frac{\partial \psi}{\partial x}\right] = \frac{1}{(\Delta x)^2}\left[\frac{\psi_{i+1,j} - \psi_{i,j}}{H_{i+\frac{1}{2},j}} - \frac{\psi_{i,j} - \psi_{i-1,j}}{H_{i-\frac{1}{2},j}}\right] \tag{B.11}$$

and $\frac{\partial}{\partial y}\left[\frac{1}{H}\frac{\partial \psi}{\partial y}\right]$ is dealt with similarly. This means that we never divide by $H_0 = 0 = H_N$. Essentially, the multigrid method just described is a sophisticated relaxation method. No attempt is made to solve the elliptic equation (even the discretised version) exactly. I tracked the error induced by this method by re-substituting the value of ψ emerging from the algorithm back into (B.10). By adjusting the various parameters[7], I was able to ensure that the error of the whole multigrid step was (considerably) less than 0.5%. Typical values were about 0.1%[8].

B.4 Newton-Raphson methods

There are basically two methods of solving systems of coupled boundary value ordinary differential equations. One is to guess all unknown values and derivatives at one end of the boundary, *shoot* this solution with an ODE stepper (such as a Runge–Kutta method) to the other end of the domain and then attempt to adjust the original guesses so that the solution fits the boundary conditions at the far end. The alternative approach is to replace the differential equations by finite–difference equations on a mesh of points covering the range of integration. An initial guess is made as to the value of the solution at each of the

[7] These include the number of relaxation steps to take on a down-stroke (going from a fine to a coarse grid) (typically two), number of relaxation steps on an up-stroke (typically four), number of times to refine solution at one resolution before attempting to refine at next resolution (typically two).

[8] This checking procedure is relatively time consuming so once the accuracy of the multigrid method had been tested, the checking was turned off.

mesh points. This initial guess does not need to satisfy either the boundary conditions or the difference equations. The idea is to perform some iteration, or *relaxation*, to bring these values closer and closer to satisfying both the equations and the boundary conditions.

Standard wisdom [59] is to "*shoot first, then relax*". This is because the relaxation method only tends to work if you have a good initial guess. Fortunately, in our case (§2.2), the solution of equations for the baroclinic instability of a (quasi) two-layer flow, we do have a good initial guess because we can determine the quasi–geostrophic limit (shallow interface) analytically. We can therefore, increase the interface gradient slowly and use our most recently determined solution as the first guess for the next gradient. Consequently, I chose to solve these equations by a relaxation method.

To explain the method, we take a simple example of a first–order differential equation

$$\frac{dy}{dx} = g(x, y) \tag{B.12}$$

which we replace by the algebraic equation

$$y_k - y_{k-1} - (x_k - x_{k-1})\, g\left[\frac{1}{2}(x_k + x_{k+1}), \frac{1}{2}(y_k + y_{k+1})\right] = 0 \tag{B.13}$$

for $k = 1...M$. The aim of the iterative procedure is to find the y_k that solve (B.13).

Let

$$E_k = y_k - y_{k-1} - (x_k - x_{k-1})\, g\left[\frac{1}{2}(x_k + x_{k+1}), \frac{1}{2}(y_k + y_{k+1})\right]. \tag{B.14}$$

At the boundaries we simply solve

$$0 = E_1 = B_1(x_1, y_1), \qquad 0 = E_M = B_M(x_M, y_M). \tag{B.15}$$

If an initial guess is made for the y_k, then it is unlikely that $E_k = 0$ at the interior points. We attempt to modify the y_k via

$$y_k^{n+1} = y_k^n + \Delta y_k. \tag{B.16}$$

Then, Taylor's Theorem gives

$$E_k^{n+1} = E_k\left(y_k + \Delta y_k, y_{k-1} + \Delta y_{k-1}\right) \approx E_k\left(y_k, y_{k-1}\right) + \frac{\partial E_k}{\partial y_k}\Delta y_k + \frac{\partial E_k}{\partial y_{k-1}}\Delta y_{k-1} \tag{B.17}$$

for the interior points $k = 2...M-1$. This is a generalisation of the Newton–Raphson method of solving nonlinear equations.

For a solution we require $E(y + \Delta y) = 0$. This, in turn, requires the solution of the $M \times 2M$ system (B.17) $= 0$.

In general, we have an N^{th} order differential equation to solve. This is equivalent to solving a system of N coupled first–order ODE's. The whole theory follows as before, replacing y, E by their vector equivalents, $\mathbf{y}, \mathbf{E}$.

$$\frac{\partial E_k}{\partial y_k}\Delta y_k \text{ becomes } \sum_{n=1}^{N} \frac{\partial \mathbf{E}_k}{\partial y_{n,k}}\Delta y_{n,k} \text{ etc.} \tag{B.18}$$

and we now have an $NM \times 2NM$ system to solve. This is done by a modified Gaussian elimination which takes advantage of the special block structure of the resulting matrix. (For further details see [59]).

Once we have our new estimate for y_k, we feed this back into the loop again and continue to iterate until Δy_k is sufficiently close to zero.

Finally, I offer some remarks about the order of the systems to be solved in §2.2 and in §3.6. In each case there exists a pair of coupled second–order complex ODE's. Treating the real and imaginary parts separately gives us an eighth–order system. However, it is also an eigenvalue problem, with complex eigenvalue ω. Eigenvalue problems are converted to standard boundary value problems by introducing a new dependent variable $y_{N+1} = \omega$ and another differential equation $\frac{dy_{N+1}}{dx} = 0$. Since ω is complex, this adds another two orders to the problem. There are two further degrees of freedom in the problem. One is taken up by specifying the phase of the wave (which converts to a boundary condition at one end ($\frac{d\phi}{dy} = 0$)). The other is taken up by specifying the amplitudes of the waves. To do this, another dependent variable y_0 is introduced[9] and corresponding equation $\frac{dy_0}{dx} = y_1^2 + y_2^2$ with boundary conditions $y_0 = 0$ at $x = x_{min}$ and $y_0 = 1$ at $x = x_{max}$. Thus, the final order of the system to be solved is 11. Acceptable results can usually obtained by using a mesh with $O(100)$ points so we are left to solve a 1100×2200 system. This would be inviable were it not for the modified Gaussian elimination technique and the fact that the Newton scheme converges typically after two or three iterations.

For the problems in §§2.2, 3.6, I used meshes with 100–500 points and specified an accuracy of 10^{-7} at each gridpoint. On a DEC-alpha 250 the solution (for one set of parameters, see 2.42, 2.43, 2.53, 2.54, 3.111) can be obtained in approximately one second.

[9]This is actually the sum of the moduli of the real parts of the two variables η and ϕ. It allows for the possibility that either η or ϕ might be zero (clearly,$\eta = \phi = 0$ is *a* solution but it is the trivial solution and we would like to prohibit the algorithm from locating it).

Appendix C

Weakly Nonlinear Analysis for DIT baroclinic instability

In this appendix are explicit representations of all the terms in the weakly non-linear analysis of §3.3.2. A note concerning notation may help: the subscripts are all chosen to reflect the order of δ which they represent. Thus, the sum of all the subscripts in any term at any stage is equal to the order of δ at which we are currently expanding. Because of our choice of scaling of the *slow* variables ξ, τ, there is therefore no such operator as $\mathcal{L}_m$ for any odd value of m.

C.1 Equations for η_n

$$\mathcal{L}_0\eta_1 = 0 \tag{C.1}$$

$$\mathcal{L}_0\eta_2 = N_2 \tag{C.2}$$

$$\mathcal{L}_0\eta_3 + \mathcal{L}_2\eta_1 = N_3 \tag{C.3}$$

$$\mathcal{L}_0\eta_4 + \mathcal{L}_2\eta_2 = N_4 \tag{C.4}$$

$$\mathcal{L}_0\eta_5 + \mathcal{L}_2\eta_3 + \mathcal{L}_4\eta_1 = N_5 \tag{C.5}$$

C.2 Linear operators

$$\mathcal{L}_0 = \mathsf{Re}^{-1}\kappa\left(\nabla^2\right)^3 + \frac{T_c^2}{12}\partial_x^2\nabla^2 \tag{C.6}$$

$$\mathcal{L}_2 = -6\mathsf{Re}^{-1}\kappa\partial_x\partial_\xi\left(\nabla^2\right)^2 - \frac{T_c^2}{12}\partial_x\partial_\xi\left(4\partial_x^2 + 2\partial_y^2\right) \tag{C.7}$$

$$\begin{aligned}\mathcal{L}_4 = {} & \left(\nabla^2\right)^2(\kappa + \mathsf{Re}^{-1})\partial_\tau - \mathsf{Re}^{-1}\kappa\left[3\left(\nabla^2\right)^2 + 12\partial_x^2\nabla^2\right]\partial_\xi^2 \\ & - \frac{T_c^2}{12}\left[6\partial_x^2 + \partial_y^2\right]\partial_\xi^2 - \frac{\chi T_c^2}{12}\partial_x^2\nabla^2\end{aligned} \tag{C.8}$$

C.3 Nonlinear terms

$$\begin{aligned}N_2 = {} & \left[\partial_y\phi_1\partial_x\nabla^2\phi_1 - \partial_x\phi_1\partial_y\nabla^2\phi_1 + \frac{1}{12}\left(\partial_y\eta_1\partial_x\nabla^2\eta_1 - \partial_x\eta_1\partial_y\nabla^2\eta_1\right)\right] \\ & + \mathsf{Re}^{-1}\left(\nabla^2\right)^2\left[\partial_y\phi_1\partial_x\eta_1 - \partial_x\phi_1\partial_y\eta_1\right]\end{aligned} \tag{C.9}$$

$$N_3 = \frac{T_c}{12}\partial_x\left[\partial_y\eta_2\partial_x\nabla^2\eta_1 - \partial_x\eta_1\partial_y\nabla^2\eta_2\right] - \mathsf{Re}^{-1}\left(\nabla^2\right)^2\partial_x\phi_1\partial_y\eta_2 \tag{C.10}$$

$$\begin{aligned}N_4 = T_c\partial_x\Bigg[& \left(\partial_y\phi_1\partial_x\nabla^2\phi_3 - \partial_x\phi_1\partial_y\nabla^2\phi_3 + \partial_y\phi_3\partial_x\nabla^2\phi_1 - \partial_x\phi_3\partial_y\nabla^2\phi_1\right) \\ & + \frac{1}{12}\left(\partial_y\eta_1\partial_x\nabla^2\eta_3 - \partial_x\eta_1\partial_y\nabla^2\eta_3 + \partial_y\eta_3\partial_x\nabla^2\eta_1 - \partial_x\eta_3\partial_y\nabla^2\eta_1\right) \\ & \partial_y\phi_1\partial_\xi(3\partial_x^2 + \partial_y^2)\phi_1 - 2\partial_x\phi_1\partial_x\partial_y\partial_\xi\phi_1 - \partial_\xi\phi_1\partial_y\nabla^2\phi_1 \\ & + \frac{1}{12}\left(\partial_y\eta_1\partial_\xi(3\partial_x^2 + \partial_y^2)\eta_1 - 2\partial_x\eta_1\partial_x\partial_y\partial_\xi\eta_1 - \partial_\xi\eta_1\partial_y\nabla^2\eta_1\right)\Bigg] \\ & T_c\partial_\xi\left[\partial_y\phi_1\partial_x\nabla^2\phi_1 - \partial_x\phi_1\partial_y\nabla^2\phi_1 + \frac{1}{12}\partial_y\eta_1\partial_x\nabla^2\eta_1 - \partial_x\eta_1\partial_y\nabla^2\eta_1\right] \\ & + \mathsf{Re}^{-1}\left(\nabla^2\right)^2\left[\partial_y\phi_1\partial_x\eta_3 - \partial_x\phi_1\partial_y\eta_3 + \partial_y\phi_3\partial_x\eta_1 - \partial_x\phi_3\partial_y\eta_1 + \partial_y\phi_1\partial_\xi\eta_1 - \partial_\xi\phi_1\partial_y\eta_1\right] \\ & + \mathsf{Re}^{-1}\partial_\xi\partial_x 4\left[\partial_y\phi_1\partial_x\eta_1 - \partial_x\phi_1\partial_y\eta_1\right]\end{aligned} \tag{C.11}$$

$$\begin{aligned}N_5 = T_c\partial_x\Bigg[& \partial_y\phi_1\partial_x\nabla^2\phi_4 - \partial_x\phi_1\partial_y\nabla^2\phi_4 + \partial_y\phi_4\partial_x\nabla^2\phi_1 - \partial_x\phi_4\partial_y\nabla^2\phi_1 \\ & + \frac{1}{12}\left(\partial_y\eta_1\partial_x\nabla^2\eta_4 - \partial_x\eta_1\partial_y\nabla^2\eta_4 + \partial_y\eta_4\partial_x\nabla^2\eta_1 - \partial_x\eta_4\partial_y\nabla^2\eta_1\right) \\ & + \frac{1}{12}\left(\partial_y\eta_1\partial_\xi(3\partial_x^2 + \partial_y^2)\eta_2 - \partial_\xi\eta_1\partial_y\nabla^2\eta_2 + \partial_y\eta_2\partial_\xi(3\partial_x^2 + \partial_y^2)\eta_1 - \partial_\xi\eta_2\partial_y\nabla^2\eta_1\right)\Bigg] \\ & + \frac{T_c}{12}\partial_\xi\left[\partial_y\eta_2\partial_x\nabla^2\eta_1 - \partial_x\eta_1\partial_y\nabla^2\eta_2\right] \\ & + \mathsf{Re}^{-1}\left(\nabla^2\right)^2\left[-\partial_x\phi_1\partial_y\eta_4 - \partial_x\phi_3\partial_y\eta_2 + \partial_y\phi_4\partial_x\eta_1 - \partial_x\phi_4\partial_y\eta_1 + \partial_y\phi_1\partial_\xi\eta_2 - \partial_\xi\phi_1\partial_y\eta_2\right] \\ & + \mathsf{Re}^{-1}\nabla^2\partial_\xi 4\left[-\partial_x\phi_1\partial_y\eta_2\right] \\ & \quad + \text{non-resonant terms ...}\end{aligned} \tag{C.12}$$

C.4 Equations for ϕ_n

$$T_c \partial_x \phi_1 = \kappa \nabla^2 \eta_1 \tag{C.13}$$

$$T_c \partial_x \phi_2 = \kappa \nabla^2 \eta_2 + \partial_y \phi_1 \partial_x \eta_1 - \partial_x \phi_1 \partial_y \eta_1 \tag{C.14}$$

$$T_c \partial_x \phi_3 + T_c \partial_\xi \phi_1 = \kappa \nabla^2 \eta_3 - 2\kappa \partial_\xi \partial_x \eta_1 - \partial_x \phi_1 \partial_y \eta_2 \tag{C.15}$$

$$\begin{aligned} T_c \partial_x \phi_4 =& \kappa \nabla^2 \eta_4 + \partial_y \phi_1 \partial_x \eta_3 - \partial_x \phi_1 \partial_y \eta_3 + \partial_y \phi_3 \partial_x \eta_1 - \partial_x \phi_3 \partial_y \eta_1 \\ &+ \partial_y \phi_1 \partial_\xi \eta_1 - \partial_\xi \phi_1 \partial_y \eta_1 \end{aligned} \tag{C.16}$$

Bibliography

[1] Abramowitz, M & Stegun, I.A : 1965 Handbook of Mathematical Functions. *Dover*

[2] Allen, J.S., Barth, J.A. & Newberger, P.A. : 1990 On intermediate models for barotropic continental shelf and slope fields PART I : formulation and comparison of exact solutions. *J. Phys. Oceanogr.* **20** 1017–1042

[3] Allen, J.S., Barth, J.A. & Newberger, P.A. : 1990 On intermediate models for barotropic continental shelf and slope fields PART III : comparison of numerical model solutions in periodic channels. *J. Phys. Oceanogr.* **20** 1949–1973

[4] Allen, J.S. & Newberger, P.A. : 1993 On intermediate models for stratified flow. *J. Phys. Oceanogr.* **23** 2462–2486

[5] Barth, J.A., Allen, J.S. & Newberger, P.A. : 1990 On intermediate models for barotropic continental shelf and slope fields PART II : comparisons of numerical solutions in doubly periodic domains. *J. Phys. Oceanogr.* **20** 1044–1076

[6] Battisti, D.S., Bhatt, U.S. & Alexander, M.A. : 1995 A modeling study of the interannual variability in the wintertime North Atlantic Ocean. *J. Climate* **8** 3067–3083

[7] Becker, J.M. & Salmon, R. : 1997 Eddy formation on a continental slope. *J. Mar. Res.* **55** 181–200

[8] Benilov, E.S. : 1993 Baroclinic instability of large amplitude geostrophic flows. *J. Fluid Mech.* **251** 501–514

[9] Berloff, P. & Meacham, S.P. : 1997 The dynamics of an equivalent-barotropic model of the wind-driven circulation. *J. Mar. Res.* **55** 407–451

[10] Berloff, P. & Meacham, S.P. : 1998 The dynamics of a simple baroclinic model of the wind-driven circulation. *J. Phys. Oceanogr.* **28** 361–388

[11] Berloff, P. & Meacham, S.P. : 1998 On the stability of wind-driven circulation. *J. Mar. Res.* **56** 937–993

[12] Bhatt, U.S., Battisti, D.S., Houghton, D.H. & Keller, L.M. : 1998 Atmosphere-ocean interaction in the North Atlantic : near surface climate variability. *J. Climate* **11** 1615–1632

[13] Bhattarcharjee, J.K. : 1987 Convection and Chaos in Fluids. *World Scientific*

[14] Bryan, K. : 1963 A numerical investigation of a nonlinear model of a wind-driven ocean. *J. Atmos. Sci.* **20** 594–606

[15] Cessi, P. & Ierley, G.R. : 1995 Symmetry-breaking multiple equilibria in quasi-geostrophic wind-driven flows. *J. Phys. Oceanogr.* **25** 1196–1205

[16] Chao, Y., Gangopadhyay, A., Bryan, F.O. & Holland, W.R. : 1996 Modeling the Gulf Stream system: how far from reality? *Geophys. Res. Lett.* **23** 3155–3158

[17] Charney, J.G. : 1947 On the scale of atmospheric motions. *Geophys. Publ.* **17**

[18] Chen, D., Busalacchi, A.J. & Rothstein, L.M. : 1994 A hybrid vertical mixing scheme and its applications to tropical ocean models. *J. Phys. Oceanogr.* **24** 2156–2179

[19] Cummins, P.F. : 1992 Inertial gyres in decaying and forced geostrophic turbulence. *J. Mar. Res.* **50** 545–566

[20] Cushman-Roisin, B. : 1986 Frontal geostrophic dynamics. *J. Phys. Oceanogr.* **16** 132–143

[21] Cushman-Roisin, B. & Tang, B.Y. : 1990 Geostrophic turbulence end emergence of eddies beyond the radius of deformation. *J. Phys. Oceanogr.* **20** 97–113

[22] Cushman-Roisin, B., Sutyrin, G.G. & Tang, B.Y. : 1992 Two-layer geostrophic dynamics. Part I: governing equations. *J. Phys. Oceanogr.* **22** 117–127

[23] Dengg, J. : 1993 : The problem of Gulf-Stream separation - a barotropic approach. *J. Phys. Oceanogr.* **23** 2182–2200

[24] Dewar, W.K. : 1998 Topography and barotropic transport control by bottom friction. *J. Mar. Res.* **56** 295–328

[25] Eady, E.T. : 1949 Long waves and cyclone waves. *Tellus* **1** 33–52

[26] Fofonoff, N.P. : 1954 Steady flow in a frictionless homogeneous ocean. *J. Mar. Res.* **13** 254–262

[27] Ford, R. : 1999 Interaction between a baroclinic western boundary current and a continental slope. *in preparation.*

[28] Gent, P.R. & McWilliams, J.C. : 1983 Consistent balanced models in bounded and periodic domains. *Dyn. Atmos. Ocean.* **7** 67–93

[29] Gent, P.R., Bryan, F.O., Danabasoglu, G., Doney, S.C., Holland, W.R., Large, W.B. & McWilliams, J.C. : 1998 The NCAR climate system model ocean component. *J. Climate* **11** 1287–1306

[30] Hackbusch, W. : 1995 Multi-grid methods and applications. *Springer*

[31] Haine, T.W.N. & Marshall, J. : 1998 Gravitational, symmetric and baroclinic instabilities of the ocean mixed layer. *J. Phys. Oceanogr.* **28** 634–658

[32] Hecht, M., Holland, W.R. & Rasch, P.J. : 1995 Upwind-weighted advection and schemes for ocean tracer transport: an evaluation in a passive tracer context. *J. Geophys. Res.* **100** 763–778

[33] Held, I.M., Pierrehumbert, R.T., Garner, S.T. & Swanson, K.L. : 1995 Surface quasi-geostrophic dynamics. *J. Fluid Mech.* **282** 1–20

[34] Hellerman, S. & Rosenstein, M.: 1983 Normal monthly wind stress over the world ocean with error estimates. *J. Phys. Oceanogr.* **13** 1093–1104

[35] Holland, W.R. : 1967 On the wind-driven circulation in an ocean with bottom topography. *Tellus* **19** 582–599

[36] Hoskins, B.J. : 1975 The geostrophic momentum approximation and the semigeostrophic equations. *J. Atmos. Sci.* **32** 233-242

[37] Ierley, G.R. & Sheremet, V.A. : 1995 Multiple solutions and advection-dominated flows in the wind-driven circulation. Part I: slip. *J. Mar. Res.* **53** 703–737

[38] Jiang, S.F., Jin, F. & Ghil, M. : 1995 Multiple equilibria and periodic solutions in a wind-driven double gyre, shallow water model. *J. Phys. Oceanogr.* **25** 764–786

[39] Johns, W.E., Shay, J.M. Bane, J.M. & Watts, D.R. : 1995 Gulf Stream structure, transport and recirculation near 68°W *J. Geophys. Res.* **100** 817–838

[40] Julien, K., Legg, S., McWilliams, J.C. & Werne, J. : 1996 Rapidly rotating turbulent Rayleigh Bénard convection. *J. Fluid Mech.* **322** 243–273

[41] Julien, K., Legg, S., McWilliams, J.C. & Werne, J. : 1996 Hard turbulence in rotating Rayleigh Bénard convection. *Phys. Rev. E* **53** 5557R–5560R

[42] Kawase, M. : 1993 Effects of a concave bottom geometry on the upwelling-driven circulation in an abyssal ocean basin. *J. Phys. Oceanogr.* **23** 400–405

[43] Kamenkovich, V., Sheremet, V.A., Pastushkov, A. & Belotserkovsky, S. : 1995 Analysis of the barotropic model of the subtropical gyre in the ocean for finite Reynolds Numbers. Part I. *J. Mar. Res.* **53** 959–994

[44] Lavoie, R.L. : 1972 A mesoscale numerical model of lake-effect storms. *J. Atmos. Sci.* **29** 1025–1040

[45] Leonard, B.P. : 1984 Third-order upwinding as a rational basis for computational fluid dynamics, *in* Computational Techniques and Applications: CTAC-83, J. Noye & C. Fletcher, eds., *Elsevier Nort-Holland* 106–120

[46] Lesieur, M. : 1990 Turbulence in Fluids. 2nd. Ed.*Kluwer Academic Publshers*

[47] McWilliams, J.C. & Gent, P.R. : 1980 Intermediate models of planetary circulation in the atmosphere and ocean. *J. Atmos. Sci.* **37** 1657–1678

[48] McWilliams, J.C. : 1984 The emergence of isolated coherent vortices in turbulent flow. *J. Fluid Mech.* **146** 21–43

[49] Meacham, S.P. & Berloff, P.: 1997 Barotropic wind-driven circulation in a small basin. *J. Mar. Res.* **55** 523–563

[50] Meacham, S.P. & Berloff, P.: 1997 Instabilities of a steady barotropic wind-driven circulation in a small basin. *J. Mar. Res.* **55** 885–913

[51] McCreary, J.P. & Anderson, D.L.T. : 1984 A simple model of El-Niño and the southern oscillation. *Monthly Weath. Rev.* **112** 934–946

[52] Munk, W.H. : 1950 On the wind-driven ocean circulation. *J. Meteorol.* **7** 79–93

[53] Moro, B. : 1990 On the nonlinear Munk model.II. Stability. *Dyn. Atmos. Ocean.* **14**203–227

[54] Newell, A.C. & Whitehead, J.A. : 1969 Finite bandwidth, finite amplitude convection. *J. Fluid Mech.* **38** 279–303

[55] Nishigaki, H. : 1995 Internal boundary layer with a velocity front: how the bottom slope controls the western boundary current path. *J. Phys. Oceanogr.* **25** 216–225

[56] Özgökmen, T.M., Chassignet, E.P. & Paiva, A.M. : 1997 Impact of wind forcing, bottom topography and inertia on midlatitude jet separation in a quasigeostrophic model. *J. Phys. Oceanogr.* **27** 2460–2476

[57] Pedlosky, J. : 1987 Geophysical Fluid Dynamics 2nd Ed. *Springer*

[58] Phillips, N.A. : 1954 Energy transformation and meridional circulations associated with simple baroclinic waves in a two-layer quasi-geostrophic model. *Tellus* **6** 273–286

[59] Press, W.H., Flannery, B.P., Teukolsky, S.A. & Vetterling, W.T. : 1992 Numerical recipes on C: the art of scientific computing 2nd. Ed. *C.U.P.*

[60] Ripa, P. : 1995 On improving a one-layer ocean model with thermodynamics. *J. Fluid Mech.* **303** 169–201

[61] Ripa, P. : 1999 On the validity of layered models of ocean dynamics and thermodynamics with reduced vertical resolution. *Dyn. Atmos. Ocean.* **29** 1–40

[62] Sakai, S. : 1988 Rossby-Kelvin instability; a new type of ageostrophic instability caused by a resonance between Rossby waves and gravity waves. *J. Fluid Mech.* **202** 149–176

[63] Robinson, A.R. & Stommel, H. : 1959 The oceanic thermocline and the associated thermohaline circulation. *Tellus* **11** 295–308

[64] Salmon, R. : 1978 Two-layer quasi-geostrophic turbulence in a simple case. *Geophys. Astrophys. Fluid. Dyn.* **10** 25–52

[65] Salmon, R. : 1980 Baroclinic instability and geostrophic turbulence. *Geophys. Astrophys. Fluid. Dyn.* **15** 167–211

[66] Salmon, R. : 1983 Practical use of Hamilton's principle. *J. Fluid Mech.* **132** 431–444

[67] Salmon, R. : 1985 New equations for nearly geostrophic flow. *J. Fluid Mech.* **153** 461–477

[68] Salmon, R, : 1988 Semigeostrophic theory as a Dirac Bracket projection. *J. Fluid Mech.* **196** 345–358

[69] Salmon, R. : 1988 Hamiltonian fluid mechanics. *Ann. Rev. Fluid Mech.* **20** 225–256

[70] Salmon, R. : 1990 The thermocline as an "internal boundary layer". *J. Mar. Res.* **48** 437–469

[71] Salmon, R. : 1992 A two-layer Gulf Stream over a continental slope. *J. Mar. Res.* **50** 211–230

[72] Salmon, R. : 1994 Generalised two-layer models of ocean circulation. *J. Mar. Res.* **52** 865–908

[73] Salmon, R. : 1996 Large-scale semigeostrophic equations for use in ocean circulation models. *J. Fluid Mech.* **318** 85–105

[74] Salmon, R. : 1998 Lectures On Geophysical Fluid Dynamics. *O.U.P.*

[75] Salmon, R. & Ford, R. : 1995 A simple model of the joint effect of baroclinicity and relief. *J. Mar. Res.* **53** 211–230

[76] Samelson, R.M. & Vallis, G.K. : 1997 Large-scale circulation with small diapycnal diffusion: the two- thermocline limit. *J. Mar. Res.* **55** 223–275

[77] Saravanan, R. & McWilliams, J.C. : 1998 Advective ocean-atmosphere interaction: an analytical stochastic model with implications for decadal variability. *J. Climate* **11** 165–188

[78] Sarkisyan, A.S. & Ivanov, V.F. : 1971 Joint effect of baroclinicity and bottom relief as an important factor in the dynamics of sea currents. *Bull. Acad. Sci. USSR Atmos. and Ocean Phys.* **7** 173–178

[79] Sheremet, V.A., Kamenkovich, V. & Pastushkov, A. : 1995 Analysis of the barotropic wind-driven ocean circulation problem. Part II. *J. Mar. Res.* **53** 995–1024

[80] Sheremet, V.A., Ierley, G.R. & Kamenkovich, V. : 1997 Eigenanalyis of the two-dimensional wind-driven ocean circulation problem *J. Mar. Res.* **55** 57–92

[81] Stoer, J. & Bulirsch, R. : 1993 Introduction to numerical analysis. 2nd. Ed. *Springer*

[82] Stommel, H. : 1948 The westward intensification of wind-driven oceanic currents. *Trans. Am. Geophys. Union* **29** 202–206

[83] Tang, B.Y. & Cushman-Roisin, B. : 1992 Two-layer geostrophic dynamics. Part II: geostrophic turbulence. *J. Phys. Oceanogr.* **22** 128–138

[84] Veronis, G. : 1966 Wind-driven circulation-Part 2. Numerical solution of the nonlinear problem. *Deep-Sea Res.* **13** 30–55

[85] Welander, P. : 1968 Wind-driven circulation in one- and two- layer oceans of variable depth. *Tellus* **20** 1–16

[86] Young, W.R. : 1994 The sub-inertial mixed layer approximation. *J. Phys. Oceanogr.* **24** 1812–1826

[87] Young, W.R. & Chen, L.G. : 1995 Baroclinic instability and thermocline gradient alignment in the mixed layer. *J. Phys. Oceanogr.* **25** 3172–3185

[88] Zebiak, S.E. & Caine, M.A. : 1987 A model El-Niño southern oscillation. *Monthly Weath. Rev.* **115** 2262–2278